GEOCHEMICAL CONTROLS ON THE DISTRIBUTION AND COMPOSITION OF BIOGENIC AND SEDIMENTARY CARBON

By

Emily Racz Estes

BA Geosciences
Wellesley College, 2010

Submitted in partial fulfillment of the requirements for the degree of
Doctor of Philosophy
at the
MASSACHUSETTS INSTITUTE OF TECHNOLOGY
and the
WOODS HOLE OCEANOGRAPHIC INSTITUTION

February 2017

Signature of Author:
Signature redacted
Joint Program in Oceanography/Applied Ocean Science and Engineering
Massachusetts Institute of Technology
and Woods Hole Oceanographic Institution
January 20, 2017

Certified by:
Signature redacted
Colleen M. Hansel
Thesis Supervisor

Accepted by:
Signature redacted
Shuhei Ono
Chair, Joint Committee for Chemical Oceanography
Woods Hole Oceanographic Institution

GEOCHEMICAL CONTROLS ON THE DISTRIBUTION AND COMPOSITION OF BIOGENIC AND SEDIMENTARY CARBON

By

Emily Racz Estes

ABSTRACT

Organic carbon (OC) preserved in marine sediments acts as a reduced carbon sink that balances the global carbon cycle. Understanding the biogeochemical mechanisms underpinning the balance between OC preservation and degradation is thus critical both to quantifying this carbon reservoir and to estimating the extent of life in the deep subsurface biosphere. This work utilizes bulk and spatially-resolved X-ray absorption spectroscopy to characterize the OC content and composition of various environmental systems in order to identify the role of minerals and surrounding geochemistry in organic carbon preservation in sediments. Biogenic manganese (Mn) oxides formed either in pure cultures of Mn-oxidizing microorganisms, in incubations of brackish estuarine waters, or as ferromanganese deposits in karstic cave systems rapidly associate with OC following precipitation. This association is stable despite Mn oxide structural ripening, suggesting that mineral-associated OC could persist during early diagenetic reactions. OC associated with bacteriogenic Mn oxides is primarily proteinaceous, including intact proteins involved in Mn oxidation and likely oxide nucleation and aggregation. Pelagic sediments from 16 sites underlying the South Pacific and North Atlantic gyres and spanning a gradient of sediment age and redox state were analyzed in order to contrast the roles of oxygen exposure, OC recalcitrance, and mineral-based protection of OC as preservation mechanisms. OC and nitrogen concentrations measured at these sites are among the lowest globally (<0.1%) and, to a first order, scale with sediment oxygenation. In the deep subsurface, however, molecular recalcitrance becomes more important than oxygen exposure time in protecting OC against remineralization. Deep OC consists of primarily amide and carboxylic carbon in a scaffolding of aliphatic and O-alkyl moieties, corroborating the extremely low C/N values observed. These findings suggest that microbes in oxic pelagic sediments are carbon-limited and may preferentially remove carbon relative to nitrogen from the organic matter pool. As a whole, this work documents how interactions with mineral surfaces and exposure to oxygen generate a reservoir of OC stabilized in sediments on at least 25-million year time scales.

Thesis supervisor: Colleen Hansel, Associate Scientist with Tenure, WHOI

Acknowledgments

This thesis exists due to the incredible efforts, insight, and encouragement of a wide range of people. First and foremost, I want to thank my advisor, Colleen Hansel, for introducing me to just how interesting the ocean is, letting me explore a diversity of projects before the perfect one coalesced, and for offering constant guidance and support. I am grateful to consider you both a mentor and friend. The rest of my committee also offered the perfect blend of guidance, interest, and critical thinking. Scott Wankel aided my thinking on sediment processes and metabolisms, set me up on the EA-IRMS, and took me sailing. I thank Dan Repeta both for teaching Marine Organic Geochemistry, where I first brainstormed many of the hypotheses tested in my thesis, and for acting as resident organic geochemistry expert and reality-checker in thinking about carbon composition. And for always have the spare lab supplies needed to help me execute experiments. I am so glad Ben Kocar moved to MIT when he did, so that he was able to advise and commiserate with me as we learned the ropes of STXM-NEXAFS and tried to push it further. Finally, I want to thank Meg Tivey not only for chairing my defense and providing some very good thoughts, but also for her dedication to students and the Joint Program.

I am grateful to have had the opportunity to sail on expedition KN223 and grateful to the amazing set of scientists and new friends I got to interact through that experience. In particular, I thank Rick Murray and Art Spivack for being great at their respective roles as Chief Scientist and head of the Geochem lab, and for their continued support and involvement following the cruise. Steve D'Hondt convinced me to try analyzing the South Pacific Gyre samples and consistently keeps me on track in regards to what research questions I'm actually answering with my data. To Chloe, Claire, and Ann, thank you for making those long days enjoyable and often hilarious, for being great models of early career scientists, and for convening our first (and second) AGU session! The captain, crew, and coring crew of KN223 deserve mention for being awesome people facilitating awesome science. Finally, I thank Dr. Andreas Teske for providing IODP site 1231 samples and Dr. Suzanna Brauer and Mara Cloutier at Appalachian State University for facilitating my cave fieldwork in Tennessee and Virginia.

I also have unending gratitude to the technicians and synchrotron staff scientists who facilitated all my data collection. In particular, I thank Carl Johnson at the WHOI mass spec facility for his dedication to analyzing tricky samples. Dennis Nordlund, our collaborator at SSRL, put so much energy into working with environmental samples, optimizing data quality, and teaching me to wrangle NEXAFS data into a meaningful form.

Within Hansel Lab, I've been lucky to have fantastic colleagues. Chris, Adiari, Carolyn, Wil, Yuanzhi, Julia, Pete, Tong, Gabriela, and Kevin all taught me so much and made for good company. My cohort at WHOI is also phenomenal—you've been great friends and science-discussion-partners. Thanks to my housemates Winn and Sarah, and officemates Rene and Randie, for friendship and riding the rollercoaster of life + thesis. Carly, thanks for being a friend and fellow dog-owner. CBC for the zaniness throughout. Kyrstin (my official mentor), Nick, Sophie, Ellie, Izi, Harriet, Julie, Jamie, Adam and Hannah, and Adam—thanks for all the adventures and making Woods Hole a place I've loved living. I cannot think of a dog more perfectly suited for me than Moxie; I am incredibly lucky to have her as a constant companion, even when she judges me for doing very boring things like writing a thesis. Finally, thanks to

Academic Programs Office and the MC&G administrators for making the Joint Program function so seamlessly. In particular, thanks to Lea Fraser for her work with the reps!

My family has supported and encouraged me in an infinite number of ways over the years. I thank my parents, Karen Racz and Terry Estes, for encouraging exploration, always letting me take the unexpected path, and teaching me to love the outdoors. Hiking up Enchanted Rock will always be a favorite childhood experience, even if I cried and came down with the flu the next day. Amy and Tobin, my grandparents, Adrienne, and Mark and Imogen, as well as Jim and Kirsten, also deserve big thank yous. And to Stella and Mabel, thank you for providing inspiration and reminding me of why science is so exciting and important. Keep on investigating the world in your own charming ways.

This research was supported by the NSF graduate research fellowship 1122374, NSF EAR-82279000, NASA Exobiology grant NNX15AM04G, WHOI Coastal Ocean Institute and Ocean Ventures Fund grants, the NSF Center for Dark Energy Biosphere Investigations (C-DEBI, OCE-0939564) graduate fellowship, and C-DEBI research grant CH20655. This work is C-DEBI contribution number 359. Portions of this research were conducted at the Stanford Synchrotron Radiation Lightsource (Stanford, CA) and the Advanced Light Source (Berkeley, CA). Use of the Stanford Synchrotron Radiation Lightsource, SLAC National Accelerator Laboratory, is supported by the U.S. Department of Energy, Office of Science, Office of Basic Energy Sciences under Contract No. DE-AC02-76SF00515. The Advanced Light Source is supported by the Director, Office of Science, Office of Basic Energy Sciences, of the U.S. Department of Energy under Contract No. DE-AC02-05CH11231.

Table of contents pg

LIST OF TABLES

LIST OF FIGURES

Chapter 1: Introduction

1.1 Motivation

Organic carbon (OC) preserved in marine sediments acts as a reduced carbon sink that balances the global carbon cycle and maintains an oxygenated atmosphere. But with greater than 99.5% of organic matter remineralized during transport and early diagenesis (Hedges spec synth), a remaining question in our understanding is how even 0.5% survives. Three primary hypotheses explain the endurance of organic matter: (a) that certain biological molecules are intrinsically resistant to degradation and/or biotic and abiotic modifications (e.g. polymerization) to organic matter increase recalcitrance, (b) that electron acceptor limitation in anoxic sediments protects organic carbon, and (c) that physical or chemical protection via association with mineral surfaces shields a fraction of otherwise labile organic matter from remineralization (Burdige, 2007). These mechanisms are not mutually exclusive and likely co-occur, but paradigmatically the predominant mechanism of preservation in a given environment will vary over time, with biotic exclusion (anoxia and chemical/physical protection) increasing in importance. Figure 1 outlines these predicted mechanisms and timescales. This work explores the prevalence of these mechanisms in a range of systems, focusing on the balance between OC preservation and degradation in carbon-poor environments.

The balance has important implications in both directions. Preservation allows OC burial, a primary flux that transfers carbon from the more rapid surface carbon cycle to the geological carbon cycle. Perturbations in the size of that flux influence earth's climate. Conversely, the quantity and quality of OC determines the extent and limits of life. Understanding how geochemical parameters such as sediment redox state and lithology may influence OC content,

composition, and bioavailability is thus vital to predicting where and how organisms may eke out a living.

1.2 Importance and prevalence of mineral-organic interactions in environmental systems

1.2.1 Mineral-based protection of organic matter and the nature of mineral-organic interactions

Bulk composition studies of sinking POM (Hedges *et al.*, 2001; Brandes *et al.*, 2004) and oxygen-exposed turbidite deposits (Cowie *et al.*, 1995) demonstrate non-selective preservation, where the composition remains approximately the same even with decreasing total organic carbon. This trend led Hedges *et al.* (2001) to propose that physical protection is the dominant preservation mechanism, as (a)biotic modifications and chemical protection via adsorption to mineral surfaces will result in selective preservation of specific biomolecules, while physical protection promotes non-selective preservation of all compound classes. Observed correlations between mineral surface area and TOC are a function of clay content (along with oxy-hydroxides and biominerals) (Ransom *et al.*, 1998), implying that preservation depends on the mineral assemblage and involve chemical mineral-OM interactions. Kleber et al. (2007) developed a schematic to describe these interactions in soil systems; an inner layer of molecules forms inner-sphere complexes with the mineral surfaces, preferentially selecting for carboxyl and amide groups that bind surface hydroxyls, followed by a mid-layer of hydrophobic compounds, and an outer layer of organic molecules and metal cations bound together via electrostatic attractions. Aging and degradation will strip away these layers, leaving only the tightly-sorbed inner layer. As shown in Figure 1, it is this layer of chemisorbed OC that is predicted to persist on the longest time scales.

Chapter 2 examines the early stages of mineral-OC interactions including templation, co-precipitation, aggregation, and adsorption using the precipitation of biogenic manganese oxides as a model system. This characterization enhances prediction of the fate of this mineral-hosted OC on longer timescales. We document the kinetics of mineral-OC interactions, varying sources of OC and association mechanisms, and the stability of mineral-OC associations.

1.2.2 Relevance of manganese oxides in environmental systems

Iron (Fe) and manganese (Mn) oxides are ubiquitous in the environment and mediate a range of interaction with organic carbon. They may promote preservation via protection or by catalyzing polymerization reactions that generate more recalcitrant OC. Conversely, Mn and Fe oxides are strong oxidants that act as electron acceptors during anaerobic remineralization. At concentrations of only 3-4 weight % in anaerobic sediments, Mn(IV) can act as the exclusive electron acceptor, with Fe(III) and SO_4^{2-} reduction predominating elsewhere (Canfield *et al.*, 1993a). By contrasting Fe and Mn residence times with carbon turnover, Canfield *et al.* (1993b) calculated that an individual atom will cycle 100-300 times in this manner, giving metal oxides a role in remineralization disproportional to their concentration.

While clays have historically been viewed as the primary control on mineral-hosted carbon (Ransom *et al.*, 1998; Bock & Mayer, 2000; Arnarson & Keil, 2001; Dickens *et al.*, 2006; Dümig *et al.*, 2012), iron (Fe) oxides have more recently been shown to serve as a substantial sink for carbon in a wide range of marine and terrestrial environments, and even in systems where Fe oxides are not considered stable (Kaiser & Guggenberger, 2000; Poulton & Raiswell, 2005; Lalonde *et al.*, 2012; Roy *et al.*, 2013; Picard *et al.*, 2015). Specifically, Fe oxides in marine sediments host an average of 20% of total organic carbon, levels that are

disproportionally higher than their abundance (Lalonde *et al.*, 2012). In addition to Fe oxides, manganese (Mn) oxides have a propensity to be associated with organic carbon (Stone & Morgan, 1984; Sunda & Kieber, 1994; Roy *et al.*, 2013; Johnson *et al.*, 2015) but have been less extensively studied. Carbon molecules can adsorb to mineral surfaces, serve as templates for mineral nucleation, and/or co-precipitate with minerals during mineral growth and aggregation (Mann *et al.*, 1993; Moreau *et al.*, 2007; Kleber *et al.*, 2015 and references therein). In fact, Fe(II)- and Mn(II)-oxidizing organisms utilize secreted organic molecules as templates for mineral growth (Emerson *et al.*, 1989; Chan *et al.*, 2011) such that the association of certain biomolecule classes with oxide minerals may serve as a signature for biomineralization.

Conversely, metal oxides can serve as strong oxidants of organic matter (Stone & Morgan, 1984; Sunda & Kieber, 1994). Oxidized Mn species also drive microbially-mediated litter decomposition in terrestrial systems (Berg *et al.*, 2010; Keiluweit *et al.*, 2015). In fact, both preservation and alteration of oxide-hosted carbon may take place, perhaps simultaneously, within a given deposit. Mn oxide deposits formed in a wastewater treatment facility contained alternating layers of Mn oxides and physically and chemically protected organic carbon; yet, evidence for OC degradation in that system pointed to simultaneous Mn oxide-induced carbon oxidation to low molecular weight OC (Johnson *et al.*, 2015). Thus, these metal oxides appear to play an outsized role both in the preservation and transformation of OC. Despite this, there remains a paucity of information on the abundance and composition of carbon associated with Mn oxides within biogenic precipitates and environmental systems, limiting our understanding of the underlying mechanisms and the potential role of such minerals as archives of organic molecules. As such, biogenic Mn oxides were selected as a model system for Chapter 2; not only do they have environmental relevance, their reactivity is likely to generate an observable

chemical signature that, once identified, can be used when attempting to track mineral-OC interactions in environmental samples.

1.3 Content and composition of sedimentary organic matter

1.3.1 Geochemistry and microbiology of pelagic sediments

By volume, about half of global sediments are pelagic (Hay *et al.*, 1988). Typified by slow sedimentation rates and sparse inputs of organic carbon, these environments nonetheless sustain active microbial communities (Biddle *et al.*, 2008; Orcutt *et al.*, 2011; Kallmeyer *et al.*, 2012; Jørgensen *et al.*, 2013; Lloyd *et al.*, 2013; Russell *et al.*, 2016) at depths of up to ~2.5 km below seafloor (Inagaki *et al.*, 2015) utilizing a range of adaptations to garner energy from the environment (Lever *et al.*, 2015). Oxygenated sediments comprise 9-37% of the global seafloor and likewise contain active microbial communities that couple aerobic respiration to oxidation of organic matter, despite its scarcity in those environments (Archer *et al.*, 2002; D'Hondt *et al.*, 2009, 2015; Roy *et al.*, 2012).

Depth profiles of OC concentrations in sediments can be modeled by describing OC as a single pool that becomes increasingly less reactive with depth (Middelburg, 1989; Boudreau & Ruddick, 1992; Arndt *et al.*, 2013). A range of mechanisms, however, likely contribute to decreased reactivity, from recalcitrance to preservation of otherwise more "labile" OC due to association with mineral surfaces or electron acceptor limitation. Indeed, sediment geochemical parameters structure the microbial communities present with lithology, redox, and OC all appearing to play major roles (Parkes *et al.*, 2005; Durbin & Teske, 2011; Picard & Ferdelman, 2011; Jorgensen *et al.*, 2012; Jørgensen *et al.*, 2013). Whether this correlation is due to changes

in chemical potential, geochemistry-induced shifts in compound bioavailability (e.g. pH or redox changes liberate adsorbed OC), or other factors remains unknown. Nonetheless, due to these factors, OC content alone is not a predictor of availability (Durbin & Teske, 2012) or potential energy yields (LaRowe & Van Cappellen, 2011).

1.3.2 Oxygen exposure, recalcitrant carbon, and the generation of recalcitrant molecules

Oxygen exposure time is a common metric used to explain the concentration and distribution of organic carbon in sediments, where organic carbon burial is inversely correlated with time of exposure to molecular oxygen (Cowie *et al.*, 1995; Meyers & Silliman, 1996; Hartnett *et al.*, 1998; Arnarson & Keil, 2007). The parameter nicely encapsulates other metrics that have been considered (age, primary productivity, distance from shore, etc.) but studies targeting this effect have not yet extrapolated results from millennia to the million-year time scales that organic matter in pelagic sediments experience. Chapter 3 addresses this discrepancy, characterizing the content and composition of the small fraction of OC persisting in oxygenated sediments at up to 25 m below seafloor and over ~24 Ma and questioning why the fraction remaining is not more available to microbial life.

Oxidative degradation of OC may be additionally limited by molecular recalcitrance that makes a compound thermodynamically or enzymatically inaccessible to heterotrophic organisms. The origin of recalcitrant molecules remains a topic of debate; evidence exists both for a selective winnowing of compounds to only the most recalcitrant as well as the generation of these compounds via biotic and abiotic reactions. Likely, the composition of persistent carbon reflects a combination of those mechanisms, with bacteria transforming simple organic molecules into recalcitrant exudates (Lechtenfeld *et al.*, 2014). Flerus *et al.* (2012) find an

inverse correlation between dissolved organic matter age and average mass, where mass and unsaturations increase over time. These trends are further interpreted as evidence for bacterial transformations of organic matter generating recalcitrant compounds (Flerus *et al.*, 2012).

As sedimentary OC is notoriously difficult to describe and oftentimes referred to as "molecularly-uncharacterized organic matter" (Wakeham *et al.*, 1997; Hedges *et al.*, 2000), it is typically presumed to be recalcitrant. Sedimentary OC and the uncharacterizable fraction of DOC and sinking particulate matter is typified by a high amino acid or peptide-like component (Hedges *et al.*, 2001; Brandes *et al.*, 2004; Hertkorn *et al.*, 2006) and alkyl and O-alkyl groups (Brandes *et al.*, 2004; Dickens *et al.*, 2006; Hertkorn *et al.*, 2006; Mao *et al.*, 2011) interpreted as partial oxidation reactions resulting in substituted and copolymerized carbohydrate structures (Mao *et al.*, 2011). Chapters 3 and 4 further contribute to our understanding of this material by applying a novel spectroscopic technique to characterize OC and better assess its molecular recalcitrance, or conversely, whether there are other underlying reasons for its persistence.

1.4 Environmental applications of near-edge X-ray absorption fine structure spectroscopy

This work employs synchrotron x-ray based scanning transmission x-ray microscopy (STXM) coupled to near edge x-ray absorption fine structure spectroscopy (NEXAFS). As applied to environmental samples, STXM-NEXAFS is a relatively new technique permitting observations of spatial associations and identification of organic functional groups, classes of biological molecules, and metal valence states. Under highly controlled experimental conditions, NEXAFS is additionally sensitive to molecular orientation and adsorption mechanisms, discerning, for instance, how orientation of mineral-adsorbed amino acids varies with degree of surface coverage (Camargo *et al.*, 2003; Feyer *et al.*, 2011). These studies further distinguish

between chemi- and physiosorption based on the degree of observed hydrogen bonding as well as whether both the mineral and C spectra reveal shifts suggestive of bonding. Metzler *et al.* (2008) document protein conformational changes during polypeptide templation of calcite biomineralization. In comparison to other spectroscopic approaches, STXM-NEXAFS can probe a smaller spatial scale than NMR and is more quantitative than μ-FTIR. As a synchrotron-based technique, it is also non-invasive, non-destructive and does not require chemical extractions or demineralization procedures (as for NMR) that might alter composition or associations (Templeton & Knowles, 2009). Further, as synchrotrons provide a high flux of X-rays, and as X-rays are tunable, synchrotron techniques are optimal for characterizing very low concentrations of elements of interest in complicated matrices (Templeton & Knowles, 2009).

Differences in orientation and protein conformation are unlikely to be observed in environmental samples given their heterogeneity, but STXM-NEXAFS can still provide insight into how organic carbon partitions within mineral aggregates and sediments and what adsorption mechanisms are operative. For instance, Solomon *et al.* (2012) emphasize the heterogeneity of soil aggregates, finding pyrogenic carbon sequestered a few microns from microbially-produced carbon. In marine particles, Brandes *et al.* (2004) also find significant heterogeneity, but determine that POM retains the same four basic classes of carbon, in varying proportions, at all depths. Chapter 4 represents the first application of STXM-NEXAFS to pelagic sediments and develops the technique for use in extremely carbon-poor systems.

1.5 References

Archer DE, Morford JL, Emerson SR (2002) A model of suboxic sedimentary diagenesis suitable for automatic tuning and gridded global domains. *Global Biogeochemical Cycles* **16**, 17-1-17–21.

Arnarson TS, Keil RG (2001) Organic–mineral interactions in marine sediments studied using density fractionation and X-ray photoelectron spectroscopy. *Organic Geochemistry* **32**, 1401–1415.

Arnarson TS, Keil RG (2007) Changes in organic matter-mineral interactions for marine sediments with varying oxygen exposure times. *Geochimica et Cosmochimica Acta* **71**, 3545–3556.

Arndt S, Jørgensen BB, LaRowe DE, Middelburg JJ, Pancost RD, Regnier P (2013) Quantifying the degradation of organic matter in marine sediments: A review and synthesis. *Earth-Science Reviews* **123**, 53–86.

Berg B, Davey MP, De Marco A, Emmett B, Faituri M, Hobbie SE, Johansson M-B, Liu C, McClaugherty C, Norell L, Rutigliano F a., Vesterdal L, Virzo De Santo a. (2010) Factors influencing limit values for pine needle litter decomposition: a synthesis for boreal and temperate pine forest systems. *Biogeochemistry* **100**, 57–73.

Biddle JF, Fitz-Gibbon S, Schuster SC, Brenchley JE, House CH (2008) Metagenomic signatures of the Peru Margin subseafloor biosphere show a genetically distinct environment. *Proceedings of the National Academy of Sciences of the United States of America* **105**, 10583–10588.

Bock MJ, Mayer LM (2000) Mesodensity organo-clay associations in a near-shore sediment. *Marine Geology* **163**, 65–75.

Boudreau BP, Ruddick BR (1992) Erratum; On a reactive continuum representation of organic matter diagenesis. *American Journal of Science* **292**, 79–0.

Brandes J, Lee C, Wakeham S, Peterson M, Jacobsen C, Wirick S, Cody G (2004) Examining marine particulate organic matter at sub-micron scales using scanning transmission X-ray microscopy and carbon X-ray absorption near edge structure spectroscopy. *Marine Chemistry* **92**, 107–121.

Burdige DJ (2007) Preservation of organic matter in marine sediments: controls, mechanisms, and an imbalance in sediment organic carbon budgets? *Chemical reviews* **107**, 467–85.

Camargo PM, Baumgärtel H, Donner C (2003) Coadsorption of the DNA bases thymine and adenine at the Au(111) electrode. *Physical Chemistry Chemical Physics* **5**, 1657–1664.

Canfield DE, Jorgensen BB, Fossing H, Glud R, Gundersen J, Ramsing NB, Thamdrup B, Hansen JW, Nielsen LP, Hall PO (1993a) Pathways of organic carbon oxidation in three continental margin sediments. *Marine geology* **113**, 27–40.

Canfield DE, Thamdrup B, Hansen JW (1993b) The anaerobic degradation of organic matter in Danish coastal sediments: iron reduction, manganese reduction, and sulfate reduction. *Geochimica et cosmochimica acta* **57**, 3867–83.

Chan CS, Fakra SC, Emerson D, Fleming EJ, Edwards KJ (2011) Lithotrophic iron-oxidizing bacteria produce organic stalks to control mineral growth: implications for biosignature formation. *The ISME journal* **5**, 717–27.

Cowie GL, Hedges JI, Prahl FG, Lange GJ de (1995) Elemental and major biochemical changes across an oxidation front in a relict turbidite: An oxygen effect. *Geochimica et Cosmochimica Acta* **59**, 33–46.

D'Hondt S, Inagaki F, Zarikian CA, Abrams LJ, Dubois N, Engelhardt T, Evans H, Ferdelman T, Gribsholt B, Harris RN, Hoppie BW, Hyun J-H, Kallmeyer J, Kim J, Lynch JE, McKinley CC, Mitsunobu S, Morono Y, Murray RW, Pockalny R, Sauvage J, Shimono T, Shiraishi F, Smith DC, Smith-Duque CE, Spivack AJ, Steinsbu BO, Suzuki Y, Szpak M, Toffin L, Uramoto G, Yamaguchi YT, Zhang G, Zhang X-H, Ziebis W (2015) Presence of oxygen and aerobic communities from sea floor to basement in deep-sea sediments. *Nature Geoscience* **8**, 299–304.

D'Hondt S, Spivack AJ, Pockalny R, Ferdelman TG, Fischer JP, Kallmeyer J, Abrams LJ, Smith DC, Graham D, Hasiuk F, Schrum H, Stancin AM (2009) Subseafloor sedimentary life in the South Pacific Gyre. *Proceedings of the National Academy of Sciences of the United States of America* **106**, 11651–11656.

Dickens AF, Baldock J, Smernik RJ, Wakeham SG, Arnarson TS, Gélinas Y, Hedges JI (2006) Solid-state 13C NMR analysis of size and density fractions of marine sediments: Insight into organic carbon sources and preservation mechanisms. *Geochimica et Cosmochimica Acta* **70**, 666–686.

Dümig A, Häusler W, Steffens M, Kögel-Knabner I (2012) Clay fractions from a soil chronosequence after glacier retreat reveal the initial evolution of organo–mineral associations. *Geochimica et Cosmochimica Acta* **85**, 1–18.

Durbin AM, Teske A (2011) Microbial diversity and stratification of South Pacific abyssal marine sediments. *Environmental Microbiology* **13**, 3219–3234.

Durbin AM, Teske A (2012) Archaea in organic-lean and organic-rich marine subsurface sediments: An environmental gradient reflected in distinct phylogenetic lineages. *Frontiers in Microbiology* **3**, 1–26.

Emerson D, Garen RE, Ghiorse WC (1989) Formation of Metallogenium-like structures by a manganese-oxiding fungus. *Archives of Microbiology* 223–231.

Feyer V, Plekan O, Šutara F, Cháb V, Matolín V, Prince KC (2011) Guanine adsorption on the Cu(110) surface. *Surface Science* **605**, 361–365.

Flerus R, Lechtenfeld OJ, Koch BP, McCallister SL, Schmitt-Kopplin P, Benner R, Kaiser K, Kattner G (2012) A molecular perspective on the ageing of marine dissolved organic matter. *Biogeosciences* **9**, 1935–1955.

Hartnett HE, Keil RG, Hedges JI, Devol AH (1998) Influence of oxygen exposure time on organic carbon preservation in continental margin sediments. *Nature* **391**, 572–575.

Hay WW, Sloan Ii JL, Wold CN (1988) Mass/Age Distribution and Composition of Sediments on the Ocean Floor and the Global Rate of Sediment Subduction. *Journal of Geophysical Research* **93940**, 933–14.

Hedges J, Eglinton G, Hatcher P, Kirchman D., Arnosti C, Derenne S, Evershed R., Kögel-Knabner I, Leeuw J. de, Littke R, Michaelis W, Rullkötter J (2000) The molecularly-uncharacterized component of nonliving organic matter in natural environments. *Organic Geochemistry* **31**, 945–958.

Hedges JI, Baldock J a, Gélinas Y, Lee C, Peterson M, Wakeham SG (2001) Evidence for non-selective preservation of organic matter in sinking marine particles. *Nature* **409**, 801–4.

Hertkorn N, Benner R, Frommberger M, Schmitt-Kopplin P, Witt M, Kaiser K, Kettrup A, Hedges JI (2006) Characterization of a major refractory component of marine dissolved organic matter. *Geochimica et Cosmochimica Acta* **70**, 2990–3010.

Inagaki F, Kubo Y, Bowles MW, Heuer VB, Ijiri A, Imachi H, Ito M, Kaneko M, Lever MA, Morita S, Morono Y, Tanikawa W, Bihan M, Bowden SA, Elvert M, Glombitza C, Gross D,

Harrington GJ, Hori T, Li K, Limmer D, Murayama M, Ohkouchi N, Ono S, Purkey M, Sanada Y, Sauvage J, Snyder G, Takano Y, Tasumi E, Terada T, Tomaru H, Wang DT, Yamada Y (2015) Exploring deep microbial life in coal-bearing sediment down to ~2.5 km below the ocean floor. *Science* **349**, 420–424.

Johnson K, Purvis G, Lopez-Capel E, Peacock C, Gray N, Wagner T, März C, Bowen L, Ojeda J, Finlay N, Robertson S, Worrall F, Greenwell C (2015) Towards a mechanistic understanding of carbon stabilization in manganese oxides. *Nature Communications* **6**, 7628.

Jorgensen SL, Hannisdal B, Lanzen A, Baumberger T, Flesland K, Fonseca R, Ovreas L, Steen IH, Thorseth IH, Pedersen RB, Schleper C (2012) Correlating microbial community profiles with geochemical data in highly stratified sediments from the Arctic Mid-Ocean Ridge. *Proceedings of the National Academy of Sciences* **109**, E2846–E2855.

Jørgensen SL, Thorseth IH, Pedersen RB, Baumberger T, Schleper C (2013) Quantitative and phylogenetic study of the Deep Sea Archaeal Group in sediments of the Arctic mid-ocean spreading ridge. *Frontiers in Microbiology* **4**, 1–11.

Kaiser K, Guggenberger G (2000) The role of DOM sorption to mineral surfaces in the preservation of organic matter in soils. *Organic Geochemistry* **31**, 711–725.

Kallmeyer J, Pockalny R, Adhikari RR, Smith DC, D'Hondt S (2012) Global distribution of microbial abundance and biomass in subseafloor sediment. *Proceedings of the National Academy of Sciences* **109**, 16213–16216.

Keiluweit M, Nico P, Harmon ME, Mao J, Pett-Ridge J, Kleber M (2015) Long-term litter decomposition controlled by manganese redox cycling. *Proceedings of the National Academy of Sciences* **112**, E5253–E5260.

Kleber M, Eusterhues K, Keiluweit M, Mikutta C, Mikutta R, Nico PS (2015) Mineral–Organic Associations: Formation, Properties, and Relevance in Soil Environments. *Advances in Agronomy* **130**, 1–140.

Kleber M, Sollins P, Sutton R (2007) A conceptual model of organo-mineral interactions in soils: self-assembly of organic molecular fragments into zonal structures on mineral surfaces. *Biogeochemistry* **85**, 9–24.

Lalonde K, Mucci A, Ouellet A, Gélinas Y (2012) Preservation of organic matter in sediments promoted by iron. *Nature* **483**, 198–200.

LaRowe DE, Cappellen P Van (2011) Degradation of natural organic matter: A thermodynamic analysis. *Geochimica et Cosmochimica Acta* **75**, 2030–2042.

Lechtenfeld OJ, Kattner G, Flerus R, McCallister SL, Schmitt-Kopplin P, Koch BP (2014) Molecular transformation and degradation of refractory dissolved organic matter in the Atlantic and Southern Ocean. *Geochim. Cosmochim. Acta* **126**, 321–337.

Lever MA, Rogers KL, Lloyd KG, Overmann J, Schink B, Thauer RK, Hoehler TM, Jørgensen BB (2015) Life under extreme energy limitation: A synthesis of laboratory- and field-based investigations. *FEMS Microbiology Reviews* **39**, 688–728.

Lloyd KG, Schreiber L, Petersen DG, Kjeldsen KU, Lever M a, Steen AD, Stepanauskas R, Richter M, Kleindienst S, Lenk S, Schramm A, Jørgensen BB (2013) Predominant archaea in marine sediments degrade detrital proteins. *Nature* **496**, 215–8.

Mann S, Archibald DD, Didymus JM, Douglas T, Heywood BR, Meldrum FC, Reeves NJ (1993) Crystallization at Inorganic-organic Interfaces: Biominerals and Biomimetic Synthesis. *Science (New York, N.Y.)* **261**, 1286–1292.

Mao J, Tremblay L, Gagné JP (2011) Structural changes of humic acids from sinking organic matter and surface sediments investigated by advanced solid-state NMR: Insights into

sources, preservation and molecularly uncharacterized components. *Geochimica et Cosmochimica Acta* **75**, 7864–7880.
Mayer LM (2004) The inertness of being organic. *Marine Chemistry* **92**, 135–140.
Metzler R a, Kim IW, Delak K, Evans JS, Zhou D, Beniash E, Wilt F, Abrecht M, Chiou J-W, Guo J, Coppersmith SN, Gilbert PUPA (2008) Probing the organic-mineral interface at the molecular level in model biominerals. *Langmuir : the ACS journal of surfaces and colloids* **24**, 2680–7.
Meyers PA, Silliman JE (1996) Organic Matter in Pleistocene to Quaternary turbidites from sites 897, 898, 899 and 900, Iberia Abyssal Plain. *In Proceedings of the Ocean Drilling Program: Scientific results* **149**, 305–313.
Middelburg JJ (1989) A simple rate model for organic matter decomposition in marine sediments. *Geochimica et Cosmochimica Acta* **53**, 1577–1581.
Moreau JW, Weber PK, Martin MC, Gilbert B, Hutcheon ID, Banfield JF (2007) Extracellular proteins limit the dispersal of biogenic nanoparticles. *Science (New York, N.Y.)* **316**, 1600–3.
Orcutt BN, Sylvan JB, Knab NJ, Edwards KJ (2011) Microbial ecology of the dark ocean above, at, and below the seafloor. *Microbiology and molecular biology reviews : MMBR* **75**, 361–422.
Parkes RJ, Webster G, Cragg BA, Weightman AJ, Newberry CJ, Ferdelman TG, Kallmeyer J, Jørgensen BB, Aiello IW, Fry JC (2005) Deep sub-seafloor prokaryotes stimulated at interfaces over geological time. *Nature* **436**, 390–4.
Picard A, Ferdelman TG (2011) Linking microbial heterotrophic activity and sediment lithology in oxic, oligotrophic sub-seafloor sediments of the north atlantic ocean. *Frontiers in microbiology* **2**, 263.
Picard A, Kappler A, Schmid G, Quaroni L, Obst M (2015) Experimental diagenesis of organo-mineral structures formed by microaerophilic Fe(II)-oxidizing bacteria. *Nature communications* **6**, 6277.
Poulton SW, Raiswell R (2005) Chemical and physical characteristics of iron oxides in riverine and glacial meltwater sediments. *Chemical Geology* **218**, 203–221.
Ransom B, Kim D, Kastner M, Wainwright S (1998) Organic matter preservation on continental slopes: importance of mineralogy and surface area. *Geochimica et Cosmochimica Acta* **62**, 1329–1345.
Roy H, Kallmeyer J, Adhikari RR, Pockalny R, Jorgensen BB, D'Hondt S (2012) Aerobic Microbial Respiration in 86-Million-Year-Old Deep-Sea Red Clay. *Science* **336**, 922–925.
Roy M, McManus J, Goñi M, Chase Z, Borgeld JC, Wheatcroft R a., Muratli JM, Megowan MR, Mix A (2013) Reactive iron and manganese distributions in seabed sediments near small mountainous rivers off Oregon and California (USA). *Continental Shelf Research* **54**, 67–79.
Russell JA, León-Zayas R, Wrighton K, Biddle JF (2016) Deep subsurface life from North Pond: Enrichment, isolation, characterization and genomes of heterotrophic bacteria. *Frontiers in Microbiology* **7**, 1–13.
Solomon D, Lehmann J, Harden J, Wang J, Kinyangi J, Heymann K, Karunakaran C, Lu Y, Wirick S, Jacobsen C (2012) Micro- and nano-environments of carbon sequestration: Multi-element STXM–NEXAFS spectromicroscopy assessment of microbial carbon and mineral associations. *Chemical Geology* **329**, 53–73.
Stone A, Morgan J (1984) Reduction and dissolution of manganese(III) and manganese(IV) oxides by organics: 2. Survey of the reactivity of organics. *Environmental science & technology* **18**, 617–624.

Sunda W, Kieber D (1994) Oxidation of humic substances by manganese oxides yields low-molecular-weight organic substrates. *Nature* **367**, 62–64.

Templeton A, Knowles E (2009) Microbial Transformations of Minerals and Metals: Recent Advances in Geomicrobiology Derived from Synchrotron-Based X-Ray Spectroscopy and X-Ray Microscopy. *Annual Review of Earth and Planetary Sciences* **37**, 367–391.

Wakeham SG, Lee C, Hedges JI, Hernes PJ, Peterson MLJ (1997) Molecular indicators of diagenetic status in marine organic matter. *Geochimica et Cosmochimica Acta* **61**, 5363–5369.

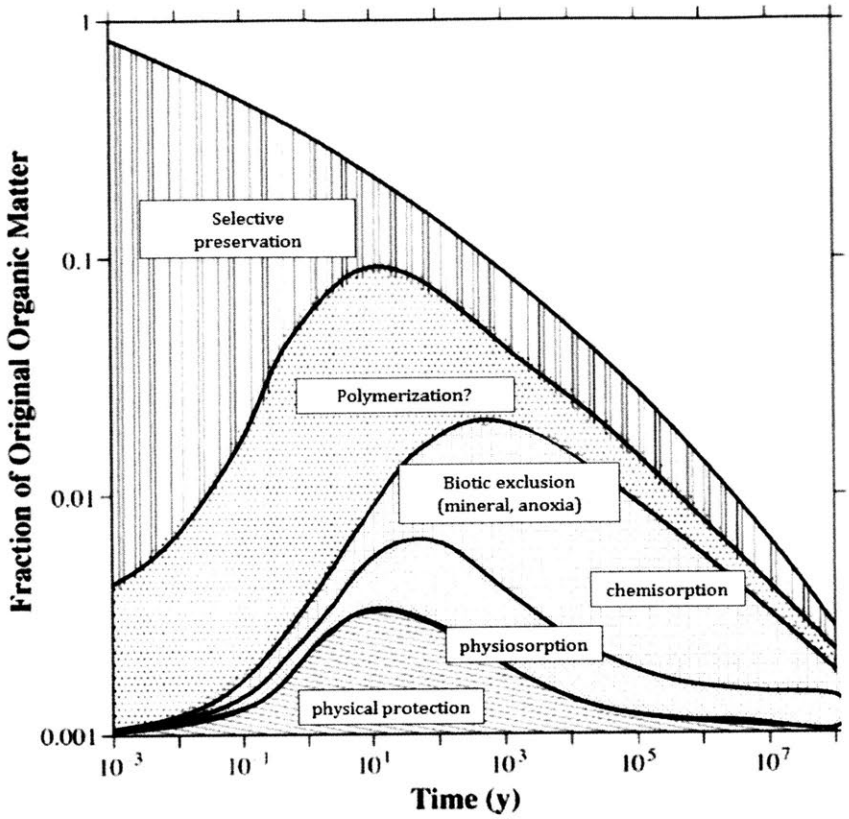

Figure 1. *(Adapted from Mayer, 2004; Burdige, 2007)* Schematic demonstrating the hypothetical relative importance and time scales on which different preservation mechanisms operate. The "biotic exclusion" category refers to three types of mineral-OC interactions (a) physical protection, (b) physiosorption, and (c) chemisorption as well as protection due to anoxia and electron-acceptor limitation. Following this schematic, mineral-OC associations provide protection against remineralization on the longest time-scales. Chapters 3 and 4 extrapolate this diagram to > 1 Ma timescales and document the occurrence of these different preservation mechanisms.

Chapter 2: Biogenic manganese oxides as reservoirs of organic carbon and proteins in terrestrial and marine environments

ABSTRACT

Manganese (Mn) oxides participate in a range of interactions with organic carbon (OC) that can lead to either carbon degradation or preservation. Here, we examine the abundance and composition of OC associated with biogenic and environmental Mn oxides to elucidate the role of Mn oxides as a reservoir for carbon and their potential for selective partitioning of particular carbon species. Mn oxides precipitated in natural brackish waters and by Mn(II)-oxidizing marine bacteria and terrestrial fungi harbor considerable levels of organic carbon (4.1-17.0 mol OC/kg mineral) compared to ferromanganese cave deposits which contain 1-2 orders of magnitude lower OC. Spectroscopic analyses indicate that the chemical composition of Mn oxide-associated OC from microbial cultures is homogeneous with bacterial Mn oxides hosting primarily proteinaceous carbon and fungal Mn oxides containing both protein- and lipopolysaccharide-like carbon. The bacterial Mn oxide-hosted proteins are involved in both Mn(II) oxidation and metal binding by these bacterial species, and could be involved in the mineral nucleation process as well. By comparison, the composition of OC associated with Mn oxides formed in natural settings (brackish waters and particularly in cave ferromanganese rock coatings) is more spatially and chemically heterogeneous. Cave Mn oxide-associated organic material is enriched in aliphatic C, which together with the lower carbon concentrations, points to more extensive microbial- or mineral-processing of carbon in this system relative to the other

systems examined in this study, and as would be expected in oligotrophic cave environments. This study highlights Mn oxides as a reservoir for carbon in varied environments. The presence and in some cases dominance of proteinaceous carbon within the biogenic and natural Mn oxides may contribute to preferential preservation of proteins in sediments and dominance of protein-dependent metabolisms in the subsurface biosphere.

2.1 Introduction

The availability of organic carbon (OC) to microbes is controlled by the concentration and composition of carbon, and the geochemical parameters that control its reactivity. In oxygenated environments, OC not immediately remineralized by microbes is typically described as "recalcitrant," generally implying that its molecular structure makes it intrinsically resistant to degradation. Molecular characterization of organic matter supports the idea of a reservoir of complex material (Hertkorn et al., 2006; Lechtenfeld et al., 2014, for instance) generated either by microbial processing, polymerization, or partial degradation reactions (Jiao et al., 2010 and references therein; Flerus et al., 2012; Johnson et al., 2015). Preservation of organic carbon, however, may be non-selective, whereby the chemical composition remains constant despite near-complete remineralization (Cowie et al., 1995; Hedges et al., 2001; Brandes et al., 2004) Further, presumed "stable" OC is not necessarily inherently resistant to degradation (Keil et al., 1994; Carlson et al., 2004; Kleber et al., 2011). In aggregate, these studies imply that the chemical composition of OC itself is not a primary control on OC preservation and that there must be other underpinning biogeochemical mechanisms at play.

Physical and/or chemical protection of OC by minerals within soils and sediments is one such mechanism of preservation. In particular, the concentration and availability of OC can be

substantially impacted by the mineralogical composition of soils/sediments and abundance of reactive mineral phases (Ransom et al., 1998; Heckman et al., 2011; Dümig et al., 2012; Lalonde et al., 2012; Doetterl et al., 2015; Keiluweit et al., 2015a); yet the underlying mechanisms remain unclear. While clays have historically been viewed as the primary control on mineral-hosted carbon (Ransom et al., 1998; Bock & Mayer, 2000; Arnarson & Keil, 2001; Dickens et al., 2006; Dümig et al., 2012), iron (Fe) oxides have more recently been shown to serve as a substantial sink for carbon in a wide range of marine and terrestrial environments, and even in systems where Fe oxides are not considered stable (Kaiser & Guggenberger, 2000; Poulton & Raiswell, 2005; Lalonde et al., 2012; Roy et al., 2013; Picard et al., 2015). Specifically, Fe oxides in marine sediments host an average of 20% of total organic carbon, levels that are disproportionally higher than their abundance (Lalonde et al., 2012). In addition to Fe oxides, manganese (Mn) oxides have a propensity to be associated with organic carbon (Stone & Morgan, 1984; Sunda & Kieber, 1994; Roy et al., 2013; Johnson et al., 2015) but have been less extensively studied. Carbon molecules can adsorb to mineral surfaces, serve as templates for mineral nucleation, and/or co-precipitate with minerals during mineral growth and aggregation (Mann et al., 1993; Moreau et al., 2007; Kleber et al., 2015 and references therein). In fact, Fe(II)- and Mn(II)-oxidizing organisms utilize secreted organic molecules as templates for mineral growth (Emerson et al., 1989; Chan et al., 2011) such that the association of certain biomolecule classes with oxide minerals may serve as a signature for biomineralization.

Conversely, metal oxides can serve as strong oxidants of organic matter (Stone & Morgan, 1984; Sunda & Kieber, 1994). In coastal sediments, comparison of carbon turnover rates with the residence times of Fe and Mn suggests that each metal atom experiences 100-300 redox cycles, often coupled to OC oxidation (Canfield et al., 1993). Oxidized Mn species also

drive microbially-mediated litter decomposition in terrestrial systems (Berg et al., 2010; Keiluweit et al., 2015b). In fact, both preservation and alteration of oxide-hosted carbon may take place, perhaps simultaneously, within a given deposit. Mn oxide deposits formed in a wastewater treatment facility contained alternating layers of Mn oxides and physically and chemically protected organic carbon; yet, evidence for OC degradation in that system pointed to simultaneous Mn oxide-induced carbon oxidation to low molecular weight OC (Johnson et al., 2015). Thus, these metal oxides appear to play an outsized role both in the preservation and transformation of OC. Despite this, there remains a paucity of information on the abundance and composition of carbon associated with Mn oxides within biogenic precipitates and environmental systems, limiting our understanding of the underlying mechanisms and the potential role of such minerals as archives of organic molecules.

Accordingly, we investigated the concentration, distribution, and composition of organic carbon associated with environmental and biogenic Mn oxides. Mn(II)-oxidizing bacteria and fungi are considered primary organisms responsible for the formation of Mn oxides within marine waters and terrestrial sediments/rock coatings (Tebo et al., 2004). To explore potential differences in the concentration and chemical composition of organic carbon associated with Mn oxides in these environments, we characterized and compared OC-Mn oxide relationships within natural Mn oxides formed in brackish marine waters and a terrestrial cave system, as well as axenic cultures of representative Mn(II)-oxidizing organisms from each environment: two coastal marine bacteria (*Roseobacter* sp. AzwK-3b and *Erythrobacter* sp. SD-21) and two terrestrial fungi (*Pyrenochaeta* sp. DS3sAY3a and *Stagonospora* sp. SRC1lsM3a). This comparison provided insight into the range of OC-Mn oxide interactions that occur throughout mineral precipitation and preservation.

2.2 Materials and Methods

2.2.1 Preparation of biological Mn oxide samples from Mn(II)-oxidizing cultures

Biogenic manganese oxides were precipitated by two alphaproteobacteria (*Roseobacter* sp. AzwK-3b and *Erythrobacter* sp. SD-21) and two ascomycete fungi (*Pyrenochaeta* sp. DS3sAY3a and *Stagnospora* sp. SRC1IsM3a). The two bacterial species are well-characterized Mn(II) oxidizers isolated from coastal surface sediments (*Erythrobacter*; Francis et al., 2001) and a coastal estuary (*Roseobacter*; Hansel & Francis, 2006). The two fungi are cosmopolitan species found in a wide variety of terrestrial habitats that were isolated from Mn-rich wetlands treating coal mine drainage (Santelli et al., 2010).

Roseobacter sp. AzwK-3b was grown on J+acetate media consisting of 10 mM sodium acetate, 10 mL/L vitamin mix (in mg/L: biotin, 320; niacin, 32; thiamin, 16; 4-aminobenzoic acid, 32; calcium pantothenic acid, 16; pyridoxine, 160; vitamin B12, 16; riboflavin, 32; folic acid, 32), 1 mL/L 8% NH_4Cl, 2 mM $KHCO_3$, 0.2 mL/L 10% KH_2PO_4, and 3.6 μM iron (as $FeSO_4 \bullet 7H_2O$) complexed to 78 μM nitrilotriacetic acid, buffered to pH 7.6 with 20 mM HEPES and prepared as 50% (volume) artificial seawater. *Erythrobacter* sp. SD-21 was grown in K-media (2 g/L peptone, 0.5 g/L yeast extract, buffered to pH 7.6 with 20 mM HEPES in 100% artificial seawater). Artificial seawater (Van Waasbergen et al., 1993) contains 0.3 M NaCl, 0.05 M $MgSO_4 \bullet 7H_2O$, 0.01 M $CaCl_2 \bullet 2H_2O$, and 0.01 M KCl. Fungi were grown in AY media consisting of 0.25 g/L sodium acetate, 0.15 g/L yeast extract, 1 mL/L trace elements stock (in mg/L: $CuSO_4 \bullet 5H_2O$, 10; $ZnSO_4 \bullet 7H_2O$, 44; $CoCl_2 \bullet 6H_2O$, 20; $Na_2MoO_4 \bullet 2H_2O$; 13) and 20 mM HEPES buffer. All cultures were grown at room temperature under ambient light. The bacterial cultures were shaken (150 rpm), while fungi were grown under static conditions with occasional manual stirring.

Minerals were precipitated in cell-free filtrate following the procedure outlined in Learman et al. (2011). The bacterial cultures were grown to mid-log phase (as determined by absorption at 600 nm). Fungi were grown for either 8-10 days (*Stagonospora*) or 14 days (*Pyrenochaeta*), consistent with optimum Mn(II) oxidation capacity of their secretomes (Zeiner, 2015). Cultures were centrifuged at 4000 x g for 15 minutes and then filtered through a 0.2 μm PVDF membrane to produce cell-free filtrates. The cell-free filtrates were amended with 100 μM Mn(II) (from a stock solution of $MnCl_2 \bullet 4H_2O$), and shaken at 150 rpm at room temperature in the light for 6 to 96 hours, following the procedure optimized in Learman et al. (2011). Learman et al. (2011) demonstrated that 96 hours is sufficient for near-complete oxidation, and for approximately 50% of the initial hexagonal birnessite phase to ripen into triclinic birnessite. For spectroscopic work, 200 μM Mn(II) was added to fungal filtrates. Previous characterization of the Mn oxides formed by fungi grown in liquid under these conditions produce solely hexagonal birnessite over the course of 96 hours (Santelli et al., 2011), but no time series were conducted for these species. In all experiments, reaction progress was tracked using the colorimetric reagent leucoberbelin blue (method described below).

At the end of the reaction period, precipitated minerals were collected by centrifugation (12500 x g) and then decanting the supernatant. Minerals were re-suspended in a smaller volume of sterile DI water and transferred to 50 mL centrifuge tubes, pelleted a second time, re-suspended in 2 mL sterile DI water, and transferred to microcentrifuge tubes. After a final centrifugation and decanting of supernatant, samples consisted of a mineral pellet in approximately 0.2 mL sterile DI. Previous experiments (data not shown) demonstrated that rinsing with DI is preferable to rinsing with natural water or media as the former does not affect

the concentration or composition of mineral-associated OC as determined by element analyzer (EA, see below).

2.2.2 Incubation experiments

2.2.2.1 Biomineralization of Mn oxides in natural waters

Five to 10 L brackish water from Oyster Pond (Falmouth, MA) was collected from a depth of 1 meter twice in late May/early June 2014. A YSI 556MPS handheld multiparameter system was used to measure pH, conductivity, salinity, temperature, and dissolved oxygen *in situ*. Duplicate 40 mL subsamples for time zero (t0) measurements of dissolved organic carbon (DOC) were collected, filtered immediately through a 0.2 μm membrane, and acidified with 40 μL concentrated hydrochloric acid (HCl). In lab, 500 mL aliquots of the unfiltered water were dispensed into sterile glass bottles and 100 μM Mn(II) (from a stock solution of $MnCl2•4H2O$) added to each. Duplicate bottles were left at 25°C, still, and in the dark, to prevent photo-oxidation, for either 4 or 8 weeks.

At the end of the incubation period, Mn(II)-amended treatments had produced a large quantity of Mn oxide particles. Quantification was not possible as a portion of particles adhered to the sides of the bottles. Mineral samples were collected by filtering water through a 0.2 μm membrane, rinsing the membrane with sterile DI twice, and rinsing the particulate mineral and associated OC off the membrane into a microcentrifuge tube. As with the culture experiments, the final product consisted of a mineral pellet in approximately 0.2 mL sterile DI. Samples for DOC were taken from the filtrate and preserved as above.

2.2.2.2 Adsorption of natural organic matter to synthetic Mn oxides

δ-MnO_2 was synthesized following the method described in Villalobos et al. (2003). Brackish water was collected from Oyster Pond in early September 2014 and analyzed at t0 for geochemical parameters as described above. Half the collected water was filtered through a 0.2 μm membrane ("0.2 μm-filtered") while the other half was left whole. 500 mL aliquots of the filtered and unfiltered water were amended with 100 μM synthetic δ-MnO_2 and incubated in the dark at 25°C for either 6 or 96 hours. At the end of the experiment, DOC and mineral samples were collected as in the biomineralization incubation experiments above.

2.2.3 Cave site description and sample collection

Ferromanganese precipitates from Daniel Boone Caverns, a relatively pristine epigene karst cave in the Tennessee River Basin, (Carmichael et al. 2013a; Carmichael et al. 2013b) were collected in June 2014. Mn oxides form within biofilms, as coatings on rocks in pools or under seeps, as crusts along cave walls and speleothems, and as particles within mud formed by mineral weathering processes. Mn oxide-coated rock samples were taken at two sites where coatings were actively forming under pooled water. Samples were placed in sterile centrifuge tubes or sample bags; coatings utilized in analyses were removed from the rock surface in lab using a sterile razor blade after mud was removed using sterile ultrapure water.

2.2.4 Quantification of Mn(III/IV) oxides

Mn(III/IV) oxide concentrations were quantified at 620 nm (Cary 60 UV-Vis spectrophotometer, Varian) using the colorimetric reagent leucoberbelin blue (LBB, Sigma; Krumbein & Altmann, 1973) which reacts with both Mn(III) and Mn(IV). Concentrations were calibrated using a permanganate standard ($KMnO_4$, EDM). A conversion factor of 2.5 was used, as 1 mole $KMnO_4$

can oxidize 5 moles LBB relative to the 2 moles LBB oxidized by a Mn(IV) oxide. This calculation assumes that the Mn oxide is 100% Mn(IV), which is largely consistent with the Mn(IV)-dominated δ-MnO_2 phases observed for the cultures (as indicated above; and in Learman et al. (2011), Santelli et al., (2011)) and the Oyster Pond incubations and cave deposits (see Results below). However, for samples containing triclinic birnessite, the Mn(III) content can be higher. Thus, this LBB conversion factor would result in an underestimation of Mn oxide concentrations for samples containing triclinic birnessite. To quantify Mn oxides in cave samples, 3-10 mg of dried and ground ferromanganese deposit from each sample was weighed in duplicate and reacted with 2 mL LBB reagent for 15 minutes with periodic shaking. The reacted solution was then filtered through a 0.2 μm membrane and analyzed.

2.2.5 Spectroscopic analysis of Mn oxides

Extended X-ray absorption fine structure (EXAFS) spectroscopy was conducted on beamline 4-3 at the Stanford Synchrotron Radiation Lightsource (SSRL) to determine the structure of the natural Mn oxides. Measurements were made using a Si(111) monochromator (Φ=90°) and calibrated with a $KMnO_4$ standard (6543.34 eV). Fluorescence data were collected with a Vortex silicon drift detector, with 3-4 scans per sample taken at room temperature from about -200 to +1000 around the Mn K-edge (6539 eV). Data processing was conducted using the SIX-PACK software program (Webb, 2005). XAS scans were averaged, background-subtracted, normalized, and converted to $\chi(k)$ spectra. Spectra were k^3-weighted and fit using a k range of 3-12$Å^{-1}$, as a substantial Fe K-edge was observed in the natural samples. Linear combination fitting was performed as described in detail in Learman et al. 2011 and Bargar et al., 2005, using δ-MnO_2, Na-birnessite, acid birnessite, groutite (α-MnOOH), feitknechite (β-MnOOH),

hausmannite (Mn_3O_4), Na-buserite, synthetic todorokite ((Na,Ca,K)(Mg,Mn)Mn_6O_{14}•5H20), pyrolusite (β-MnO_2), manganese iron oxide ($MnFe_2O_4$), groutite (Mn(III)OOH), 10-Å manganate, rhodocrosite ($MnCO_3$), and aqueous $MnSO_4$ as model compounds.

2.2.6. Carbon spectroscopic analyses

2.2.6.1 Collection of STXM-NEXAFS data

Scanning transmission X-ray microscopy (STXM) coupled to NEXAFS spectroscopy was conducted on beamline 11.0.2 at the Advanced Light Source (ALS). The STXM endstation uses Fresnel zone plates to focus the monochromatic X-ray beam and plane grating monochromator to resolve the energy. Mineral samples (1-10 μL) were pipetted onto silicon nitride membranes (Si_3N_4, Silson, Ltd., Northampton, England) and air-dried. For each sample, 200x200 μm transmission images were used to find a region that was not too optically dense. Then, optical density (OD) maps ranging between 50x50 and 15x15 μm in size were taken over the C, N, Al, and Si K-edge and the Mn and Fe L_3 edge, with OD = ln (I_0/I), and maps achieved by subtracting a pre-edge transmission image from a post-edge image. Finally, a C K-edge stack was collected from 279 to 320 eV at step sizes as small as 0.1 eV, a dwell time of 1 ms, and a spatial resolution of 75-100 nm. Image processing, alignment, and i0 normalization was conducted using the IDL package aXis2000. Regions of interest were selected based on sample morphology and element distributions as observed in element OD maps and C NEXAFS spectra extracted. Between 4-12 spectral regions were extracted per sample; representative regions were selected for analysis in this work. Spectra were imported into Igor Pro and intensity-normalized.

2.2.6.2 NEXAFS spectral peak deconvolution

Gaussian deconvolution of spectra from both bulk NEXAFS and STXM-NEXAFS was conducted using PeakFit software (SeaSolve Software Inc., San Jose, CA, USA) and following the peak assignments and parameters described in Keiluweit et al. (2012) and references therein. In brief, spectra were fit using six Gaussian peaks corresponding to approximate positions of major functional group resonances, according to the convention followed in the literature (Schumacher et al., 2005; Solomon & Lehmann, 2005; Kleber et al., 2011; Keiluweit et al., 2012). Peak magnitude and energy were allowed to vary freely, and always constrained themselves to the energy ranges expected for each functionality. As in previous works, (Kleber et al. 2011; Keiluweit et al. 2012) the ionization threshold was fit using a "transition" function in PeakFit set at 290 eV that approximates the arctangent function used by other researchers (Solomon et al. 2005), while σ* transitions were fit with two additional Gaussians. Fit results were expressed as "percent of the fit area," excluding the transition function and σ* Gaussians as they were above the energy range of interest and did not affect peak areas.

2.2.7 Quantification of organic carbon

Mineral-associated OC was quantified via elemental analyzer (elementar vario PYRO cube, Hanau, Germany). Freeze-dried, weighed samples were analyzed in triplicate as sample material allowed. Concentration calibrations were made using NIST-certified standard USGS40 L-glutamic acid as well as Na-EDTA diluted tenfold in silicon dioxide (Unimin, Spruce Pine, NC) and homogenized. A set of 4 standards were run every 10-12 samples to correct for size and drift. Cave samples were analyzed in quadruplicate. These samples were weighed into silver boats, wet with 20 μL ultrapure water, and acid fumed in a desiccator with a beaker containing

50 mL concentrated hydrochloric acid for 24 hours to remove inorganic carbon. Following this procedure, samples were dried at 60°C for 12 hours and folded into a second silver boat.

Protein associated with Mn oxides was quantified using Qubit fluorescent reagent (Life Technologies) and calibrated using BSA standards (BioRad). Proteins were removed from mineral surfaces by suspending the sample in 1.5 mL ultrapure water and sonicating three times at 40% duty cycle, keeping the samples on ice between sonication cycles. 300 μL of 6N hydrochloric was then added to the solution and incubated at 37°C for 30 minutes. Then, 75 μL 10 M trichloroacetic acid was added and the mixture incubated on ice for 30 minutes. Finally, samples were spun down, the supernatant transferred, and an additional 500 μL of 0.1 N NaOH was added. Samples were boiled for 5 minutes and cooled to room temperature prior to analysis. (Protocol modified from Ehrenreich & Widdel (1994).)

2.2.8 Protein extraction and identification

Protein extractions were performed on rinsed, concentrated Mn oxide minerals collected from cell-free filtrate of both *R.* AzwK-3b and *E.* SD-21 cultures embedded in polyacrylamide gel. Protein digestions followed a protocol adapted from Lu & Zhu (2005). Because metals interfere with acrylamide polymerization, the Mn oxide slurry (87 μL) was not mixed with the acrylamide solution (103 μL of 30% acrylamide diluted in 1M Tris) until ~30 seconds after the addition of TEMED (3 μL), ammonium persulfate (7 μL of 1% solution), and LCMS grade water (37 μL). The DTT (10 mM) incubation and washing steps in the protocol were sufficient to remove the Mn oxides prior to digestion with Trypsin (20 μg/mL, Promega). Following digestion, extracted proteins were purified and concentrated by binding to a C_8 frit (Michrom) and eluted with acetonitrile (Sigma Aldrich). Due to concerns about low protein concentrations,

samples were not controlled for mass and therefore peptide abundances are not comparable between samples. Purified samples were analyzed using an LTQ XL linear ion trap mass spectrometer in the Woods Hole Oceanographic Institution Mass Spectrometer Facility as described previously (Andeer et al., 2015). Peptides were then compared to sequences for *Roseobacter* AzwK-3b or *Erythrobacter* SD-21 respectively using Bioworks v3.3.1 SP1 (Thermo Scientific) and further analyzed using Scaffold v4 (Proteome Software). A blank containing the sterile ultrapure water used in the mineral rinsing procedure was also analyzed.

2.3 Results

2.3.1 Mn Oxide Characterization

Mn oxides formed by the Mn(II)-oxidizing bacteria and fungi explored here and grown under similar conditions were identified as a nanocrystalline hexagonal birnessite phase similar to δ-MnO_2 in previous investigations (Learman et al., 2011; Santelli et al., 2011). For *Roseobacter* AzwK-3b, however, the initial hexagonal birnessite phase is colloidal and ripens to a larger particulate triclinic birnessite phase over 96 hours (Learman et al. 2011).

Incubation of Oyster Pond water with aqueous Mn(II) led to visible Mn oxide particles starting after approximately 4 weeks. Linear combination fitting of the Mn EXAFS spectra revealed that the Mn oxides precipitated after 4 weeks consisted of hexagonal birnessite similar to δ-MnO_2 with a small contribution from either adsorbed or structurally-bound Mn(II) (8%) (Supplementary Figure S1 and Table S1). After 8-weeks, the Mn oxides remain as primarily hexagonal birnessite, but contains more Mn(II) (12%) and a substantial amount of triclinic Na-birnessite (38%). (Supplementary Figure S1 and Table S1).

The cave ferromanganese deposits, unlike the axenic cultures and brackish water incubations, contained a mixture of oxide and non-oxide mineral phases (carbonates, clays). Concentrations of Mn(III/IV) in ferromanganese rock coatings forming in two different pools within Daniel Boone Caverns, Cliff Ledge and Bacon Cove, were therefore determined to be 12.8 and 31.4 mmol Mn oxide/kg solid, respectively. Linear combination fitting of Mn EXAFS spectra collected of the ferromanganese coating samples indicated that the solid-phase Mn is dominated by δ-MnO_2 (92-93%) with the remaining either adsorbed or structurally incorporated Mn(II) (Supplementary Figure S1 and Table S1).

2.3.2 Carbon Quantification

Manganese oxides formed in the cell-free filtrate of *Roseobacter* AzwK-3b and *Erythrobacter* SD-21 harbored a substantial amount of organic carbon (Figure 1). After 96 hours, the OC concentration associated with the *Roseobacter* Mn oxides was 8.50 ± 0.84 mol OC/kg mineral. In comparison, Mn oxides formed in the *Erythrobacter* filtrate contained significantly more OC (17.00 ± 0.43 mol OC/kg mineral) than that accumulated by *Roseobacter* Mn oxides over the same timeframe ($p<0.001$, two-tailed t-test).

Mn oxides formed with cell free filtrate from the fungi *Pyrenochaeta* sp. DS3sAY3a and *Stagonospora* sp. SRC1lsM3a also harbored organic carbon (Figure 1). The concentration of carbon associated with Mn oxides precipitated by *Stagonospora* sp. and *Pyrenochaeta* sp. was 5.34 ± 0.45 and 4.15 ± 0.44 mol OC/kg mineral respectively, levels that are significantly lower than those observed for the bacterial Mn oxides ($p<0.001$, one way ANOVA) (Figure 1).

Mn oxide precipitates formed via Mn(II) oxidation within Oyster Pond water incubated for 4 weeks and 8 weeks contained 11.4 ± 0.3 and 6.2 ± 2.0 mol OC/kg mineral, respectively -

levels that are similar to those measured for the fungal and bacterial cultures (Figure 1, Supplementary Figure S2). The amount of OC associated with synthetic Mn oxides added to the Oyster Pond water was 3.4 ± 0.1 and 5.0 ± 0.1 mol OC/kg mineral after 96 hours and 4 weeks, respectively (Figure 2). The DOC associated with the synthetic Mn oxides added to filtered (0.2 μm) water after 96 hours of incubation was 1.8 ± 0.1 mol OC/kg mineral. The initial DOC concentration within the Oyster Pond water was 0.74 ± 0.02 mmol DOC/L.

Ferromanganese rock coatings from the karstic cave system contain 1-2 orders of magnitude less OC than the Mn oxides formed by axenic cultures or Oyster Pond water incubations (Figure 1). Concentrations of total organic carbon associated with the rock coatings (although not explicitly mineral-associated) ranged from 0.107 ± 0.009 to 0.123 ± 0.007 mol OC/kg solid.

2.3.3 Mn Oxide-Organic Carbon Associations and Carbon Composition

A clear association between bacteriogenic and mycogenic Mn oxide particles and organic carbon was visually observed via STXM (Figure 3). STXM C and Mn optical density (OD) maps demonstrated close spatial correlation between carbon and Mn oxide minerals formed in *Roseobacter* and *Erythrobacter* cell free filtrate (Figure 3, left panel). The chemical composition of the organic carbon associated with the biogenic Mn oxides produced in both the *Roseobacter* and *Erythrobacter* axenic cultures was spatially homogeneous. C NEXAFS spectra extracted from 4 different regions of the STXM-NEXAFS stacks for each organism, as denoted on the Mn and C OD maps, appeared nearly identical despite variations in sample morphology and relative Mn and C density (Figure 3, top right panel). The C NEXAFS spectrum from region 2a of the *Erythrobacter* Mn oxides was particularly enriched in amide/carboxylic C (~288.3 eV), but

otherwise appeared similar to regions 2b-d. For the primary functional groups, (aromatic, aliphatic, amide/carboxylic, and O-alkyl- carbon) average relative standard deviation between regions within a sample was ~10%, demonstrating homogeneity and reproducibility. Overall, *Erythrobacter* Mn oxides contained about half as much aromatic C as *Roseobacter* Mn oxides, comparable contributions from aliphatic and amide/carboxylic C, and slightly more O-alkyl-C than *Roseobacter* Mn oxides (Supplementary Table S2).

As chemical composition appeared spatially homogeneous, a spectrum was extracted from the entire particle. This "total" C spectral signature for Mn oxides produced both in the *Roseobacter* and *Erythrobacter* filtrate was most similar to a protein standard, containing peaks corresponding to aromatic, aliphatic, and amide/carboxylic C (Figure 4) and with an average amide/carboxylic C contribution of 44 ± 2% (Figure 5; Supplementary Table S2). Bulk carbon 1s NEXAFS spectra for *Roseobacter* Mn oxides (Figure S3) as well as *Erythrobacter* Mn oxides (not shown) were consistent with the STXM spectra (Figure 4). Nitrogen 1s NEXAFS (Figure S3, right panel) confirmed the identification of OC associated with Mn oxides precipitated by *Roseobacter* as a protein, with the primary N NEXAFS peak at 401.4 eV corresponding to amide N (Supplemental Figure S3). The C NEXAFS spectra of Mn oxides from *Roseobacter* and particularly *Erythrobacter* contained an additional contribution from O-alkyl-C groups at ~289.4 eV, which is not found in the protein standard.

NEXAFS spectra extracted from 4 different regions of the STXM-NEXAFS stacks appeared nearly identical for *Pyrenochaeta* sp. (Figure 3, top right panel). However, spectra extracted from morphologically distinct regions of the *Stagonospora* sp. Mn oxides differed slightly, as shown in the bottom right panel of Figure 3. These differences derive from peak intensities rather than peak positions or the presence/absence of certain peaks. Region 4a is

relatively Mn- and C-poor and contained less aliphatic and O-alkyl-C groups and more amide/carboxylic C than the other regions, based on peak fitting results, although these differences were not substantial (Supplementary Table S2). Regions 4b and 4c were both Mn- and C-rich and have more distinct shoulders at ~287.3 eV, corresponding to aliphatic C. Peak fitting results nonetheless demonstrated that *Pyrenochaeta* sp. and *Stagonospora* sp. Mn oxides were similar to each other in overall composition, only differing significantly in their O-alkyl-C content (~289.3 eV, $p=0.038$, one way ANOVA) (Supplementary Table S2). In fact, for the most prominent functional groups (aromatic, aliphatic, amide/carboxylic, and O-alkyl-C), the average relative standard deviation was 11.8% across all regions of both fungal samples.

Carbon associated with the two mycogenic Mn oxide precipitates had a distinctly different C NEXAFS signature from the bacterial oxides, and specifically is more similar to the lipopolysaccharide and neutral polysaccharide standards (Figure 4). The sample spectra were defined by shoulders for aliphatic C (~287.3 eV, average 7.2 ± 0.6% of total area) and amide or carboxyl C, (~288.3 eV, average 25.6 ± 3.0%) rising to a primary peak corresponding to O-alkyl-C at ~289.3-289.5 eV (average 42.9 ± 2.5%). Both mycogenic Mn oxide samples harbored carbon with a greater contribution from aromatic groups (~285.4 eV, average 7.7 ± 0.4%) and lower aliphatic C than pure lipopolysaccharides, but the match was otherwise strong in overall spectral shape and contribution of functional groups (LPS contains: aromatic C, 0.8%; aliphatic C, 25.9%; amide/carboxylic C, 42.3%; O-alkyl-C 13.8%). The greater contribution from O-alkyl-C and the more minor contribution from amide and carboxylic C in the fungal samples compared to the lipopolysaccharide standard likely reflected a component of neutral polysaccharides, as fitting revealed that the agarose standard is comprised of 75.2% O-alkyl-C and no amide/carboxylic C (Figure 4; Supplementary Table S2). In contrast to the average OC

composition of bacterial Mn oxides, then, mycogenic Mn oxides contained significantly less phenolic/ketonic C ($p=0.04$, one-way ANOVA), less amide/carboxylic C ($p<0.001$, one-way ANOVA), and more O-alkyl-C ($p<0.001$, one-way ANOVA) (Figure 5, Supplementary Table S2).

Similar to Mn oxides formed by axenic bacteria and fungi (Figure 3), both synthetic and actively biomineralized Mn oxides formed within the coastal water incubations had a close association with carbon (Figure 6, Supplementary Figure S4). Overlaid Mn, C, and Fe OD maps (red, green, and blue respectively) of Mn oxides formed in the unfiltered Oyster Pond water incubated for 8 weeks revealed some particulate organic C not associated with Mn oxides (regions 6 and 7, green-only) as well as some accumulated Fe (blue), but an overall spatial correlation in the distribution of Mn and C.

In contrast to the biogenic Mn oxides formed in the axenic cultures, Mn oxides formed within the Oyster Pond water incubations contained carbon with a more spatially heterogeneous chemical composition (Figure 6). C NEXAFS spectra extracted from distinct regions showed a diversity of spectral signatures that could not be matched with individual standard compounds. Instead, the spectra contained a variety of spectral features indicative of a more complex carbon composition. Regions where carbon was associated with Mn oxides had similar spectral signatures (8 week incubation, excluding C-only regions 6 and 7). C NEXAFS spectra from these regions showed the presence of aromatic, aliphatic, amide/carboxylic, and O-alkyl-C carbon, (285.4, shoulder at ~287.3, ~288.4, and ~289.4 eV, comprising $7.3 \pm 1.6\%$, $11.3 \pm 2.1\%$, $33.3 \pm 2.4\%$, and $25.7 \pm 2.1\%$ of the total fit area respectively) with the peak corresponding to amide/carboxylic C making the greatest contribution to fit area (Figure 5, Supplementary Table S2). Two regions (6 and 7) were composed of particulate carbon not associated with Mn (Figure

6). Like the Mn-bearing regions in this sample, the peak corresponding to amide/carboxylic C still made the largest contribution to overall fit area, at 36.0± 4.2% (Supplementary Table S2). These two regions differed from each other as much as from the Mn-bearing regions; region 6 had the highest aliphatic content of all analyzed regions (14.5%) and region 7 the lowest (5.9%), while the relative contribution to fit area of the other functional groups fell within the same range as the Mn-bearing regions.

STXM elemental mapping of two cave samples showed distinct regions for each element with a lesser degree of C-Mn coupling (Figure 7, left panel) than observed in the culture and water incubation samples (Figures 3 and 6). In sample "Bacon Cove 1", Mn rich regions also contained C, which in some instances was observed as what appears to be a coating around a particle (see bottom middle particle in map, Figure 7). Particulate carbon was also observed that was not associated with Mn. Iron regions are closely aligned with Mn, and thus this particulate carbon was either not mineral associated or the minerals did not contain Fe or Mn. Si maps also did not overlap with this particulate carbon (not shown). Unlike Bacon Cove, Mn and Fe were distributed as discrete particles in sample "Cliff Ledge 3," with both Mn-rich and Fe-rich particles bearing associated carbon, including coatings along the mineral grains. The samples also contained a substantial amount of C, both organic and inorganic, that was not associated with Mn- and Fe-rich regions. Some of the visible C associated with Si-bearing phases, but these were often too optically dense to extract spectra from.

C NEXAFS spectra extracted from various regions of the cave samples had similar spectral features to the biogenic Mn oxides from the cultures and coastal water incubations, including a peak identified as aromatic C at ~285.5 eV, a shoulder corresponding to aliphatic C around 287.4 eV, a primary amide/carboxylic C peak at ~288.6 eV, and a minor feature at

~289.6 eV identified as O-alkyl-C functional groups (Figure 7 right panel). Several of the regions contained inorganic carbon, identified by the sharp peak between 290.2 and 290.6 eV. Based on peak fitting results, however, inorganic C accounted for only 4-18% of the total carbon in all regions (Supplementary Table S2).

To look for differences in OC composition between spectra, regions were averaged either by site or by whether the region represented Mn oxide-associated OC or bulk OC. By site, Cliff Ledge had a higher content of amide/carboxylic C (~288.6 eV, $p=0.031$, two-tailed t-test, 41.5 ± 9.3% relative to 31.5 ± 1.0%) but lower aliphatic C (~287.5 eV, $p=0.004$, two-tailed t-test, 17.1 ± 1.6% compared to 25.1 ± 3.4% of total fit area) (Supplementary Table S2). When classified as Mn oxide-OC or bulk OC, the C-rich regions that did not contain Mn had higher aromatic and phenolic/ketonic C (~285.4 eV, $p=0.010$, two-tailed t-test, 11.3 ± 1.7% relative to 7.3 ± 1.7% and ~286.4 eV, $p=0.012$, two-tailed t-test, 3.2 ± 0.8% relative to 1.1 ± 1.0%) (Supplementary Table S2) but had no other significant differences.

Overall, the most striking difference between spectra extracted from the ferromanganese coating samples relative to bacterial/fungal and Oyster Pond Mn oxides was the contribution from aliphatic C groups (~287.3—287.5 eV). Averaging peak fitting results from all regions extracted from each sample type together showed that OC in cave samples contains 22 ± 5% aliphatic groups relative to 11 ± 3% and 7 ± 1% for the incubation and culture samples respectively ($p<0.001$, one-way ANOVA) (Figure 5, Supplementary Table S2).

2.3.4 Protein Quantification

For some samples, enough material was obtained to specifically quantify the proteins associated with the Mn oxides (Figure 1). Within the *Roseobacter* filtrate, the concentration of

proteins associated with the Mn oxides was 40.24 ± 1.12 mg protein/g mineral after 96 hours of incubation. Similar to OC, Mn oxides formed within the *Erythrobacter* filtrate contained significantly more protein (187.96 ± 26.18 mg protein/g mineral) than the *Roseobacter* Mn oxides after 96 hours ($p<0.001$, two-tailed t-test).

Not enough biogenic Mn oxides were recovered to allow for quantification of the proteins associated with *Stagonospora* sp. Mn oxides, but *Pyrenochaeta* sp. Mn oxides contained 84.55 mg protein/g mineral (Figure 1), proportionally more of the OC pool than that found associated with bacterial Mn oxides.

The concentration of OC associated with Mn oxides formed via Mn(II) oxidation within the Oyster Pond water after 8 weeks was 11.8 mg protein/g mineral (Figure 1).

For the cave samples, protein concentrations are several orders of magnitude lower than that associated with Mn oxides formed in axenic cultures, ranging from 0.05 ± 0.01 (Bacon Cove) to 0.09 ± 0.05 (Cliff Ledge 3) mg protein/g mineral (Figure 1).

2.3.5 Protein Identification

As proteins were the primary form of OC associated with bacterial Mn oxides based on C- and N-NEXAFS spectroscopy, we extracted and identified the Mn oxide-harbored proteins to gain insight into the types of proteins present in the minerals. The majority of peptides identified in the *Roseobacter* sp. AzwK-3b Mn oxide minerals (>55%, Supplementary Table S3) were associated with animal heme peroxidases (AHPs) encoded by its genome (Andeer et al., 2015). Several other proteins were identified in the *Roseobacter* extractions, but were detected at much lower relative abundances (as measured by relative spectrum counts). The Mn oxide minerals generated by *Erythrobacter* sp. SD-21 also contain a homolog to the AHPs found in

Roseobacter, MopA (Dick et al., 2008). However several other proteins were also identified in these Mn oxide minerals with similar spectral counts to MopA (ca. 7.9%).

In addition to these peroxidases, there were several other Mn oxide-associated proteins involved with ion binding or transport. One such protein in the *Roseobacter* Mn oxides was a putative metal permease belonging to a family associated with the cellular uptake of Mn^{2+} and Zn^{2+} (Claverys, 2001). Also identified were a pair of hemolysin proteins that belong to a family of proteins that are capable of binding Ca^{2+} and Zn^{2+} (Ostolaza et al., 1995). Many TonB-receptor family proteins, which are involved with the uptake of substrates such as iron-complexes (Koebnik et al., 2000), along with a number of proteases and peptidases, including at least one putative metalloprotease, were identified in the *Erythrobacter* Mn oxides. While most metalloproteases are associated with Zn, examples of proteases with improved activity when bound to manganese (Graham et al., 2005) or in the presence of manganese (Kuddus & Ramteke, 2008) have been reported.

2.4 Discussion

Mn oxides formed within brackish water incubations and as cave ferromanganese rock coatings are composed of δ-MnO_2, a poorly ordered layered birnessite phase, similar to the Mn oxides formed by the bacterial and fungal cultures (see Learman et al., 2011; Santelli et al., 2011). δ-MnO2 is the primary type of Mn oxide formed by microorganisms (Bargar et al., 2005; Webb, 2005; Santelli et al., 2011) and within near surface environments (review by Tebo et al., 2004 and references therein, Bargar et al., 2009). Similar to *Roseobacter* Mn oxides, the hexagonal birnessite phase formed in the brackish water incubations ripens to a more crystalline

triclinic birnessite phase over several weeks (Supplementary Figure S1, Supplementary Table S1).

These biogenic and natural Mn oxides harbor substantial concentrations of organic carbon, ranging from 4.2-17.0 mol OC/kg solid in bacterial and fungal cultures and brackish pond water incubations (Figure 1). In contrast, cave ferromanganese deposits host far less OC (0.09-0.12 mol OC/kg solid) (Figure 1). By assigning an approximate formula of MnO_2 to culture- and brackish water-derived Mn oxides, an OC:Mn ratio (mol:mol) can be calculated and ranges from 0.36-1.47. For cave samples, we calculate an OC:Mn of 2.99-8.37, but these values are artificially high as they reflect TOC and not just Mn oxide-associated OC. Nonetheless, the magnitude and range of OC:Mn observed in this study are consistent with other carbon-metal deposits, including Mn oxide deposits in a wastewater treatment facility (>0.22 OC:Mn) (calculated from Johnson et al., 2015), estuarine and deltaic sediments (OC:Fe of 0.2-4.72, reported by Lalonde et al., 2012), hydrothermal plume particles (OC:Fe+Mn ~2.69-17.8 calculated from Toner et al., 2009), and DOM removal by Fe-based coagulants (OC:Fe 1.9-3.5, Henneberry et al., 2012).

Within axenic microbial cultures, uniform and distinct carbon signatures are observed for marine bacteria versus terrestrial fungi (Figures 3 and 4). Specifically, OC associated with marine bacterial Mn oxides is primarily proteinaceous (Figure 4, Supplemental Figure S3), while terrestrial mycogenic Mn oxides harbor both protein and (lipo)polysaccharide-like material (Figure 4). These signatures could derive from amino sugars, which would produce spectra with strong peaks corresponding to both amine C and O-alkyl-C (Solomon et al., 2009). However, the spectra closely match protein and/or lipopolysaccharide standards (for bacterial and fungal Mn oxides respectively) and the additional N NEXAFS (Supplementary Figure S3), protein

quantification (Figure 1), and protein extraction and identification data (Supplementary Table S3) for the bacterial samples affirm this interpretation. These and closely related organisms are known to have extensive secretomes (Christie-Oleza et al., 2012; Learman & Hansel, 2014; Zeiner, 2015; Johnson et al., 2016;); thus, while amino sugars could be present and associating with the mineral, it is not surprising to find that Mn-associated OC derives from extracellular proteins and lipopolysaccharides.

While the organic carbon composition of the initial growth media varied between the cultures, the fungal and *Erythrobacter* sp. media is quite similar and therefore cannot account for the differences observed between these organisms. Further, ascomycete fungi, including the two species explored here, have extensive exoproteomes (Zeiner 2015 and references therein), and yet their Mn oxides are dominated by a (lipo)polysaccharide signature. As the type and structure of the Mn oxides formed by these bacteria and fungi are similar (Learman et al., 2011; Santelli et al., 2011), these findings could point to specific biomolecules involved in Mn biomineralization by bacteria versus fungi. However, a range of polysaccharides, proteins, and specific amino acids has been implicated in the nucleation, precipitation and aggregation of a wide diversity of minerals with specific organic classes not specific to particular microbial groups. For instance, while here we see a primarily (lipo)polysaccharide signature associated with the fungal biooxides, proteins or proteinaceous material have also been documented as templates in fungal Mn oxide formation (Emerson et al., 1989). Conversely, the carbon associated with the bacterial Mn oxides here is dominated by proteins, but polysaccharides template Fe oxides associated with the sheath forming iron oxidizer *M. ferroxidans* (Chan et al., 2009). Similarly, Mn oxide precipitates formed within biofilms of the bacterium *Psuedomonas putida* strain MnB1 were completely enveloped by the same polysaccharide material that comprised its biofilms, where

this association was likely a combination of templated and adsorbed organic carbon (Toner et al., 2005). Clearly, this association of organic carbon and minerals does not appear to be unique to particular microbial groups and rather comprises a number of factors that may vary with lifestyle (e.g., surface associated versus planktonic) and Mn oxidation pathway.

For the Mn(II)-oxidizing bacteria utilized in this study, the proteins involved in Mn(II) oxidation are sequestered and potentially preserved within the ensuing Mn oxide precipitates. Heme peroxidases and homologs, in particular, are among the most abundant mineral-hosted proteins within the *Roseobacter* and *Erythrobacter* Mn oxides and have been linked to both the direct and indirect (superoxide mediated) oxidation of Mn(II) by these organisms (Anderson et al., 2009; Andeer et al., 2015). Their presence in the mineral may be attributed to their additional function as a template (either passively or actively) or in inducing particle aggregation (Moreau et al., 2007). Alternatively, these proteins may play no role in particle formation or growth and instead may simply be adsorbed between particles and/or onto the Mn oxide surfaces. In fact, these heme peroxidases are the most abundant protein in both cell-free filtrate and the outer membrane fraction in *Roseobacter* AzwK-3b (Andeer et al., 2015) and, thus their prevalent association with the Mn oxides may simply be a function of their high abundance. Yet, minerals produced in both bacterial cultures harbor proteins specifically related to ion binding and transport of metals. Their metal-binding capability may lead to their preferential association with Mn(II) or Mn oxide particles. If so, carbon ultimately sequestered within biogenic Mn oxides may, in fact, provide some indication of the mechanism of Mn(II) oxidation and Mn oxide formation in some cases.

Similar to the bacterial cultures, Mn oxides formed in brackish Oyster Pond waters form in a C-rich environment and incorporate substantial quantities of OC into the mineral (Figure 1).

The OC associated with Mn oxides formed in incubation samples is dominated by aromatic, aliphatic, amide/carboxyl, and O-alkyl-C functional groups (Figures 5 and 6). Further, proteins were specifically observed associated with the Mn oxides formed in the water incubations (Figure 1). As these Mn oxides were formed during active Mn(II) oxidation and oxide mineralization within the Oyster Pond water, we anticipate that, similar to the marine bacterial cultures, at least a proportion of this carbon is associated with the Mn(II)-oxidizing organisms responsible for Mn oxide formation within these waters. We further hypothesize that associated OC has additional sources not associated with the Mn(II) oxidation process, including biomass, POC, and DOC. Indeed, synthetic Mn oxides (as δ-MnO_2) directly incubated within Oyster Pond water contained substantial levels of OC, indicating that Mn oxides also passively adsorb or aggregate OC in these waters (Figure 2 and Supplemental Figure S2). By comparing the carbon associated with Mn oxides formed during active mineralization in the Oyster Pond water versus synthetic Mn oxides of similar structure added to the same water, ~44% of the OC associated with the biomineralized Mn oxides can be attributed to a solely passive adsorption reaction (see Figure 2). Further, synthetic Mn oxides incubated in 0.2 μm-filtered Oyster Pond water also accumulated OC, about ~50% as much as the OC in the unfiltered water, indicating that a substantial proportion of this mineral-associated OC derived from the dissolved pool (see Figure 2). Given the initial DOC concentration of 0.74 ± 0.02 mmol DOC/L and an added concentration of 100 μM synthetic Mn oxide, we calculate that the Mn oxide-associated OC in that synthetic oxide + filtered water treatment represents ~4% of the initial DOC. This minor fraction of carbon removed within these carbon-rich coastal waters precludes robust quantification of Mn oxide-induced compositional changes to the DOC pool or evidence for selective partitioning to the Mn oxides.

Thus, OC associated with the Mn oxides formed via biomineralization in Oyster Pond water likely reflects adsorption or incorporation of biomass and/or metabolites generated by Mn(II)-oxidizing microorganisms during Mn oxide formation as well as OC not associated with active Mn mineralization. Chen et al. (2014) observed an enrichment of aromatic C at low solid phase OC:Fe ratios, similar to those OC:Mn ratios found in samples here. Eusterhues et al. (2011) examined fractionation of both polysaccharide-rich DOM and lignin material by ferrihydrite, observing that co-precipitation resulted in greater fractionation than adsorption-only, and that mineral-associated lignin material was enriched in aromatics relative to the original composition. Yet, aromatic C is not enriched in the Mn oxides formed during biomineralization in the Oyster Pond water; in fact, aromatic C comprises a significantly smaller percentage of the total fit area for biomineralized incubations than incubations of synthetic Mn oxides (Supplementary figures S4 and S5; Supplementary Table S2), inverting what would be expected if these experiments truly represented "adsorption-only" or "co-precipitation-only" scenarios. This observation instead emphasizes that the chemical composition of OC associated with Mn oxides in incubation samples derives from a combination of source (microbial material, POC, DOC) and mineral-induced fractionation, and that OC interacts with the mineral via several mechanisms.

In contrast to the low complexity and homogeneous nature of organic molecules associating with Mn oxides precipitated in cell-free filtrate of the bacterial and fungal cultures, Mn oxides formed in brackish Oyster Pond water and particularly in terrestrial caves bear OC that is more complex and spatially heterogeneous in chemical composition. Compared to culture-derived Mn oxides, C NEXAFS spectra extracted from regions within incubation and cave samples do not clearly match singular biomolecule standards, but contain instead a diversity of

organic carbon functional groups. Although the proportions of the different functional groups vary both within regions of the same sample and between samples, all contain predominantly aromatic, aliphatic, amide/carboxyl, and O-alkyl C groups. The distribution of functional groups does not, in general, vary significantly between Mn oxides formed in cultures, brackish water, and terrestrial caves when peak fitting results from spectra are averaged by sample type (Figure 4). Other studies of marine particles (Brandes et al., 2004) and soil aggregates (Lehmann et al., 2008) have found similar results, where different samples nonetheless contain the same classes of compounds.

One notable exception to the similarity in functional group distributions is an observed higher proportion of aliphatic C within the terrestrial cave samples (Figure 9). Previous work has interpreted enrichment of aliphatic and amide C as evidence of microbial lipids and proteins that selectively partition onto mineral surfaces. Like this work, Keiluweit et al. (2012) found lipids and proteins intermixed within iron-oxide rich soils, while Liu et al. (2013) found lipids and proteins in separate 100-200 nm^2 domains after adsorption of extracellular polymeric substances to goethite. Mineral-associated OC in soil samples studied by Heckman et al. (2013) were dominated by polysaccharides, but also enriched in lipids and proteins which were interpreted as microbial residues. The cave ferromanganese coatings, however, lack the O-alkyl-C enrichment that would be more indicative of polysaccharide material (as with the mycogenic oxides) and have a variable amide/carboxyl C content comparable to incubation and culture samples, suggesting a relatively higher lipid:protein content than that found in those previous studies on soil. The C-rich/no Mn regions (Figure 7, BC regions 6 and 7, CL regions 8 and 9) are significantly enriched in aromatic and phenolic/ketonic groups ($p = 0.01$, two-tailed t-test). These regions could represent the fraction of non-microbially processed, more terrestrial (lignin or

otherwise plant-derived) OC in the sample (Heckman et al., 2013) or intact fungal hyphae-like material (Keiluweit et al. 2012). Conversely, more Mn-rich regions could be interpreted as depleted in aromatics due to oxidative degradation by Mn oxides, as observed in Johnson et al. (2015) who documented preferential breaking of aromatic C-C bonds and conversion to low molecular weight compounds. However, as Mn-containing regions do not otherwise significantly differ from C-rich regions, we cannot conclusively attribute slight compositional differences to mineral-driven fractionation of microbial OC. Ultimately, the high aliphatic C content of cave Mn oxides may reflect differing C sources, differences in lifestyle (i.e. more lipid-rich biofilm formation for rock-associated microbes in cave systems), or a greater extent of microbial processing of OC. Given the oligotrophic cave environment and low measured carbon concentrations, this last option seems most feasible.

2.5 Conclusions

Here we show that manganese oxides harbor substantial concentrations of organic carbon that remain stable despite mineral ripening and particle aggregation (Supplemental Figures S2 and S3). Biomolecules hosted within Mn oxides formed by bacteria and fungi are distinctly different, which could point to the potential for Mn oxide-hosted carbon as a biosignature. However, the concentration of OC associating with Mn oxides under different incubation conditions, in addition to the complex spectroscopic signature of OC within natural Mn oxides from the caves and brackish water incubations, suggest that environmental Mn oxides accumulate organic carbon from a range of sources through a range of mechanisms, which will overwrite any clear biomolecular signature.

Regardless of the OC source, Mn oxides sequester OC at substantial levels, as long appreciated for clay minerals and more recently Fe oxides. This association is established rapidly within cultures and brackish water incubations (Figures S2 and S3). Thus, Mn oxides may be an additional and important source and/or sink of OC within terrestrial and marine systems, including the subsurface or otherwise carbon-limited environments. In marine sediments or cave environments, Mn oxides may shuttle OC to depths where it is subsequently released and made bioavailable either by reductive dissolution of Mn oxide minerals, other diagenetic reactions, or an increased prevalence of exoenzymes that target the types of OC present at Mn oxide surfaces. Of particular interest is the attenuation and possible preservation of proteinaceous carbon within/on Mn oxide minerals (Figures 1 and 4, Supplemental Figures S2 and S3). If this preservation endures on time scales sufficiently greater than sedimentation and burial, then this mineral-hosted protein has the potential to fuel heterotrophic life in the deep subsurface. This brings up the intriguing possibility that mineral-derived proteins could explain the abundance of protein-degrading peptidases and protein-based metabolisms within some subsurface sediments (Lloyd et al., 2013). Conversely, if associated OC remains inaccessible to microbes and is stabilized over much longer time scales, Mn oxides may provide a mechanism for transferring organic carbon from the surface carbon cycle to the geological carbon cycle, facilitating burial and inhibiting remineralization. Moving forward, correlative approaches and micro-scale techniques will be invaluable for elucidating micro-zones representing different types of mineral-organic interactions within sediments and how the composition of Mn oxide-associated OC changes over time and throughout diagenesis.

2.6 ACKNOWLEDGEMENTS

The authors are grateful to Dan Repeta, Ben Kocar, Deric Learman, Matt McIlvin, Dawn Moran, Clara Chan, Brandy Toner, and Marco Keiluweit for their helpful insight, and to Suzanna Brauer and Mara Cloutier for access to and help collecting the cave samples, and to Brad Tebo for providing *Erythrobacter* strain SD-21. We also thank two anonymous reviewers, whose thoughtful comments greatly improved this manuscript. This research was supported by an NSF GRF (1122374) (ERE), NSF EAR-82279000 to CMH and a WHOI Coastal Ocean Institute grant to ERE. Portions of this research were conducted at the Stanford Synchrotron Radiation Lightsource (Stanford, CA) and the Advanced Light Source (Berkeley, CA). Use of the Stanford Synchrotron Radiation Lightsource, SLAC National Accelerator Laboratory, is supported by the U.S. Department of Energy, Office of Science, Office of Basic Energy Sciences under Contract No. DE-AC02-76SF00515. The Advanced Light Source is supported by the Director, Office of Science, Office of Basic Energy Sciences, of the U.S. Department of Energy under Contract No. DE-AC02-05CH11231. The authors also acknowledge Tolek Tyliszczak for his support on beamline 11.0.2 at the ALS.

2.7 References

Andeer, P. F., Learman, D. R., McIlvin, M., Dunn, J. a, & Hansel, C. M. (2015). Extracellular haem peroxidases mediate Mn(II) oxidation in a marine Roseobacter bacterium via superoxide production. *Environmental Microbiology*, (Ii), 1–33. http://doi.org/10.1111/1462-2920.12893

Anderson, C. R., Johnson, H. a, Caputo, N., Davis, R. E., Torpey, J. W., & Tebo, B. M. (2009). Mn(II) oxidation is catalyzed by heme peroxidases in "Aurantimonas manganoxydans" strain SI85-9A1 and Erythrobacter sp. strain SD-21. *Applied and Environmental Microbiology*, *75*(12), 4130–8. http://doi.org/10.1128/AEM.02890-08

Arnarson, T. S., & Keil, R. G. (2001). Organic–mineral interactions in marine sediments studied using density fractionation and X-ray photoelectron spectroscopy. *Organic Geochemistry*, *32*(12), 1401–1415. http://doi.org/10.1016/S0146-6380(01)00114-0

Bargar, J. R., Fuller, C. C., Marcus, M. a., Brearley, A. J., Perez De la Rosa, M., Webb, S. M., & Caldwell, W. a. (2009). Structural characterization of terrestrial microbial Mn oxides from Pinal Creek, AZ. *Geochimica et Cosmochimica Acta*, *73*(4), 889–910. http://doi.org/10.1016/j.gca.2008.10.036

Bargar, J. R., Tebo, B. M., Bergmann, U., Webb, S. M., Glatzel, P., Chiu, V. Q., & Villalobos, M. (2005). Biotic and abiotic products of Mn(II) oxidation by spores of the marine Bacillus sp. strain SG-1. *American Mineralogist*, *90*(1), 143–154. http://doi.org/10.2138/am.2005.1557

Berg, B., Davey, M. P., De Marco, a., Emmett, B., Faituri, M., Hobbie, S. E., … Virzo De Santo, a. (2010). Factors influencing limit values for pine needle litter decomposition: a synthesis for boreal and temperate pine forest systems. *Biogeochemistry*, *100*(1–3), 57–73. http://doi.org/10.1007/s10533-009-9404-y

Bock, M. J., & Mayer, L. M. (2000). Mesodensity organo-clay associations in a near-shore sediment. *Marine Geology*, *163*(1–4), 65–75. http://doi.org/10.1016/S0025-3227(99)00105-X

Brandes, J. a., Lee, C., Wakeham, S., Peterson, M., Jacobsen, C., Wirick, S., & Cody, G. (2004). Examining marine particulate organic matter at sub-micron scales using scanning transmission X-ray microscopy and carbon X-ray absorption near edge structure spectroscopy. *Marine Chemistry*, *92*(1–4), 107–121. http://doi.org/10.1016/j.marchem.2004.06.020

Canfield, D. E., Thamdrup, B., & Hansen, J. W. (1993). The anaerobic degradation of organic matter in Danish coastal sediments: iron reduction, manganese reduction, and sulfate reduction. *Geochimica et Cosmochimica Acta*, *57*(16), 3867–83. Retrieved from http://www.ncbi.nlm.nih.gov/pubmed/11537734

Carlson, C. A., Giovannoni, S. J., Hansell, D. A., Goldberg, S. J., Parsons, R., & Vergin, K. (2004). Interactions among dissolved organic carbon, microbial processes, and community structure in the mesopelagic zone of the northwestern Sargasso Sea, *49*(4), 1073–1083.

Carmichael, M. J., Carmichael, S. K., Santelli, C. M., Strom, A., & Bräuer, S. L. (2013). Mn(II)-oxidizing Bacteria are Abundant and Environmentally Relevant Members of Ferromanganese Deposits in Caves of the Upper Tennessee River Basin. *Geomicrobiology*

Journal, *30*(9), 779–800. http://doi.org/10.1080/01490451.2013.769651

Carmichael, S., Carmichael, M. J., Strom, A., Johnson, K., Roble, L., Gao, Y., & Brauer, S. (2013). Sustained Anthropogenic Impact in Carter Saltpeter Cave, Carter County, Tennessee and the Potential Effects on Manganese Cycling. *Journl of Cave and Karst Studies*, *75*(3), 189–204. http://doi.org/10.4311/2012MB0267

Chan, C. S., Fakra, S. C., Edwards, D. C., Emerson, D., & Banfield, J. F. (2009). Iron oxyhydroxide mineralization on microbial extracellular polysaccharides. *Geochimica et Cosmochimica Acta*, *73*(13), 3807–3818. http://doi.org/10.1016/j.gca.2009.02.036

Chan, C. S., Fakra, S. C., Emerson, D., Fleming, E. J., & Edwards, K. J. (2011). Lithotrophic iron-oxidizing bacteria produce organic stalks to control mineral growth: implications for biosignature formation. *The ISME Journal*, *5*(4), 717–27. http://doi.org/10.1038/ismej.2010.173

Chen, C., Dynes, J. J., Wang, J., & Sparks, D. L. (2014). Properties of Fe-Organic Matter Associations via Coprecipitation versus Adsorption. *Environmental Science & Technology*, *48*(23), 13751–9. http://doi.org/10.1021/es503669u

Christie-Oleza, J. A., Piña-Villalonga, J. M., Bosch, R., Nogales, B., & Armengaud, J. (2012). Comparative proteogenomics of twelve Roseobacter exoproteomes reveals different adaptive strategies among these marine bacteria. *Molecular & Cellular Proteomics : MCP*, *11*(2), M111.013110. http://doi.org/10.1074/mcp.M111.013110

Claverys, J. P. (2001). A new family of high-affinity ABC manganese and zinc permeases. *Research in Microbiology*, *152*(3–4), 231–243. http://doi.org/10.1016/S0923-2508(01)01195-0

Cowie, G. L., Hedges, J. I., Prahl, F. G., & de Lange, G. J. (1995). Elemental and major biochemical changes across an oxidation front in a relict turbidite: An oxygen effect. *Geochimica et Cosmochimica Acta*, *59*(1), 33–46. http://doi.org/10.1016/0016-7037(94)00329-K

Dick, G. J., Podell, S., Johnson, H. a, Rivera-Espinoza, Y., Bernier-Latmani, R., McCarthy, J. K., … Tebo, B. M. (2008). Genomic insights into Mn(II) oxidation by the marine alphaproteobacterium Aurantimonas sp. strain SI85-9A1. *Applied and Environmental Microbiology*, *74*(9), 2646–58. http://doi.org/10.1128/AEM.01656-07

Dickens, A. F., Baldock, J. a., Smernik, R. J., Wakeham, S. G., Arnarson, T. S., Gélinas, Y., & Hedges, J. I. (2006). Solid-state 13C NMR analysis of size and density fractions of marine sediments: Insight into organic carbon sources and preservation mechanisms. *Geochimica et Cosmochimica Acta*, *70*(3), 666–686. http://doi.org/10.1016/j.gca.2005.10.024

Doetterl, S., Stevens, A., Six, J., Merckx, R., Oost, K. Van, Pinto, M. C., … Boeckx, P. (2015). Soil carbon storage controlled by interactions between geochemistry and climate. *Nature Geoscience*, *8*(August). http://doi.org/10.1038/NGEO2516

Dümig, A., Häusler, W., Steffens, M., & Kögel-Knabner, I. (2012). Clay fractions from a soil chronosequence after glacier retreat reveal the initial evolution of organo–mineral associations. *Geochimica et Cosmochimica Acta*, *85*, 1–18. http://doi.org/10.1016/j.gca.2012.01.046

Ehrenreich, A., & Widdel, F. (1994). Anaerobic Oxidation of Ferrous Iron by Purple Bacteria, a

New-Type of Phototrophic Metabolism. *Applied and Environmental Microbiology*, *60*(12), 4517–4526. Retrieved from <Go to ISI>://A1994PU39900042

Emerson, D., Garen, R. E., & Ghiorse, W. C. (1989). Formation of Metallogenium-like structures by a manganese-oxiding fungus. *Archives of Microbiology*, (t 989), 223–231.

Eusterhues, K., Rennert, T., Knicker, H., Kögel-Knabner, I., Totsche, K. U., & Schwertmann, U. (2011). Fractionation of organic matter due to reaction with ferrihydrite: Coprecipitation versus adsorption. *Environmental Science and Technology*, *45*(2), 527–533. http://doi.org/10.1021/es1023898

Flerus, R., Lechtenfeld, O. J., Koch, B. P., McCallister, S. L., Schmitt-Kopplin, P., Benner, R., ... Kattner, G. (2012). A molecular perspective on the ageing of marine dissolved organic matter. *Biogeosciences*, *9*(6), 1935–1955. http://doi.org/10.5194/bg-9-1935-2012

Francis, C. A., Co, E. M., & Tebo, B. M. (2001). Enzymatic Manganese(II) Oxidation by a Marine alpha-Proteobacterium. *Applied and Environmental Microbiology*, *67*(9), 4024–4029. http://doi.org/10.1128/AEM.67.9.4024

Graham, S. C., Bond, C. S., Freeman, H. C., & Guss, J. M. (2005). Structural and functional implications of metal ion selection in aminopeptidase P, a metalloprotease with a dinuclear metal center. *Biochemistry*, *44*(42), 13820–13836. http://doi.org/10.1021/bi0512849

Hansel, C. M., & Francis, C. A. (2006). Coupled Photochemical and Enzymatic Mn (II) Oxidation Pathways of a Planktonic Roseobacter -Like Bacterium Coupled Photochemical and Enzymatic Mn (II) Oxidation Pathways of a Planktonic Roseobacter -Like Bacterium. *Applied and Environmental Microbiology*, *72*(Ii), 3543–3549. http://doi.org/10.1128/AEM.72.5.3543

Heckman, K., Grandy, a. S., Gao, X., Keiluweit, M., Wickings, K., Carpenter, K., ... Rasmussen, C. (2013). Sorptive fractionation of organic matter and formation of organo-hydroxy-aluminum complexes during litter biodegradation in the presence of gibbsite. *Geochimica et Cosmochimica Acta*, *121*, 667–683. http://doi.org/10.1016/j.gca.2013.07.043

Heckman, K., Vazquez-Ortega, A., Gao, X., Chorover, J., & Rasmussen, C. (2011). Changes in water extractable organic matter during incubation of forest floor material in the presence of quartz, goethite and gibbsite surfaces. *Geochimica et Cosmochimica Acta*, *75*(15), 4295–4309. http://doi.org/10.1016/j.gca.2011.05.009

Hedges, J. I., Baldock, J. a, Gélinas, Y., Lee, C., Peterson, M., & Wakeham, S. G. (2001). Evidence for non-selective preservation of organic matter in sinking marine particles. *Nature*, *409*(6822), 801–4. http://doi.org/10.1038/35057247

Henneberry, Y. K., Kraus, T. E. C., Nico, P. S., & Horwath, W. R. (2012). Structural stability of coprecipitated natural organic matter and ferric iron under reducing conditions. *Organic Geochemistry*, *48*, 81–89. http://doi.org/10.1016/j.orggeochem.2012.04.005

Hertkorn, N., Benner, R., Frommberger, M., Schmitt-Kopplin, P., Witt, M., Kaiser, K., ... Hedges, J. I. (2006). Characterization of a major refractory component of marine dissolved organic matter. *Geochimica et Cosmochimica Acta*, *70*(12), 2990–3010. http://doi.org/10.1016/j.gca.2006.03.021

Jiao, N., Herndl, G. J., Hansell, D. a., Benner, R., Kattner, G., Wilhelm, S. W., ... Azam, F. (2010). Microbial production of recalcitrant dissolved organic matter: long-term carbon

storage in the global ocean. *Nature Reviews Microbiology*, *8*(8), 593–599. http://doi.org/10.1038/nrmicro2386

Johnson, K., Purvis, G., Lopez-Capel, E., Peacock, C., Gray, N., Wagner, T., ... Greenwell, C. (2015). Towards a mechanistic understanding of carbon stabilization in manganese oxides. *Nature Communications*, *6*(May), 7628. http://doi.org/10.1038/ncomms8628

Johnson, W. M., Soule, M. C. K., & Kujawinski, E. B. (2016). Evidence for quorum sensing and differential metabolite production by the marine heterotroph, *Ruegeria pomeroyi*, in response to DMSP. *The ISME Journal*, 1–13. http://doi.org/10.1038/ismej.2016.6

Kaiser, K., & Guggenberger, G. (2000). The role of DOM sorption to mineral surfaces in the preservation of organic matter in soils. *Organic Geochemistry*, *31*(7–8), 711–725. http://doi.org/10.1016/S0146-6380(00)00046-2

Keil, R. G., Montluçon, D. B., Prahl, F. G., & Hedges, J. I. (1994). Sorptive preservation of labile organic matter in marine sediments. *Nature*. http://doi.org/10.1038/370549a0

Keiluweit, M., Bougoure, J. J., Nico, P. S., Pett-Ridge, J., Weber, P. K., & Kleber, M. (2015). Mineral protection of soil carbon counteracted by root exudates. *Nature Clim. Change*, *5*(6), 588–595. http://doi.org/10.1038/nclimate2580

Keiluweit, M., Bougoure, J. J., Zeglin, L. H., Myrold, D. D., Weber, P. K., Pett-Ridge, J., ... Nico, P. S. (2012a). Nano-scale investigation of the association of microbial nitrogen residues with iron (hydr)oxides in a forest soil O-horizon. *Geochimica et Cosmochimica Acta*, *95*, 213–226. http://doi.org/10.1016/j.gca.2012.07.001

Keiluweit, M., Bougoure, J. J., Zeglin, L. H., Myrold, D. D., Weber, P. K., Pett-Ridge, J., ... Nico, P. S. (2012b). Nano-scale investigation of the association of microbial nitrogen residues with iron (hydr)oxides in a forest soil O-horizon. *Geochimica et Cosmochimica Acta*, *95*, 213–226. http://doi.org/10.1016/j.gca.2012.07.001

Keiluweit, M., Nico, P., Harmon, M. E., Mao, J., Pett-Ridge, J., & Kleber, M. (2015). Long-term litter decomposition controlled by manganese redox cycling. *Proceedings of the National Academy of Sciences*, *112*(38), E5253–E5260. http://doi.org/10.1073/pnas.1508945112

Kleber, M., Eusterhues, K., Keiluweit, M., Mikutta, C., Mikutta, R., & Nico, P. S. (2015). Mineral–Organic Associations: Formation, Properties, and Relevance in Soil Environments. *Advances in Agronomy*, *130*, 1–140. http://doi.org/10.1016/bs.agron.2014.10.005

Kleber, M., Nico, P. S., Plante, A., Filley, T., Kramer, M., Swanston, C., & Sollins, P. (2011). Old and stable soil organic matter is not necessarily chemically recalcitrant: implications for modeling concepts and temperature sensitivity. *Global Change Biology*, *17*(2), 1097–1107. http://doi.org/10.1111/j.1365-2486.2010.02278.x

Koebnik, R., Locher, K. P., & Van Gelder, P. (2000). Structure and function of bacterial outer membrane proteins: Barrels in a nutshell. *Molecular Microbiology*. http://doi.org/10.1046/j.1365-2958.2000.01983.x

Krumbein, W. E., & Altmann, H. J. (1973). A new method for the detection and enumeration of manganese oxidizing and reducing microorganisms. *Helgoländer Wissenschaftliche Meeresuntersuchungen*, *25*(2–3), 347–356. http://doi.org/10.1007/BF01611203

Kuddus, M., & Ramteke, P. W. (2008). A cold-active extracellular metalloprotease from Curtobacterium luteum (MTCC 7529): enzyme production and characterization. *The*

Journal of General and Applied Microbiology, *54*(6), 385–392. http://doi.org/10.2323/jgam.54.385

Lalonde, K., Mucci, A., Ouellet, A., & Gélinas, Y. (2012). Preservation of organic matter in sediments promoted by iron. *Nature*, *483*(7388), 198–200. http://doi.org/10.1038/nature10855

Learman, D. R., & Hansel, C. M. (2014). Comparative proteomics of Mn(II)-oxidizing and non-oxidizing Roseobacter clade bacteria reveal an operative manganese transport system but minimal Mn(II)-induced expression of manganese oxidation and antioxidant enzymes. *Environmental Microbiology Reports*, *6*(5), 501–509. http://doi.org/10.1111/1758-2229.12164

Learman, D. R., Wankel, S. D., Webb, S. M., Martinez, N., Madden, a. S., & Hansel, C. M. (2011). Coupled biotic–abiotic Mn(II) oxidation pathway mediates the formation and structural evolution of biogenic Mn oxides. *Geochimica et Cosmochimica Acta*, *75*(20), 6048–6063. http://doi.org/10.1016/j.gca.2011.07.026

Lechtenfeld, O. J., Kattner, G., Flerus, R., McCallister, S. L., Schmitt-Kopplin, P., & Koch, B. P. (2014). Molecular transformation and degradation of refractory dissolved organic matter in the Atlantic and Southern Ocean. *Geochim. Cosmochim. Acta*, *126*, 321–337. http://doi.org/10.1016/j.gca.2013.11.009

Lehmann, J., Solomon, D., Kinyangi, J., Dathe, L., Wirick, S., & Jacobsen, C. (2008). Spatial complexity of soil organic matter forms at nanometre scales. *Nature Geoscience*, *1*(4), 238–242. http://doi.org/10.1038/ngeo155

Liu, X., Eusterhues, K., Thieme, J., Ciobota, V., Höschen, C., Mueller, C. W., … Totsche, K. U. (2013). STXM and NanoSIMS investigations on EPS fractions before and after adsorption to goethite. *Environmental Science & Technology*, *47*(7), 3158–66. http://doi.org/10.1021/es3039505

Lloyd, K. G., Schreiber, L., Petersen, D. G., Kjeldsen, K. U., Lever, M. a, Steen, A. D., … Jørgensen, B. B. (2013). Predominant archaea in marine sediments degrade detrital proteins. *Nature*, *496*(7444), 215–8. http://doi.org/10.1038/nature12033

Lu, X., & Zhu, H. (2005). Tube-gel digestion: a novel proteomic approach for high throughput analysis of membrane proteins. *Molecular & Cellular Proteomics : MCP*, *4*(12), 1948–58. http://doi.org/10.1074/mcp.M500138-MCP200

Mann, S., Archibald, D. D., Didymus, J. M., Douglas, T., Heywood, B. R., Meldrum, F. C., & Reeves, N. J. (1993). Crystallization at Inorganic-organic Interfaces: Biominerals and Biomimetic Synthesis. *Science (New York, N.Y.)*, *261*(September), 1286–1292. http://doi.org/10.1126/science.261.5126.1286

Moreau, J. W., Weber, P. K., Martin, M. C., Gilbert, B., Hutcheon, I. D., & Banfield, J. F. (2007). Extracellular proteins limit the dispersal of biogenic nanoparticles. *Science (New York, N.Y.)*, *316*(5831), 1600–3. http://doi.org/10.1126/science.1141064

Ostolaza, H., Soloaga, A., & Goni, F. M. (1995). The Binding of Divalent Cations to Escherichia coli alpha-Haemolysin. *European Journal of Biochemistry*, *228*(1), 39–44. http://doi.org/10.1111/j.1432-1033.1995.tb20225.x

Picard, A., Kappler, A., Schmid, G., Quaroni, L., & Obst, M. (2015). Experimental diagenesis of

organo-mineral structures formed by microaerophilic Fe(II)-oxidizing bacteria. *Nature Communications*, *6*(May 2014), 6277. http://doi.org/10.1038/ncomms7277

Poulton, S. W., & Raiswell, R. (2005). Chemical and physical characteristics of iron oxides in riverine and glacial meltwater sediments. *Chemical Geology*, *218*(3–4), 203–221. http://doi.org/10.1016/j.chemgeo.2005.01.007

Ransom, B., Kim, D., Kastner, M., & Wainwright, S. (1998). Organic matter preservation on continental slopes: importance of mineralogy and surface area. *Geochimica et Cosmochimica Acta*, *62*(8), 1329–1345. http://doi.org/10.1016/S0016-7037(98)00050-7

Roy, M., McManus, J., Goñi, M. a., Chase, Z., Borgeld, J. C., Wheatcroft, R. a., … Mix, A. (2013). Reactive iron and manganese distributions in seabed sediments near small mountainous rivers off Oregon and California (USA). *Continental Shelf Research*, *54*, 67–79. http://doi.org/10.1016/j.csr.2012.12.012

Santelli, C. M., Pfister, D. H., Lazarus, D., Sun, L., Burgos, W. D., & Hansel, C. M. (2010). Promotion of Mn(II) oxidation and remediation of coal mine drainage in passive treatment systems by diverse fungal and bacterial communities. *Applied and Environmental Microbiology*, *76*(14), 4871–5. http://doi.org/10.1128/AEM.03029-09

Santelli, C. M., Webb, S. M., Dohnalkova, A. C., & Hansel, C. M. (2011). Diversity of Mn oxides produced by Mn(II)-oxidizing fungi. *Geochimica et Cosmochimica Acta*, *75*(10), 2762–2776. http://doi.org/10.1016/j.gca.2011.02.022

Schumacher, M., Christl, I., Scheinost, A. C., Jacobsen, C., & Kretzschmar, R. (2005). Chemical heterogeneity of organic soil colloids investigated by scanning transmission X-ray microscopy and C-1s NEXAFS microspectroscopy. *Environmental Science & Technology*, *39*(23), 9094–100. Retrieved from http://www.ncbi.nlm.nih.gov/pubmed/16382929

Solomon, D., & Lehmann, J. (2005). Carbon K-Edge NEXAFS and FTIR-ATR Spectroscopic Investigation of organic carbon speciation in soils. *Soil Science Society of America Journal*, 107–119. Retrieved from https://dl.sciencesocieties.org/publications/sssaj/abstracts/69/1/0107

Solomon, D., Lehmann, J., Kinyangi, J., Liang, B., Heymann, K., Dathe, L., … Jacobsen, C. (2009). Carbon (1s) NEXAFS Spectroscopy of Biogeochemically Relevant Reference Organic Compounds. *Soil Science Society of America Journal*, *73*(6), 1817. http://doi.org/10.2136/sssaj2008.0228

Stone, A., & Morgan, J. (1984). Reduction and dissolution of manganese(III) and manganese(IV) oxides by organics: 2. Survey of the reactivity of organics. *Environmental Science & Technology*, *18*(8), 617–624. Retrieved from http://pubs.acs.org/doi/pdf/10.1021/es00126a010

Sunda, W., & Kieber, D. (1994). Oxidation of humic substances by manganese oxides yields low-molecular-weight organic substrates. *Nature*, *367*, 62–64. Retrieved from http://www.nature.com/nature/journal/v367/n6458/abs/367062a0.html

Tebo, B. M., Bargar, J. R., Clement, B. G., Dick, G. J., Murray, K. J., Parker, D., … Webb, S. M. (2004). Biogenic Manganese Oxides: Properties and Mechanisms of Formation. *Annual Review of Earth and Planetary Sciences*, *32*(1), 287–328. http://doi.org/10.1146/annurev.earth.32.101802.120213

Toner, B., Fakra, S., Villalobos, M., Warwick, T., & Sposito, G. (2005). Spatially resolved characterization of biogenic manganese oxide production within a bacterial biofilm. *Applied and Environmental Microbiology*, *71*(3), 1300–1310. http://doi.org/10.1128/AEM.71.3.1300

Toner, B. M. B., Fakra, S. S. C., Manganini, S. S. J., Santelli, C. M., Marcus, M. a., Moffett, J. W., … Edwards, K. J. (2009). Preservation of iron(II) by carbon-rich matrices in a hydrothermal plume. *Nature Geoscience*, *2*(3), 197–201. http://doi.org/10.1038/ngeo433

Van Waasbergen, L. G., Hoch, J. a., & Tebo, B. M. (1993). Genetic analysis of the marine manganese-oxidizing Bacillus sp. strain SG- 1: Protoplast transformation, Tn917 mutagenesis, and identification of chromosomal loci involved in manganese oxidation. *Journal of Bacteriology*, *175*(23), 7594–7603.

Villalobos, M., Toner, B., Bargar, J., & Sposito, G. (2003). Characterization of the manganese oxide produced by pseudomonas putida strain MnB1. *Geochimica et Cosmochimica Acta*, *67*(14), 2649–2662. http://doi.org/10.1016/S0016-7037(03)00217-5

Webb, S. M. (2005). SIXpack: a graphical user interface for XAS analysis using IFEFFIT. *Physica Scripta*, *T115*, 1011–1014.

Webb, S. M. (2005). Structural characterization of biogenic Mn oxides produced in seawater by the marine bacillus sp. strain SG-1. *American Mineralogist*, *90*(8–9), 1342–1357. http://doi.org/10.2138/am.2005.1669

Zeiner, C. A. (2015). *Role of the secretome in manganese and carbon oxidation by filamentous ascomycete fungi.*

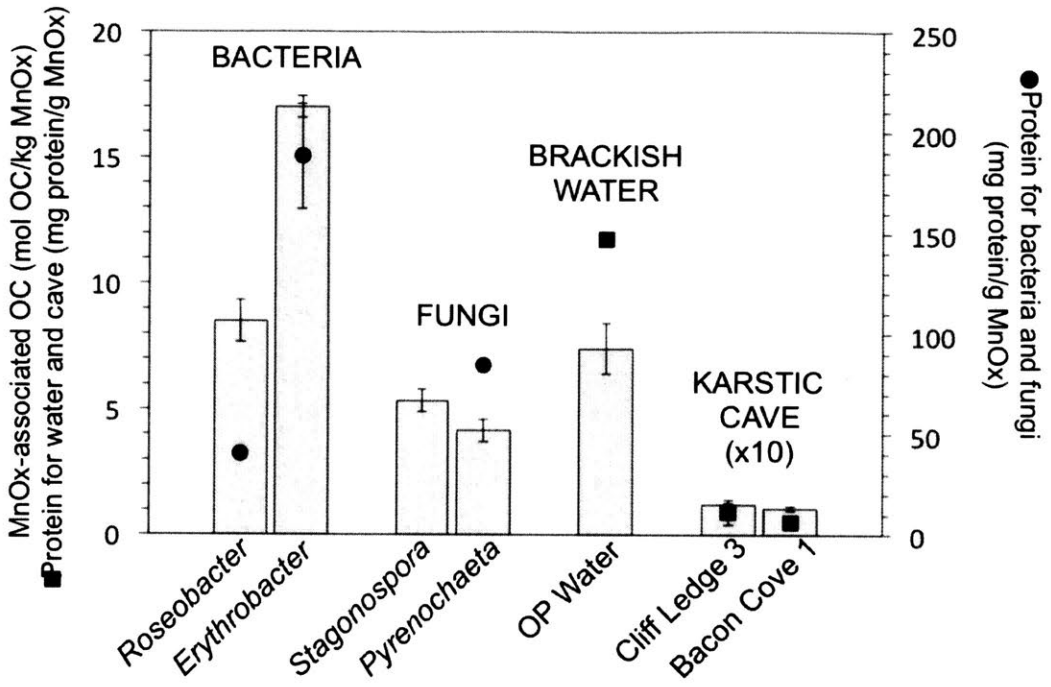

Figure 1. Organic carbon and protein concentrations associated with Mn oxides formed in the cell-free filtrate of bacterial and fungal cultures. Bacterial and fungal samples came from 96-hour incubations while the brackish Oyster Pond water sample was incubated for 8 weeks. The *Stagonospora* sample did not contain enough volume to allow measurement of proteins. TOC and protein concentrations for cave samples are multiplied 10x such that they are visible on the graph.

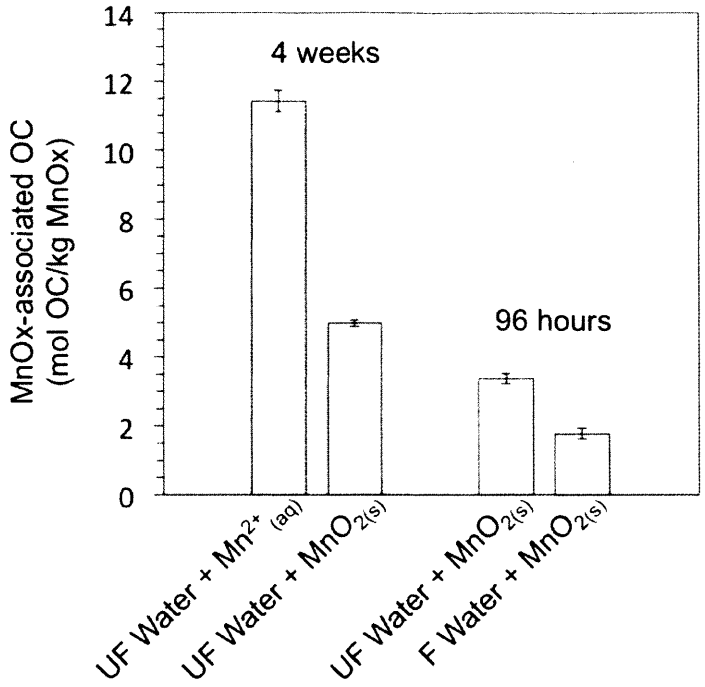

Figure 2. Organic carbon concentrations associated with Mn oxides following different incubation treatments in brackish Oyster Pond water: Mn oxides formed from Mn(II) over the course of 4 weeks (UF Water+$Mn^{2+}_{(aq)}$), synthetic Mn oxides incubated for 4 weeks (UF Water+MnO_2), synthetic Mn oxides incubated for 96 hours (UF Water+MnO_2), and synthetic Mn oxides incubated in 0.2 μm-filtered water for 96 hours (F Water+MnO_2).

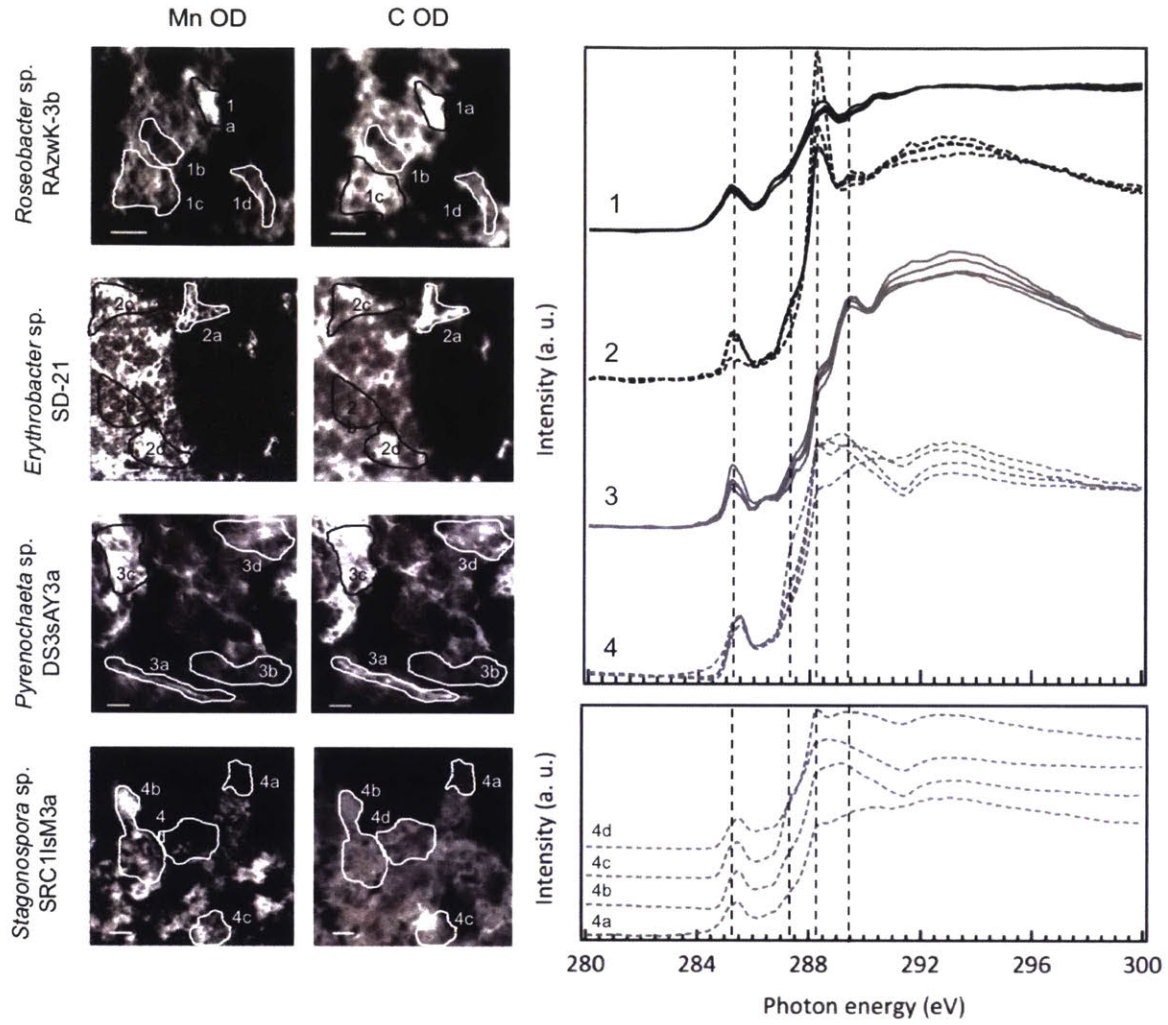

Figure 3. Mn and C STXM OD maps of Mn oxides formed in cell-free filtrate of bacterial and fungal cultures (left) generated by subtraction of a pre-edge transmission image from a post-edge image (see methods). C 1s NEXAFS spectra (right) extracted from regions denoted on the STXM maps. Lower right panel expands spectra taken from *Stagonospora* Mn oxides. Guide lines are at 285.3, 287.4, 288.3, and 289.45 eV.

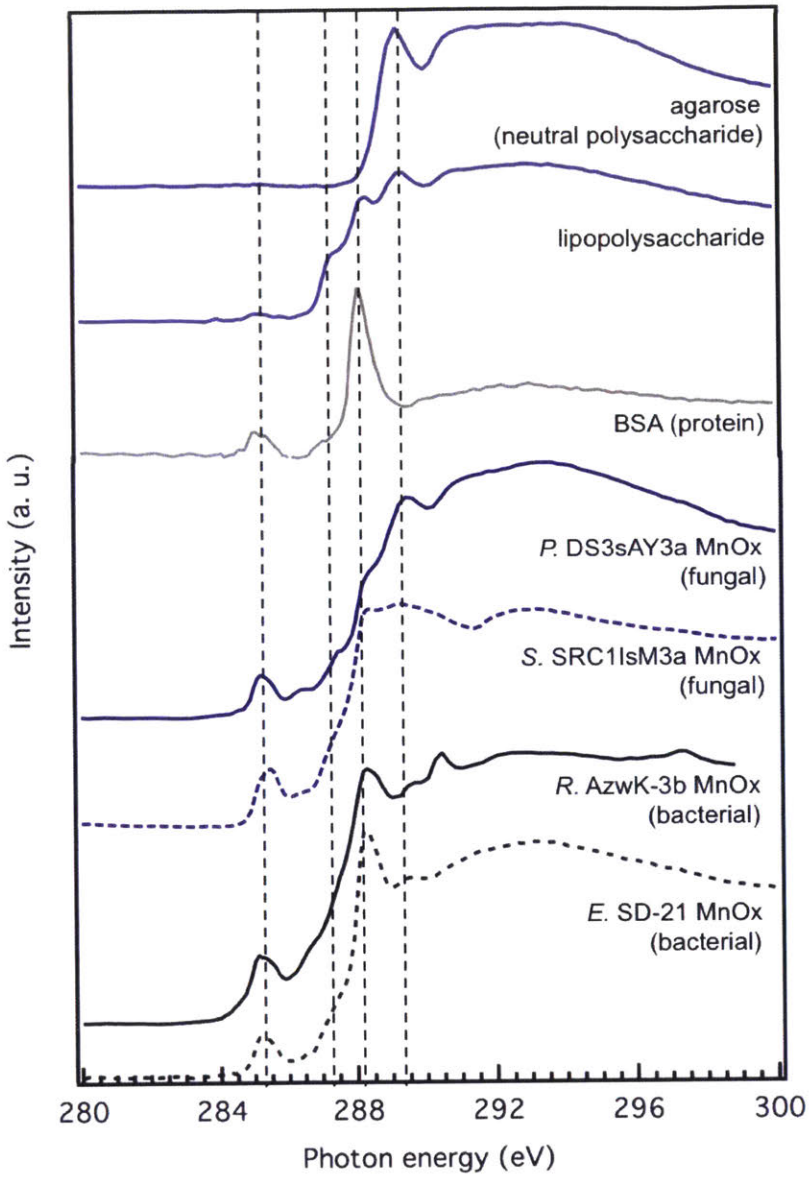

Figure 4. Representative C 1s NEXAFS spectra of carbon associated with Mn oxides precipitated in the cell-free filtrate of fungal (blue) and bacterial cultures (black) generated by extracting the entirety of the STXM image for each species, shown with matching standards. Guidelines are at 285.3, 287.4, 288.3, and 289.45 eV.

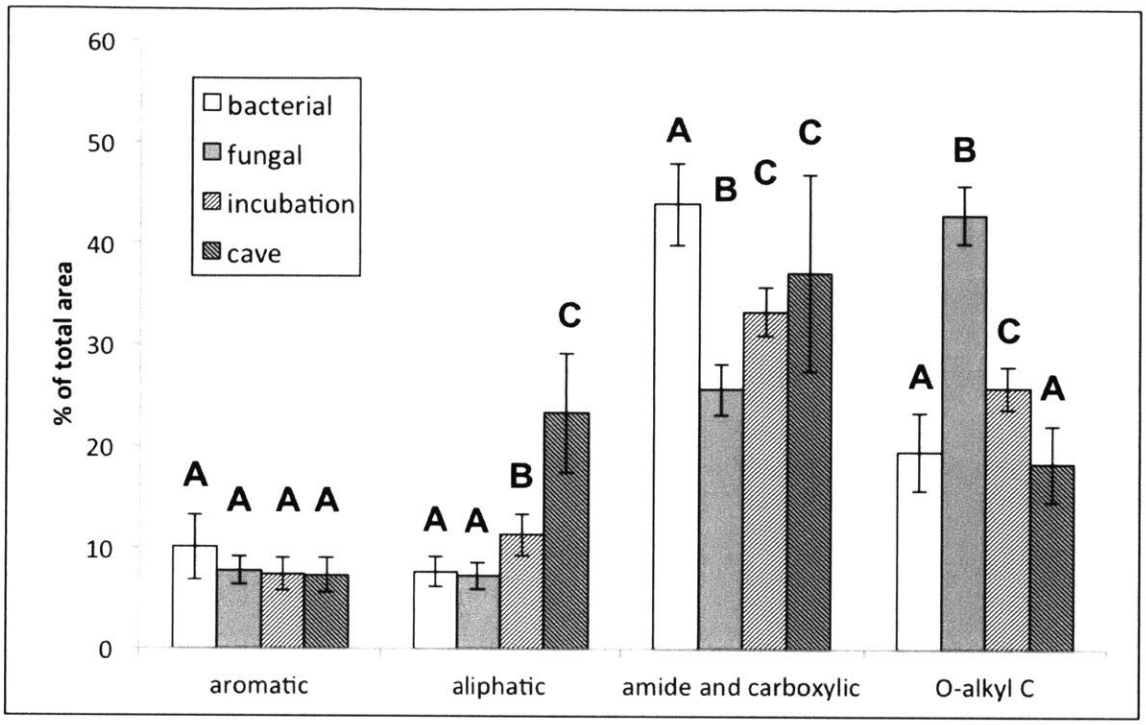

Figure 5. Average percent contribution of primary functional groups to total spectral area. Statistical differences determined by one-way ANOVAs. Letters designate significant differences between sample types ($p<0.05$, see text).

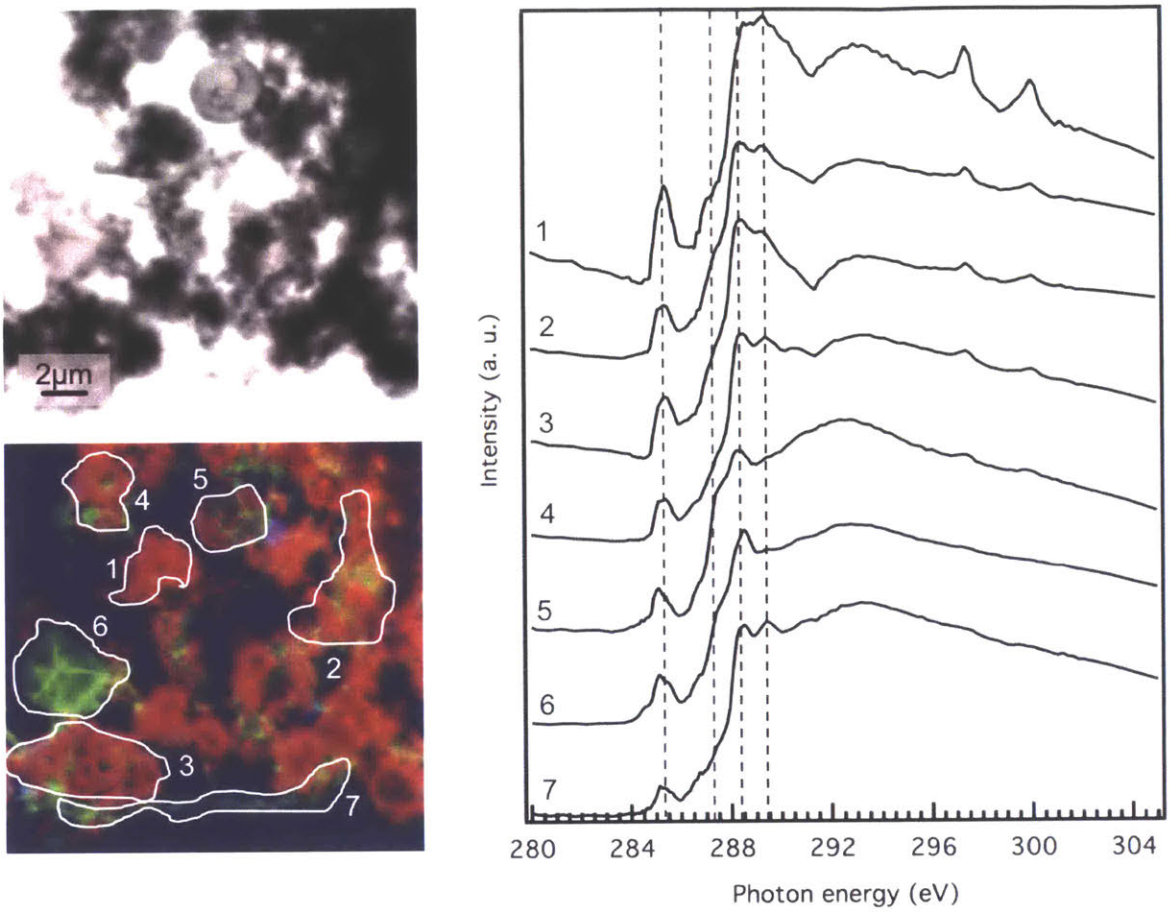

Figure 6. Transmission image (top left) and C (green), Mn (red), and Fe (blue) overlaid STXM OD maps of Mn oxides formed in Oyster Pond brackish water after 8 weeks (bottom left) and corresponding C 1s NEXAFS spectra (right). Guide lines are at 285.4, 287.2, 288.4, and 289.45 eV.

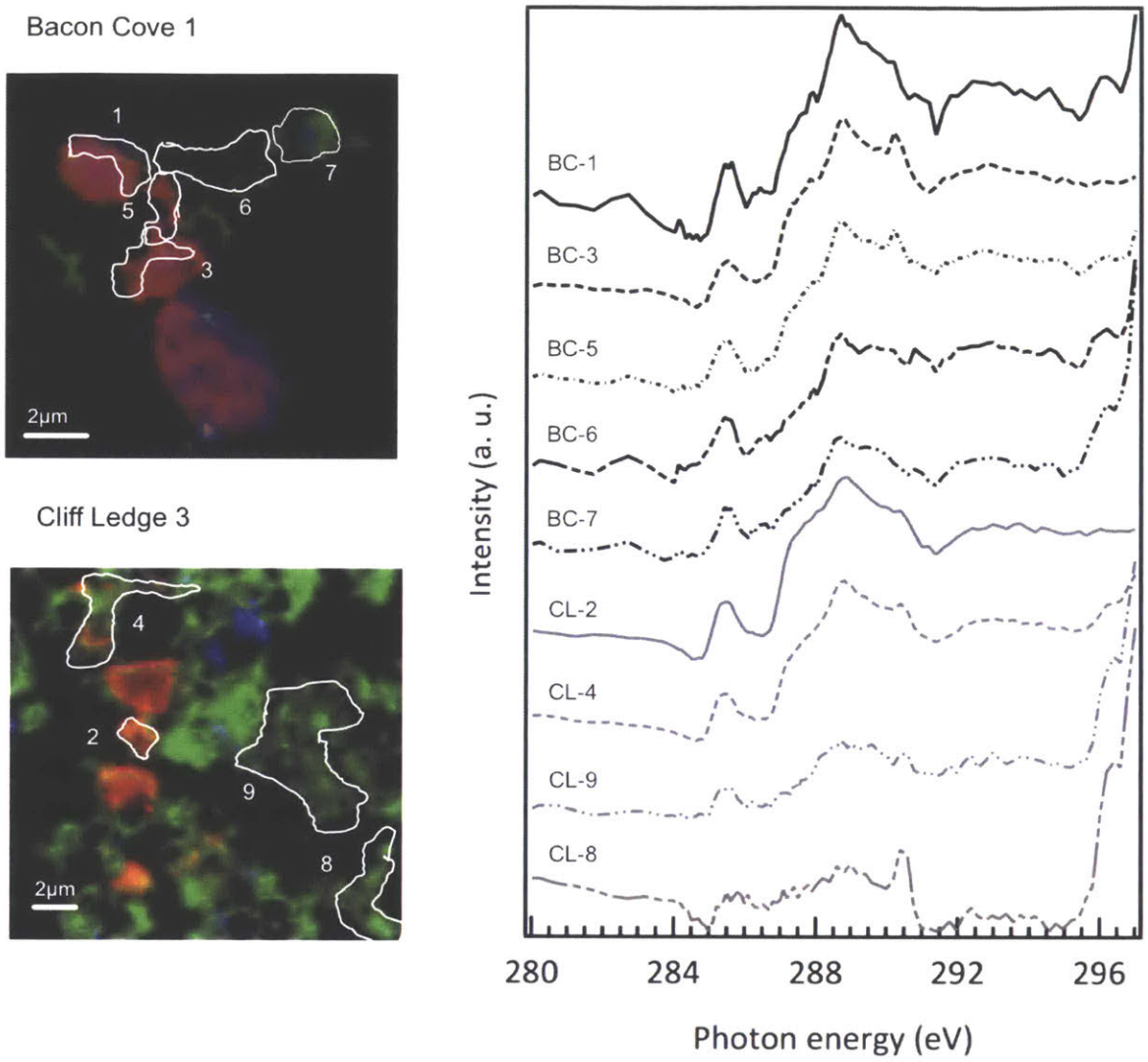

Figure 7. C (green), Mn (red), and Fe (blue) overlaid STXM OD maps of cave ferromanganese rock coatings (left) and corresponding C 1s NEXAFS spectra (right) for samples Bacon Cove 1 (top, black spectra) and Cliff Ledge 3 (bottom, grey spectra).

CHAPTER 2 SUPPORTING INFORMATION

Supplementary materials and methods

Bulk NEXAFS of Roseobacter *Mn oxides*

Bulk near edge X-ray absorption fine structure (NEXAFS) spectroscopy was conducted on beamline 8-2 at SSRL on mineral samples precipitated by bacterial and fungal cultures. 10-100 μL of concentrated biogenic MnOx were pipetted onto individual silicon wafers and dried at 30°C, covered (~ 2 hrs). Carbon and nitrogen standards were prepared in ultrapure water at an approximate concentration of 10 mM. Standards include bovine serum albumin (protein, BioRad), phenylalanine and lysine (amino acids), alginate and agarose (anionic and neutral polysaccharides), lipopolysaccharide (from *Escherichia coli* 055:B5), phospholipids (as 1,2-dipalmitoyl-*sn*-glycero-3-phosphoethanolamine), and oxalic acid. Unless otherwise specified, all standards were purchased from Sigma Aldrich.

The beamline was operated with a 500 l/mm spherical grating monochromator and an entrance and exit slit set to 40um, yielding an absolute energy resolution of less than 0.3 eV. The samples were attached to an aluminum sample stick in a single load and analyzed under ultrahigh vacuum conditions (pressure ~10^-9 mbar). Measurements were made in total electron yield (TEY) mode on a spot size of less than 1 mm^2, using a grazing incidence angle of either 20° or 35°, where incidence angle did not yield a difference in results (data not shown). Spectra were collected around the carbon 1s edge, from 260 to 340 eV, with a dwell time of 2 seconds. To avoid beam damage and variation of background due to charging, scans were taken at different positions on the sample. Spectra shown are either single scans or the average of 2-3 scans taken at different positions on the sample. A series of scans taken in a transect across several samples confirmed reproducibility.

Dark current in the sample current was measured prior to the collection of each spectrum and subtracted from the raw data. Spectra were then normalized to i0 current measured by a mesh upstream of the chamber with freshly evaporated gold. An absolute energy calibration of the carbon spectra was achieved by shifting the energy such that the first dip in the incoming intensity due to carbon contamination on the beamline optics (carbon dip) occurs at 284.7 eV. Spectral processing was completed by subtracting a line fit to the pre-edge region (281-283), followed by an area normalization between 282 and 310 eV, while keeping the high-energy intensity constant (atomic normalization). All data were processed in Igor Pro (WaveMetrics, Inc, Lake Oswego, Oregon).

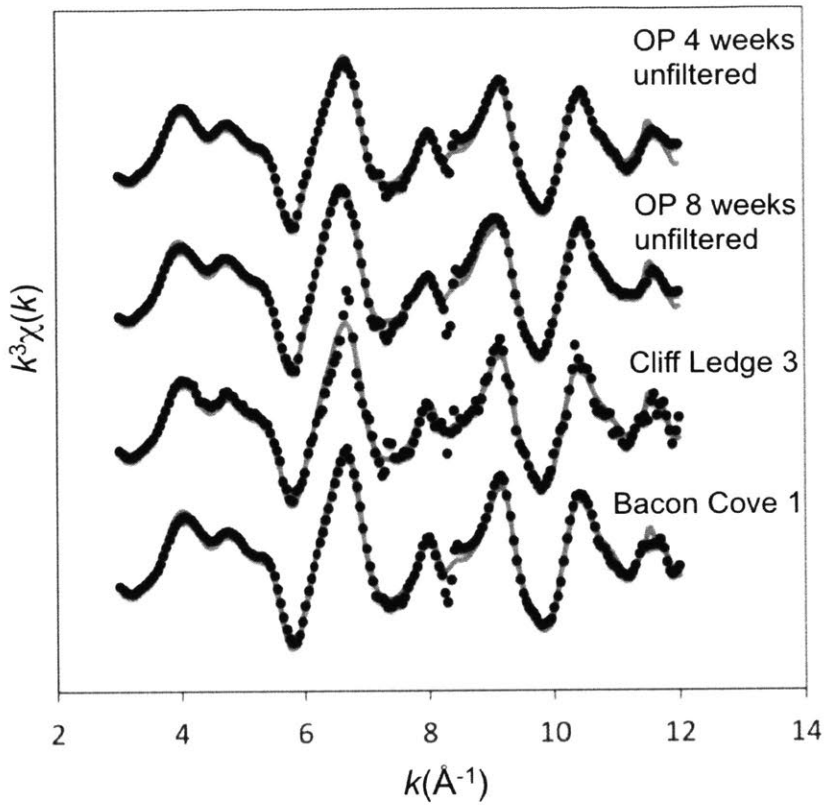

Figure S1. k^3-weighted Mn EXAFS spectra (dotted black line) and linear combination fit (solid gray line) for the Oyster Pond water incubations in the presence of aqueous Mn(II) reacted for 4 weeks (OP4) and 8 weeks (OP8), and ferromanganese coatings from Daniel Boone Caverns (C1, C3). Corresponding fitting results are provided in Table S1.

Table S1. Linear combination fits for the Mn EXAFS shown in Figure S1. Data provided as mole percent of each phase in the total Mn signal.

	Oyster Pond Incubations		**Ferromanganese Coatings**	
	4 weeks	**8 weeks**	**C1**	**C3**
Hexagonal Birnessite as δ-MnO2	92	51	92	93
Triclinic Birnessite	0	38	0	0
Mn(II)	8	11	8	7
R-factor	0.03	0.03	0.05	0.03

[a]goodness of fit established by the minimization in the *R*-factor (as in Newville M. (2001) IFEFFIT: interactive XAFS analysis and FEFF fitting. *J. Synch. Rad.* 8, 322-324)

Supporting results and discussion

Observation and implications of temporal changes in Mn oxide-associated organic carbon in culture and incubation experiments

Between 24 and 96 hours, OC associated with Mn oxides generated in Roseobacter filtrate significantly increased from 7.21 ± 0.42 to 8.50 ± 0.84 mol OC/kg mineral ($p= 0.002$, two-tailed t-test, Figure S2). The concentration of proteins associated with the Mn oxides also increased significantly over this time period (~3x) from 13.51 ± 4.02 to 40.24 ± 1.12 mg protein/g mineral ($p<0.001$, two-tailed t-test). In contrast, the concentration of TOC and proteins associated with Mn oxides formed upon oxidation of Mn(II) within brackish water from Oyster Pond (Cape Cod, MA), decreases between 4 to weeks (Figure S2). During this time period the initial Mn oxides within the Roseobacter and water incubations ripen from hexagonal to triclinic birnessite (see Learman et al., 2011, Figure S1, and Table S1). Despite this ripening, substantial levels of OC are associated with the Mn oxide precipitates.

Thus, carbon associates rapidly with Mn oxides under biomineralizing conditions within both cell free Roseobacter filtrate and Oyster Pond brackish water incubations. The mechanism(s) behind this rapid association are unknown, but may implicate extracellular biomolecules in assisting mineral nucleation and/or particle aggregation, as demonstrated in various mineralizing systems (Mann et al., 1993; Moreau et al., 2007; Kleber et al., 2015). Polysaccharides associated with stalks of the Fe(II)-oxidizing bacterium Mariprofundus ferroxydans have been described as templating Fe oxides that encrust the stalks (Chan et al. 2009; Chan et al., 2011; Bennett et al., 2014). However, in contrast to the rapid association of OC and Mn oxides in the Roseobacter secretomes observed here, concentrations of organic carbon were low during log phase growth and corresponding Fe oxide precipitation, with

substantial levels of mineral-associated OC only observed once M. ferroxydans entered stationary phase. Cell lysis was hypothesized as the source of this later carbon (Bennett et al., 2014). Thus, in that system, organic carbon templates constitute a small fraction of the total OC associated with the biogenic Fe oxides. In our systems, Mn oxide formation occurs in cell-free filtrate, in the absence of bacterial (or fungal) cells; instead, precipitation is mediated via extracellular enzymes and biomolecules secreted during growth. Nonetheless, the concentration and composition of this Mn oxide-associated carbon is established rapidly upon the onset of Mn oxide formation.

The association between carbon and Mn oxides is also established rapidly under passive adsorption conditions. For instance, incubation of brackish Oyster Pond waters with synthetic Mn oxides revealed substantial carbon associated with the Mn oxides after just 6 hours of reaction. The concentration of TOC increased moderately overtime. The concentration of OC accumulated by the synthetic minerals incubated is significantly less than that associated with biomineralized Mn oxides ($p<0.001$, one way ANOVA). Further, part of this Mn oxide associated OC can be attributed to rapid adsorption of DOC on the Mn oxides, as evidenced by the OC on synthetic Mn oxides that were incubated in filtered (0.2 μm) Oyster Pond water.

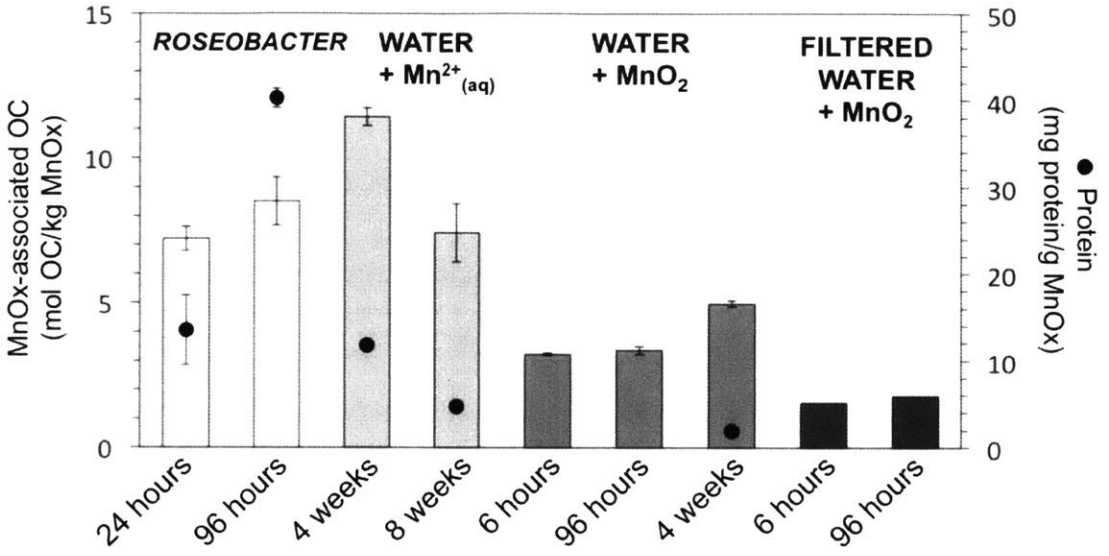

Figure S2. Changes in TOC and proteins associated with Mn oxides formed by *Roseobacter* filtrate and brackish water incubations over time.

Table S2. C 1s NEXAFS spectra peak fitting results for all samples and regions

		Functional group	quinone	aromatic	phenolic and ketonic	aliphatic	amide and carboxylic	O-alkyl-C	carbonate
		peak position (eV)	283.7-284.3	284-285.5	286.5-287.2	287.1-287.7	288.0-288.8	289.2-289.7	290-290.5
bulk NEXAFS	Roseobacter --8 hours	*bulk*	0	10.31	4.24	11.25	52.06	19.53	2.62
	Roseobacter --24 hours	*bulk*	0	11.67	1.91	8.93	58.40	18.28	0.80
	Roseobacter --72 hours	*bulk*	0	15.26	3.77	10.19	49.18	18.94	2.65
	Roseobacter --96 hours	*bulk*	0	12.87	2.25	8.12	58.66	16.96	1.13
STXM-NEXAFS	Roseobacter --6 hours	region 1	0.34	13.58	10.71	8.80	41.34	15.34	9.89
		region 2	0.48	13.64	11.88	7.40	40.69	18.23	7.68
		region 3	0.50	13.35	11.07	8.26	42.44	14.08	10.30
		region 4	0.46	13.19	9.26	9.15	42.51	15.16	10.27
		average	0.45	13.44	10.73	8.40	41.74	15.70	9.53
		stdev	0.07	0.21	1.09	0.76	0.88	1.77	1.25
	Roseobacter --24 hours	region 1	0.70	11.29	7.67	6.29	43.79	21.18	9.07
		region 2	0.13	10.05	8.57	5.61	45.18	19.04	11.42
		region 3	0.10	10.12	8.64	5.66	45.27	18.95	11.27
		region 4	0.15	10.51	7.51	6.64	43.37	18.72	13.11
		average	0.27	10.49	8.10	6.05	44.40	19.47	11.22
		stdev	0.29	0.57	0.59	0.50	0.97	1.15	1.66
	Erythrobacter --24 hours	region 1	0.25	3.97	4.10	6.16	55.87	19.30	10.35
		region 2	0.21	7.37	4.74	9.65	41.31	25.68	11.03
		region 3	0.21	6.97	5.02	9.10	44.35	22.87	11.48
		region 4	0.23	6.47	4.29	8.83	41.48	25.85	12.85
		average	0.22	6.20	4.54	8.44	45.75	23.43	11.43
		stdev	0.02	1.53	0.42	1.56	6.89	3.07	1.06
	bacterial average	**average**	0.31	10.04	7.79	7.63	43.97	19.53	10.73
		stdev	0.18	3.22	2.74	1.50	4.05	3.82	1.50
	Pyrenochaeta	region 1	0.91	10.06	6.46	7.83	28.67	37.31	8.76
		region 2	1.53	6.71	5.52	6.01	26.87	43.39	9.98
		region 3	1.19	7.35	6.12	7.13	28.07	41.40	8.74

	region 4	0.79	7.81	5.72	6.18	27.61	42.34	9.54
	average	1.11	7.98	5.95	6.79	27.80	41.11	9.25
	stdev	0.33	1.46	0.42	0.85	0.76	2.66	0.61
Stagonospora	region 1	1.06	9.81	6.62	5.92	25.28	42.30	9.01
	region 2	0.53	7.26	5.22	8.30	22.52	46.26	9.91
	region 3	0.54	6.56	5.04	9.85	23.87	44.06	10.08
	region 4	0.93	6.25	5.94	6.67	22.36	46.04	11.81
	average	0.77	7.47	5.70	7.69	23.51	44.66	10.20
	stdev	0.27	1.61	0.73	1.75	1.36	1.86	1.17
fungal average	**average**	0.94	7.73	5.83	7.24	25.66	42.89	9.73
	stdev	0.33	1.45	0.56	1.36	2.51	2.85	1.00
culture average	**average**	0.56	9.12	7.00	7.47	36.64	28.87	10.33
	stdev	0.40	2.85	2.33	1.42	9.83	12.22	1.39

Table S2, continued. C 1s NEXAFS spectra peak fitting results for all samples and regions

			Functional group	quinone	aromatic	phenolic and ketonic	aliphatic	amide and carboxylic	O-alkyl-C	carbonat
		inc time	**peak position (eV)**	283.7-284.3	284-285.5	286.5-287.2	287.1-287.7	288.0-288.8	289.2-289.7	290-290.5
syn MnOx	whole water	96 hours	region 1	0.00	11.58	2.27	11.32	40.93	21.79	12.11
	whole water	96 hours	region 3	0.00	12.56	2.20	11.17	40.44	21.65	11.97
	whole water	96 hours	region 4	0.00	12.03	2.30	11.15	40.25	21.02	13.25
	whole water	96 hours	region 5	0.00	11.54	2.03	11.11	40.74	21.28	13.30
			average	0.00	11.78	2.17	11.13	40.50	21.15	13.27
			stdev	0.00	0.35	0.19	0.03	0.35	0.18	0.04
syn MnOx average			**average**	0.00	11.93	2.20	11.19	40.59	21.44	12.66
			stdev	0.00	0.48	0.12	0.09	0.30	0.35	0.71
mineralized	whole water	8 weeks	region 1	0.00	10.08	4.98	8.43	29.96	24.87	21.68
	whole water	8 weeks	region 2	0.00	6.60	5.87	11.59	34.82	25.58	15.53
	whole water	8 weeks	region 3	0.00	7.57	6.32	11.70	34.72	27.07	12.62
	whole water	8 weeks	region 4	0.00	6.33	5.29	10.71	35.64	28.44	13.59
	whole water	8 weeks	region 5	0.00	6.16	3.89	14.17	31.59	22.96	21.22
	whole water	8 weeks	region 6	0.00	8.78	4.49	14.47	33.03	23.34	15.90
	whole water	8 weeks	region 7	0.00	5.42	6.63	5.91	39.02	29.16	13.86
			average	0.00	7.28	5.35	11.00	34.11	25.92	16.34
			stdev	0.00	1.64	0.99	3.04	2.95	2.41	3.67
mineralized average*			**average**	0.00	7.35	5.27	11.32	33.35	25.78	16.93
			stdev	0.00	1.62	0.93	2.06	2.45	2.10	4.26
incubation average*			**average**	0.00	9.38	3.91	11.26	36.57	23.85	15.03
			stdev	0.00	2.69	1.75	1.46	4.20	2.74	3.79

* excludes unfiltered water regions 6 and 7, which contains no/low Mn

		Functional group	quinone	aromatic	phenolic and ketonic	aliphatic	amide and carboxylic	O-alkyl-C	carbonate
		peak position (eV)	283.7-284.3	284-285.5	286.5-287.2	287.1-287.7	288.0-288.8	289.2-289.7	290-290.5
Bacon Cove	low/no Mn	region 7	1.02	10.70	4.11	21.69	30.43	27.65	4.40
	low/no Mn	region 6	1.03	12.11	2.37	21.27	31.62	26.12	5.48
	Mn-rich	region 5	0.04	9.18	1.24	26.70	29.06	24.81	8.97
	Mn-rich	region 3	2.18	7.37	1.20	28.88	30.10	17.02	13.25
	Mn-rich	region 1	0.86	8.72	2.65	27.17	31.12	18.13	11.36
Bacon Cove, low/no Mn		**average**	1.02	11.41	3.24	21.48	31.03	26.88	4.94
		stdev	0.01	1.00	1.23	0.29	0.84	1.08	0.76
Bacon Cove, Mn-rich		**average**	1.02	8.42	1.70	27.58	30.09	19.99	11.19
		stdev	1.08	0.94	0.82	1.14	1.03	4.21	2.14
Bacon Cove all		**average**	1.02	9.62	2.31	25.14	30.47	22.75	8.69
		stdev	0.76	1.83	1.20	3.44	0.98	4.84	3.76
Cliff Ledge	low/no Mn	region 9	0.43	9.18	3.75	15.64	42.64	19.91	8.45
	low/no Mn	region 8	0.92	13.17	2.65	18.87	28.08	18.23	18.09
	Mn-rich	region 4	0.07	5.36	0.27	15.80	47.55	16.23	14.72
	Mn-rich	region 2B	0.01	5.72	0.08	18.22	47.78	15.56	12.63
Cliff Ledge, low/no Mn		**average**	0.67	11.17	3.20	17.26	35.36	19.07	13.27
		stdev	0.34	2.82	0.78	2.28	10.30	1.19	6.82
Cliff Ledge, Mn-rich		**average**	0.04	5.54	0.18	17.01	47.67	15.89	13.68
		stdev	0.04	0.25	0.14	1.71	0.16	0.47	1.48
Cliff Ledge all		**average**	0.36	8.36	1.69	17.13	41.51	17.48	13.47
		stdev	0.42	3.64	1.80	1.66	9.27	1.98	4.04
Mn-rich regions		**average**	0.63	7.27	1.09	23.35	37.12	18.35	12.19
		stdev	0.93	1.72	1.02	5.91	9.65	3.74	2.17
low/no Mn regions		**average**	0.85	11.29	3.22	19.37	33.19	22.98	9.11
		stdev	0.28	1.73	0.84	2.78	6.47	4.60	6.23
cave average		**average**	0.73	9.06	2.04	21.58	35.38	20.41	10.82
		stdev	0.69	2.66	1.43	4.98	8.16	4.57	4.42

Supporting results and discussion

Lack of change in chemical composition of Mn oxide-associated organic carbon despite mineral transformation

As shown in Figure S2, an OC-Mn oxide association remains intact despite mineral ripening and coarsening of Mn oxides. In particular, despite the ripening of initial colloidal hexagonal birnessite to more crystalline and particulate triclinic birnessite in the *Roseobacter* filtrate (Learman et al., 2011) the chemical composition of the carbon shows no concomitant transformation and in fact has the same composition at 96 hours as at 8 hours (Figure S3). Similarly, organic carbon was retained during transformation of ferrihydrite to more stable Fe oxides under surface conditions (Chen et al., 2015) and simulated diagenesis (Picard et al., 2015); however, in the surface-condition experiments, at the final experiment time point (90 days), a greater proportion of OC was desorbable with $H_2PO_4^-$ (Chen et al., 2015), implying decreased preservation potential. Organic carbon associated with Fe oxides formed by the Fe(II)-oxidizing *M. ferroxydans* became more enriched in aromatic- and unsaturated-C throughout the growth cycle and as the Fe oxide ripened (Bennett et al., 2014). This shift may be due to changes in the source carbon, however, rather than mineral-induced alteration of the carbon or preferential associations with specific mineral structures, as the organism transitioned from log to stationary phase during the course of the experiment, generating additional OC from cell lysis. In the experiments shown here, cells were removed prior to mineral precipitation such that lysis cannot contribute additional carbon.

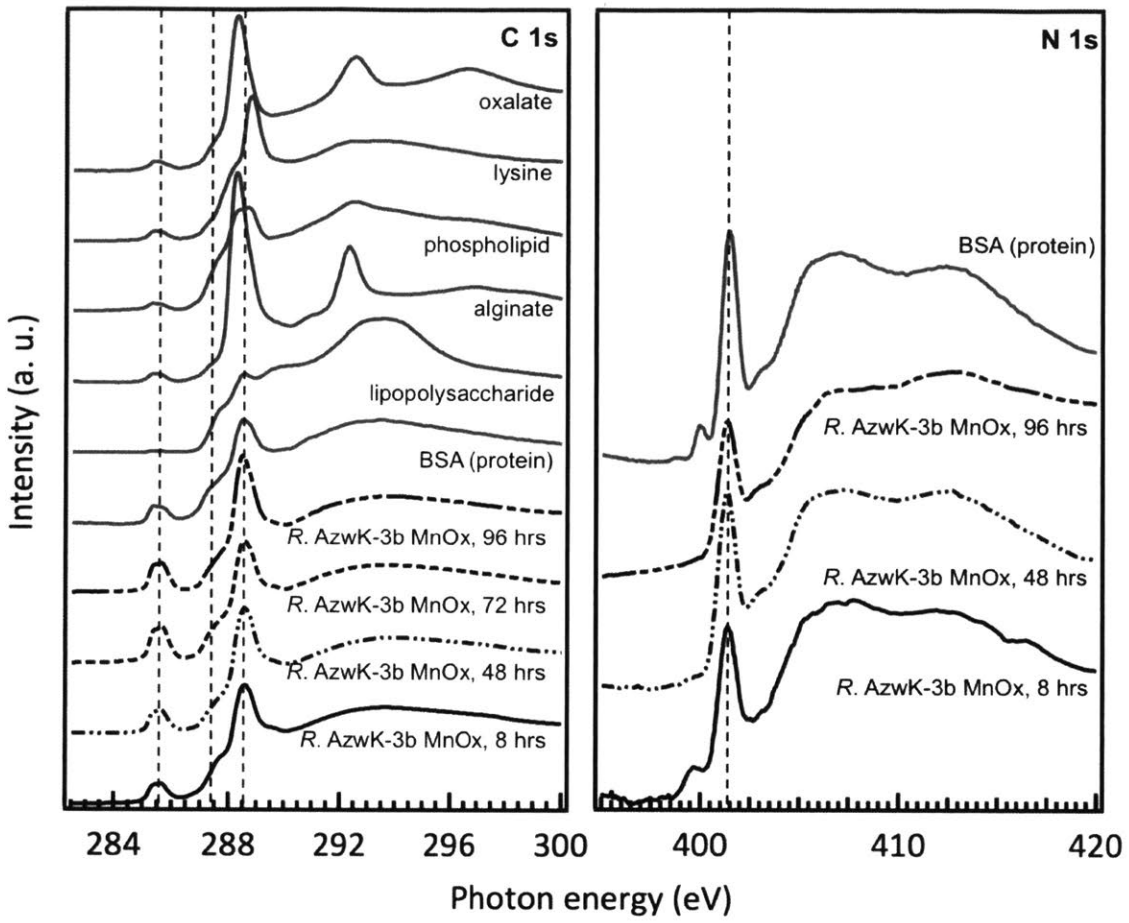

Figure S3. Bulk C 1s (left) and N 1s (right) NEXAFS spectra for organic matter associated with Mn oxides formed in *Roseobacter* filtrate following 8 to 96 hours of incubation. Carbon spectra are shown with accompanying standard compounds.

Supporting results and discussion

Chemical composition of organic carbon associating with biomineralized vs. synthetic Mn oxides following brackish water incubations

In comparison to the Mn oxides formed during active Mn(II) oxidation in the brackish Oyster Pond waters (Figure 6), the carbon associated with the synthetic Mn oxide additions was more homogeneous in chemical composition (average relative standard deviation of ~3% for peak fitting of all functionalities, relative to ~19% for the mineralized sample). The C NEXAFS spectra have with very intense aromatic C peaks at 285.4 eV, (11.9 ± 0.5% of total fit area) visible shoulders ~287.1 eV (aliphatic C, 11.2 ± 0.1%), and somewhat of a plateau between 288.5 and 289.4 eV (amide/carboxylic C, 40.6 ± 0.3%; O-alkyl-C, 21.4 ± 0.4%) (Figures S4 and S5). Results from peak fitting of extracted spectra were averaged to allow a statistical comparison between mineralization (n=5 regions, excluding the low/no-Mn regions 6 and 7) and synthetic Mn oxide (n=4 regions) incubations. This comparison shows that synthetic Mn oxides accumulated a greater proportion of OC with aromatic functionalities (p= 0.005, two-tailed t-test) but fewer O-alkyl-C groups (p=0.05, two-tailed t-test) (Figure S5).

Thus, differences were observed in the carbon distribution and composition within Mn oxides formed either within the Oyster Pond water (active mineralization; carbon may adsorb or co-precipitate with the oxides) or added as synthetic Mn oxides of similar structure to the same water (adsorption only). Mn oxides produced during active Mn(II) oxidation within the pond waters are enriched in O-alkyl-C but depleted in aromatic groups relative to the pre-formed synthetic Mn oxides directly added to the same pond water. These functional differences may reflect the incorporation of specific organic carbon molecules involved in templating and/or aggregating Mn oxides as opposed to non-specific adsorption processes.

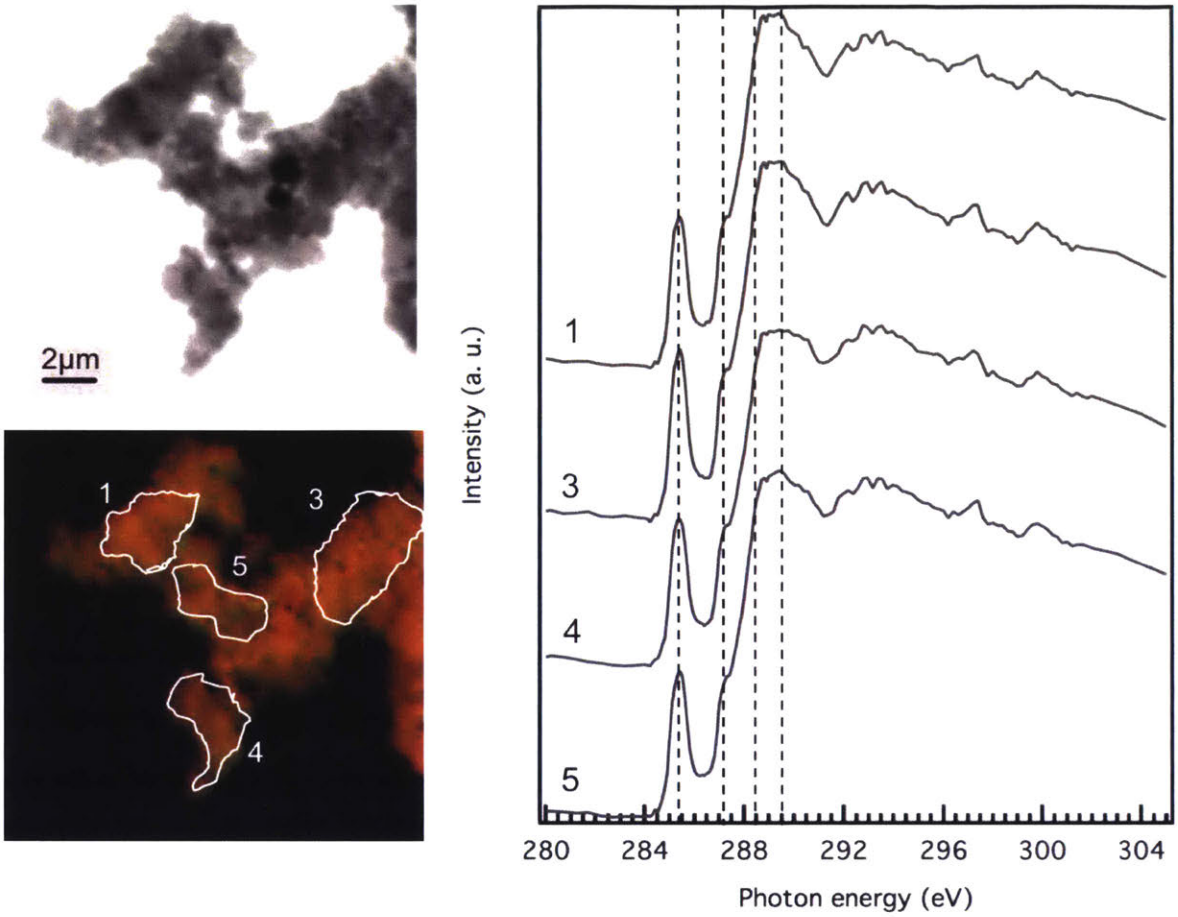

Figure S4. Transmission image (top left) and C (green), Mn (red), and Fe (blue) overlaid STXM OD maps of synthetic Mn oxides incubated in Oyster Pond brackish water for 96 hours (bottom left) and corresponding C 1s NEXAFS spectra (right). Guide lines are at 285.4, 287.2, 288.4, and 289.45 eV.

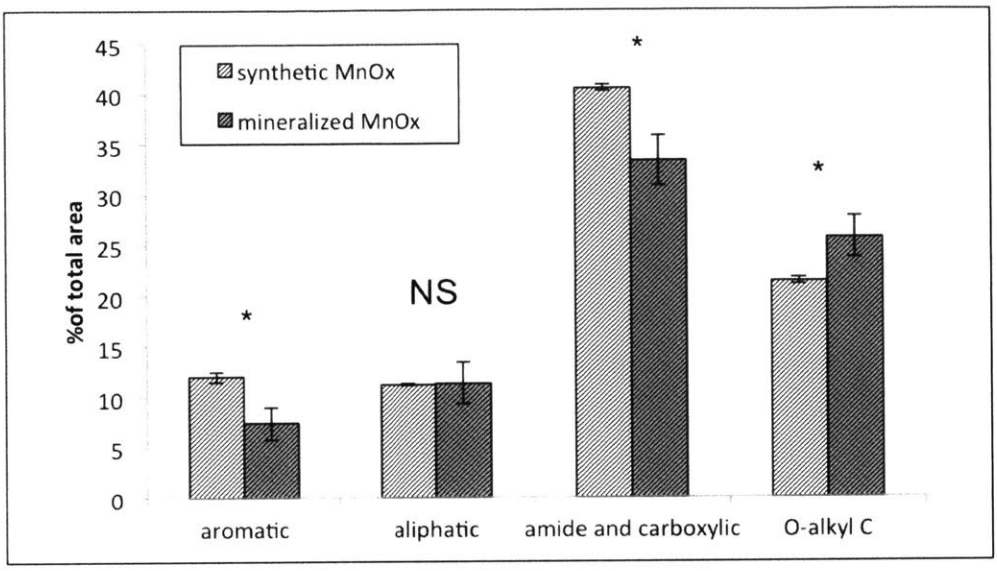

Figure S5. Comparison of average percent contribution of primary functional groups to total spectral area for Mn oxides mineralized over 8 weeks in brackish Oyster Pond water vs. synthetic Mn oxides incubated for 96 hours in Oyster Pond water. An asterisk denotes statistically significant differences between treatments (p=0.05, two-tailed t-test) while "NS" denotes no significance.

Table S3 Identified MnOx associated proteins*

Putative Protein Description**	NCBI Protein Reference Sequence	% of Spectra assigned to genome*
***Roseobacter* sp. AzwK-3b**		
AhpL	AKH40935.1***	55.5
Sulfate ABC transporter, periplasmic substrate binding protein	WP_007811278.1	5.9
Hemolysin-type calcium binding region, PAP2 haloperoxidase_like superfamily	WP_007813058.1	4.2
Hemolysin-type calcium binding region, PAP2 haloperoxidase_like superfamily	WP_007817497.1	4.2
Ribosomal protein	WP_007817149.1	3.4
Malate-CoA ligase beta subunit	WP_007812203.1	3.4
ABC transporter,periplasmic substrate binding protein	WP_007817006.1	2.5
S-adnosylmethionine synthetase	WP_007813992.1	2.5
Carbon-monoxide dehydrogenase	WP_007813459.1	2.5
TroA-family Zinc/manganese transport protein	WP_050774151.1	2.5

Table S3, continued. Identified MnOx associated proteins*

Putative Protein Description**	NCBI Protein Reference Sequence	% of Spectra assigned to genome*
***Erythrobacter* sp. SD-21**		
Porin, TonB-dependent heme/hemoglobin receptor family	WP_006833849.1	11.9
Porin superfamily, TonB-dependent receptor	WP_006833853.1	10.3
MopA	WP_006834642.1	7.9
Peptidase	WP_006833852.1	7.9
Outer membrane cobalamin receptor protein	WP_006831923.1	6.3
peptidoglycan-associated protein (outer membrane OmpA)/MotB flagellar motor protein	WP_034921711.1/EDL49045.1	4.8
Outer membrane receptor protein (possible Fe-trans)	WP_006833976.1	4.0
Predicted zinc metalloprotease	WP_006832538.1	4.0
Peptidase	WP_006833325.1	4.0
Hypothetical protein	WP_006832146.1	4.0
Outer membrane receptor protein (possible Fe-trans)	WP_006832482.1	3.2
Putative secreted calcium binding protein	WP_006833235	3.2
Outer membrane, OmpA related	WP_034921497.1/EDL49884.1	3.2
Hypothetical protein, peptidase	WP_006834582.1	3.2
Periplasmic peptidase, serine protease	WP_006833952.1	3.2
Outer membrane receptor protein (possible Fe-trans)	WP_006833518.1	2.4
TonB-dependent receptors	WP_006833718.1***	2.4
Hypothetical	WP_006833057.1	2.4
Outer membrane receptor protein (possible Fe-trans)	WP_034922553.1	2.4

* - proteins were included in the table that met the following criteria using Scaffold v.4.4.6: Protein threshold at least 99% with a minimum of 2 peptides with a peptide threshold of 95%. Identities with less than 3 spectral counts were also omitted

** - refer to current descriptions in NCBI's protein database

** - indicate other proteins present in the genome with near identical sequences

Supporting information: References

Bennett, S.A., Toner, B.M., Barco, R., & Edwards, K.J. (2014). Carbon adsorption onto Fe oxyhydroxides stalks produced by a lithotrophic iron-oxidizing bacteria. *Geobiology, 12*(2), 146—156. doi: 10.1111/gbi.12074

Chan, C. S., Fakra, S. C., Edwards, D. C., Emerson, D., & Banfield, J. F. (2009). Iron oxyhydroxide mineralization on microbial extracellular polysaccharides. *Geochimica et Cosmochimica Acta, 73*(13), 3807–3818. doi:10.1016/j.gca.2009.02.036

Chan, C. S., Fakra, S. C., Emerson, D., Fleming, E. J., & Edwards, K. J. (2011). Lithotrophic iron-oxidizing bacteria produce organic stalks to control mineral growth: implications for biosignature formation. *The ISME Journal, 5*(4), 717–27. doi:10.1038/ismej.2010.173

Chen, C., Kukkadapu, R., & Sparks, D. (2015). Influence of coprecipitated organic matter on Fe2+(aq)-catalyzed transformation of ferrihydrite: Implications for carbon dynamics. *Environmental Science and Technology, 49*(18), 10927-10936. doi: 10.1021/acs.est.5b0244

Kleber, M., Eusterhues, K., Keiluweit, M., Mikutta, C., Mikutta, R., & Nico, P. S. (2015). Mineral–Organic Associations: Formation, Properties, and Relevance in Soil Environments. *Advances in Agronomy, 130*, 1–140. doi:10.1016/bs.agron.2014.10.005

Learman, D. R., Wankel, S. D., Webb, S. M., Martinez, N., Madden, a. S., & Hansel, C. M. (2011). Coupled biotic–abiotic Mn(II) oxidation pathway mediates the formation and structural evolution of biogenic Mn oxides. *Geochimica et Cosmochimica Acta, 75*(20), 6048–6063. doi:10.1016/j.gca.2011.07.026

Mann, S., Archibald, D. D., Didymus, J. M., Douglas, T., Heywood, B. R., Meldrum, F. C., & Reeves, N. J. (1993). Crystallization at Inorganic-organic Interfaces: Biominerals and Biomimetic Synthesis. *Science (New York, N.Y.), 261*(September), 1286–1292. doi:10.1126/science.261.5126.1286

Moreau, J. W., Weber, P. K., Martin, M. C., Gilbert, B., Hutcheon, I. D., & Banfield, J. F. (2007). Extracellular proteins limit the dispersal of biogenic nanoparticles. *Science (New York, N.Y.), 316*(5831), 1600–3. doi:10.1126/science.1141064

Picard, A., Kappler, A., Schmid, G., Quaroni, L., & Obst, M. (2015). Experimental diagenesis of organo-mineral structures formed by microaerophilic Fe(II)-oxidizing bacteria. *Nature Communications, 6*(May 2014), 6277. doi:10.1038/ncomms7277

Chapter 3: The distribution and composition of persistent organic carbon in oxygenated pelagic sediments

ABSTRACT

Sediments cover 70% of the earth's surface and up to 40% of that area may be oxygenated through basement. These oxic sediments are found underlying oligotrophic regions of the ocean and, in contrast to anoxic systems, microbial life is electron donor rather than acceptor-limited. Thus, understanding the concentration and chemical composition of organic carbon (OC) that exist in these regions provides insight into the geochemical constraints on subsurface life and the mechanisms contributing to the preservation of OC. To that end, here we interrogate oxic sediments from the oligotrophic North Atlantic and South Pacific gyres using near edge X-ray absorption fine structure spectroscopy (NEXAFS). We measure among the lowest concentrations of sedimentary OC found globally (<0.1 %OC) with OC and nitrogen concentrations decreasing rapidly over the first 1.5 m below seafloor then plateauing to a relatively stable concentration over depths of 25 m below seafloor and estimated sediment ages up to 24 Myr. Further, we find measurable quantities of intact proteins, although these extractable proteins account for <<1% of the total OC. The relative abundances of OC functional groups show substantial variation on the bulk scale throughout the cores, but show no discernable trend with depth. The strongest correlation between functionalities on both the bulk and micro-scale exists between aliphatic and amide/carboxylic carbon which may be indicative of carboxylic-rich alicyclic material (CRAM). However, the overall variability in relative functional group abundances raises the possibility that this material consists of a spectrum of carbon species with a wide gradient in bioavailability and chemical potential.

3.1 INTRODUCTION

The total number of microbial cells in the subseafloor matches that found in soils and seawater (Kallmeyer *et al.*, 2012). These organisms survive at the limits of life, at depths of up to ~2.5 km below seafloor (Inagaki *et al.*, 2015) using a diverse range of metabolisms and adaptations to garner energy from the environment (Jørgensen and Marshall 2016; Lever et al. 2015). Heterotrophic metabolisms are active in the deep subsurface (Biddle et al. 2008; Jørgensen et al. 2013; Lloyd et al. 2013; Orcutt et al. 2011; Russell et al. 2016), sustained by buried organic carbon and electron acceptors from the photosynthetic surface environment (D'Hondt *et al.*, 2004; Lomstein *et al.*, 2012). Oxygenated sediments comprise 9-37% of the global seafloor and likewise contain active microbial communities that couple aerobic respiration to oxidation of organic matter, despite its scarcity in those environments (Archer *et al.*, 2002; D'Hondt *et al.*, 2009, 2015; Roy *et al.*, 2012). In contrast to coastal sediments that have high organic carbon loads and rapidly consume electron acceptors in the process of microbially-mediated remineralization, oxic sediments are found underlying oligotrophic regions of the ocean and are electron donor-limited. Thus, predictions of the extent and limits on microbial life in oxygenated sediments hinge on determining the quantity and quality of organic carbon (OC) available.

Depth profiles of OC concentrations in sediments can be modeled by describing OC as a single pool that becomes increasingly less reactive with depth (Middelburg, 1989; Boudreau & Ruddick, 1992; Arndt *et al.*, 2013). A range of mechanisms, however, likely contribute to decreased reactivity, from recalcitrance to preservation of otherwise more "labile" OC due to association with mineral surfaces or electron acceptor limitation. Due to these factors, OC content alone is not a predictor of availability (Durbin & Teske, 2012) or potential energy yields

(LaRowe & Van Cappellen, 2011). Indeed, a review of over 250 published models of OC degradation emphasizes that no model parameters correlate with single environmental variables such that a model may be easily transferred from one environmental system to another (Arndt *et al.*, 2013).

Improved characterization of the chemical composition of OC in a range of environments, particularly understudied regions such as oxygenated pelagic sediments, will undoubtedly contribute to our understanding of the mechanisms contributing to OC preservation, degradation, and bioavailability to the deep biosphere. However, sedimentary OC is notoriously difficult to describe, and oftentimes referred to as "molecularly-uncharacterized organic matter" (Wakeham *et al.*, 1997; Hedges *et al.*, 2000). Sedimentary OC and the uncharacterizable fraction of DOC and sinking particulate matter is typified by a high amino acid or peptide-like component (Brandes et al. 2004; Hedges et al. 2001; Hertkorn et al. 2006) and alkyl and O-alkyl groups (Brandes *et al.*, 2004; Dickens *et al.*, 2006; Hertkorn *et al.*, 2006; Mao *et al.*, 2011) interpreted as products of partial oxidation reactions that result in substituted and copolymerized carbohydrate structures (Mao *et al.*, 2011). Carbon characterization using Fourier transform ion cyclotron resonance mass spectromertry (FT-ICR-MS) indicates an increase in the number of compounds observed as well as larger compounds with depth in the sediments or between bottom water and porewater, both for porewater (Schmidt *et al.*, 2009, 2011) and sedimentary "water extractable organic matter" (Oni *et al.*, 2015). Finally, N-bearing organic compounds appear enriched in sedimentary interstitial waters relative to the marine water column (Schmidt *et al.*, 2009, 2011), which has been interpreted as evidence of protein degradation (Schmidt *et al.*, 2011).

Despite recent advances, NMR and FT-ICR-MS analyses remain limited in the fraction of OC they can characterize due to requisite sample pre-processing, including demineralization to remove paramagnetic minerals, solid phase extractions, and/or other chemical extractions. This limitation prohibits a non-invasive, detailed characterization of organic carbon, particularly within complex samples. In contrast, X-ray absorption spectroscopy provides an attractive alternative to sediment characterization as it is non-invasive, non-destructive and does not require any sample pre-processing prior to analysis. Further, as synchrotron X-rays are tunable and have a high flux, they are ideally suited for analyzing elements present in low concentrations and in complicated matrices (Templeton & Knowles, 2009). Further, near-edge X-ray absorption fine structure spectroscopy (NEXAFS) provides equivalent information to NMR and FT-ICR-MS of the structural composition of OC in sediments on the bulk scale. As such, here we examine the content and chemical composition of OC in oxygenated pelagic sediments in order to gain insight into carbon cycling and bioavailability in an important, understudied marine ecosystem.

3.2 Methods

3.2.1 Sample Collection

Sediment samples were collected via long piston corer on expeditions Knox02-RR on the R/V Roger Revelle (South Pacific) and KN223 on the R/V Knorr (North Atlantic). Sites South Pacific Gyre (SPG) 1 and 9 are at -23°51'N -165°39'W and -38°04'N -133°06'W, with water depths of 5697 and 4925 m, and sedimentation rates of 0.031 and 0.05 cm/kyr, respectively (D'Hondt *et al.*, 2009). North Atlantic (NA) sites 11 and 12 are at 22°47'N 56°31'W and 29°41'N 58°20'W with water depths of 5557 and 5367 m, and sedimentation rates of 0.143 and

0.109 cm/kyr respectively. Sedimentation rates were taken from D'Hondt et al. 2009 or estimates derived from sediment thickness (Divins, 2003) and crustal age (Müller *et al.*, 2008), or, for SPG 1, the 65 Ma Cretaceous/Paleogene iridium anomaly (D'Hondt *et al.*, 2009). All samples were kept at 4°C until analysis. Coring sites were selected as being in oligotrophic waters with extremely low export and sedimentation rates where sediments remain oxygenated until basement. All four sites have lithologies consisting of primarily pelagic clay; SPG sites have a manganese oxide-rich layer at the core top with additional nodules at depth (D'Hondt *et al.*, 2009) while NA sites have accessory mineral phases including iron oxide, quartz, and plagioclase dispersed throughout (Murray et al. 2014 KN223 cruise report). Site NA 11 contains evidence of bioturbation mottling throughout the core and occasional layers of zeolitic clay and chertified radiolarian tests (Murray et al. 2014 KN223 cruise report).

3.2.2 Organic Carbon Quantification

Organic carbon and nitrogen were analyzed via element-analyzer isotope ratio mass spectrometry (EA-IRMS) at the WHOI mass spectrometry facility using a Carlo Erba Elemental Analyzer Model 1108 and a Finnigan-MAT DeltaPlus Isotope Ratio Monitoring Mass Spectrometer. Prior to analysis, samples were freeze-dried then acidified to remove carbonate following the procedure described in Whiteside et al. 2011. Every tenth sample was analyzed in triplicate to determine analytical error; concentrations were calibrated and drift corrected using USGS 40 (L-glutamic acid) reference material and an in-house glycine standard.

Intact proteins were extracted following the protocol of Ehrenreich and Widdel 1994 with modification as described in Estes et al. 2016. Briefly, sediments were suspended in 1.5 mL ultrapure water and sonicated three times at 40% duty cycle, keeping the samples on ice between

sonication cycles. 300 μL of 6N hydrochloric was then added to the solution and incubated at 37°C for 30 minutes. Then, 75 μL 10 M trichloroacetic acid was added and the mixture incubated on ice for 30 minutes. Finally, samples were centrifuged at 14,000 rcf for 15 minutes, the supernatant decanted, and an additional 500 μL of 0.1 N NaOH was added. Samples were boiled for 5 minutes and cooled to room temperature prior to analysis via Qubit fluorescent reagent (Life Technologies). Fluorescence was calibrated using a six-point calibration from zero (18 MΩ water) to 187.5 μg/mL bovine serum albumin standard (BioRad). R^2 values for the calibration curves were always >0.9 and usually >0.95; often decreased R^2 values came from the zero-protein standard being non-linear, in which case it was excluded from the calibration curve.

3.2.3 Organic Carbon Characterization

Bulk carbon near edge X-ray absorption fine structure (NEXAFS) spectroscopy was conducted on beamlines 8-2 and 10-1 at Stanford Synchrotron Radiation Lightsource (SSRL). Sediment slurries were generated by subsampling ~0.1 g wet sediment from samples stored at 4 °C into a sterile microcentrifuge tube. 0.2 to 0.5 mL of 0.2 μm-filtered 18MΩ water was then added and the sample shaken. Sediment slurry (1-10 μL) was pipetted onto silicon wafers and air-dried. The beamline was operated with a 500 l/mm spherical grating monochromator and entrance and exit slits set to 40 μm, yielding an absolute energy resolution of less than 0.3 eV. The samples were attached to an aluminum sample stick in a single load and analyzed under ultrahigh vacuum conditions (pressure ~10^-9 mbar). Measurements were made in total electron yield (TEY) mode on a spot size of less than 1 mm^2, using a grazing incidence angle of 45°, where previous trials determined that incidence angle did not yield a difference in results (Estes *et al.*, 2016). Spectra were collected around the carbon 1s edge, from 260 to 340 eV, with a dwell

time of 0.2 seconds. To avoid beam damage and variation of background due to charging, scans were taken at different positions on the sample. Spectra analyzed were the average of 2-3 scans taken at different positions on the sample. A series of scans taken in a transect across several samples confirmed reproducibility. Dark current in the sample current was measured prior to the collection of each spectrum and subtracted from the raw data. Spectra were then normalized to I0 current measured by a mesh upstream of the chamber with freshly evaporated gold. An absolute energy calibration of the carbon spectra was achieved by shifting the energy such that the first dip in the incoming intensity due to carbon contamination on the beamline optics (carbon dip) occurs at 284.7 eV. Spectral processing was completed by subtracting a line fit to the pre-edge region (281-283 eV), followed by an area normalization between 282 and 310 eV, while keeping the high-energy intensity constant (atomic normalization). The entire pre-edge region appeared linear; fitting and background subtraction was conducted over a smaller energy range due to the presence of oxygen harmonic peaks. All data were processed in Igor Pro (WaveMetrics, Inc, Lake Oswego, Oregon).

3.3 RESULTS

3.3.1. Site Geochemistry

To assess how oxygenated sediments preserve or degrade organic carbon (OC) globally, we compared the geochemistry and OC chemical composition at two sites from the South Pacific and two sites from the North Atlantic (Figure 1). The South Pacific Gyre (SPG) sites 1 and 9 were cored during expedition KNOX02-RR in 2006—2007, an IODP site survey. Site geochemistry, lithology, and cell abundances are described in previous work (D'Hondt *et al.*, 2009, 2011; Fischer *et al.*, 2009) while site metadata are summarized in Table 1. Core SPG 1

recovered 7.8 meters sediment and core SPG 9 recovered 7.0 meters, accounting for 11% and 35% of total sediment depth at those sites (D'Hondt *et al.*, 2009). Sedimentation rates were 0.031 and 0.051 cm/kyr, respectively (D'Hondt *et al.*, 2009). Assuming a constant sedimentation rate, this estimate translates into sediment ages of 24.0 and 11.2 Ma at core bottom. Due to low productivity in the overlying water column in addition to water depths greater than the calcite compensation depth at both sites, these sedimentation rates are among the lowest observed on Earth (D'Hondt *et al.*, 2009). At both sites, dissolved O_2 in interstitial waters was >150 μM and nitrate between ~35-45 μM (D'Hondt et al. 2011, Figure 2). Sediment collected from SPG sites consisted of homogeneous dark brown clay bearing manganese nodules and crusts; SPG 9 is slightly lighter brown than SPG 1 and contains occasional yellow-brown mottling (D'Hondt *et al.*, 2011).

Cores from the western subtropical North Atlantic were taken during expedition KN223 in 2014 at sites 11 and 12. At site NA 11, 28.2 meters sediment out of an estimated 100 m sediment thickness was recovered (28%), compared to 26.0 m out of 98 m total sediment thickness (26%) at site 12. Based on estimated sedimentation rates of 0.14 and 0.11 cm/kyr, sediment ages at core bottoms are 18.5 and 23.4 Myr. At site NA 11, dissolved O_2 in interstitial waters declined from bottom water levels of ~300 μM to ~20 μM at core bottom, while at site NA 12 concentrations remained ~70 μM at core bottom (Figure 2). Nitrate concentrations in interstitial waters increased along the length of the core, reaching values of 58 and 45 μM at core bottom at sites NA 11 and NA 12 respectively (Figure 2). At both sites, pH calculated from alkalinity and DIC decreases along the length of the core (Figure 2). For site NA 11, this decrease is nearly linear while at NA 12 the profile curves down, with a rapid decrease in the first five meters, plateauing below that. Lithologically, both North Atlantic sites consist of

pelagic clays, with a small fraction of radiolarian tests altered to chert towards the base of the core (Murray et al. 2014 KN223 Cruise Report). Site NA 12 also contains a zeolite layer at 17 m below seafloor not sampled in this study.

3.3.2. Sedimentary Carbon and Nitrogen Concentrations

Total sedimentary organic carbon concentrations in oxygenated pelagic sediments are extremely low (<0.3 %OC) and decrease rapidly to <0.1 %OC within the first 1.5 meters below seafloor at all four sites. Using sedimentation rate estimates derived as described above, this initial decrease occurs over ~ 1 Ma for sites SPG 9, NA 11, and NA 12 and more slowly, over ~ 3.3 Ma for site SPG 1 (Figure 3). After the initial, rapid decrease, sites SPG 1, NA 11, and NA 12 show a steady, linear decrease in OC content, reaching values ≤0.05 %OC at core bottom, corresponding to sediment ages of roughly 18.5 Ma (NA 11) to 24.0 Ma (SPG 1) over sediment depths of 26.5 meters (NA 11) and 7.0 meters (SPG 1). At site SPG 9, OC content decreases from 0.089 % at 1.1 Ma to 0.07% at 6.0 Ma at a rate comparable to that of the other sites. However, OC content jumps lower at 7.4 Ma, ultimately reaching 0.033 %OC at 11.23 Ma sediment age (5.7 meters below seafloor). This jump represents a substantial depletion of OC over a shorter time interval relative to the other sites. At all sites, the minimum %OC measured at core bottom represented an 80-90% decrease of the maximal value at core top.

Like %OC, %N is substantially higher in surface sediments and decreases rapidly with depth along the core (Figure 3). At sites SPG 1 and SPG 9, %N shows greater variability along the length of the core than %OC, but minimum values at core bottom likewise represent an ~80% decrease from the maximal values at core top (0.060 and 0.055 %N respectively decreasing to 0.010 %N). Conversely, sites NA 11 and NA 12 decrease only by 57% and 50%

and have secondary maxima down the length of the core, including one between 10-12 Ma (15.5 and 12.5 mbsf respectively). For sites NA 11 and 12, this muted decrease results in C/N values <2 along most of the length of the cores, from an initial value of just below 5 at core tops (Figure 3). SPG sites have comparable C/N values at core tops but decline less along the length of the core (varying between 2 and 4) due to the proportional decrease in %N relative to %OC.

3.3.3. Bulk Carbon Composition

Spectral deconvolution of bulk NEXAFS spectra indicates that in all samples from all cores (sites SPG 1, SPG 9, and NA 12), amide and carboxylic carbon functionalities comprise the majority of the fit area (Figures 4 and 5). Amide and carboxylic carbon have resonances between 288.0 and 288.9 eV (SI Figure 1) and, in most spectra, were best fit as two peaks. However, as the resonances overlap, they are considered as a single contribution from amide and carboxylic carbon and will be referred to as amide/carboxylic peak1 and peak 2. Here, peak 1, which has more amide-like character, comprises 12—20% of the overall fit area, and peak 2, representing more carboxylic-like carbon, comprises 26—50% of the fit area, for a sum of 39—65% of the total fit area (average: 55%, Figure 4). O-alkyl carbon is the next most abundant functionality, averaging 17% of the total fit area, and aliphatic carbon, at 10%. Aromatic carbon is also consistently present in samples, averaging 6% of the total fit area. Carbonate averages 7% of the total fit area, with the exception of the "nodule-rich" region of SPG 9 consisting of 32% carbonate (Figure 4, SI Figure 1).

The average functional group composition (e.g. the relative fractions of each functionality) of each core varies by site (Figure 4). SPG 9 has significantly less of an overall contribution from aromatic carbon ($p=0.05$, one-way ANOVA) and slightly more from aliphatic

(not significant), while O-alkyl carbon is enriched in SPG 1. Despite wide variances, the average values for amide and carboxylic carbon peak 1, peak 2, and their sum are comparable across sites.

None of the cores demonstrate trends in functional group abundance with depth, though subsurface maxima and minima exist (Figure 5). Aromatic and aliphatic carbon, for instance, oscillate sharply and inversely in the top half of the core from NA 12. Amide and carboxylic carbon increase in the top half of the NA 12 core, before declining and plateauing in percent contribution with depth. The net increase is driven by an increase in peak 1 (more amide-like), followed by an increase in peak 2 (more carboxylic-like) two meters further down. The contribution from amide and carboxylic peaks 1 and 2 in the SPG 9 core varies widely, but often cancelling itself out such that the sum does not vary substantially. Amide and carboxylic carbon at SPG 1, likewise, lacks a clear trend in abundance with depth. In the NA 12 core, the subsurface maxima in amide and carboxylic carbon peak 2 correlates with the minima in both O-alkyl carbon and carbonate, which decrease from the core top then stabilize with depth. Manganese nodule-like material removed from SPG 9 at 5.1 m (10.0 Ma) was enriched in carbonate relative to all other samples (Figure 4, SI Figure 1). When normalized to carbonate content, the sample appears similar to the bulk sample taken from the same depth, though contains a slightly greater percent contribution from aliphatic carbon (Figure 5).

Few consistent correlations between relative functional group abundances hold between sites. Aromatic carbon has a loose inverse correlation with aliphatic carbon at sites NA 12 and SPG 1 (Pearson correlation coefficients -0.54 and -0.56 respectively, Figure 6). A stronger inverse correlation holds for aromatic carbon and the sum of amide/carboxylic carbon peaks 1 and 2. Aliphatic carbon and the sum of amide/carboxylic peaks 1 and 2 have a positive

correlation, driven entirely by a correlation between aliphatic carbon and amide/carboxylic carbon peak 1 (Figure 6). Similarly, amide/carboxylic carbon peak 1 has a strong inverse correlation with carbonate content, but when carbonate is compared to the sum of the two amide/carboxylic peaks, the trend only holds for site NA 12 while the rest of the data scatter over a small range (Pearson correlation coefficient -0.84, Figure 6).

3.3.5 Protein Quantification

Protein concentrations are static with depth compared to %OC or %N. Only site NA 12 has a depth profile where extracted protein concentrations are higher in surface sediments and show an initial, rapid decrease; for the other sites, values are nearly constant or increase slightly with depth (Figure 7). All samples from NA 11 have an average protein concentration of 1.48 μg protein/mg sediment ± 16%; a value comparable to the standard deviation of the triplicate extractions (average rsd 18% for site 11). Excluding the multicore samples from NA 12 (the three towards core top that form the initial decrease), average protein along the length of the core from NA 12 is 1.05 μg protein/mg sediment ± 33%, showing that concentrations are also more variable at this site. Samples from SPG 1 have an average protein concentration of 1.83 μg protein/mg sediment ± 12%, while site SPG 9 has substantially higher but still invariable concentrations, with an average of 2.98 μg protein/mg sediment ± 14%; again, the variability is comparable to the average relative standard deviation for each of these sites of 10% and 15% respectively. Nonetheless, the averages for each core pooled over all sample depths are statistically different from each other at p=0.05 (one-way ANOVA).

3.4 Discussion

3.4.1. Organic Carbon in the Deep Subsurface

Given the low %OC content, low C/N, and low but measurable content of extractable proteins (Figures 3,7) of these sediments, a reasonable consideration is the degree to which the OC measured reflects biomass that slowly recycles itself rather than a relatively stable pool of carbon delivered from the surface. Assuming an average cell carbon content of 14 fg (Kallmeyer *et al.*, 2012) and a sediment density of ~2.5 g/cm^3, we calculate that if all OC was in living biomass, there would be 5-7 orders of magnitude more cells in sediments than the numbers counted for the SPG (D'Hondt *et al.*, 2011). Likewise, assuming that nitrogen accounts for 16% of the weight of protein, the extractable proteins quantified here via extraction and fluorescence account for <<1% of the total %N measured in the sediment samples by EA-IRMS (0.18 ± 0.13 % of total %N for SPG sites; 0.047 ± 0.013 % of total %N for NA sites). Assuming that carbon accounts for 53% of protein weight, carbon from extractable proteins accounts for 0.22 ± 0.14 % of the total %OC for SPG sites, and 0.09 ± 0.04 % of the total %OC from NA sites. Thus, the majority of OC measured is not present in living biomass, nor do intact extractable proteins (e.g., an indicator of labile OC or biomass) account for a substantial portion of the OC reservoir. This result does not rule out rapid, cryptic recycling of labile cellular material as a mechanism of biomass maintenance, but does imply that the majority of the OC in deep sediments turns over on extremely long time scales and likely derives from the photosynthetic surface.

Nonetheless, that small concentration of extractable proteins may still be bioavailable and contribute to fueling heterotrophy as posited in Lloyd *et al.* (2013) and Tully and Heidelberg (2016). Assuming that an average cell in the deep subsurface with a carbon content of 14 fg has a total mass of 20 fg, ~half of which is protein, we can convert protein measurements into an

estimate of how many cells should be present if all protein is locked up in biomass. From this approach, we predict ~8*10^7 – 4*10^8 cells/cm^3 sediment, exceeding the 10^3 – 10^4 cells/cm^3 actually present in the SPG (D'Hondt *et al.*, 2011). Assuming a much larger cell with 100 fg of protein puts cell estimates within an order of magnitude of actual cell counts; however, other researchers have shown that deep subsurface cells tend to be small and to decrease protein content under starvation conditions (Lever *et al.*, 2015; Braun *et al.*, 2016). The difference implies a substantial fraction of intact, extracellular carbon and proteins present in this environment. Proteins may be bound to mineral surfaces, or may be actively cycled in and out of the biomass stock. The lack of a clear trend in protein concentration (Figure 7) with depth could be explained by either of these phenomena, or the two in combination. Protein concentrations in these homogeneous pelagic clay sediments may be maintained in steady state via equilibrium with mineral surfaces, some rate of exchange on and off mineral surfaces, and some consumption and regeneration rate of the proteins by microorganisms.

3.4.2. Evidence of Carbon Degradation

Geochemical data collected at all four sites implicate aerobic metabolisms coupled to organic carbon degradation. These data include the oxygen profiles, which were used to calculate a carbon mineralization rate of ~0.4 to 4.5 gC/m^2/yr for the South Pacific Gyre samples (Fischer *et al.*, 2009). Microprofiles suggest that half the reactive organic matter is removed in the top 6 mm of sediment, with extremely low O_2 consumption rates at depth (Fischer *et al.*, 2009). Measurements of OC in this study were not high-resolution enough to observe that substantial remineralization, but we do observe decreases in concentration between 66-72% of the value measured at core top by ~ 3 m below seafloor and a total decrease of 80-87% (Figure 3). For

nitrogen, only 18-52% is removed by ~ 3 m below seafloor, for a total decrease of 50-83% between core top and bottom (Figure 3). Increasing nitrate over the length of the core (Figure 2) is likely a combination of preformed nutrients diffusing upwards (Adkins & Schrag, 2003) and production of nitrate from nitrification of ammonia released during the degradation of organic matter (D'Hondt *et al.*, 2009). Decreasing pH with depth along the core at NA sites 11 and 12 (where pH was calculated) further suggests active respiration of OC (Figure 2).

The decrease in OC along the core length is exponential (Figure 3) and follows the pattern observed globally and modeled in reactive continuum models. Rates of degradation, however, appear faster than that predicted by LaRowe and Amend (unpublished, personal communication), who model that ~50% of the initial OC reaching sediments at the start of the Pleistocene at 2.6 Mya still endures. Here, we find that number is between 30-45%, assuming constant sedimentation rate and OC delivery. This deviation is likely attributable to oxygen exposure time, which controls both extent of degradation (Cowie *et al.*, 1995; Hartnett *et al.*, 1998) and potentially chemical composition by enhancing the relative importance of preservation mechanisms such as chemically selective adsorption of OC to mineral surfaces (Arnarson & Keil, 2007).

Though faster than predicted, degradation rates are still exceedingly slow. From the OC and N concentrations, we calculate degradation rates over the first ~1.5 m, and between 1.5 m and core bottom. In the first ~1.5 m where OC and N concentrations decrease rapidly, degradation rates range from 0.132 mol $C/m^3/kyr$ at both NA 11 and NA 12 to 0.048 and 0.034 mol $C/m^3/kyr$ at sites SPG 1 and SPG 9. Rates are an order of magnitude lower in the deep subsurface than in the surface interval at SPG sites, and two orders of magnitude lower in the deep interval relative to the surface interval at NA sites: 0.002 and 0.006 mol $C/m^3/kyr$ for SPG

1 and SPG 9 and 0.0011 mol C/m^3/kyr for both NA sites. Nitrogen rates follow similar trends, but are less than an order of magnitude lower in the deep subsurface than in the 0-1.5 m interval. These data demonstrate a much lower utilization of OC in the deep subsurface in the North Atlantic gyre than at comparable sediment depths and ages in the South Pacific. This difference could signify a more active microbial community in the SPG sediments, a community with greater genomic potential for accessing recalcitrant OC, a difference in the chemical composition of organic carbon buried in the two oceans, or a geochemical mechanism favoring preservation or degradation.

3.4.3 Preferential Carbon Sequestration and/or Utilization

The stoichiometry of the organic matter preserved in the deep subsurface contradicts the paradigm from studies of organic matter (OM) remineralization in the overlying water column, where preferential degradation of nitrogen compounds generates particulate and dissolved OM increasingly enriched in C. Here, C/N at core top is extremely low and decreases with depth in the sediments (Figure 3). Core top C/N values of ~4.5-5.5 are already lower than Redfield biomass (6.625) and quickly drop below 3.85, the C/N of protein, one of the most N-rich biomolecules. Interestingly, the stoichiometry of degradation rates also deviates from what Redfield stoichiometry would predict. Degradation rate C/N values are between 11 and 14 from core top to 1.5 m, with the exception of SPG 9 at 5.4, and decline to between 2-4 from 1.5 m to core bottom. In the top interval, these elevated numbers imply either preferential utilization of OC relative to N or a mechanism that makes N less bioavailable. Below 1.5 m, degradation rate C/N values roughly match the composition of the organic matter at those depths; hence, organic

matter in the deep subsurface is degraded non-selectively, with microbes using exactly what's present, assuming all N is organic N.

Low C/N in sedimentary OM has been previously observed but typically attributed to adsorption or fixation of NH_4^+ produced by OM remineralization in clays (Meyers, 1997) or analytical uncertainty (Ziebis *et al.*, 2012). Here, we rule out analytical uncertainty, as sample peak areas were on average 32x greater than the average blank size. Seven samples from SPG 1 and SPG 9 were less than 10x the blank; the lowest was still 4x greater than the blank. Further, a subset of sections from core NA 12 were resampled and the separate sediment aliquots were separately analyzed for C and N concentrations. Equivalent results to the previous sediment analysis demonstrate reproducibility (SI Figure 2). A final subset of samples from core NA 12 was washed in 18MΩ water and sonicated three times to remove readily exchangeable N (such as electrostatic or outer-sphere adsorption); these samples also reproduced previous measurements verifying that contributions from those forms of N are minimal (SI Figure 2).

Nevertheless, strongly adsorbed or fixed NH_4^+ could be a more viable explanation as these pelagic sediments consist primarily of clays (D'Hondt et al. 2011; Murray et al. 2014 KN223 Cruise Report), although some discrepancies remain. In sediments from the central North Pacific, exchangeable nitrogen accounted for <5% of total nitrogen, while fixed NH_4^+ comprised 19-45% of the total nitrogen (Muller, 1977). Thus, a conservative estimate would assume 50% of the total nitrogen we measure derives from inorganic nitrogen. Recalculating C/N values under that assumption gives a still-low C/N range of 2.6-11.2 instead of 1.3-5.6. Further, data from a carbonate-dominated site in the North Atlantic show equivalently low C/N values between 1.7-5.1 despite lower clay content (data not shown). Combined, these data suggest that another mechanism must be responsible for enriching sedimentary organic matter in N. Preferential

preservation of N-rich compounds at mineral surfaces may explain observed C/N (Lalonde et al. 2012; Muller 1977). In fact, adsorption to mineral surfaces is likely the predominant OC preservation mechanism operative in oxic sediments on the time scales considered here (Arnarson & Keil, 2007). Fixation of NH_4^+ in clays may, however, contribute to the non-stoichiometric decrease in C and N at NA sites 11 and 12, where the total decrease in OC exceeds the decrease in N. As these sites experience higher sedimentation rates and become more depleted in oxygen toward core bottom relative to SPG sites, NH_4^+ produced by the microbial degradation of organic matter may have a longer residence time in the system with which to react with clays prior to nitrification.

A final explanation for preferential preservation of N is the formation of alkyl amides via abiotic amidation of esters with NH_4^+ produced by organic matter degradation (McKee & Hatcher, 2010). However, this process has only been studied in organic-rich anoxic sediments and whether that reaction is viable in oxic, carbon-poor sediments remains unknown. The prevalence of O-alkyl carbon transitions in NEXAFS spectra (Figures 4, 5, and discussion below) suggests the presence of ester groups available for amidation, but such a reaction would have to occur faster than the energetically favorable nitrification of NH_4^+. As peptide bonds contain similar carbon configurations to alkyl amides, the moieties are likely indistinguishable via either C 1s or N 1s NEXAFS spectroscopy and therefore the presence of alkyl amides cannot be tested in this study.

3.4.4 Composition of Organic Carbon

With extractable proteins comprising a vanishingly small fraction of the total OC as discussed above, spectroscopic characterization is essential to describing the rest. NEXAFS

reveals that amide and carboxylic carbon predominate in all samples with additional contributions from O-alkyl (likely alcohol or ether groups), aliphatic, and aromatic carbon (Figures 4 and 5). These results align with previous studies on dissolved organic matter, sinking particles and sediments, which identify amino acid- or peptide-like material including preserved proteins, carbohydrates, and alkyl or O-alkyl groups as primary components (Hedges *et al.*, 2001; Brandes *et al.*, 2004; Dickens *et al.*, 2006; Hertkorn *et al.*, 2006; Mao *et al.*, 2011; Hatcher *et al.*, 2014). In terms of relative contribution of each functional group and overall spectral shape, humic acid and bovine serum albumin protein standard most closely match sample spectra (Figure 8). These similarities further affirm our interpretation of this material as N- and O-rich proteinaceous material, with aliphatic and aromatic carbon secondary to amide/carboxylic and O-alkyl groups.

The elevated proportion of amide/carboxylic carbon observed could also denote the presence of carboxylic-rich alicyclic material (CRAM) or aminosugars, or both. CRAM derives from biomolecules structurally similar to sterol and hopanoids (Hertkorn *et al.*, 2006) while aminosugars are abundant in POM (Benner & Kaiser, 2003) and the building blocks of peptidoglycan, a constituent of bacterial cell walls resistant to microbial degradation. In examining ultrafiltered dissolved OM samples from the surface and 4000 m depth in the Pacific, Hertkorn et al. (2006) uses NMR to document a substantial increase in CRAM-like material and a lesser increase in peptidic material with depth at the expense of heteropolysaccharides. Both compound classes may thus persist in sediments as well.

Gaussian deconvolution of spectra shows that aliphatic C comprises only ~10% of the fit area on average, but correlates strongly with amide/carboxylic C (Figure 6). This trend could indicate a substantial contribution from CRAM-like material. However, Hertkorn et al. (2006)

describe CRAM as having carboxylic-C:aliphatic-C ratios of between 1:2 to 1:7, while here the ratio here in terms of peak area is ~5-6:1 on average, with SPG 9 having slightly less amide/carboxylic carbon. The molar absorption coefficient of aliphatic carbon is weak in comparison to amide/carboxylic carbon (Brandes *et al.*, 2004); yet differences in resonance strength cannot account fully for that difference in ratio. Further, peaks in the 287.0—287.9 eV range represent C 1s-$\pi^*_{C\text{-}H}$ and C 1s-$\sigma^*_{C\text{-}H}$/3p Rydberg-like transitions of CH and CH_2 groups (Hitchcock & Ishii, 1987; Solomon *et al.*, 2009); in amino acids, σ^* C-H excitations may dominate over π^*, resulting in a broad hump that represents a series of unresolved transitions (Kaznacheyev & Osanna, 2002) and in-line with the relatively broad peaks observed in sediment samples here. Thus, the observed aliphatic peak may represent a combination of aliphatic carbon in alicyclic configurations as well as C-H bonds in amide-rich material, whether proteins or aminosugars.

While aminosugars are a theoretically reasonable component of sedimentary organic matter, they likely constitute a minor component. If samples contained a significant fraction of aminosugars, we would expect O-alkyl carbon to correlate more strongly with amide/carboxylic carbon (Figure 6). Aminosugar standard compounds have sharp peaks above 289 eV corresponding to the C 1s-3p/σ^* transitions of C-OH (Solomon *et al.*, 2009). In sediment samples analyzed here, the O-alkyl carbon peak manifests as a subtle hump (Figure 8, SI Figure 1) and represents ~17% of the total fit area (Figures 4 and 5). Like aliphatic carbon, resonances for the C-OH σ^* transition of O-alkyl carbon is disproportionately weaker than that for amide/carboxylic π^* transitions (Solomon *et al.*, 2009; Hawkins & Russell, 2010) such that an absence of distinct peaks at ~289.5 eV does not imply an absence of aminosugars. However, we argue that the peak fit here as O-alkyl carbon contains contributions from a broad band of σ^*

transitions generated by a range of alcohols, ethers, and esters (e.g. partially oxidized functionalities) in this material and not purely the C-OH σ* transition of aminosugars. We draw this conclusion based on the peak width and its variable position between ~289.5 and 289.7 eV, slightly higher than that of aminosugar standard compounds (Solomon *et al.*, 2009). Specific measurements of four aminosugars made in coastal Peruvian sediments found that aminosugars in total accounted for <2.5% of total OC and <4% of total N and that the ratio of glucosamine to muramic acid (13—68) did not suggest the presence of peptidoglycan, which has a 1:1 ratio (Niggemann & Schubert, 2006). Similar proportional abundances were found in a study on particulate and dissolved organic matter, where particulate organic matter actually contained *less* aminosugars that dissolved (Benner & Kaiser, 2003) such that particles may not act as an effective delivery mechanism for aminosugars in the sediments.

Ultimately, NEXAFS spectra reveal an organic carbon composition common to all three of the oxic sites examined via NEXAFS: amide- and carboxylic-rich functionalities in a scaffolding of aliphatic/alicyclic and O-alkyl carbons. Aromatics are probably present as side chains of amino acids in peptidic material and aminosugars, or as unsaturations in CRAM-like material. This finding of extremely high amide/carboxylic and O-alkyl content may represent a more extreme version of the observations of Mao et al. (2011) who found substituted and copolymerized carbohydrates and O-enriched compounds increased in abundance from sinking particles to surface sediments and attribute that finding to partial oxidation reactions. Alternately, this overall composition could reflect a carbon-limited environment that allows for the selective preservation of proteinaceous (protein-derived) material. The persistence of oxygen-bearing compounds in these oxic sediments demonstrates the unique set of degradation mechanisms

operative over kyr- and myr-time scales, contrasting anoxic settings where O/C of organic compounds typically decreases with depth (Hatcher *et al.*, 2014).

3.5 Conclusions

Here we quantified organic carbon, nitrogen, and protein content of ~20 Ma oxic pelagic sediments deposited in the North Atlantic and South Pacific gyres. These sediments have some of the slowest known sedimentation rates and lowest microbial abundances globally, yet maintain life despite limitation. Organic carbon and nitrogen content are among the lowest measured globally, but by comparing OC, N, and protein content, we calculate that living biomass accounts for very little of the observed OC and that intact, extracellular proteins persist but are potentially bioavailable in this environment. C/N values are extremely low and subvert the paradigm that N-bearing compounds are selectively degraded producing organic matter depleted in nitrogen. Alternate explanations such as fixation in clays cannot fully account for the abundance of nitrogen in these samples; thus, we conclude that in these oxic, carbon-limited sediments, N-bearing compounds that are likely proteinaceious in origin are well-preserved. Calculated degradation rates for both carbon and nitrogen imply that organic matter utilization in the deep subsurface (>1.5 m below seafloor) is non-selective, with microbes consuming organic matter of approximately the same composition as the bulk. In the top ~1.5 m of three of the four cores analyzed, however, we find that carbon is preferentially utilized over nitrogen. We posit that in such a carbon-poor environment, microbes are more limited by carbon than other nutrients and may thus generate N-enriched compounds by preferential degradation of carbon.

This paper also represents the first attempt to spectroscopically characterize OC from oxic sediments using NEXAFS. We find that amide and carboxylic carbon functional groups

predominate in all samples and likely exist in a scaffolding of aliphatic/alicyclic and O-alkyl carbons, whether esters, alcohols, or ethers. We hypothesize that this material may be an extremely O-rich version of carboxylic-rich alicyclic material (CRAM, Hertkorn et al. 2006) or the product of successive partial oxidation reactions (e.g. Mao, Tremblay, and Gagné 2011) carried to a greater extreme than previously observed. In either case, low C/N ratios, the presence of intact proteins, and NEXAFS spectroscopy results suggest the material is proteinaceous in origin. We observe that despite substantial processing of this material, no substantial changes in composition occur along the depth of the cores. The persistence of a diversity of molecules implies non-selective preservation, at least on these long time scales. Our findings suggest that this diversity of compounds, including a fraction of intact proteins, may sustain heterotrophic metabolisms in the deep subsurface.

3.6 References

Adkins JF, Schrag DP (2003) Reconstructing Last Glacial Maximum bottom water salinities from deep-sea sediment pore fluid profiles. *Earth and Planetary Science Letters* **216**, 109–123.

Archer DE, Morford JL, Emerson SR (2002) A model of suboxic sedimentary diagenesis suitable for automatic tuning and gridded global domains. *Global Biogeochemical Cycles* **16**, 17-1-17–21.

Arnarson TS, Keil RG (2007) Changes in organic matter-mineral interactions for marine sediments with varying oxygen exposure times. *Geochimica et Cosmochimica Acta* **71**, 3545–3556.

Arndt S, Jørgensen BB, LaRowe DE, Middelburg JJ, Pancost RD, Regnier P (2013) Quantifying the degradation of organic matter in marine sediments: A review and synthesis. *Earth-Science Reviews* **123**, 53–86.

Benner R, Kaiser K (2003) Abundance of amino sugars and peptidoglycan in marine particulate and dissolved organic matter. *Limnology and Oceanography* **48**, 118–128.

Biddle JF, Fitz-Gibbon S, Schuster SC, Brenchley JE, House CH (2008) Metagenomic signatures of the Peru Margin subseafloor biosphere show a genetically distinct environment. *Proceedings of the National Academy of Sciences of the United States of America* **105**, 10583–10588.

Boudreau BP, Ruddick BR (1992) Erratum; On a reactive continuum representation of organic matter diagenesis. *American Journal of Science* **292**, 79–0.

Brandes J, Lee C, Wakeham S, Peterson M, Jacobsen C, Wirick S, Cody G (2004) Examining marine particulate organic matter at sub-micron scales using scanning transmission X-ray microscopy and carbon X-ray absorption near edge structure spectroscopy. *Marine Chemistry* **92**, 107–121.

Braun S, Morono Y, Becker KW, Hinrichs KU, Kjeldsen KU, Jørgensen BB, Lomstein BA (2016) Cellular content of biomolecules in sub-seafloor microbial communities. *Geochimica et Cosmochimica Acta* **188**, 330–351.

Cowie GL, Hedges JI, Prahl FG, Lange GJ de (1995) Elemental and major biochemical changes across an oxidation front in a relict turbidite: An oxygen effect. *Geochimica et Cosmochimica Acta* **59**, 33–46.

D'Hondt S, Abrams LJ, Anderson R, Dorrance J, Durbin A, Ellett L, Ferdelman T, Fischer J, Forschner S, Fuldauer R, Goldstein H, Graham D, Griffith W, Halm H, Harris R, Harrison B, Hasiuk F, Horn G, Kallmeyer J, Lever M, Meyer J, Morse L, Moser C, Murphy B, Nordhausen A, Parry L, Pockalny R, Puschell A, Rogers J, Schrum H, Smith DC, Soffientino B, Spivack AJ, Stancin A, Steinman M, Walczak P (2011) KNOX-02RR: drilling site survey--life in subseafloor sediments of the South Pacific Gyre. In: *Proceedings of the Integrated Ocean Drilling Program.*

D'Hondt S, Inagaki F, Zarikian CA, Abrams LJ, Dubois N, Engelhardt T, Evans H, Ferdelman T, Gribsholt B, Harris RN, Hoppie BW, Hyun J-H, Kallmeyer J, Kim J, Lynch JE, McKinley CC, Mitsunobu S, Morono Y, Murray RW, Pockalny R, Sauvage J, Shimono T, Shiraishi F, Smith DC, Smith-Duque CE, Spivack AJ, Steinsbu BO, Suzuki Y, Szpak M, Toffin L, Uramoto G, Yamaguchi YT, Zhang G, Zhang X-H, Ziebis W (2015) Presence of oxygen and aerobic communities from sea floor to basement in deep-sea sediments. *Nature Geoscience* **8**, 299–304.

D'Hondt S, Jørgensen BB, Miller DJ, Batzke A, Blake R, Cragg B a, Cypionka H, Dickens GR, Ferdelman T, Hinrichs K-U, Holm NG, Mitterer R, Spivack A, Wang G, Bekins B, Engelen B, Ford K, Gettemy G, Rutherford SD, Sass H, Skilbeck CG, Aiello IW, Guèrin G, House CH, Inagaki F, Meister P, Naehr T, Niitsuma S, Parkes RJ, Schippers A, Smith DC, Teske A, Wiegel J, Padilla CN, Acosta JLS (2004) Distributions of microbial activities in deep subseafloor sediments. *Science* **306**, 2216–21.

D'Hondt S, Spivack AJ, Pockalny R, Ferdelman TG, Fischer JP, Kallmeyer J, Abrams LJ, Smith DC, Graham D, Hasiuk F, Schrum H, Stancin AM (2009) Subseafloor sedimentary life in the South Pacific Gyre. *Proceedings of the National Academy of Sciences of the United States of America* **106**, 11651–11656.

Dickens AF, Baldock J a., Smernik RJ, Wakeham SG, Arnarson TS, Gélinas Y, Hedges JI (2006) Solid-state 13C NMR analysis of size and density fractions of marine sediments: Insight into organic carbon sources and preservation mechanisms. *Geochimica et Cosmochimica Acta* **70**, 666–686.

Divins DL (2003) Total Sediment Thickness of the World's Oceans & Marginal Seas.

Durbin AM, Teske A (2012) Archaea in organic-lean and organic-rich marine subsurface sediments: An environmental gradient reflected in distinct phylogenetic lineages. *Frontiers in Microbiology* **3**, 1–26.

Ehrenreich A, Widdel F (1994) Anaerobic Oxidation of Ferrous Iron by Purple Bacteria, a New-Type of Phototrophic Metabolism. *Applied and Environmental Microbiology* **60**, 4517–4526.

Estes ER, Andeer PF, Nordlund D, Wankel SD, Hansel CM (2016) Biogenic manganese oxides as reservoirs of organic carbon and proteins in terrestrial and marine environments.

Geobiology.
Fischer JP, Ferdelman TG, Hondt SD, Røy H, Wenzhöfer F (2009) Oxygen penetration dep into the sediments of the South Pacific gyre. *Biogeosciences* **6**, 1467–1478.
Hartnett HE, Keil RG, Hedges JI, Devol AH (1998) Influence of oxygen exposure time on organic carbon preservation in continental margin sediments. *Nature* **391**, 572–575.
Hatcher PG, Ravin A, Behar F, Baudin F (2014) Diagenesis of organic matter in a 400 m organic rich sediment core from offshore Namibia using solid state 13C NMR and FTIR. *Organic Geochemistry* **75**, 8–23.
Hawkins LN, Russell LM (2010) Polysaccharides, Proteins, and Phytoplankton Fragments: Four Chemically Distinct Types of Marine Primary Organic Aerosol Classified by Single Particle Spectromicroscopy. *Advances in Meteorology* **2010**, 1–14.
Hedges J, Eglinton G, Hatcher P, Kirchman D., Arnosti C, Derenne S, Evershed R., Kögel-Knabner I, de Leeuw J, Littke R, Michaelis W, Rullkötter J (2000) The molecularly-uncharacterized component of nonliving organic matter in natural environments. *Organic Geochemistry* **31**, 945–958.
Hedges JI, Baldock J, Gélinas Y, Lee C, Peterson M, Wakeham SG (2001) Evidence for non-selective preservation of organic matter in sinking marine particles. *Nature* **409**, 801–4.
Hertkorn N, Benner R, Frommberger M, Schmitt-Kopplin P, Witt M, Kaiser K, Kettrup A, Hedges JI (2006) Characterization of a major refractory component of marine dissolved organic matter. *Geochimica et Cosmochimica Acta* **70**, 2990–3010.
Hitchcock AP, Ishii I (1987) Carbon K-shell excitation spectra of linear and branched alkanes. *Journal of Electron Spectroscopy and Related Phenomena* **42**, 11–26.
Inagaki F, Kubo Y, Bowles MW, Heuer VB, Ijiri A, Imachi H, Ito M, Kaneko M, Lever MA, Morita S, Morono Y, Tanikawa W, Bihan M, Bowden SA, Elvert M, Glombitza C, Gross D, Harrington GJ, Hori T, Li K, Limmer D, Murayama M, Ohkouchi N, Ono S, Purkey M, Sanada Y, Sauvage J, Snyder G, Takano Y, Tasumi E, Terada T, Tomaru H, Wang DT, Yamada Y (2015) Exploring deep microbial life in coal-bearing sediment down to ~2.5 km below the ocean floor. *Science* **349**, 420–424.
Johnson K, Purvis G, Lopez-Capel E, Peacock C, Gray N, Wagner T, März C, Bowen L, Ojeda J, Finlay N, Robertson S, Worrall F, Greenwell C (2015) Towards a mechanistic understanding of carbon stabilization in manganese oxides. *Nature Communications* **6**, 7628.
Jørgensen BB, Marshall IPG (2016) Slow Microbial Life in the Seabed. *Annual Review of Marine Science* **8**, 311–332.
Jørgensen SL, Thorseth IH, Pedersen RB, Baumberger T, Schleper C (2013) Quantitative and phylogenetic study of the deep sea archaeal group in sediments of the arctic mid-ocean spreading ridge. *Frontiers in Microbiology* **4**, 1–11.
Kallmeyer J, Pockalny R, Adhikari RR, Smith DC, D'Hondt S (2012) Global distribution of microbial abundance and biomass in subseafloor sediment. *Proceedings of the National Academy of Sciences* **109**, 16213–16216.
Kaznacheyev K, Osanna A (2002) Innershell absorption spectroscopy of amino acids. *The Journal of Physical Chemistry A* 3153–3168.
Lalonde K, Mucci A, Ouellet A, Gélinas Y (2012) Preservation of organic matter in sediments promoted by iron. *Nature* **483**, 198–200.
LaRowe DE, Cappellen P Van (2011) Degradation of natural organic matter: A thermodynamic analysis. *Geochimica et Cosmochimica Acta* **75**, 2030–2042.
Lever MA, Rogers KL, Lloyd KG, Overmann J, Schink B, Thauer RK, Hoehler TM, Jørgensen

BB (2015) Life under extreme energy limitation: A synthesis of laboratory- and field-based investigations. *FEMS Microbiology Reviews* **39**, 688–728.

Lloyd KG, Schreiber L, Petersen DG, Kjeldsen KU, Lever M a, Steen AD, Stepanauskas R, Richter M, Kleindienst S, Lenk S, Schramm A, Jørgensen BB (2013) Predominant archaea in marine sediments degrade detrital proteins. *Nature* **496**, 215–8.

Lomstein BA, Langerhuus AT, D'Hondt S, Jørgensen BB, Spivack AJ (2012) Endospore abundance, microbial growth and necromass turnover in deep sub-seafloor sediment. *Nature* **484**, 101–104.

Mao J, Tremblay L, Gagné JP (2011) Structural changes of humic acids from sinking organic matter and surface sediments investigated by advanced solid-state NMR: Insights into sources, preservation and molecularly uncharacterized components. *Geochimica et Cosmochimica Acta* **75**, 7864–7880.

McKee GA, Hatcher PG (2010) Alkyl amides in two organic-rich anoxic sediments: A possible new abiotic route for N sequestration. *Geochimica et Cosmochimica Acta* **74**, 6436–6450.

Meyers PA (1997) Organic geochemical proxies of paleoceanographic, paleolimnologic, and paleoclimatic processes. *Organic Geochemistry* **27**, 213–250.

Middelburg JJ (1989) A simple rate model for organic matter decomposition in marine sediments. *Geochimica et Cosmochimica Acta* **53**, 1577–1581.

Muller PJ (1977) C/N ratios in Pacific deep sea sediments effect on inorganicammonium and organic nitrogen compounds sorbed by clays. *Geochimica Et Cosmochimica Acta* **41**, 765–776.

Müller RD, Sdrolias M, Gaina C, Roest WR (2008) Age, spreading rates, and spreading asymmetry of the world's ocean crust. *Geochemistry, Geophysics, Geosystems* **9**, 1–19.

Murray RW, Spivack AJ, D'Hondt S, Pockalny R (2014) *R/V Knorr Cruise 223 Report.*

Niggemann J, Schubert CJ (2006) Sources and fate of amino sugars in coastal Peruvian sediments. *Geochimica et Cosmochimica Acta* **70**, 2229–2237.

Oni OE, Schmidt F, Miyatake T, Kasten S, Witt M, Hinrichs KU, Friedrich MW (2015) Microbial communities and organic matter composition in surface and subsurface sediments of the Helgoland mud area, North Sea. *Frontiers in Microbiology* **6**, 1–16.

Orcutt BN, Sylvan JB, Knab NJ, Edwards KJ (2011) Microbial ecology of the dark ocean above, at, and below the seafloor. *Microbiology and molecular biology reviews : MMBR* **75**, 361–422.

Roy H, Kallmeyer J, Adhikari RR, Pockalny R, Jorgensen BB, D'Hondt S (2012) Aerobic Microbial Respiration in 86-Million-Year-Old Deep-Sea Red Clay. *Science* **336**, 922–925.

Russell JA, León-Zayas R, Wrighton K, Biddle JF (2016) Deep subsurface life from North Pond: Enrichment, isolation, characterization and genomes of heterotrophic bacteria. *Frontiers in Microbiology* **7**, 1–13.

Schmidt F, Elvert M, Koch BP, Witt M, Hinrichs KU (2009) Molecular characterization of dissolved organic matter in pore water of continental shelf sediments. *Geochimica et Cosmochimica Acta* **73**, 3337–3358.

Schmidt F, Koch BP, Elvert M, Schmidt G, Witt M, Hinrichs K-U (2011) Diagenetic transformation of dissolved organic nitrogen compounds under contrasting sedimentary redox conditions in the Black Sea. *Environmental science & technology* **45**, 5223–9.

Solomon D, Lehmann J, Kinyangi J, Liang B, Heymann K, Dathe L, Hanley K, Wirick S, Jacobsen C (2009) Carbon (1s) NEXAFS spectroscopy of biogeochemically relevant reference organic compounds. *Soil Science Society of America Journal* **73**, 1817.

Templeton A, Knowles E (2009) Microbial Transformations of Minerals and Metals: Recent Advances in Geomicrobiology Derived from Synchrotron-Based X-Ray Spectroscopy and X-Ray Microscopy. *Annual Review of Earth and Planetary Sciences* **37**, 367–391.

Tully BJ, Heidelberg JF (2016) Potential mechanisms for microbial energy acquisition in oxic deep- sea sediments. *Applied and Environmental Microbiology* **82**, 4232–4243.

Wakeham SG, Lee C, Hedges JI, Hernes PJ, Peterson MLJ (1997) Molecular indicators of diagenetic status in marine organic matter. *Geochimica et Cosmochimica Acta* **61**, 5363–5369.

Whiteside JH, Olsen PE, Eglinton TI, Cornet B, McDonald NG, Huber P (2011) Pangean great lake paleoecology on the cusp of the end-Triassic extinction. *Palaeogeography, Palaeoclimatology, Palaeoecology* **301**, 1–17.

Ziebis W, McManus J, Ferdelman T, Schmidt-Schierhorn F, Bach W, Muratli J, Edwards KJ, Villinger H (2012) Interstitial fluid chemistry of sediments underlying the North Atlantic gyre and the influence of subsurface fluid flow. *Earth and Planetary Science Letters* **323–324**, 79–91.

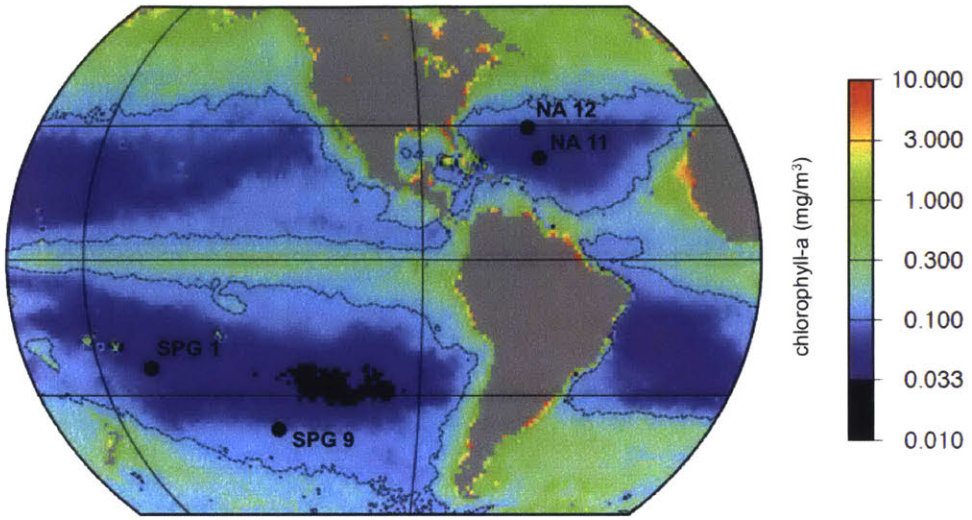

Figure 1. Study site locations (labeled points) overlaid on map of surface ocean chlorophyll-a concentrations. Black dashed lines delineate regions with <0.14 mg/m^3 chlorophyll-a, used to define the boundaries of oligotrophic gyres.

Table 1. Site locations and sediment properties

Site	latitude/longitude	water depth (m)	sediment recovered (m)	sediment thickness (m)*	basement age (Ma)**	sedimentation rate (cm/kyr)	O_2 at 1.5 m depth (μM)
SPG 1***	23°51.0'S, 165°38.6'W	5699	7.79	71	100	0.031	207
SPG 9 ***	38°03.7'S, 133°05.5'W	4924	7.015	20	39	0.051	159
NA 11	22°47.0'N, 56°31.1'W	5557	26.75	100	70	0.143	187
NA 12	29°40.6'N, 58°19.7'W	5367	25.92	98	98	0.1	158

* Divins 2003
**Müller et al. 2008
***SPG values taken from D'Hondt *et al.* 2009, 2011

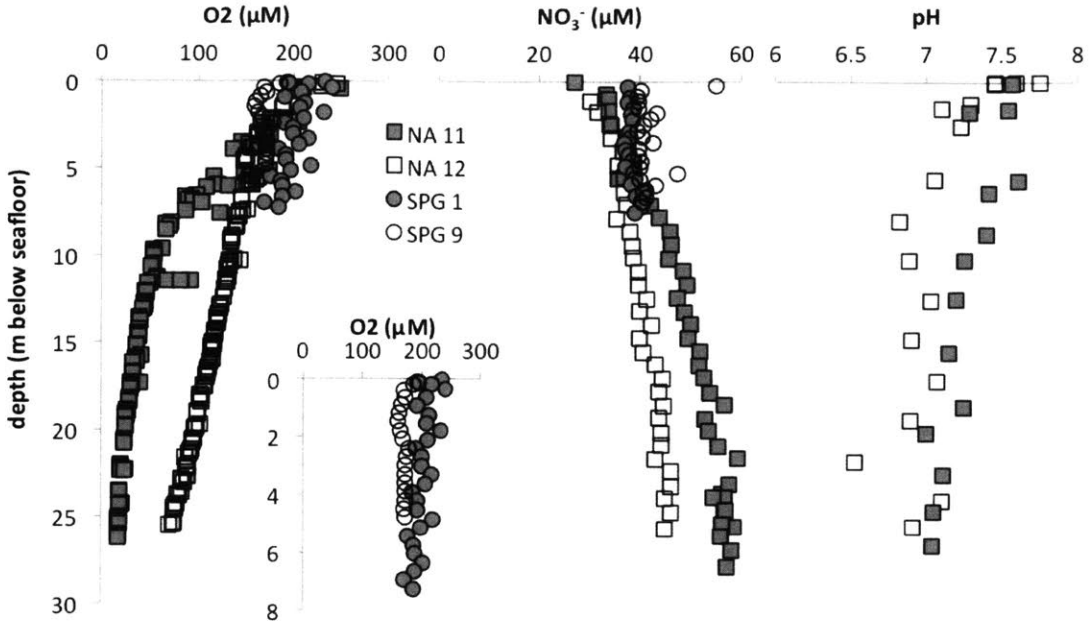

Figure 2. Depth profiles of oxygen, nitrate, and pH of interstitial waters. pH is calculated from measurements of alkalinity and DIC and only done for North Atlantic sites. Inset shows oxygen profiles of South Pacific Gyre sites on a different depth scale than the North Atlantic sites for clarity.

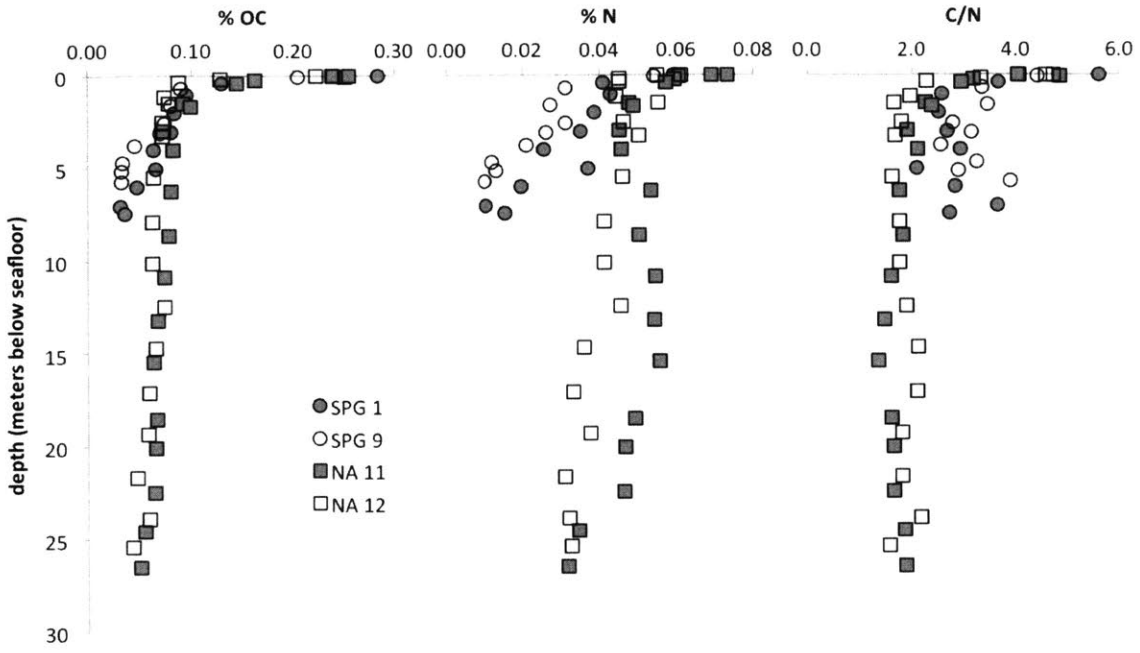

Figure 3. Percent organic carbon (left) and nitrogen (middle) (w/w), and C/N (mol/mol) measured following freeze-drying and acid fumigation of sediments. Estimated sediment ages at the bottom of the cored intervals are 24.0, 11.2, 18.5, and 23.4 Ma for SPG 1, SPG 9, NA 11, and NA 12 respectively.

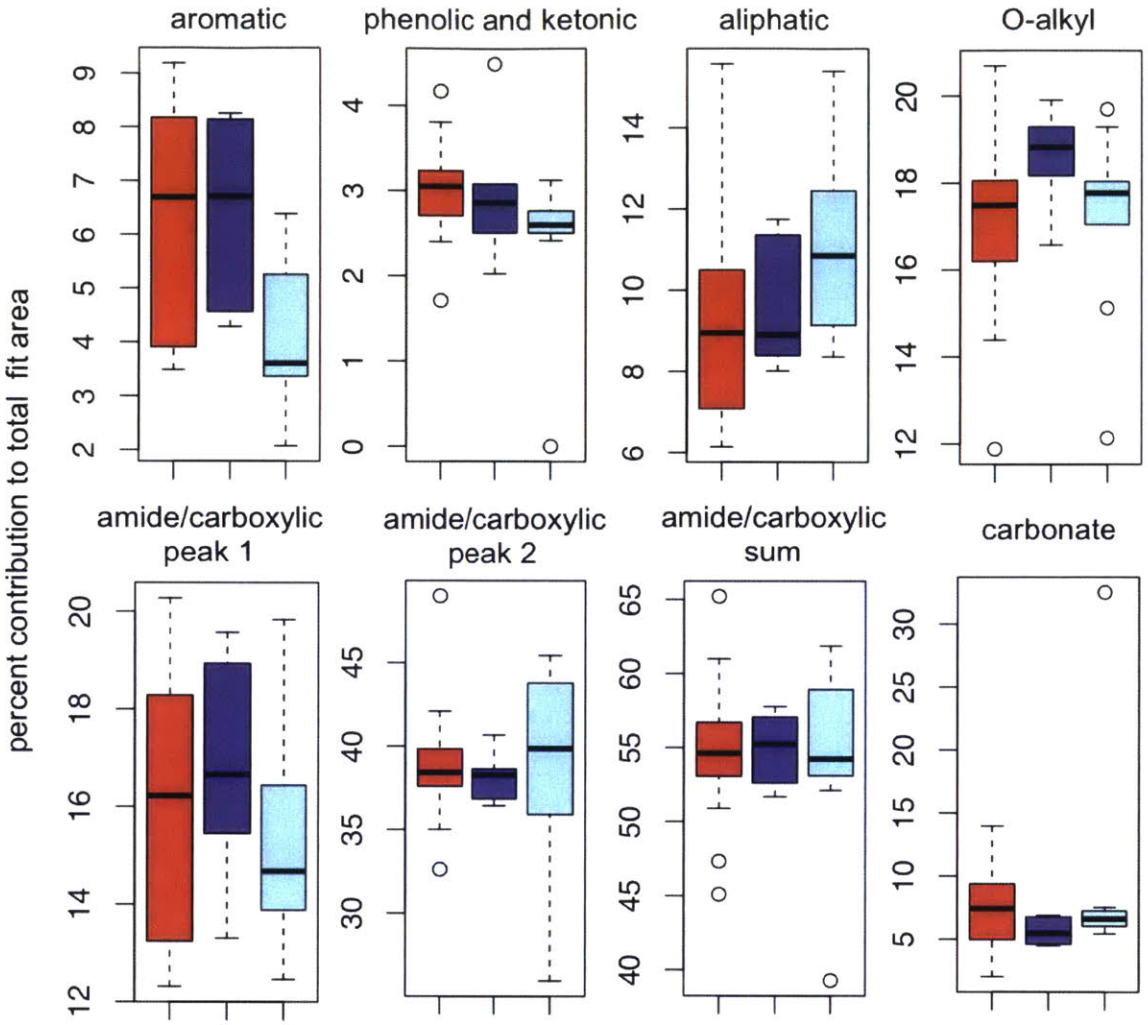

Figure 4. Box plots showing overall variability in percent contribution to total fit area for each site (red = NA 12, dark blue = SPG 1, light blue = SPG 9). The high outlier from site SPG 9 in the carbonate plot is from analysis of concentrated Mn nodule-like material at 5.125 m below seafloor (see text).

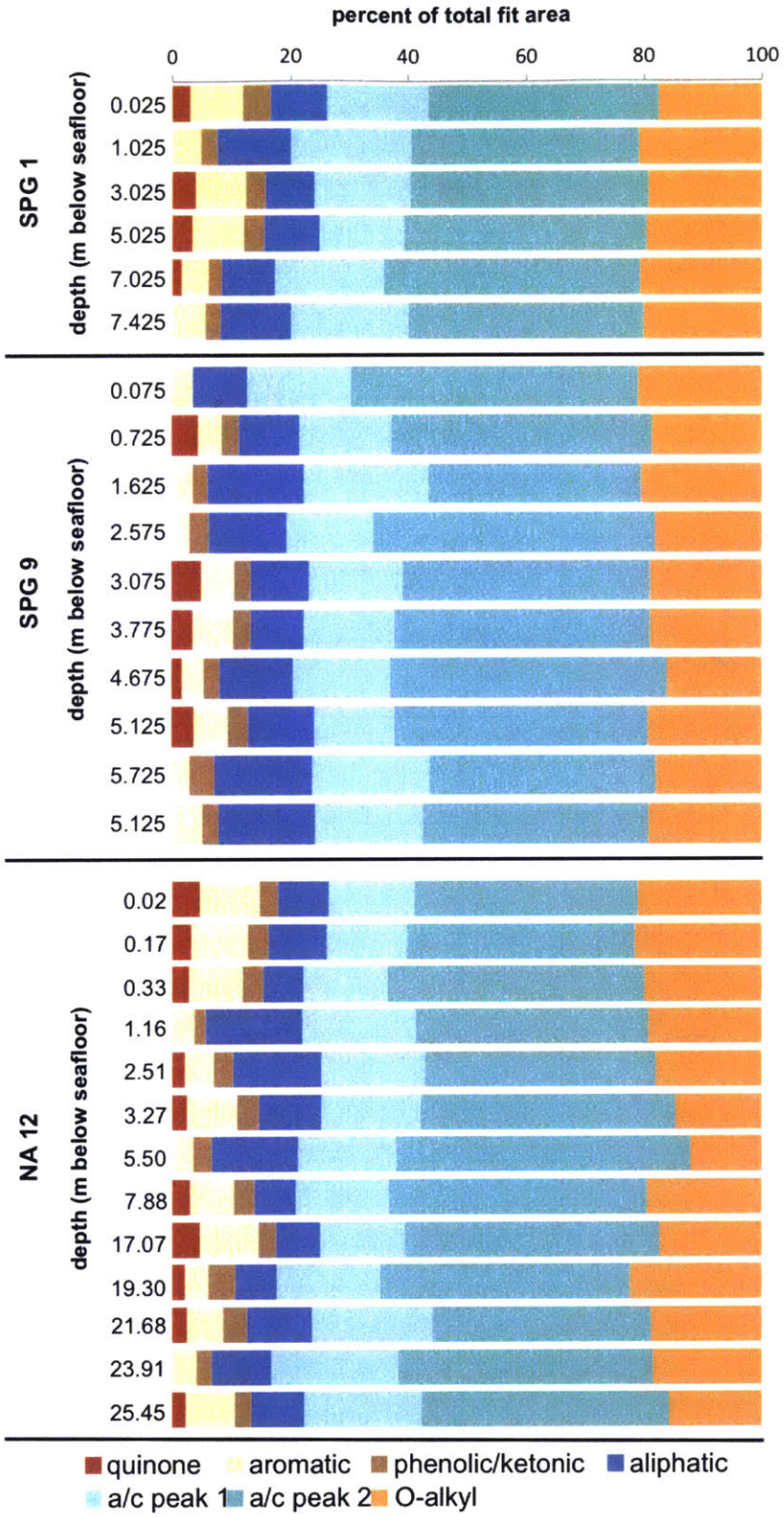
percent of total fit area
0
20
40
60
80
100
SPG 1
depth (m below seafloor)
0.025
1.025
3.025
5.025
7.025
7.425
SPG 9
depth (m below seafloor)
0.075
0.725
1.625
2.575
3.075
3.775
4.675
5.125
5.725
5.125
NA 12
depth (m below seafloor)
0.02
0.17
0.33
1.16
2.51
3.27
5.50
7.88
17.07
19.30
21.68
23.91
25.45
quinone
aromatic
phenolic/ketonic
aliphatic
a/c peak 1
a/c peak 2
O-alkyl

Figure 5. Stacked bar plots showing relative percent of total fit area of functional groups with depth along the core for SPG 1 (top), SPG 9 (mid), and NA 12 (bottom). Note that amide and carboxylic were best fit as two separate peaks but that each likely contain a contribution from the other. The two amide and carboxylic peaks are indicated here as "a/c peak 1" and "a/c peak 2." As carbonate content varies between samples and sites semi-independent of organic carbon composition, percent contributions to total fit area were normalized excluding carbonate.

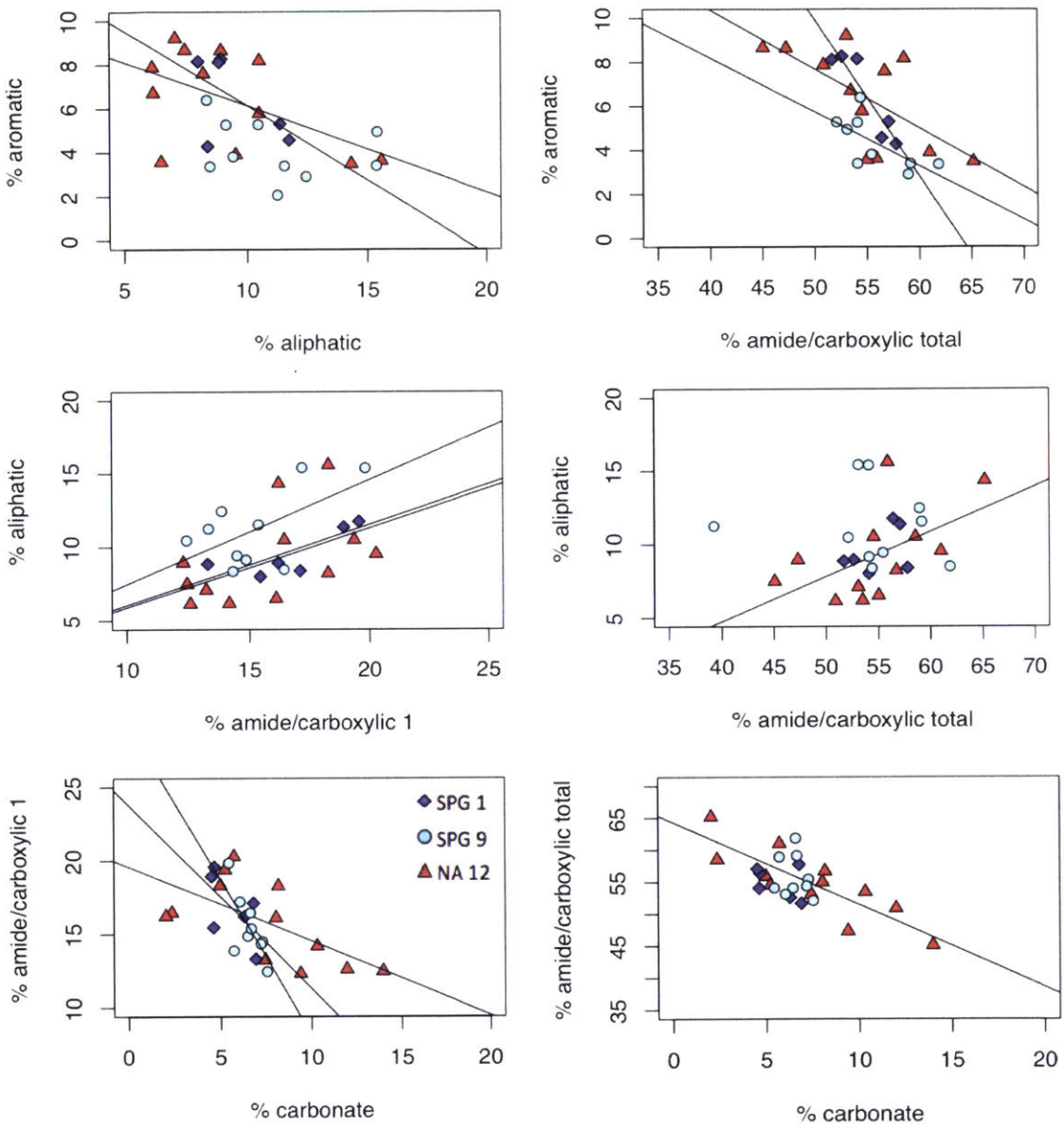

Figure 6. Correlation plots showing relationships between percent contribution to total fit area of different functional groups, by site. Fit lines with Pearson correlation coefficients > 0.5 are plotted.

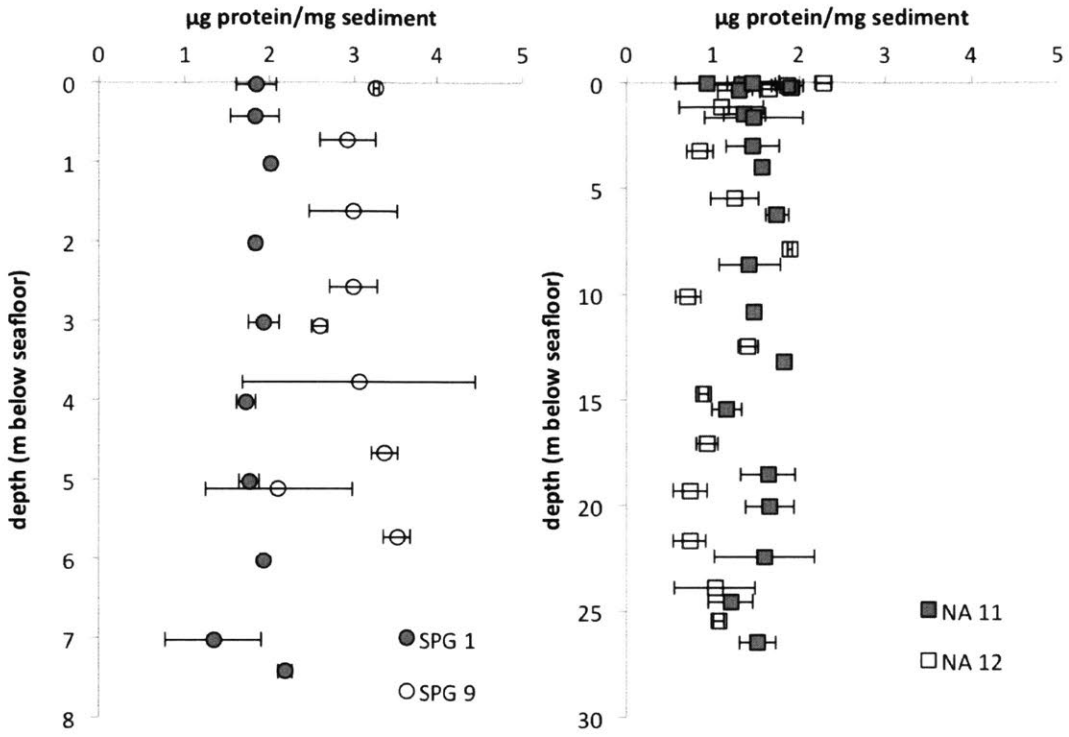

Figure 7. Protein content of freeze-dried sediments from SPG sites (left) and NA sites (right); error is the standard deviation of triplicate extractions. Note differing depth scales.

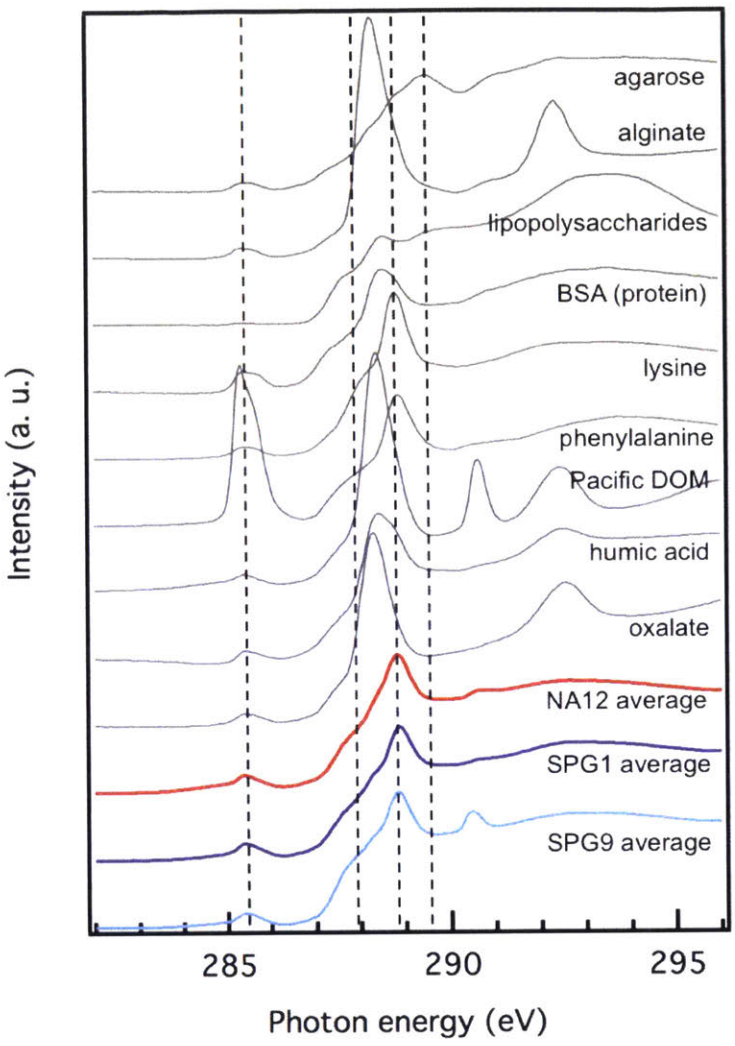

Figure 8. C 1s spectra of standard compounds shown with average spectra from each core, obtained by averaging spectra from all depths along the core. Dashed guide lines at 285.4, 287.7, 288.8, and 289.4 eV correspond to approximate peak centers for aromatic, aliphatic, amide and carboxylic, and O-alkyl carbon.

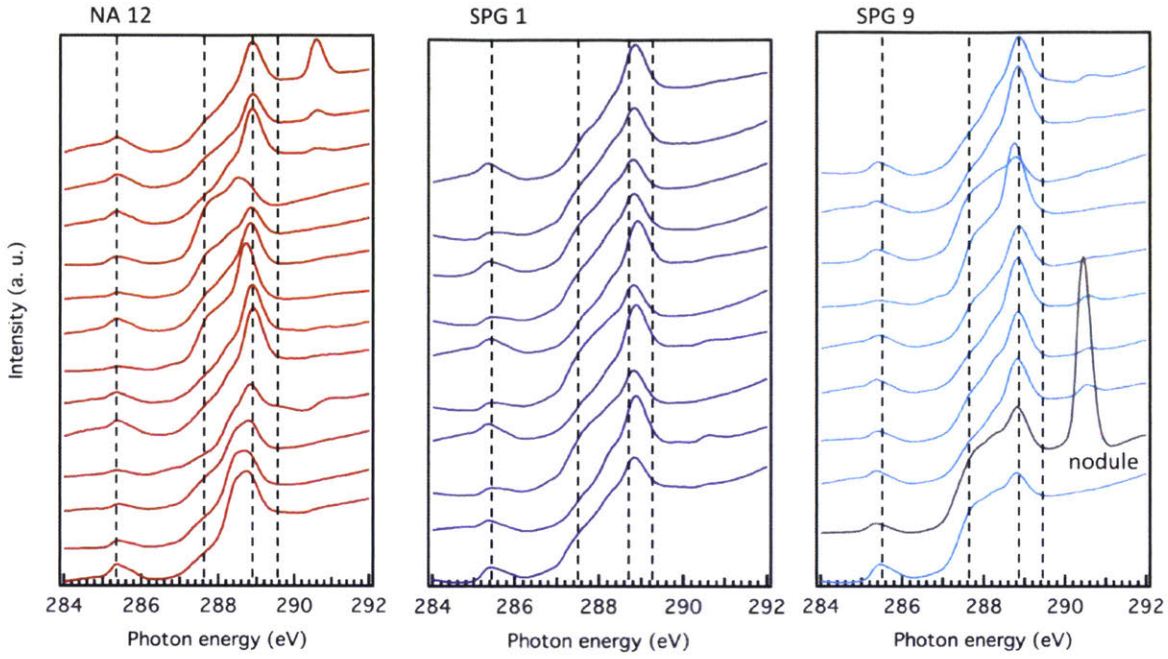

SI Figure 1. Raw C 1s NEXAFS spectra from all sites and depths, stacked so that samples from core top appear at the top of the figure and descending in order of depth. The spectra shown in grey from SPG 9 represents Mn nodule-like material concentrated from sediment from the same depth as the spectra above. It appears enriched in carbonate (290.4 eV) and aliphatic carbon relative to other samples. Dashed guide lines at 285.4, 287.7, 288.8, and 289.4 eV correspond to approximate peak centers for aromatic, aliphatic, amide and carboxylic, and O-alkyl carbon.

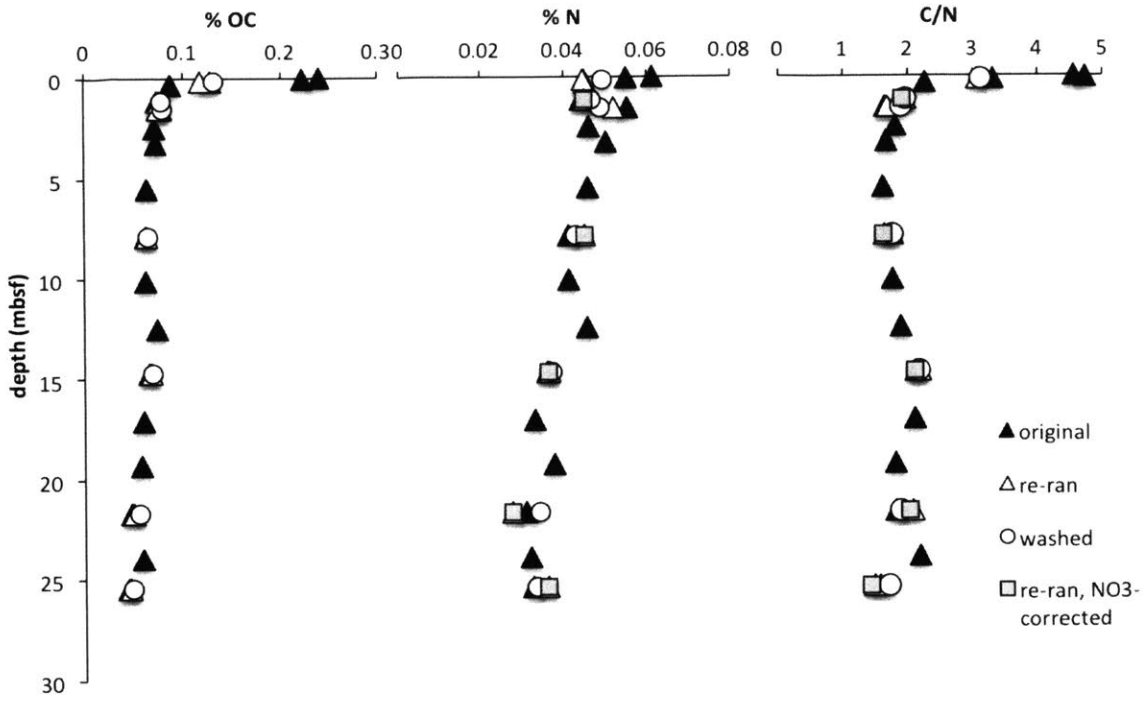

SI Figure 2. OC, N, and the C/N ratio measured during a series of methods checks on sediment samples from NA 12. Black triangles reflect the original data shown in the paper; white triangles ("re-ran") are separate aliquots of those original samples, freeze-dried and acid-fumigated six months after the original data to test for reproducibility and storage artifacts. White circles represent samples that were rinsed in 18.2 MΩ water and placed in a sonicating bath for 10 minutes three times in order to test whether elevated %N values were due to adsorbed nitrate or nitrate salts. Gray squares are the re-ran data where porewater content was calculated from weight change before and after freeze-drying and the porewater nitrate content was subtracted. Neither washing nor nitrate corrections substantially alter the value of OC or N measured.

Chapter 4: Coupled microscopic and spectroscopic approach to evaluating the compositional diversity of organic carbon in pelagic sediments on the microscale

ABSTRACT

Sediments cover 70% of the earth's surface and more than half of their volume is pelagic. Because of their inaccessibility and the analytical challenges inherent in analyzing low concentrations of carbon, we lack an understanding of the rates and mechanisms of carbon cycling in pelagic sediments. This dearth of information limits insight into predicting the extent of life and the carbon storage capacity of these environments. Here we contrast sediment cores from 14 locations in the South Pacific and North Atlantic spanning a range of estimated ages from two to 50 million years and a gradient of geochemical conditions from fully oxygenated to crustal basement to fully anoxic within millimeters below the seafloor. Organic carbon and nitrogen concentrations are extremely low (max values of 0.6 and 0.1 % respectively) and, at the majority of sites, decrease by an order of magnitude from sediment surface to the bottom of the cored interval but do not reach zero. Carbon and nitrogen degradation processes show unique stoichiometry, as carbon may be a more limited resource in these environments. Coupled scanning transmission X-ray microscopy and near edge X-ray absorption fine structure (STXM-NEXAFS) spectroscopy reveals a diversity in the chemical composition of organic matter on the microscale. Overall composition is similar between sites and we posit that in extremely old pelagic sediments with extended redox gradients, electron donor availability is the best metric for determining organic carbon concentration and composition rather than oxygen exposure, age, or sedimentation rate as have been applied previously.

4.1 INTRODUCTION

Pelagic sediments comprise more than half of global sediments but are understudied relative to more accessible near-shore environments. As exploration of these sediments continues, there is increasing awareness that pelagic environments contain key differences from coastal sediments and that global estimates of sediment chemical composition, nutrient cycling and storage, and the extent of life need to be more carefully considered. Kallmeyer *et al.* (2012) lowered estimates of total microbial mass in ocean sediments by 1-2 orders of magnitude from previous estimates following the collection of new data from low productivity regions of the ocean. D'Hondt *et al.* (2015) determined that 9-37% of the global seafloor is oxygenated; thus, cell abundance, active microbial metabolisms, and carbon content and composition may be strikingly different than that described in electron acceptor-limited organic-rich coastal environments.

Low sedimentation rates generate old, carbon-starved sediments with organisms utilizing an array of metabolisms and adaptations to garner energy from the environment (Lever *et al.*, 2015; Jørgensen & Marshall, 2016) and partitioning into niches along gradients in organic carbon concentrations (Durbin & Teske, 2012; Jørgensen *et al.*, 2013). This biomass turns over on extremely long time scales (Lomstein *et al.*, 2012) and may primarily be dormant or engaging in cell repair but not division (Lomstein *et al.*, 2012; Lever *et al.*, 2015). Despite the scarcity of energy, heterotrophic metabolisms are active and measurable in the deep subsurface (Biddle *et al.*, 2008; Orcutt *et al.*, 2011; Jorgensen *et al.*, 2012; Lloyd *et al.*, 2013) and, in oxygenated sediments, couple aerobic respiration to the oxidation of organic matter (D'Hondt *et al.*, 2009, 2015; Roy *et al.*, 2012; Russell *et al.*, 2016). While microbial communities could maintain populations via necromass recycling, buried organic carbon from the photosynthetic surface

ultimately sustains life (D'Hondt *et al.*, 2004; Lomstein *et al.*, 2012). Understanding the concentration, distribution, and chemical composition of organic carbon in pelagic sediments is thus integral to predicting the extent and limits of life and, conversely, determining the quantity of carbon stored in these sediments and its stability on geological timescales.

Oxygen exposure time is a common metric used to explain the concentration and distribution of organic carbon in sediments, where organic carbon burial is inversely correlated with time of exposure to molecular oxygen (Cowie *et al.*, 1995; Hartnett *et al.*, 1998; Arnarson & Keil, 2007). The parameter nicely encapsulates other metrics that have been considered (age, primary productivity, distance from shore, etc.) but studies targeting this effect have not yet extrapolated results from millennia to the million-year time scales that organic matter in pelagic sediments experience. Chapter 3 describes low but stable concentrations of OC in oxic, pelagic sediments that well exceed the concentration of OC predicted were it comprised of biomass alone. From these results, we predict that oxygen exposure time may be a less useful metric on extremely long time scales. Composition and other factors such as mineral-based protection may better explain OC persistence on million-year time scales. Indeed, even on millennial time scales, Arnarson and Keil (2007) found that 50% of preserved carbon was adsorbed to mineral surfaces in continental margin sediments.

This work seeks to determine the balance of these preservation mechanisms in pelagic sediments from the South Pacific and North Atlantic ranging in age from two to 50 million years and in redox state from oxic to anoxic by examining OC content and composition. In work on sediments from the South Pacific Gyre, Fischer *et al.* (2009) use oxygen microprofiles to determine that half of the organic matter delivered to the seafloor is remineralized in the top 6 mm of sediment with very little oxygen consumption occurring at depth. Yet, in the same

sediments, Durbin and Teske (2011) find that oxygen and nitrate concentrations structure microbial communities along the entire sediment column. Increased nitrate concentrations are interpreted as resulting from continued microbial activity, remineralization of organic nitrogen, and subsequent oxidation of ammonia (D'Hondt *et al.*, 2009). Reduction of oxygen coupled to oxidation of organic matter accounts for only 20% of the downward oxygen flux; low rates of organic matter degradation are attributed to increasing recalcitrance of organic matter with depth and sediment age (D'Hondt *et al.*, 2009). In these gyre sediments, therefore, oxygen exposure time is not the primary determinant of OC persistence, leaving limited bioavailability as a more viable explanation.

Recalcitrance and physical or chemical protection by minerals offer the most viable explanations for the limited bioavailability of deep subsurface OC. Lithology and interstitial water geochemistry have been linked to variations in community structure (Picard & Ferdelman, 2011; Jorgensen *et al.*, 2012; Jørgensen *et al.*, 2013). Likewise, Lalonde *et al.* (2012) find that up to 20% of OC over a range of sedimentary environments is associated with iron oxide minerals and that associated OC is enriched in $\delta^{13}C$, suggesting that the abundance of specific mineral classes could affect both the content and composition of OC. Chapter 3 determined that the composition of OC in oxic pelagic sediments is similar to that of "molecularly uncharacterizable carbon" described in other works, (Hedges *et al.*, 2000; Brandes *et al.*, 2004; Dickens *et al.*, 2006; Hertkorn *et al.*, 2006; Mao *et al.*, 2011) containing a high fraction of amide and carboxylic carbon as well as O-alkyl carbon. Mao *et al.* (2011) interpreted this composition as evidence of partial oxidation reactions resulting in substituted and copolymerized carbohydrate structures. Interactions with mineral surfaces include catalysis of aromatic bond breaking and copolymerization reactions as well as preferential sorption of carboxylate groups (Johnson *et al.*,

2015) and nitrogen-bearing compounds (Lalonde *et al.*, 2012). Thus, the chemical signature of molecularly uncharacterizable carbon could derive from a range of processes in the sediment.

By comparing the content and composition of organic carbon at geochemically distinct sites, we aim to tease apart the mechanisms dictating the balance between organic carbon preservation and degradation. We introduce the use of coupled synchrotron-based scanning transmission X-ray microscopy and near edge X-ray absorption fine structure (STXM-NEXAFS) spectroscopy to this end. X-ray absorption spectroscopy is non-invasive and non-destructive and does not require pre-processing of samples (e.g. removal of salts or demineralization to remove paramagnetic minerals for NMR analysis) that might destroy the relationships we intend to observe. As synchrotron X-rays are tunable and have a high flux, they are ideally suited for analyzing a range of elements present in low concentrations and in complicated matrices (Templeton & Knowles, 2009). Here, we analyze organic carbon content and composition via bulk and micro-scale analyses and correlate these results with varying geochemical conditions between sites, along the length of individual sediment core, and on the micro-scale. We evaluate the influence of geochemical parameters and inform the paradigmatic mechanisms of OC recalcitrance and mineral-based protection.

4.2 Methods

4.2.1 Sediment samples

4.2.1.1 Collection and storage

Sediment samples were collected via long piston corer on expeditions KNOX02-RR on the R/V Roger Revelle (South Pacific Gyre, SPG) and KN223 on the R/V Knorr (North Atlantic,

NA), or by drilling during IODP leg 201 (IODP site 1231) in the Peru Basin. SPG sediments were subsampled from split core at the University of Rhode Island Graduate School of Oceanography Core Repository. Sediment at the surface of the split core was scraped away with a sterile spatula and only underlying, unexposed sediments were sampled. NA sediments were subsampled from whole rounds on board during expedition KN223 and kept cold at 4 °C until analysis. A second set of samples was frozen at -20 °C and used to determine that no difference in carbon concentration of mineralogy, as determined by X-ray diffraction, existed due to preservation artifacts (data not shown). Samples from IODP site 1231 were received as frozen whole rounds and kept frozen at -20 °C until subsampling and analysis.

4.2.1.2 Site locations and description

Lithologically, the majority of sites are characterized as pelagic clays. SPG sites 1-4 consist of homogeneous dark brown clays with a high content of manganese nodules and micronodules (D'Hondt *et al.*, 2011). The shallower site SPG 6 contains calcerous nanofossils as it sits above the carbonate compensation depth (D'Hondt *et al.*, 2011). SPG sites 9 and 10 are also homogeneous clays, but are lighter in color and contain yellow-brown mottling throughout. Suboxic SPG 12 is situated just outside of the gyre and is composed primarily of siliceous ooze (D'Hondt *et al.*, 2011). Like oxic SPG sites, the oxic NA sites consist of pelagic clays varying from yellowish brown to dark brown. At both NA 11 and NA 12, slight mottling and ~ 5% radiolarian tests altered to chert were observed toward the bottom of the cored interval, while NA 12 additionally had a distinct layer of zeolites at 17.2 m below seafloor (Murray *et al.*, 2014 KN223 Cruise Report). Suboxic NA sites 3 and 10 consist of nanofossil clay and clayey nanofossil ooze, alternating at ~75-100 cm intervals and with clay content decreasing down core

(Murray *et al.*, 2014 KN223 Cruise Report). Short intervals (mm-scale) bearing brownish-black Mn oxides are found below 1 m depth along the cores. Both NA 15 and NA 16 host a wide variety of lithologies, including clay, silty clay, sand, and intervals of radiolarian ooze. NA 15 contains a layer of white nanofossil ooze in between turbidite deposits at ~16 m below seafloor, and has an increasing contribution from biosiliceous material at >24 m below seafloor (Murray *et al.*, 2014 KN223 Cruise Report).

Sedimentation rates (Table 1) were estimated from sediment thickness (Divins, 2003) and either basement age (Müller *et al.*, 2008) or, for SPG 1, the 65 Ma Cretaceous/Paleogene iridium anomaly (D'Hondt *et al.*, 2009). Estimates do not correct for compaction or changes in sediment porosity with depth.

4.2.2 Oxygen and nitrate measurements

For the North Atlantic cores collected during expedition KN223, dissolved oxygen concentrations were measured shipboard using needle-shaped optical O_2 sensors (optodes, Fischer *et al.* (2009), PreSens, Regensburg, Germany). Optodes were calibrated using a two-point calibration with sodium sulfite (Na_2SO_3)-saturated 18 MΩ solution (0%) and water-saturated air (100%) as standards. Conversion of the measured luminescence lifetime of the optode to oxygen values was done internally by the instrument. Sealed, capped core sections were allowed to thermally equilibrate for 6-24 hours prior to analysis. Analyses were conducting by drilling holes into the core liner, inserting the probe into the central part of the core, and allowing the sensor to stabilize over the course of 120 seconds. Temperature was monitored using a sensor (PT 1000) inserted into an adjacent hole. The optodes and temperature sensor were connected to a MICROX TX3 (PreSens) single-channel fiber-optic oxygen meter and

signals recorded with OxiView software (TX3, version 6.02). Optode and temperature measurements were conducted at 10 cm intervals near the sediment surface until three consecutive measurements showed consistently zero oxygen concentration. From that point on, optode measurements were taken at 2–4 depths per section (30–75 cm intervals). Sampling resolution increased towards core bottom at sites where the bottom of the cored interval approached basement. Diffusion of oxygen over the distance from core liner to core center did not occur during the period of time over which measurements were taken. Further, low oxygen consumption rates within the core ensured that oxygen concentrations did not change measurably during the thermal equilibration process. The sensor tip was rinsed with 18 MΩ water between measurements. Uncertainty at NA sites was 1.3 μM on average, calculated as three times the standard deviation of the residuals of detrended data. Oxygen concentration profiles of SPG cores are published in Fischer *et al.* (2009) and methods for data collection are described therein.

Samples of interstitial waters for nitrate and nitrite analysis were collected via Rhizon Soil Moisture Samplers (Rhizosphere Research Products, Wageningen, The Netherlands) and analyzed shipboard. Rhizon sampling extracts porewater from the sediment core by suction filtering through thin tubes of hydrophilic porous polymer with a mean pore diameter of 0.1 μm. Blanks consisted of 18 MΩ water pulled through a Rhizon sampler. Interstitial waters were analyzed for nitrate and nitrite via ion chromatography coupled to UV/Vis (Metrohm 844 UV/VIS Compact IC) fitted with a 150 x 4.0 mm Metrosep A SUPP 8 150 column kept at 30 °C. Approximately 0.8 mL of water was injected into the 250 μL sample loop (such that the loop was flushed with several volumes of sample water before the fraction actually analyzed) and eluted using 0.45-μm filtered 10% NaCl solution. Nitrate and nitrite absorption was quantified at 215

nm. A 50 μM sodium nitrate standard as well as a deep water sample from site NA 2 was run after every fifth or sixth sample depending on instrument stability as drift control.

4.2.3 Organic carbon and nitrogen quantification

Organic carbon and nitrogen were analyzed via element-analyzer isotope ratio mass spectrometry (EA-IRMS) at the WHOI mass spectrometry facility using a Carlo Erba Elemental Analyzer Model 1108 and a Finnigan-MAT DeltaPlus Isotope Ratio Monitoring Mass Spectrometer. Prior to analysis, samples were freeze-dried then acidified to remove carbonate following the procedure described in Whiteside *et al.* (2011). Every tenth sample was analyzed in triplicate to determine analytical error; concentrations were calibrated and drift corrected using USGS 40 (L-glutamic acid) reference material and an in-house glycine standard. Carbon integrated peak areas were, on average, 52 ± 22 times higher than the blank; ten samples were <5 times higher than the blank, with the lowest from IODP site 1231 still 3 times higher. Nitrogen measurements were 32 ± 6 times greater than the blank. Thirteen samples were <5 times greater than the blank; the two lowest were from SPG 6 and still 2.5 times greater.

Intact proteins were extracted following the protocol of Ehrenreich and Widdel (1994) with modification as described in Estes *et al.* (2016). Briefly, sediments were suspended in 1.5 mL ultrapure water and sonicated three times at 40% duty cycle, keeping the samples on ice between sonication cycles. 300 μL of 6N hydrochloric was then added to the solution and incubated at 37°C for 30 minutes. Then, 75 μL 10 M trichloroacetic acid was added and the mixture incubated on ice for 30 minutes. Finally, samples were centrifuged at 14,000 rcf for 15 minutes, the supernatant decanted, and an additional 500 μL of 0.1 N NaOH was added. Samples were boiled for 5 minutes and cooled to room temperature prior to analysis via Qubit fluorescent

reagent (Life Technologies). Fluorescence was calibrated using a six-point calibration from zero (18 MΩ water) to 187.5 μg/mL bovine serum albumin standard (BioRad). R^2 values for the calibration curves were always >0.9 and consistently >0.95; often decreased R^2 came from the zero-protein standard being non-linear, in which case it was excluded from the calibration curve.

4.2.4 Organic carbon characterization via STXM-NEXAFS

4.2.4.1 STXM-NEXAFS analyses

Scanning transmission X-ray microscopy (STXM) coupled to near edge X-ray absorption fine structure (NEXAFS) spectroscopy was conducted on beamline 11.0.2 at the Advanced Light Source (ALS, Lawrence Berkeley National Laboratory, Berkeley, CA). The STXM endstation uses Fresnel zone plates to focus the monochromatic X-ray beam and plane grating monochromator to resolve energy. Sediment slurry samples (1-10 μL) were pipetted onto silicon nitride membranes (Si_3N_4, Silson, Ltd., Northampton, England) and air-dried. For each sample, 200x200 μm transmission images were used to find a region that was not too optically dense. Then, optical density (OD) maps ranging between 50x50 and 15x15 μm in size were taken over the C, N, Al, and Si K-edge and the Mn and Fe L_3 edge, with OD = ln (I_0/I), and maps achieved by subtracting a pre-edge transmission image from a post-edge image. Finally, a C K-edge stack was collected from 279 to 320 eV at step sizes as small as 0.1 eV, a dwell time of 1 ms, and a spatial resolution of 75-100 nm. Image processing, alignment, and I0 normalization was conducted using the IDL package aXis2000. OD maps of all elements as well as specific carbon functional groups were used to generate "masks," e.g. a region from which C K-edge spectra could be extracted representing the composition of carbon in areas where a certain element or

functional group is elevated in concentration. These spectra were imported into Igor Pro (WaveMetrics, Inc, Lake Oswego, Oregon) and intensity and area normalized then further processed as described below. Finally, pixel-by-pixel correlations of the OD maps were generated by decreasing image resolution and exporting to R (R Core Team (2015), R Foundation for Statistical Computing, Vienna, Austria) where pixel intensity was normalized to a scale of 0-100, converted to a vector, and correlated. Pixels with normalized intensity <0.05 were excluded to remove noise from the correlation plots.

4.2.4.2 Gaussian deconvolution of NEXAFS spectra

Gaussian deconvolution of carbon NEXAFS spectra extracted from STXM-derived masks was conducted using PeakFit software (SeaSolve Software Inc., San Jose, CA, USA) and following the peak assignments and parameters described in Keiluweit et al. (2012) and references therein. In brief, spectra were fit using six Gaussian peaks corresponding to approximate positions of major functional group resonances, according to the convention followed in the literature (Schumacher *et al.*, 2005; Solomon & Lehmann, 2005; Kleber *et al.*, 2011; Keiluweit *et al.*, 2012); these approximate positions were also utilized to define the energies used to generate optical density maps of individual functional groups. Peak magnitude and energy were allowed to vary freely and always constrained themselves to the energy ranges expected for each functionality. As in previous works (Kleber *et al.*, 2011; Keiluweit *et al.*, 2012), the ionization threshold was fit using a 'transition' function in PeakFit set at 290 eV that approximates the arctangent function used by other researchers (Solomon *et al.*, 2005), while σ* transitions were fit with two-three additional asymmetric Gaussians. Fit results were expressed as 'percent of the fit area', excluding the transition function and σ* Gaussians as they were above

the energy range of interest and did not affect peak areas. Data presented here also exclude inorganic carbonate carbon (~290.4 eV) from the 'percent of the fit area' as its concentration varies widely between samples as a function of lithology rather than organic carbon cycling.

4.3 Results

4.3.1 Site descriptions and geochemistry

To compare the influence of geochemical parameters on the content and composition of organic carbon in pelagic sediments, samples were acquired from the South Pacific Gyre (SPG), western subtropical North Atlantic (NA), and from the Peru Basin (PB, IODP site 1231 holes B and E). Table 1 contains basic site descriptions and classifies each core as oxic, "suboxic," or anoxic. Oxic cores contain measurable dissolved oxygen in the interstitial waters throughout the length of the cored sediment, with nitrate concentrations in the interstitial waters increasing with depth (Figure 1, D'Hondt *et al.*, 2009; Fischer *et al.*, 2009). Oxygen concentrations at 1.5 meters depth range from 158 to 207 μM (Table 1). These values are depleted relative to core top and bottom water samples, but still demonstrate deep oxygen penetration and low respiration rates (e.g. Fischer *et al.*, 2009, in microprofiles of SPG sites). Cores NA 3, NA 10, and SPG 12 are considered "suboxic," meaning that oxygen is present towards core top, but depleted within 3 meters below seafloor (Figure 1). Interstitial water nitrate and nitrite profiles demonstrate an extended redox gradient; at site NA 3 in particular, the decline in nitrate between 3 and 10 meters below seafloor is coupled to increasing nitrite which peaks at ~8 meters depth and then declines to zero at ~21 meters below seafloor (Figure 1). Sites NA 3 and NA 10 were cored at the same longitude/latitude and are discussed interchangeably throughout this paper. Anoxic sites contain no measurable oxygen or nitrate in interstitial waters even in the first few millimeters. These

sites are reducing but not sulfidic, with chemical potential seemingly deriving from redox-active metals such as iron and manganese (data not shown).

All sites are pelagic, with water depths >3700 meters and ranging from 3705—5699 meters (Table 1). Sedimentation rates at SPG sites correlate with distance from gyre center, ranging from 0.008 cm/kyr (SPG 3) to 0.111 and 0.178 cm/kyr at sites SPG 6 and SPG 12 respectively (D'Hondt *et al.*, 2009). Oxic NA sites have marginally higher sedimentation rates of 0.143 and 0.100 cm/kyr (NA 11 and NA 12). These incredibly low sedimentation rates result in total sediment thicknesses between 6 and 130 meters (Table 1, D'Hondt *et al.*, 2009). The suboxic sites NA 3 and 10 have a sedimentation rate of 0.250 cm/kyr, higher than the comparable SPG site 12. Anoxic site NA 15 has a sedimentation rate very similar to that in the Peru Basin (0.376 relative to 0.338 cm/kyr), while NA 16 has the highest rate included in this study of 0.992 cm/kyr, resulting in a sediment thickness >1000 m.

4.3.2 Organic carbon and nitrogen content

4.3.2.1 Concentrations and stoichiometry

Regardless of oxygenation, solid-phase organic carbon (OC) and nitrogen (N) concentrations in the sediments analyzed in this study are among the lowest measured globally. At the oxic and suboxic sites, concentrations decrease exponentially with depth from surface maxima at oxic sites ranging from 0.076% (SPG 6) to 0.28% (SPG-1) towards deep minima of 0.018% (SPG 6) to 0.055% (SPG 10), with NA sites falling on the higher side but well within the range of the SPG sites (Figure 2). Suboxic site NA 10 displays a comparable concentration profile, while concentrations at suboxic site SPG 12 are marginally higher, decreasing from

0.33% to 0.18% (Figure 2). At the NA anoxic sites, OC concentrations are variable and, on average, higher than at the oxic and suboxic sites. OC concentrations at NA 16 initially increase with depth from core top to ~ 5 m depth, then slowly decrease towards core bottom, never going below the minimum value of 0.31% observed at 0.5 m depth (Figure 2). Concentrations at NA 15 are extremely low (0.05%) in and around the two sandy turbidite layers between ~ 13-21 meters and in the carbonate layer at 16.5 meters below seafloor, but increase again towards the bottom of the cored interval. At anoxic site IODP 1231 hole B and hole E (HB and HE respectively), concentrations plateau just above 0.01% at ~60 m below seafloor (Figure 2). These lowest values are still a factor of 3.5 greater than the average of the blank.

Nitrogen concentrations follow similar trends, decreasing with depth at the oxic and suboxic sites while not showing any clear pattern with depth at the anoxic NA sites (Figure 2). For the SPG sites, the decrease is more linear than exponential, with no rapid initial decrease at the core top excepting site SPG 12. The NA sites have a more typical rapid initial decrease at core top, but show greater variability with depth. At several sites, the overall decrease in nitrogen is less than the overall decrease in organic carbon; this trend is particularly notable for the North Atlantic sites. For the oxic sites NA 11 and 12 and the suboxic site NA 10, OC decreases by ~80% along the length of the core, while N decreases 57, 47, and 35%, respectively. At sites NA 15 and 16, OC and N profiles are more variable, but OC decreases 45 and 37% relative to the 28 and 24% decrease in N. Oxic sites SPG 2, 3, and 4 and suboxic site SPG 12 also have disproportionate decreases in OC relative to N, although the differences are not as substantial. Finally, SPG 1, 9, 6, and 10 as well as the anoxic IODP 1231 holes B and E show proportional decreases in OC relative to N, ranging from ~65% at SPG 10 to 97 and 94% for OC and N

respectively at IODP 1231 HB. These trends further emphasize partial decoupling of C and N cycling in carbon-poor environments, regardless of sediment oxygenation state.

C/N values at all sites are extremely low, ranging from 1.3 at 15.4 m below seafloor at site NA 11 to 10.5 at 1.5 m below seafloor in the core from anoxic site NA 15 (Figure 2). C/N profiles primarily follow the OC profiles, decreasing rapidly in the top interval and then stabilizing with depth, but, unlike the OC profiles, tail upwards again toward core bottoms at several sites including all the oxic sites, SPG 12, and IODP 1231 holes B and E.

4.3.2.2 Calculated stoichiometry of degradation

To further assess decoupling of C and N processing in these sediments, organic carbon and nitrogen degradation rates were calculated for the top ~1.5 meters, where concentrations decrease rapidly, and then the bottom portion of each core, where concentrations often decrease almost linearly, by taking the difference in concentration over the difference in estimated sediment age. Degradation rates at the six oxic sites in the SPG for which rates were calculable range from 0.001 to 0.049 mol $OC/m^3/kyr$ in the top interval and 0.0006 to 0.0055 mol $OC/m^3/kyr$ in the bottom (SI Table 1). Rates are approximately an order of magnitude lower in the bottom interval than in the top, though this trend does vary by site. At SPG 3, for instance, degradation rates are comparable in core top and bottom, although this observation may be a function of the extremely low sedimentation rates such that we lack the spatial resolution to capture the more rapid degradation occurring towards core top. As sedimentation rates are higher at the oxic NA sites, OC degradation rates are proportionally higher as well in the top interval, at 0.133 and 0.132 mol $OC/m^3/kyr$ for NA 11 and NA 12 respectively (SI Table 1). Rates in the bottom interval are more comparable to those in the bottom interval the in SPG, however, at

0.0011 mol OC/m^3/kyr. Likewise, OC degradation rates in the surface interval at the suboxic and anoxic sites (IODP 1231 HB was the only anoxic site at which a surface rate could be calculated) are comparable or higher than at the oxic sites (0.122, 0.419, and 0.356 mol OC/m^3/kyr for NA 10, SPG 12, and IODP 1231 HB) *and* higher in the deeper interval (0.002, 0.08, and 0.009 mol OC/m^3/kyr respectively, SI Table 1).

Comparing rates in the deeper interval to the top interval, however, does not show clear trends by site type. NA 11 and NA 12 have rates in the deeper interval <1 % of that in the top, while the oxic SPG sites have values ranging from 2.5 to 110% (at SPG 3). OC degradation rate in the deeper interval at site NA 10 is 2% of that in the top, while at SPG 12 the value is 20%. Finally, at IODP site 1231, OC degradation rate in the lower interval is 2.5% of that in the top (SI Table 1). Within a given interval, degradation rate correlates linearly with the initial concentration of OC (R^2 of 0.87 and 0.94 for the surface and deep intervals respectively, SI Figure 1), while the correlation between degradation rate and estimated sediment age follows a power law (R^2 of 0.88 and 0.71 for the surface and deep intervals). In the surface interval, oxygen content at the bottom of the interval does have a rough inverse correlation with degradation rate (linear fit, $R^2 = 0.66$), but no such correlation exists in the deep interval or if anoxic and suboxic sites are removed from the plot (SI Figure 1). Finally, we use the percent decrease in OC concentration from core top to bottom (as an estimate of OC burial efficiency) and sediment age (as a proxy for oxygen exposure time, where at the suboxic sites OET is set as the estimated sediment age where oxygen concentrations are undetectable) to directly compare organic carbon to OET, finding no correlation (R^2 of 0.02, SI Figure 1).

Figure 3 contrasts C/N of bulk material with the calculated C/N of degradation over a given interval (blue bars) for all cores where both elements decreased in concentration along the

length of the core (site NA 15 is excluded due to variable concentrations and SPG 6 excluded due to its short length and minimal data). At the majority of sites, C/N of degradation in the surface interval is substantially higher than in the deep interval, as OC is being removed at a faster rate than N. These values are as high as 21.0 at NA 10, 14.3 at NA 11 or 13.7 at both SPG 1 and IODP 1231 HB (Figure 3, SI Table 1). At depth, values decrease to match the actual composition of the organic matter present. For instance, at SPG 1, the C/N of sedimentary organic matter is 2.76 relative to a C/N of degradation of 2.36 (Figure 3, SI Table 1). Exceptions to this trend include SPG 3, where C/N of degradation in the surface interval is 2.05, increasing marginally to 2.70 in the deep interval. SPG 10 also shows only a minor decrease, while at the suboxic site NA 12, C/N of degradation actually increases from 5.90 to 8.91. At NA 10, the North Atlantic suboxic site, the extremely high surface C/N of 21.0 declines to 8.56. At the anoxic sites, NA 16 did not show a clear enough decrease in OC or N in the surface interval to calculate a degradation rate, but has a high C/N of degradation in the deep interval (11.6). IODP site 1231 HB has a C/N of 13.7 in the surface interval, decreasing to 4.72 (Figure 3, SI Table 1).

4.3.3 Protein quantification

Unlike OC and N profiles, protein concentrations do not show consistent trends with depth. As described in Chapter 3, protein concentrations in the core from site NA 12 display a more typical depth profile, decreasing rapidly in the first few meters and plateauing to a relatively constant value around 1 μg protein/mg sediment at depth (Figure 4). Average concentrations at site NA 11 and SPG 1 are slightly higher, at 1.48 ± 16% and 1.83 ± 14% μg protein/mg sediment respectively. Both sites have profiles that are static with depth, whereas site SPG 9 has higher concentrations (average 2.98 ± 14% μg protein/mg sediment) that increase

with depth in the bottom half of the cored interval (Figure 4). At all four oxic sites analyzed for protein content, the relative standard deviation of the triplicate extractions is on the same order as the total variability along the length of the cores; thus, trends with depth should be interpreted cautiously.

Protein concentrations measured at suboxic site NA 10 are substantially lower and more variable than at the oxic sites, ranging from a maximum of 1.36 ± 30% μg protein/mg sediment at 2 m below seafloor, to zero or near-zero values at 8, 11, and 26.4 m below seafloor (Figure 4). Within a meter-long interval, concentrations jump from 0.07 ± 84% to 0.57 ± 64% μg protein/mg sediment (samples at 11.1 and 11.8 m below seafloor). Again, the average for the entire core (0.48 ± 93% μg protein/mg sediment) has a standard deviation on the order of that for the relative standard deviation of an individual depth's triplicate extraction (average: 71%). The subsurface maxima and minima are reproducible and contain multiple data points such that jumps in concentration are not simply outliers or bad data. Rather, we expect that variability is real and the high error in the triplicate extractions is due to the carbonate content at this site, where the efficiency of the acidification step of the protein extraction procedure may be diminished.

At site NA 15, protein concentrations decrease across the first five meters and then stabilize until ~11 m below seafloor (Figure 4). Interestingly, concentrations drop to near-zero in the two sandy layers at ~13 and 21 m below seafloor and in the nanofossil ooze layer at 16.5 m below seafloor, but also remain comparably low in the samples taken *between* these distinct strata, at 15.6 and 18 m below seafloor. By the bottom of the cored interval, concentrations again increase to be comparable to values at core top (2.6 ± 5.8% vs. 2.5 ± 3.1% μg protein/mg sediment for core top and bottom respectively, Figure 4). IODP site 1231 HB has a more typical

depth profile, decreasing from the surface, reaching <0.2 μg protein/mg sediment by 60 m below seafloor and the declining further to ~0.02 μg protein/mg sediment at core bottom (Figure 4). IODP site 1231 HE also had a protein concentration of just over 0.02 μg protein/mg sediment toward core bottom, but reached extremely low values <0.15 μg protein/mg sediment by the shallowest sample analyzed, at 28.1 m below seafloor (Figure 4). Finding such low concentrations at that depth is anomalous relative to all other sites analyzed in this study.

4.3.4 STXM-NEXAFS

4.3.4.1 Micro-scale spatial distribution of mineral-forming elements

Transmission images, element optical density maps, and carbon 1s NEXAFS spectra were collected for five samples along the lengths of the multi-core and long core from site NA 12 (0.02, 1.74, 7.88, 14.7, and 23.9 m below seafloor), two depths along the core from suboxic site NA 3 (0.025 and 21.345 m below seafloor), and three depths along the length of the anoxic core NA 15 (0.025, 12.575, and 24.155 m below seafloor), where two regions from the mid-depth sample were analyzed to better understand microscale heterogeneity in carbon spatial distribution and chemical composition. Figures 5-7 show transmission images (column 1) and false-colored overlaid optical density maps for the distribution of iron (Fe), potassium (K), and carbonate (column 2).

Carbonate carbon likely reflects the presence of calcium carbonate minerals; in the shallowest samples the morphology suggests a biological origin. The deepest sample at NA 3 (21.345 m below seafloor) and the mid-depth samples from NA 15 (12.575 m below seafloor) still contain particle fragments that presumably derived from carbonate biominerals; however, with increasing depth, carbonate is distributed more sporadically and homogeneously and less as

discrete, morphologically distinct particles (Figures 5-7). Potassium is ubiquitous in all samples from all sites, though its predominance varies by sample. At most sites, potassium is visible as large, (>1 μm in one dimension) discrete particles, though in a number of samples it also appears more homogeneously spread across the sample, either as extremely abundant nanoparticles not resolved in the STXM imaging or as K-rich regions in larger grains (e.g. in all samples from NA 15 except 12.575 m below seafloor region 1, Figure 7). Iron is present as discrete particles, likely iron oxides, although Fe K-edge EXAFS (data not shown) identifies an additional contribution from iron-bearing clays. Iron and carbonate co-occur in several samples, especially the deepest sample analyzed from NA 12 (23.905 m below seafloor, Figure 5) and NA 15, 12.575 m below seafloor, region 1 (Figure 7). Iron and K also co-occur, primarily in samples where K is more homogeneously distributed. Carbonate and K likewise co-occur, including in the upper sample from NA 12 (0.02 m below seafloor, Figure 5) where they both comprise portions of circular features interpreted as biological carbonates and, more consistently, in the deeper sample from NA 3 (21.345 m below seafloor, Figure 6) where, likewise, particle morphology suggests a biological origin.

4.3.4.2 Micro-scale spatial distribution of organic carbon

In Figures 5-7, the third column of images shows false-colored red-green-blue (RGB) overlay maps of the distribution of three of the most abundant organic carbon functionalities, aliphatic, amide and carboxylic, and O-alkyl carbon. These functionalities are strongly co-located and together their distribution mirrors that of total OC. Organic carbon is present and enhanced both as a matrix surrounding the mineral particles and also in association with specific, discrete mineral particles. Regions where all three functionalities substantially contribute to the

composition of OC appear white in the RGB overlays. These regions tend to match the distribution of discrete mineral particles rather than appearing in the more loosely distributed matrix. These particles are often identifiable as carbonates, although there are regions in samples from NA 3 in particular where the particles bearing high concentrations of all three functionalities are composed of Fe, K, or both (Figure 6). Beyond these high-OC discrete mineral particles, there are regions where one functional group appears brighter than the others. In the surface sample from NA 12, for instance, O-alkyl carbon visibly correlates with carbonate carbon and less strongly with the distribution of the other organic carbon functionalities (Figure 5). In other samples, the functional group appearing most intense varies over <100 nm domains. We note that these images are scaled such that each individual color spans the same intensity range as the others; thus a region appearing particularly enriched in a certain functional group may still contain a large contribution from the others, if the others are relatively more enriched in different areas across the sample.

Pixel-by-pixel correlations derived from the functional group distribution maps allow examination of compositional trends on the micro-scale. Most functionalities display some degree of correlation, and all correlations with Pearson coefficients >0.15 in magnitude are positive. The strongest, most consistent correlation observed is between aliphatic and amide and carboxylic carbon (Figures 5-7, column 4). Pearson correlation coefficients are ≥0.5 for all samples, except the bottom of NA 15 where scatter is high. Amide and carboxylic carbon also correlates strongly with O-alkyl carbon, except for the previously mentioned surface sample from NA 12 where the distribution of O-alkyl carbon mirrors that of carbonate (Figure 5, SI Figure 2). Aliphatic carbon additionally correlates with O-alkyl carbon, although the strength of these correlations is more variable between samples (SI Figures 2-4, SI Table 2). At a few sites,

including the deepest sample from NA 12 and the two mid-depth samples from NA 15, all functional groups correlate strongly with each other. For the NA 12 sample, Pearson correlation coefficients are >0.7, whereas for the NA 15 samples, Pearson correlation coefficients are >0.5 with the exception of the amide and carboxylic and O-alkyl carbon correlations with carbonate, where the strength of the correlation is lowered by the existence of two trendlines (SI Figure 4, SI Table 2).

For carbonate in general, pixels can be divided into two separate correlations, one high in carbonate and the other high in organic functionalities. This trend is particularly noticeable at site NA 15. Conversely, in samples from NA 12, a correlation between amide and carboxylic carbon and carbonate develops with depth. The top sample has no correlation between the two functionalities (Pearson correlation coefficient -0.01), by the mid-depth sample a slight correlation is evident (Pearson correlation coefficient 0.67), and by the deepest sample analyzed the correlation coefficient increases to 0.83 (SI Figure 2, SI Table 2). Such a trend emphasizes the importance of micro-scale examination of carbon composition, as amide and carboxylic carbon and carbonate are inversely correlated in the core from site NA 12 on the bulk scale (Chapter 3).

The two images and carbon stacks generated from sample NA 15 12.575 m below seafloor provide an opportunity to determine the spatial scale over which carbon and mineral-forming elements vary. Both images are 20*20 μm and contain particles of similar sizes and classes (Figure 7). Region 2 contains a greater number of small (<100 nm) K-rich domains as well as a greater amount of organic carbon "matrix." For both, pixel-by-pixel correlations are strong (>0.5) for all functional groups, except for the carbonate correlations described above. Region 1 has less strong correlations between aromatic carbon and other functional groups, but

the correlations are still stronger than those found in many other samples. Their overall similarity suggests that trends observed in a 20*20 μm map scale to the entire 1*1 mm window of prepared sample and potentially the entirety of a sample from a given depth.

4.3.5 Carbon chemical composition and compositional heterogeneity

Principal component and clustering analyses can be applied to STXM-NEXAFS energy stacks in order to identify regions of a sample containing carbon of a significantly different composition than other regions. Here, instead, we quantify differences in chemical composition over the image region by mapping regions enriched in a single functional group or mineral-forming element and comparing the composition of that region to regions relatively enriched in different functional groups. Optical density maps of the individual functional groups were used to extract average spectra representing these "end-member" carbon compositions. For each organic functional group or element map, a "mask" was generated using the top 2/3 most intense pixels and a spectrum extracted from that region, showing the overall composition of carbon in regions where one particular functional group is enriched. Spectra were then fit following a Gaussian deconvolution procedure, assigning peaks within a certain energy range to electronic transitions associated with specific functional groups. Figure 8 shows an example of a raw spectrum, the fit line, and, below, the deconvoluted peaks from NA 15, 12.575 m below seafloor region 1, the "all carbon" mask. Results from peak fitting are summarized in Figure 9, where each column of the heat maps corresponds to a mask and each row shows the relative percent contribution the four most abundant functional groups make to the total fit area for a given mask. Note that relative percent abundances are calculated excluding the carbonate peak (~290.4 eV) from the total fit area as its intensity was the most variable between samples and a function more

of sample lithology than organic carbon cycling. Amide and carboxylic carbon was best fit as two peaks; however, as their transitions overlap, we report here the sum of the two peaks and do not distinguish between the two functionalities.

First, amide and carboxylic carbon is the most abundant functional group in nearly all samples from all sites (Figure 9, SI Figure 5). Relative percent abundance ranges from 17.3% (the manganese mask from the core top sample at NA 12) to 61.2% (the potassium mask from the core top sample at NA 3) and averages 39.6 ± 7.9% (SI Figure 5). O-alkyl carbon is the second most abundant functionality, averaging 19.3 ± 5.0%. These two functional groups are significantly different from each other and from aromatic and aliphatic carbon in terms of average percent abundance. Aromatic and aliphatic carbon comprise 15.9 ± 6.7 and 15.3 ± 3.6% of the total fit area on average, respectively, and are not statistically different from each other (two-tailed t-test, $p<0.05$, SI Figure 5). Excluding an extremely low outlier, O-alkyl carbon ranges from 11.5% in spectra derived from the aromatic mask in the core top sample from NA 3, to 35.1% in the O-alkyl mask of that same sample, demonstrating compositional diversity on the micro-scale. Aliphatic carbon ranges from 28.0% to 7.5%, while aromatic carbon has a broader range, from 4.7% to 44.0% (SI Figure 5). The minimum percent contributions for aliphatic and amide and carboxylic carbon are found in the same spectrum as the maximum relative percent contribution from aromatic carbon, in the manganese mask from the surface sample of NA 12.

For aromatic and O-alkyl carbon, spectra were enriched in the functional group corresponding to the mask the spectrum was extracted from (e.g. aromatic carbon enriched in the spectrum derived from the aromatic mask), though this enrichment is not substantial (Figure 9). This trend holds less true for aliphatic and amide and carboxylic carbon as they are prevalent components across all samples and co-occur.

To assess whether and how geochemical parameters affect carbon composition and distribution, we examined trends between sites, along the lengths of individual cores, and between carbon and mineral particles in individual samples. We note that the surface samples analyzed from each site have the highest variability in composition, with the average value for each functional group having a higher relative standard deviation than down-core samples. Notably, at NA 12, the variability in chemical composition on the micro-scale, within a single sample, is often comparable to or greater than the variability observed along the length of the entire core in the bulk NEXAFS spectra (chapter 2). The variability in O-alkyl carbon across all the masks for an individual sample at NA 12, for instance, ranges from 3-35%, relative to variability in bulk spectra along the entire length of the core of 16%. Likewise, relative standard deviation for amide and carboxylic carbon for all spectra extracted from masks within an individual sample at NA 12 ranges from 4-37%, relative to a relative standard deviation along the entire length of the core in bulk NEXAFS spectra of 7% (see chapter 2).

By taking the average of relative percent contributions of an individual functional group for all spectra from all masks at a given site, we can compare compositional differences between sites. Site NA 3 is significantly depleted in aromatic carbon (average 10.6 ± 3.5 % relative contribution, compared to 15.7 ± 9.1 and 18.0 ± 3.6 % for NA 12 and NA 15, one-way ANOVA, $p = 0.05$, SI Figure 5), while all sites have significantly different average relative percent contributions from amide and carboxylic carbon. NA 3 has the highest amide and carboxylic carbon content, at 45.7 ± 9.3 % relative to 36.4 ± 8.7 and 39.9 ± 4.7% for NA 12 and NA 15 respectively (one-way ANOVA, $p = 0.05$, SI Figure 5). Aliphatic and O-alkyl carbon were statistically the same at all sites.

Finally, the composition of mineral-associated organic carbon can be used to evaluate potential roles for minerals in OC preservation and degradation. While limited by challenges inherent in collecting quality data from particles of varying optical densities, this dataset reveals preliminary trends in composition as a function of mineral-association. First, spectra extracted from both the iron and manganese masks for the surface sample from NA 12 are strongly enriched in aromatic carbon and depleted in aliphatic and amide and carboxylic carbon (Figure 9). In the surface sample from site NA 3, the inverse is true; aromatic carbon is depleted in spectra derived from iron and manganese masks while aliphatic and amide and carboxylic carbon are slightly enriched but still within the range found in all spectra derived from masks of organic functional groups. At site NA 15, likewise, spectra derived from iron, manganese, and potassium maps contain relatively higher percent contributions from amide and carboxylic carbon. Thus, site lithology and the presence of specific minerals may influence the diversity in chemical composition of OC.

4.4 Discussion

4.4.1 Stoichiometry of organic matter and degradation

By contrasting OC concentration and composition in sediment cores from geochemically distinct sites, we can investigate geochemical mechanisms determining the balance between OC preservation and degradation in these environments. Concentrations of organic carbon and nitrogen do scale with sediment oxygenation state, typically being higher in the anoxic and suboxic settings (Figure 2). However, oxygenation is not the sole control on sediment OC and N content. The lowest concentrations measured were toward the bottom of the cored interval at site IODP 1231. Sites SPG 2 and 3 have older sediments at core bottom and, as these cores are oxic,

oxygen exposure times at these sites are likely on the order of millions of years greater than for IODP site 1231. Thus, oxygenation does not fully explain extent of carbon degradation. This observation lies in contrast to previous studies where oxygen exposure time effectively explains extent of degradation in younger sediments that experience a redox gradient (Cowie *et al.*, 1995; Hartnett *et al.*, 1998; Arnarson & Keil, 2007), allowing for anoxic preservation of carbon by electron acceptor limitation. However, we posit that for old sediments (>~3 Ma) that have been continually exposed to oxygen, other mechanisms must provide protection against remineralization and may, in fact, offer greater protection than at sites such as IODP 1231 where shifts in microbial community and strong chemical gradients may allow a wide variety of metabolisms to remain viable. For instance, mineral-based protection of OC may only account for a small fraction of protected carbon in OC-rich anoxic sediments, but preserve a larger fraction of OC in oxic sediments.

Disproportional decreases in OC and N with depth along the core also provides insight into organic matter degradation pathways in these systems (Figure 2). The SPG sites where the decrease in OC was proportional to that of N (SPG 1, 9, 6, and 10) have the highest downward O_2 flux at 1.5 m below seafloor (D'Hondt *et al.*, 2009, no data exist for SPG 6). Oxygen penetration and availability may thus contribute to equal remineralization of OC and N. The other two sites where the decrease in OC was proportional to that of N were the IODP site 1231 holes B and E (Figure 2). Again, this trend may be a function of the variety of active metabolisms contributing to near-complete remineralization or, conversely, may relate to an upward flux of oxygen from the basalt basement (D'Hondt *et al.*, 2011), or sediment age.

The other factor that distinguishes sites with a constant stoichiometry of degradation from those where N decreased much less than OC is sedimentation rate. Sedimentation rates at NA

oxic sites and site SPG 12 are not substantially higher than at site SPG 6, but rates in the North Atlantic are overall higher and the oxygen flux at depth (not calculated) likely lower. Calculated degradation rates correlate with initial OC content and sediment age; these parameters are partially a function of sedimentation rate (SI Table 1, SI Figure 1). These correlations are not wholly unexpected; higher concentrations should drive reaction rates while older sediments will likely host both lower concentrations of OC as well as less bioavailable OC. However, these correlations seem less strongly driven by oxygen exposure than might be expected, with no correlations existing between oxygen and degradation rates in the deeper intervals. Regardless of underlying mechanism, these data suggest decoupling of OC and N processing and that N may be retained in the organic pool relative to C.

The stoichiometry of organic matter and of organic matter degradation in these old, carbon-poor sediments is also unique and does not vary clearly with sediment oxygenation. C/N values at all sites are exceptionally low, averaging 4.0 ± 2.0 for all depths at all sites (Figure 2). Values tend to be higher at anoxic sites and lowest at the oxic sites. Redfield biomass has a C/N of 6.625, while protein, the most N-rich biomolecule, has a C/N of 3.85. The higher values found at all sites in this study fall within the range expected for marine algal organic matter (4-10, Meyers 1994), but while degradation typically increases C/N due to preferential utilization of proteinaceous material (Meyers, 1997), here C/N decreases with depth. Previous work has attributed the low C/N values found in sediments and soils to adsorption of ammonia produced by degradation of organic nitrogen to clays (Meyers, 1997) or analytical uncertainty (Ziebis *et al.*, 2012). As discussed in Chapter 3, however, we believe the contribution from ammonia to be less than previous estimates (Muller, 1977) as C/N values do not correlate with clay content and as geochemical and metagenomic data both suggest that ammonia produced by organic matter

degradation undergoes nitrification in oxic SPG sediments (D'Hondt *et al.*, 2009; Tully & Heidelberg, 2016).

An organic carbon pool dominated by intact proteins being recycled in and out of biomass could contribute to the low C/N observed here. Single-cell genomic as well as metagenomic analyses demonstrate the metabolic potential for protein degradation and uptake in the deep subsurface (Lloyd *et al.*, 2013; Tully & Heidelberg, 2016). Protein content at oxic sites does appear to reach some sort of steady-state with depth along the cores, (Figure 4) which in Chapter 3 was interpreted as evidence of equilibrium between extracellular intact proteins, proteins adsorbed to mineral surfaces, and proteins in biomass. In Chapter 3, extractable proteins quantified were primarily extracellular; if the total measured protein content were in biomass there would be 4 orders of magnitude more cells than actually found. However, extractable proteins were found to account for <<1% of total OC, making it unlikely that intact proteins exclusively fuel heterotrophy or control C/N values. Chapter 2 also describes OC at oxic sites, as determined by bulk-scale NEXAFS, to consist primarily of amide and carboxylic carbon in a scaffolding of aliphatic/alicyclic and O-alkyl carbon. This material may thus be proteinaceous in origin and reflect a degraded, N-enriched, recalcitrant sink for the intact proteins described above.

By comparing the C/N of bulk sedimentary organic matter to the calculated C/N of degradation, we find further evidence to affirm the interpretation made in Chapter 2 that, in carbon-poor sediments, carbon may be preferentially utilized relative to nitrogen. For the majority of sites, C/N of degradation in the surface interval is substantially higher than in the deep interval, where it declines to match the C/N of bulk material (Figure 3). If this C/N of degradation parameter is interpreted as a measure of what microorganisms are utilizing,

microbes preferentially consume or respire OC relative to N in the surface interval and, as organic matter becomes even more limited in the deep interval, transition to using the entirety of what is present, causing the C/N of degradation to mirror the C/N of the bulk organic matter. This trend is independent of site type; while suboxic site SPG 12 is an outlier and full data are only available for a single anoxic site, it appears that this stoichiometry of degradation is more a signature of carbon-poor environments than a function of sediment oxygenation and oxygen exposure time. Further, it is possible that the suboxic sites are not truly outliers, but rather that the chemical gradient at those sites allows for higher metabolic activity relative to other sites; indeed, cell counts are marginally higher at suboxic site SPG 12 relative to the other SPG sites (D'Hondt *et al.*, 2011). It remains plausible that up to 50% of measure N derives from ammonia fixed in clays, as discussed more extensively in Chapter 3. Subtracting this conservative estimate of fixed and exchangeable N from total N values to achieve organic N results in doubled C/N values. In the deep interval, C/N of bulk material would then fall within a more reasonable range for N-rich biological molecules, while in the surface interval C/N values approach Redfield biomass. However, such a shift does not alter interpretation of the C/N of degradation, which would also double and still implicate preferential utilization of organic carbon relative to nitrogen.

Yet, D'Hondt *et al.* (2009) argue that production of nitrate at depth and its positive flux towards the sediment-water interface at SPG sites implies that the oxidation of organic nitrogen rather than carbon supports a greater proportion microbial life in these environments. Tully and Heidelberg (2016) observe that while nitrification in these sediments is likely linked to autotrophic carbon fixation, it seems inefficient for those same microbes, or for any heterotrophic organisms, to then uptake and reduce that nitrate for biomass. Beyond measures of

genomic potential, however, identification and quantification of active metabolisms has proven difficult due to slow reaction rates. In one study of metabolic activity in anoxic, high OC sediments (1.2%) spiked with labeled ^{13}C and ^{15}N compounds, N was preferentially taken up by cells relative to C; however, ^{15}N assimilation was primarily from ammonium with glucose, pyruvate, and amino acids also stimulating growth but not methane (Morono *et al.*, 2011).

Thus, the results of Morono *et al.* (2011) do not directly contradict the findings of this study, but rather reflect environmental redox state and different operative OC-protection mechanisms (e.g. anoxia), emphasizing that pelagic sediments represent a functionally different environment in need of additional investigation.

Production of hydrogen by radiolysis of water following radioactive decay of trace radioactive elements in mineral grains may also provide an energy source (D'Hondt *et al.*, 2009). This process, however, would be entirely cryptic, with the oxygen required to re-oxidize the hydrogen equal to the oxygen produced by the initial reaction (Fischer *et al.*, 2009). Conversely, hydroxyl radicals produced in the hydrolysis reaction may react with organic matter to produce more bioavailable low molecular weight compounds (e.g. carbonyls and carboxylic acids). Hydroxyl radicals are powerful because they are non-selective and reactive with a wide range of organic compounds (Buxton *et al.*, 1988). However, they react especially rapidly with aromatic and alkene compounds (Buxton *et al.*, 1988; similar to Johnson *et al.*, 2015), which are not observed in high concentrations in oxic sediments (Chapter 2, Figure 9, SI Figure 5). These radicals may thus be quenched by other reactions given the low availability of organic reactant.

The stoichiometry of sedimentary organic matter is therefore constrained by several competing processes whose precise rates in these environments will need to be investigated

further. First, understanding the relative rates of adsorption, diffusion, and nitrification reactions will be important to fully eliminating ammonia adsorbed to clays as an explanation for elevated N. Secondly, given the excess of nitrate and dearth of organic compounds in these environments, it will be important to understand the relative energy costs of assimilating and reducing nitrate relative to solely using organic nitrogen in organic matter as a source of N in biomolecules. Based on the data presented in this study, we posit that measured C/N values are real and reflect preferential utilization of carbon in organic compounds relative to nitrogen. As this pattern holds between all sites, we further hypothesize that in old, carbon-poor sediments, oxygen exposure time is not an effective metric for carbon burial. Rather, all sites seem to sustain metabolic activity and slow carbon degradation via interactions between heterotrophs and chemolithoautotrophs, so long as some form of electron acceptor is present.

4.4.2 Spatial distribution and composition of organic carbon on the micro scale

Organic carbon is present both as discrete particles and, in some samples, as a matrix surrounding the larger mineral particles. While discrete particles bearing high concentrations of organic carbon are often identifiable as carbonates, OC also associates with Fe-rich and K-rich particles in other samples (Figures 5-7). Matrix-like OC may correlate slightly with K-rich domains smaller than could be spatially resolved in these samples (<50-100 nm), suggesting that OC associates with aluminosilicate clays. This trend would match previous observations of mineral-organic interactions, finding that, in anoxic coastal settings, clay and opal content predicted OC concentration though the slope of the trend line varied by clay type, further suggesting a chemical rather than physical mechanism of adsorption (Ransom *et al.*, 1998). Unfortunately, carbon spectra from regions with a high density of mineral grains are often

saturated due to variability in particle density, precluding determination of chemical composition and complete evaluation of mechanisms of mineral-OC associations.

Nonetheless, we note that OC was much less tightly associated with mineral particles than hypothesized (Figures 5-7). Previous bulk-scale research finds that in a wide range of environments (estuaries, coastal, pelagic, anoxic, sulfidic) ~20% of OC was extracted simultaneously with iron oxides (Lalonde *et al.*, 2012), suggesting a preferential association of OC with iron oxide mineral surfaces. On century to millennia timescales, Arnarson and Keil (2007) observe that 50% of OC was adsorbed to mineral surfaces in denser sediment fractions, with 22% preserved in diatom frustules. They contrast that finding with data from sediments years to decades old, where OC exists in mineral-organic aggregates (Arnarson & Keil, 2007), based on density fractionation followed by bulk scale X-ray photoelectron spectroscopy analysis. In another experiment utilizing density separation of sediments to roughly fractionate samples by mineral class, OC associated with dense, fine-grained mineral phases was N- and ^{13}C-enriched and of primarily marine origin relative to OC associating with other density fractions in Washington coast sediments (Dickens *et al.*, 2006). This chemical selectivity was interpreted as evidence for mineral-based protection via adsorption; no obvious trends in mineral-OC associations implicating mineral-based protection were observed in Mexican margin sediments, however, where detected OC was also of marine origin (Dickens *et al.*, 2006). Heckman *et al.* (2013) also observe that the densest fractions of soils host organics enriched in proteins, lipids, and N-bearing compounds relative to other soil density fractions.

While demonstrating an association between mineral and OC and hinting at an underlying chemical mechanism, these studies do not define the nature of the association. It is possible that STXM images in this study show relatively large mineral-OC aggregates (e.g. >1

μm^2), where lack of direct correlation does not indicate lack of interaction. However, this interpretation is unlikely. In more carbon-rich systems, aggregation is viable and we might expect the type of structuring described in Kleber *et al.* (2007), where an inner layer of molecules forms inner-sphere complexes with the mineral surfaces, preferentially selecting for carboxyl and amide groups, followed by a mid-layer of hydrophobic compounds, and an outer layer of organic molecules and metal cations bound together via electrostatic attractions. Aging and degradation will strip away these layers, leaving only the tightly-sorbed inner layer. Compositionally, we do observe high proportions of amide and carboxylic carbon (Figure 9) that likely derive from proteinaceous material, but that enrichment is general and not specifically correlated with mineralogy. Spectra derived from masks of mineral-forming elements do occasionally have extremes in carbon composition relative to spectra derived from masks of organic functionalities (e.g. surface sample of NA 12, Figure 9), but for the spectra successfully extracted and analyzed, trends are not consistent by mineral type and do not apply to all samples (e.g. NA 15, minerals do not induce compositional extremes, Figure 9).

Other research examining mineral-OC interactions on the micro-scale within more carbon-rich environments finds much closer correlations between mineral surfaces and organic carbon and clearer compositional trends. For biotic Mn oxides precipitated in brackish estuarine waters, the majority of OC in mineral aggregates was directly co-located with the minerals (Estes *et al.*, 2016). Biomineralizing iron-oxidizing bacteria likewise form minerals containing OC templates and additionally adsorb OC from the environment (Chan *et al.*, 2010; Bennett *et al.*, 2014), resulting in very strong spatial correlation between mineral particles and OC. Iron-carbon aggregates in a hydrothermal plume exhibit a more carbon-matrix-like effect, with Fe(II) adsorbed or complexed with OC (Toner *et al.*, 2009); however, those samples have OC:Fe+Mn

molar ratios of ~2.69—17.8 (Estes *et al.*, 2016, calculated from Toner *et al.*, 2009;), far exceeding the OC content observed in pelagic sediments.

Ultimately, mineralogy does not determine the spatial distribution of OC on the microscale. We therefore examine spatial variation in chemical composition in an attempt to determine both average composition and recalcitrance of pelagic OC. A majority of studies employing STXM-NEXAFS to examine carbon composition find statistically different chemical compositions in morphologically distinct regions of samples (Brandes *et al.*, 2004; Lehmann *et al.*, 2008; Solomon *et al.*, 2012; Knopf *et al.*, 2014). These studies emphasize the chemical heterogeneity of carbon on a very small spatial scale. In a study on litter decomposition in soils, organics of distinct chemical compositions were separated spatially, ranging from fungal hyphae to iron oxides hosting lipids and proteins that were interpreted as a microbial residue (Keiluweit *et al.*, 2012). In their study, and for biogenic Mn oxides documented by Estes *et al.* (2016), aliphatic and amide carbon intermixed on the mineral surface, while Liu *et al.* (2013) observed lipids and proteins in separate 100-200 nm^2 domains across the surface of goethite following reaction with extracellular polymeric substances. These separate domains more closely match the distributions observed here; OC is generally co-located, but with 50-100 nm^2 or less sized domains where one functional group appears more predominant than others (Figure 5-7). This observed scale matches well with what might be predicted for material of proteinaceous origin; with an average protein volume of 25 nm^3 (Phillips *et al.*, 2009), observing variability of composition of domains within the same magnitude suggests that these variations are real and rooted in real chemical variations. Indeed, for simpler systems, STXM-NEXAFS can be applied to mapping out the distributions of specific peptides and proteins (Stewart-Ornstein *et al.*, 2007).

In contrast to previous studies, principal component and cluster analyses do not identify significantly different carbon compositions that appear in spatially distinct regions of samples (SI Figure 6). These statistical techniques, however, function best when identifying major differences in spectra and where chemically distinct compounds are not co-occurring (Brandes *et al.*, 2004; Lehmann *et al.*, 2008; Keiluweit *et al.*, 2012; Solomon *et al.*, 2012; Knopf *et al.*, 2014), in contrast to observations in this study. Here, the variation in relative proportions of functional groups is less but there are still quantifiable differences in carbon composition across samples. To quantify these differences in lieu of cluster analysis, we generated "masks" based on the distributions of organic carbon functional groups as well as mineral-forming elements. NEXAFS spectra were then extracted from the regions defined by those masks, e.g. where that functional group or element was enriched. Using Gaussian deconvolution, we fit spectra and determine end member compositions as shown in Figure 9.

Across all samples, amide and carboxylic carbon was the predominant functional group, followed by O-alkyl carbon, and then closely followed by aromatic and aliphatic carbon. Across all samples, amide and carboxylic carbon varied the least (average relative standard deviation of 12%, range from 4 to 37%, SI Figure 5), as compounds appear evenly enriched in this functionality. This result is supported by findings from Chapter 3, where in bulk NEXAFS spectra amide and carboxylic carbon was also the most abundant functionality and the one that varied least with depth along the length of each core. O-alkyl carbon is present in approximately the same proportion as in bulk NEXAFS spectra from Chapter 3, and varies an average of 17% between different masks within a sample (range 2 to 38%, SI Figure 5). STXM-NEXAFS spectra have on average a greater content of aliphatic and aromatic carbon at the expense of amide and carboxylic carbon than the bulk spectra described in Chapter 3. Interestingly, this trend is not

simply a function of sediment oxygenation as suboxic site NA 3 has the lowest average aromatic content and NA 12 has the lowest amide and carboxylic content as quantified by STXM-NEXAFS, despite being the only site analyzed here also analyzed in the bulk spectra. Aromatic content is the most variable within a given STXM-NEXAFS sample, varying by 5-84% between masks from a single sample with an average of 22%. Finally, aliphatic carbon varies by an average of 16% between spectra derived from masks for a given sample (SI Figure 5).

By contrasting these "end member" carbon compositions derived from function group and element masks, it appears that there is spatial diversity in the chemical composition of OC on the microscale, even if the variation is only by 10-20%. These results align with the composition of bulk carbon described in Chapter 3 as amide and carboxylic carbon in a scaffolding of O-alkyl and aliphatic carbon; here, O-alkyl, aliphatic, and aromatic carbon all act as variably present side chains or, perhaps, linkages between co-polymerized compounds. OC stored in pelagic sediments may not be comprised of the same range of biomolecules as particles (Brandes *et al.*, 2004; Toner *et al.*, 2009; Knopf *et al.*, 2014), terrestrial soil systems (Lehmann *et al.*, 2008; Keiluweit *et al.*, 2012; Solomon *et al.*, 2012), or biominerals (Chan *et al.*, 2010; Bennett *et al.*, 2014; Estes *et al.*, 2016), but they do display compositional variability on the microscale (in terms of relative standard deviation in the percent abundance of a functional group between masks) that is often equivalent to variability along the length of the entire core in the bulk spectra within Chapter 3. Thus, on these million-year time scales, increased age and degradation do not seem to alter or eliminate particular compound classes.

4.5 Conclusions

This work emphasizes the uniqueness of pelagic sediments relative to better-studied coastal environments. Pelagic sediments account for nearly half the world sediment volume (Hay *et al.*, 1988) but their inaccessibility and trace carbon content historically made them difficult to study. Here, we demonstrate that carbon cycling in these environments does not strictly follow expectations and interpret our findings as they pertain to determining the limits of microbial life as well as the potential for organic carbon preservation on geological time scales. In this work, we examine the content and composition of organic carbon (OC) in pelagic sediments over a range of spatial, temporal, and geochemical gradients with the goal of identifying the primary geochemical factors that control the balance between OC preservation and degradation. These sites include South Pacific and North Atlantic gyre sediments that remain oxic to basement, suboxic sites with redox gradients extending over the course of tens of meters, and sites that are anoxic but not sulfidic due to reduction of redox-sensitive metals such as iron and manganese. We document some of the lowest OC and nitrogen (N) concentrations measured globally, yet are still also able to quantify a pool of extracellular, intact proteins <<1% of the total OC. While OC and N concentrations towards core top do scale with sediment oxygenation, concentrations in the deep subsurface are more similar. Degradation rates are extremely slow such that OC depth profiles appear stable.

In these sediments, OC and N concentrations, C/N ratio of preserved organic matter, and the C/N of degradation calculated from changes in concentration and sediment age are similar between all sites. We interpret this similarity as evidence that, for old, carbon-poor sediments that likely comprise the majority of the ocean floor, oxygen exposure time is a less useful indicator of carbon content and composition than it is for younger, carbon-rich coastal and

margin sediments. Instead, we propose that the content and composition of OC in these environments is a signature of persistent heterotrophic metabolisms despite carbon limitation that pares an initial OC pool in the surface interval down to an even barer minimum. Chemolithoautotrophs are present (Tully & Heidelberg, 2016), as partially indicated by the accumulation of nitrate, and may supplement the starving heterotrophic majority by fixing additional carbon; however, the continued slow degradation of OC along the length of the core implicates present, active heterotrophs in generating the observed content and composition of OC.

The extremely low C/N values of sedimentary organic carbon, coupled with the elevated C/N of degradation in the surface interval and the high dissolved nitrate concentrations, imply that organisms are more carbon- than nitrogen-limited and may preferentially utilize C over N from the pool of organic matter. The amide and carboxylic-rich composition of OC as measured by both bulk NEXAFS (Chapter 3) and STXM-NEXAFS affirms this interpretation, as preferential utilization of C would be a mechanism for generating such N-rich compounds.

We apply STXM-NEXAFS spectroscopy to further investigate how factors such as lithology or oxygenation may influence OC content and composition on the microscale. This technique has never been employed in sediments and is advantageous over other analytical methods for determining OC chemical composition as it is non-destructive, non-invasive and requires no preparative steps that might alter the observed composition or associations between molecules. In contrast to previous studies on terrestrial systems, marine particles, aerosols, and biominerals, we observe no clear correlations between the distribution of organic carbon and mineral particles despite the hypothesis that mineral-based protection may be an important variable in carbon preservation for old, oxic sediments. Additionally, while other studies

employing STXM-NEXAFS on environmental samples identify a greater diversity of compound classes within a single sample, we nonetheless observe compositional variability across each sample. This variability indicates that a diversity of compounds is present, despite the paradigm that this old OC is "recalcitrant." Microorganisms living in this environment will still encounter a range of substrates. Evidence that these microbes are capable of consuming proteins (Lloyd *et al.*, 2013; Tully & Heidelberg, 2016) is supplemented by quantification of intact proteins, while Tully *et al.* (2016) demonstrate the genomic potential for organisms in the South Pacific to metabolize oligosaccharides—a compound class that bears some semblance to the composition of OC (dominated by amide and carboxylic as well as O-alkyl carbon) observed here. Further microbiological studies, including isolation and culture studies, metagenomics, and metatranscriptomics, will therefore be important to determining whether proteins with specific annotations (e.g. peptidases) are also capable of degrading the more recalcitrant, proteinaceous material observed here.

The variability in chemical composition within a single sample on the microscale (<50 μm^2) as determined here by STXM-NEXAFS is often equal to or greater than the variability in bulk NEXAFS spectra along the entire length of a given core (Chapter 2). This finding could be interpreted as affirming non-selective degradation (Hedges *et al.*, 2001; Brandes *et al.*, 2004) on the one hand, as all particle types are measurable at all depths, but we contrast this conclusion with the observed stoichiometry of degradation and overall carbon composition unlike any identifiable surface molecule. It seems impossible to generate such a composition without selective degradation at some stage. Instead, we posit that for the deeper sediment intervals, where the C/N of degradation matches the C/N of bulk sedimentary organic matter, microorganisms are utilizing exactly the organic matter available to them, resulting in non-

selective preservation on geological time scales of the diversity of compounds that survive the traverse from the surface ocean to shallow sediments to the deep subsurface.

4.6 References

Arnarson TS, Keil RG (2007) Changes in organic matter-mineral interactions for marine sediments with varying oxygen exposure times. *Geochimica et Cosmochimica Acta* **71**, 3545–3556.

Bennett SA, Toner BM, Barco R, Edwards KJ (2014) Carbon adsorption onto Fe oxyhydroxide stalks produced by a lithotrophic iron-oxidizing bacteria. *Geobiology*.

Biddle JF, Fitz-Gibbon S, Schuster SC, Brenchley JE, House CH (2008) Metagenomic signatures of the Peru Margin subseafloor biosphere show a genetically distinct environment. *Proceedings of the National Academy of Sciences of the United States of America* **105**, 10583–10588.

Brandes J a., Lee C, Wakeham S, Peterson M, Jacobsen C, Wirick S, Cody G (2004) Examining marine particulate organic matter at sub-micron scales using scanning transmission X-ray microscopy and carbon X-ray absorption near edge structure spectroscopy. *Marine Chemistry* **92**, 107–121.

Buxton G V., Greenstock CL, Helman WP, Ross AB (1988) Critical Review of rate constants for reactions of hydrated electrons, hydrogen atoms and hydroxyl radicals (·OH/·O− in Aqueous Solution. *Journal of Physical and Chemical Reference Data* **17**, 513--886.

Chan CS, Fakra SC, Emerson D, Fleming EJ, Edwards KJ (2010) Lithotrophic iron-oxidizing bacteria produce organic stalks to control mineral growth: implications for biosignature formation. *The ISME Journal* **5**, 717–727.

Cowie GL, Hedges JI, Prahl FG, Lange GJ de (1995) Elemental and major biochemical changes across an oxidation front in a relict turbidite: An oxygen effect. *Geochimica et Cosmochimica Acta* **59**, 33–46.

D'Hondt S, Abrams LJ, Anderson R, Dorrance J, Durbin A, Ellett L, Ferdelman T, Fischer J, Forschner S, Fuldauer R, Goldstein H, Graham D, Griffith W, Halm H, Harris R, Harrison B, Hasiuk F, Horn G, Kallmeyer J, Lever M, Meyer J, Morse L, Moser C, Murphy B, Nordhausen A, Parry L, Pockalny R, Puschell A, Rogers J, Schrum H, Smith DC, Soffientino B, Spivack AJ, Stancin A, Steinman M, Walczak P (2011) KNOX-02RR: drilling site survey--life in subseafloor sediments of the South Pacific Gyre. In: *Proceedings of the Integrated Ocean Drilling Program.*

D'Hondt S, Inagaki F, Zarikian CA, Abrams LJ, Dubois N, Engelhardt T, Evans H, Ferdelman T, Gribsholt B, Harris RN, Hoppie BW, Hyun J-H, Kallmeyer J, Kim J, Lynch JE, McKinley CC, Mitsunobu S, Morono Y, Murray RW, Pockalny R, Sauvage J, Shimono T, Shiraishi F, Smith DC, Smith-Duque CE, Spivack AJ, Steinsbu BO, Suzuki Y, Szpak M, Toffin L, Uramoto G, Yamaguchi YT, Zhang G, Zhang X-H, Ziebis W (2015) Presence of oxygen and aerobic communities from sea floor to basement in deep-sea sediments. *Nature Geoscience* **8**, 299–304.

D'Hondt S, Jørgensen BB, Miller DJ, Batzke A, Blake R, Cragg B a, Cypionka H, Dickens GR, Ferdelman T, Hinrichs K-U, Holm NG, Mitterer R, Spivack A, Wang G, Bekins B, Engelen B, Ford K, Gettemy G, Rutherford SD, Sass H, Skilbeck CG, Aiello IW, Guèrin G, House CH, Inagaki F, Meister P, Naehr T, Niitsuma S, Parkes RJ, Schippers A, Smith DC, Teske A, Wiegel J, Padilla CN, Acosta JLS (2004) Distributions of microbial activities in deep subseafloor sediments. *Science (New York, N.Y.)* **306**, 2216–21.

D'Hondt S, Spivack AJ, Pockalny R, Ferdelman TG, Fischer JP, Kallmeyer J, Abrams LJ, Smith DC, Graham D, Hasiuk F, Schrum H, Stancin AM (2009) Subseafloor sedimentary life in the South Pacific Gyre. *Proceedings of the National Academy of Sciences of the United States of America* **106**, 11651–11656.

Dickens AF, Baldock J a., Smernik RJ, Wakeham SG, Arnarson TS, Gélinas Y, Hedges JI (2006) Solid-state 13C NMR analysis of size and density fractions of marine sediments: Insight into organic carbon sources and preservation mechanisms. *Geochimica et Cosmochimica Acta* **70**, 666–686.

Divins DL (2003) Total Sediment Thickness of the World's Oceans & Marginal Seas.

Durbin AM, Teske A (2011) Microbial diversity and stratification of South Pacific abyssal marine sediments. *Environmental Microbiology* **13**, 3219–3234.

Durbin AM, Teske A (2012) Archaea in organic-lean and organic-rich marine subsurface sediments: An environmental gradient reflected in distinct phylogenetic lineages. *Frontiers in Microbiology* **3**, 1–26.

Ehrenreich A, Widdel F (1994) Anaerobic Oxidation of Ferrous Iron by Purple Bacteria, a New-Type of Phototrophic Metabolism. *Applied and Environmental Microbiology* **60**, 4517–4526.

Estes ER, Andeer PF, Nordlund D, Wankel SD, Hansel CM (2016) Biogenic manganese oxides as reservoirs of organic carbon and proteins in terrestrial and marine environments. *Geobiology*.

Fischer JP, Ferdelman TG, Hondt SD, Røy H, Wenzhöfer F (2009) Oxygen penetration dep into the sediments of the South Pacific gyre. *Biogeosciences* **6**, 1467–1478.

Hartnett HE, Keil RG, Hedges JI, Devol AH (1998) Influence of oxygen exposure time on organic carbon preservation in continental margin sediments. *Nature* **391**, 572–575.

Hay WW, Sloan Ii JL, Wold CN (1988) Mass/Age Distribution and Composition of Sediments on the Ocean Floor and the Global Rate of Sediment Subduction. *Journal of Geophysical Research* **93940**, 933–14.

Heckman K, Grandy a. S, Gao X, Keiluweit M, Wickings K, Carpenter K, Chorover J, Rasmussen C (2013) Sorptive fractionation of organic matter and formation of organo-hydroxy-aluminum complexes during litter biodegradation in the presence of gibbsite. *Geochimica et Cosmochimica Acta* **121**, 667–683.

Hedges J, Eglinton G, Hatcher P, Kirchman D., Arnosti C, Derenne S, Evershed R., Kögel-Knabner I, Leeuw J. de, Littke R, Michaelis W, Rullkötter J (2000) The molecularly-uncharacterized component of nonliving organic matter in natural environments. *Organic Geochemistry* **31**, 945–958.

Hedges JI, Baldock J a, Gélinas Y, Lee C, Peterson M, Wakeham SG (2001) Evidence for non-selective preservation of organic matter in sinking marine particles. *Nature* **409**, 801–4.

Hertkorn N, Benner R, Frommberger M, Schmitt-Kopplin P, Witt M, Kaiser K, Kettrup A, Hedges JI (2006) Characterization of a major refractory component of marine dissolved organic matter. *Geochimica et Cosmochimica Acta* **70**, 2990–3010.

Johnson K, Purvis G, Lopez-Capel E, Peacock C, Gray N, Wagner T, März C, Bowen L, Ojeda

J, Finlay N, Robertson S, Worrall F, Greenwell C (2015) Towards a mechanistic understanding of carbon stabilization in manganese oxides. *Nature Communications* **6**, 7628.
Jørgensen BB, Marshall IPG (2016) Slow Microbial Life in the Seabed. *Annual Review of Marine Science* **8**, 311–332.
Jorgensen SL, Hannisdal B, Lanzen A, Baumberger T, Flesland K, Fonseca R, Ovreas L, Steen IH, Thorseth IH, Pedersen RB, Schleper C (2012) Correlating microbial community profiles with geochemical data in highly stratified sediments from the Arctic Mid-Ocean Ridge. *Proceedings of the National Academy of Sciences* **109**, E2846–E2855.
Jørgensen SL, Thorseth IH, Pedersen RB, Baumberger T, Schleper C (2013) Quantitative and phylogenetic study of the Deep Sea Archaeal Group in sediments of the Arctic mid-ocean spreading ridge. *Frontiers in Microbiology* **4**, 1–11.
Kallmeyer J, Pockalny R, Adhikari RR, Smith DC, D'Hondt S (2012) Global distribution of microbial abundance and biomass in subseafloor sediment. *Proceedings of the National Academy of Sciences* **109**, 16213–16216.
Keiluweit M, Bougoure JJ, Zeglin LH, Myrold DD, Weber PK, Pett-Ridge J, Kleber M, Nico PS (2012) Nano-scale investigation of the association of microbial nitrogen residues with iron (hydr)oxides in a forest soil O-horizon. *Geochimica et Cosmochimica Acta* **95**, 213–226.
Kleber M, Nico PS, Plante A, Filley T, Kramer M, Swanston C, Sollins P (2011) Old and stable soil organic matter is not necessarily chemically recalcitrant: implications for modeling concepts and temperature sensitivity. *Global Change Biology* **17**, 1097–1107.
Kleber M, Sollins P, Sutton R (2007) A conceptual model of organo-mineral interactions in soils: self-assembly of organic molecular fragments into zonal structures on mineral surfaces. *Biogeochemistry* **85**, 9–24.
Knopf DA, Alpert PA, Wang B, Brien REO, Kelly ST, Laskin A, Gilles MK, Moffet RC (2014) Journal of Geophysical Research : Atmospheres 365–381.
Lalonde K, Mucci A, Ouellet A, Gélinas Y (2012) Preservation of organic matter in sediments promoted by iron. *Nature* **483**, 198–200.
Lehmann J, Solomon D, Kinyangi J, Dathe L, Wirick S, Jacobsen C (2008) Spatial complexity of soil organic matter forms at nanometre scales. *Nature Geoscience* **1**, 238–242.
Lever MA, Rogers KL, Lloyd KG, Overmann J, Schink B, Thauer RK, Hoehler TM, Jørgensen BB (2015) Life under extreme energy limitation: A synthesis of laboratory- and field-based investigations. *FEMS Microbiology Reviews* **39**, 688–728.
Liu X, Eusterhues K, Thieme J, Ciobota V, Höschen C, Mueller CW, Küsel K, Kögel-Knabner I, Rösch P, Popp J, Totsche KU (2013) STXM and NanoSIMS investigations on EPS fractions before and after adsorption to goethite. *Environmental science & technology* **47**, 3158–66.
Lloyd KG, Schreiber L, Petersen DG, Kjeldsen KU, Lever M a, Steen AD, Stepanauskas R, Richter M, Kleindienst S, Lenk S, Schramm A, Jørgensen BB (2013) Predominant archaea in marine sediments degrade detrital proteins. *Nature* **496**, 215–8.
Lomstein BA, Langerhuus AT, D'Hondt S, Jørgensen BB, Spivack AJ (2012) Endospore abundance, microbial growth and necromass turnover in deep sub-seafloor sediment. *Nature* **484**, 101–104.
Mao J, Tremblay L, Gagné JP (2011) Structural changes of humic acids from sinking organic matter and surface sediments investigated by advanced solid-state NMR: Insights into sources, preservation and molecularly uncharacterized components. *Geochimica et Cosmochimica Acta* **75**, 7864–7880.
Meyers PA (1994) Preservation of elemental and isotopic source identification of sedimentary

organic matter. *Chem. Geology* **114**, 289–302.
Meyers PA (1997) Organic geochemical proxies of paleoceanographic, paleolimnologic, and paleoclimatic processes. *Organic Geochemistry* **27**, 213–250.
Morono Y, Terada T, Nishizawa M, Ito M, Hillion F, Takahata N, Sano Y, Inagaki F (2011) Carbon and nitrogen assimilation in deep subseafloor microbial cells. *Proceedings of the National Academy of Sciences of the United States of America* **108**, 18295–300.
Muller PJ (1977) C/N ratios in Pacific deep sea sediments effect on inorganicammonium and organic nitrogen compounds sorbed by clays. *Geochimica Et Cosmochimica Acta* **41**, 765–776.
Müller RD, Sdrolias M, Gaina C, Roest WR (2008) Age, spreading rates, and spreading asymmetry of the world's ocean crust. *Geochemistry, Geophysics, Geosystems* **9**, 1–19.
Murray RW, Spivack AJ, D'Hondt S, Pockalny R (2014) *R/V Knorr Cruise 223 Report.*
Orcutt BN, Sylvan JB, Knab NJ, Edwards KJ (2011) Microbial ecology of the dark ocean above, at, and below the seafloor. *Microbiology and molecular biology reviews : MMBR* **75**, 361–422.
Phillips R, Kondev J, Theriot J (2009) *Physical Biology of the Cell.* Garland Science, New York.
Picard A, Ferdelman TG (2011) Linking microbial heterotrophic activity and sediment lithology in oxic, oligotrophic sub-seafloor sediments of the north atlantic ocean. *Frontiers in microbiology* **2**, 263.
Ransom B, Kim D, Kastner M, Wainwright S (1998) Organic matter preservation on continental slopes: importance of mineralogy and surface area. *Geochimica et Cosmochimica Acta* **62**, 1329–1345.
RCore T (2015) R: A language and environment for statistical computing.
Roy H, Kallmeyer J, Adhikari RR, Pockalny R, Jorgensen BB, D'Hondt S (2012) Aerobic Microbial Respiration in 86-Million-Year-Old Deep-Sea Red Clay. *Science* **336**, 922–925.
Russell JA, León-Zayas R, Wrighton K, Biddle JF (2016) Deep subsurface life from North Pond: Enrichment, isolation, characterization and genomes of heterotrophic bacteria. *Frontiers in Microbiology* **7**, 1–13.
Schumacher M, Christl I, Scheinost AC, Jacobsen C, Kretzschmar R (2005) Chemical heterogeneity of organic soil colloids investigated by scanning transmission X-ray microscopy and C-1s NEXAFS microspectroscopy. *Environmental science & technology* **39**, 9094–100.
Solomon D, Lehmann J (2005) Carbon K-Edge NEXAFS and FTIR-ATR Spectroscopic Investigation of organic carbon speciation in soils. *Soil Science Society of America Journal* 107–119.
Solomon D, Lehmann J, Harden J, Wang J, Kinyangi J, Heymann K, Karunakaran C, Lu Y, Wirick S, Jacobsen C (2012) Micro- and nano-environments of carbon sequestration: Multi-element STXM–NEXAFS spectromicroscopy assessment of microbial carbon and mineral associations. *Chemical Geology* **329**, 53–73.
Solomon D, Lehmann J, Kinyangi J, Liang B, Schafer T (2005) Carbon K-Edge NEXAFS and FTIR-ATR Spectroscopic Investigation of Organic Carbon Speciation in Soils. *Soil Science Society of America Journal* **69**, 107–119.
Stewart-Ornstein J, Hitchcock AP, Cruz DH, Henklein P, Overhage J, Hilpert K, Hale JD, Hancock REW (2007) Using intrinsic X-ray absorption spectral differences to identify and map peptides and proteins. *Journal of Physical Chemistry B* **111**, 7691–7699.
Templeton A, Knowles E (2009) Microbial Transformations of Minerals and Metals: Recent

Advances in Geomicrobiology Derived from Synchrotron-Based X-Ray Spectroscopy and X-Ray Microscopy. *Annual Review of Earth and Planetary Sciences* **37**, 367–391.

Toner BMB, Fakra SSC, Manganini SSJ, Santelli CM, Marcus M a., Moffett JW, Rouxel O, German CR, Edwards KJ (2009) Preservation of iron(II) by carbon-rich matrices in a hydrothermal plume. *Nature Geoscience* **2**, 197–201.

Tully BJ, Heidelberg JF (2016) Potential mechanisms for microbial energy acquisition in oxic deep- sea sediments. *Applied and Environmental Microbiology* **82**, 4232–4243.

Whiteside JH, Olsen PE, Eglinton TI, Cornet B, McDonald NG, Huber P (2011) Pangean great lake paleoecology on the cusp of the end-Triassic extinction. *Palaeogeography, Palaeoclimatology, Palaeoecology* **301**, 1–17.

Ziebis W, McManus J, Ferdelman T, Schmidt-Schierhorn F, Bach W, Muratli J, Edwards KJ, Villinger H (2012) Interstitial fluid chemistry of sediments underlying the North Atlantic gyre and the influence of subsurface fluid flow. *Earth and Planetary Science Letters* **323–324**, 79–91.

Table 1. Site locations and sediment properties. Information for South Pacific Gyre samples taken from D'Hondt *et al.* (2009). Bolded site names indicate that STXM-NEXAFS analyses were made at these sites.

Site	Classification	latitude/longitude	water depth (m)	sediment recovered (m)	sediment thickness (m)	basement age (Ma)	sedimentation rate (cm/kyr)	O_2 at 1.5 m depth (μM)
SPG 1	oxic	23°51.0'S, 165°38.6'W	5699	7.79	71	100	0.031	207
SPG 2	oxic	26°03.1'S, 156°53.6'W	5126	8.145	17	100	0.017	179
SPG 3	oxic	27°56.5'S, 148°35.4'W	4856	5.49	6	71	0.008	198
SPG 4	oxic	26°28.9'S, 137°56.4'W	4285	7.24	10	33.5	0.028	175
SPG 6	oxic	27°55.0'S, 123°09.7'W	3705	2.585	15	13.5	0.111	198
SPG 9	oxic	38°03.7'S, 133°05.5'W	4924	7.015	20	39	0.051	159
SPG 10	oxic	39°18.6'S, 139°48.0'W	5283	5.4	22	58	0.037	176
SPG 12	suboxic	45°57.8'S, 163°11.0'W	5306	4.98	130	73	0.178	4.49
NA 3	suboxic	14°24.0'N, 50°37.2W	4453	28.66	100	40	0.250	34.9
NA 10	suboxic	14°24.0'N, 50°37.2W	4455	32.22	100	40	0.250	50.8
NA 11	oxic	22°47.0'N, 56°31.1'W	5557	26.75	100	70	0.143	187
NA 12	oxic	29°40.6'N, 58°19.7'W	5367	25.92	98	98	0.100	158
NA 15	anoxic	33°29.0'N, 54°10.0'W	5515	26.83	331	88	0.376	0
NA 16	anoxic	33°41.2'N, 57°36.9'W	4575	40.22	1012	102	0.992	0
PB-HB	anoxic	12°1'S, 81°54'W	4812	115.2	115	~34	0.338	0
PB-HE	anoxic	12°1'S, 81°54'W	4812	118.6	115	~34	0.338	0

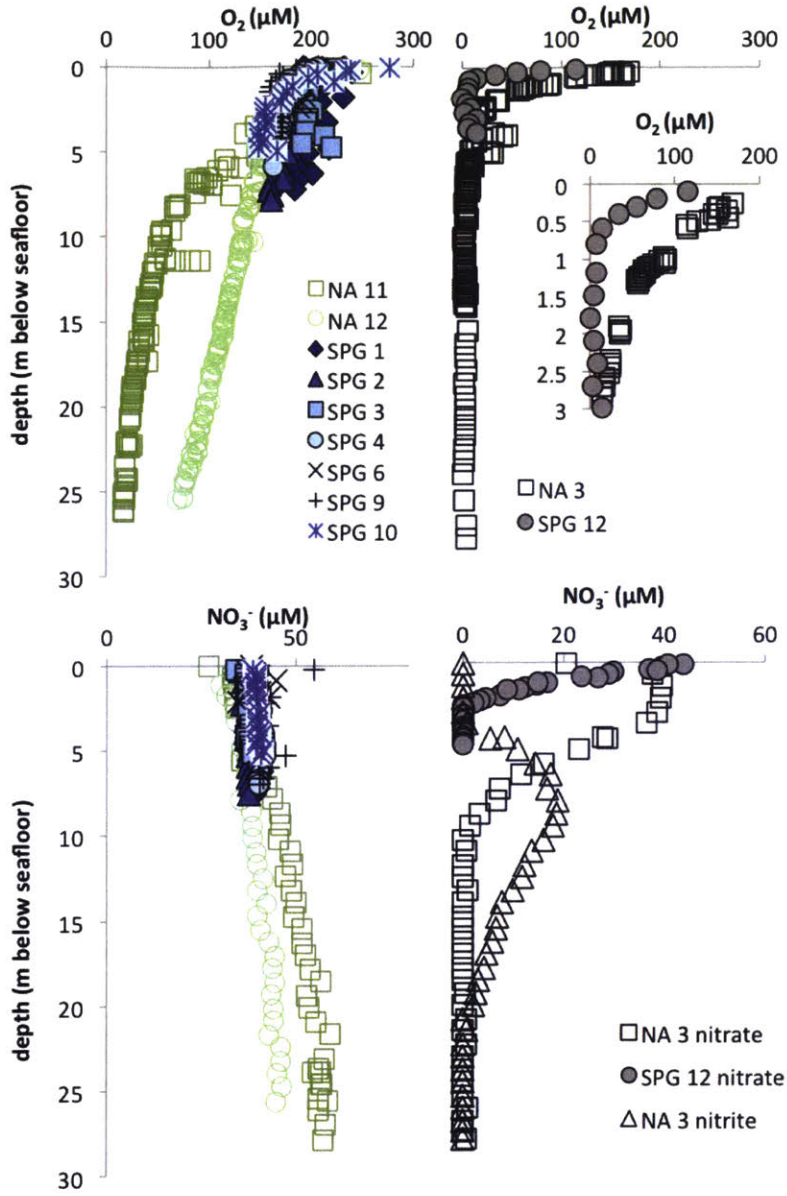

Figure 1. Depth profiles of oxygen (top) and nitrate/nitrite (bottom) for all oxic and suboxic sites. Inset at top right expands the top portion of the oxygen profile to highlight the decrease in oxygen. Nitrite data for SPG 12 do not exist.

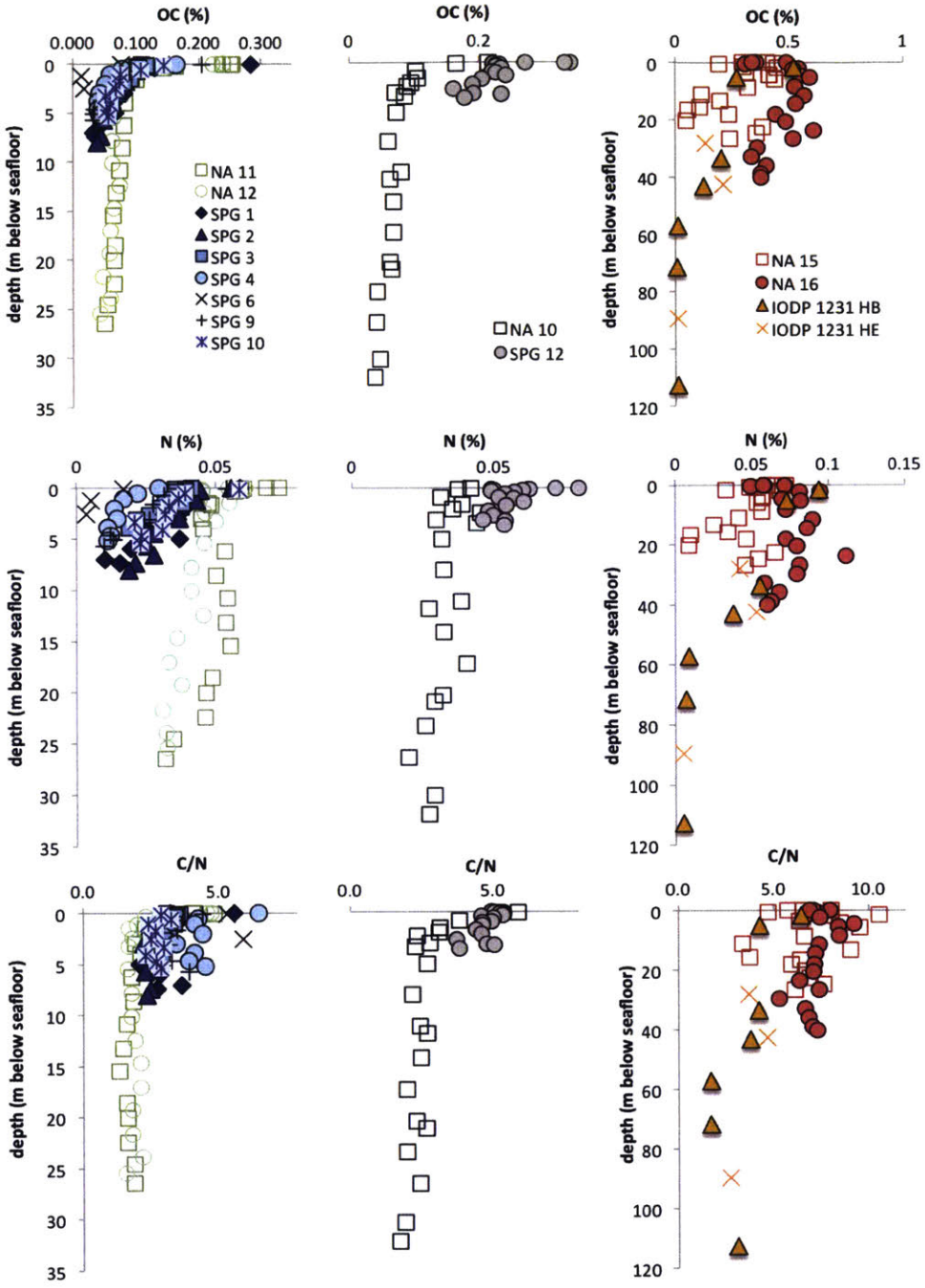

Figure 2. Depth profiles of organic carbon (top), nitrogen (middle), and C/N (bottom) for all sediment cores, organized by site classification (oxic, left; suboxic, middle; anoxic, right). Note differing depth and concentration scales.

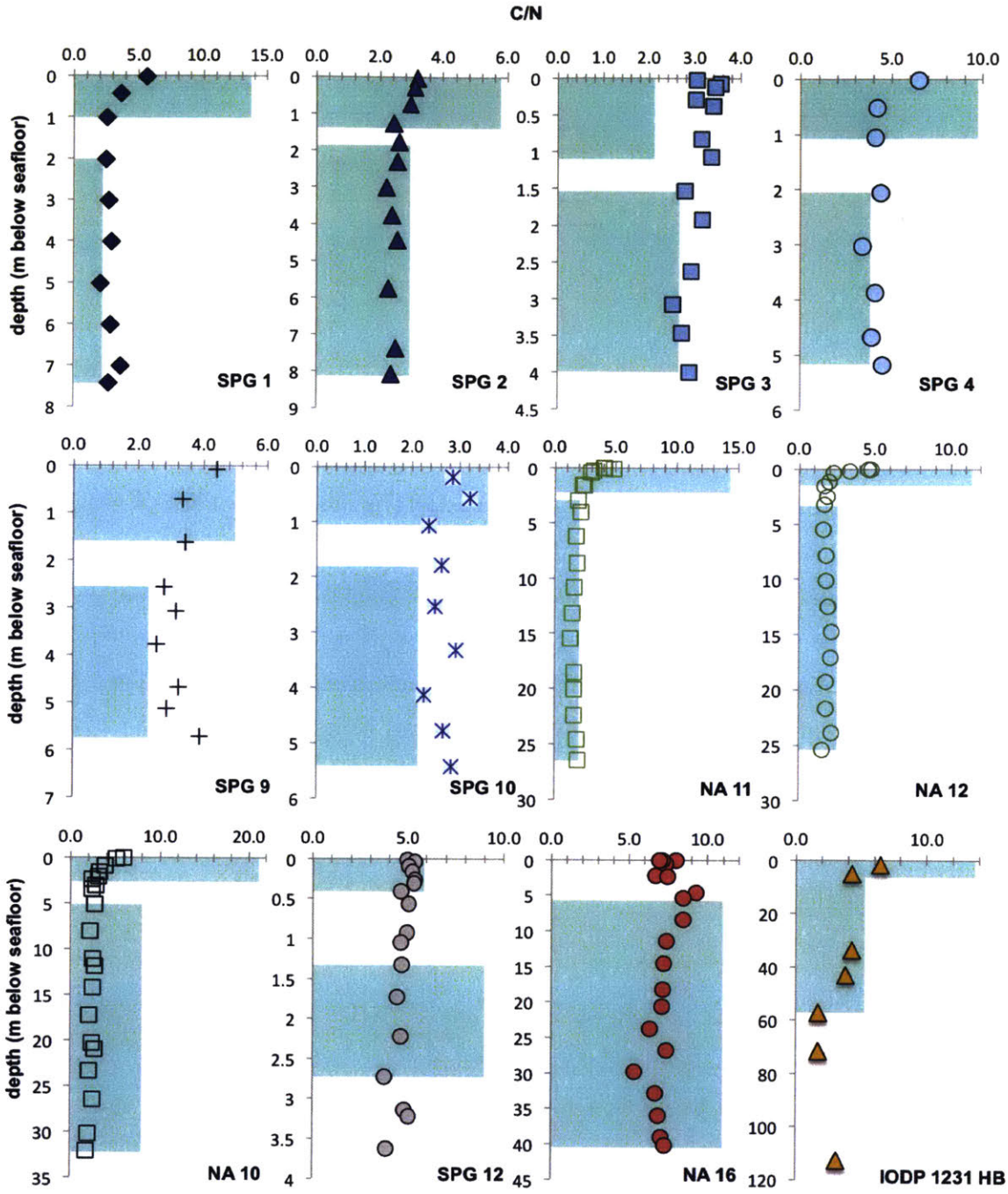

Figure 3. C/N of bulk material (data points) overlaid on calculated C/N of degradation (blue bars) for a given depth interval for all sites where OC and N profiles allowed for calculation of degradation rates. SPG 6 is excluded due to sparse data, while NA 15 does not show clear down-core trends or decreases in OC and N concentration.

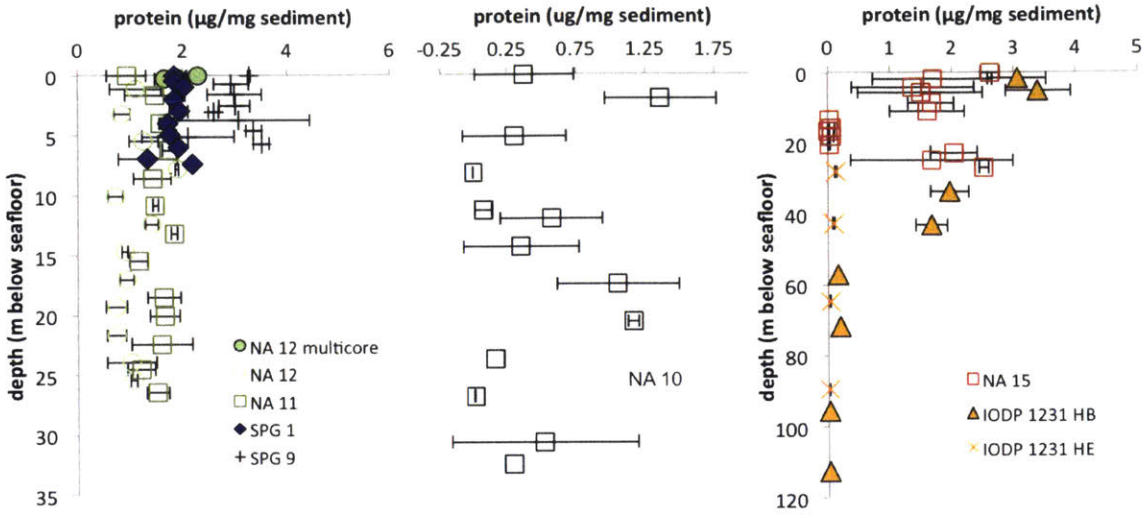

Figure 4. Depth profiles showing concentrations of intact proteins measured in oxic (left), suboxic (middle), and anoxic (right) cores. For site NA 12 (green circles) the multi core and long core samples are contrasted as the multi core data capture a rapid decrease in concentration from the surface not otherwise visible in the long core data. Error is standard deviation of triplicate extractions; for IODP site 1231 HB and HE samples, a single sample was extracted in triplicate and the error applied to the entire core. Individual error may be lesser or greater.

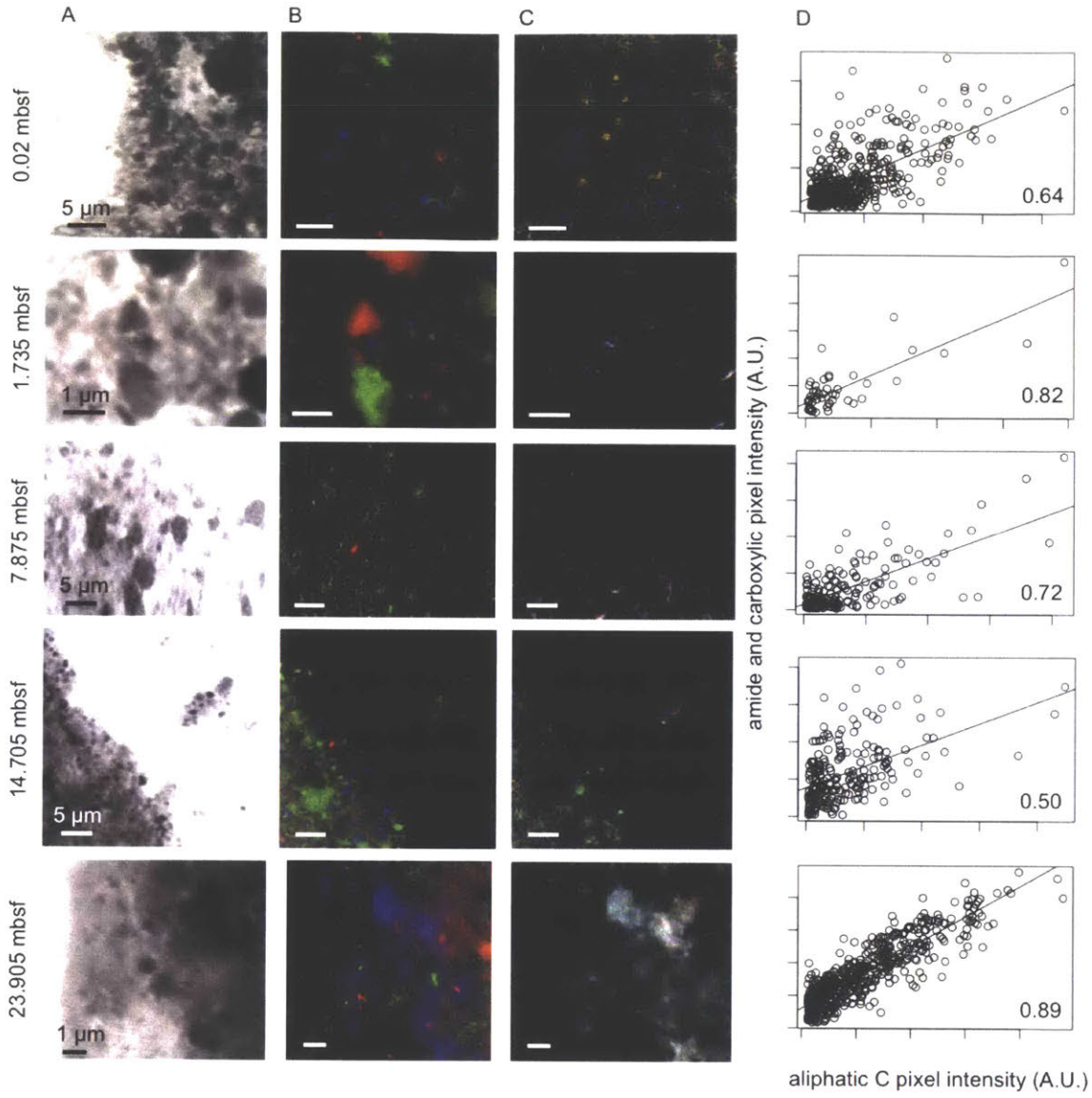

Figure 5. STXM transmission images of samples from five depths along the length of the core from oxic site NA 12 (column A) and overlaid, false-colored optical density maps showing the distribution of iron, potassium, and carbonate (red, green, and blue, column B) and aliphatic, amide and carboxylic, and o-alkyl carbon (red, green, and blue, column C). Column D shows the pixel-by-pixel correlation of aliphatic C and amide and carboxylic C, in arbitrary units, where pixels with zero value were excluded and Pearson correlation coefficients are shown in the lower corner of each plot.

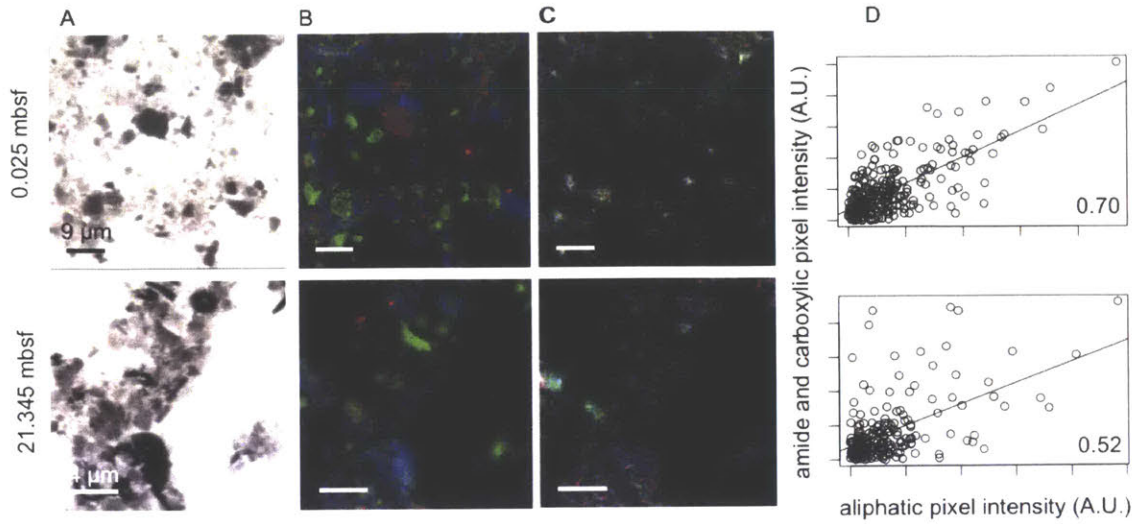

Figure 6. STXM transmission images of samples from two depths along the length of the core from suboxic site NA 3 (column A) and overlaid, false-colored optical density maps showing the distribution of iron, potassium, and carbonate (red, green, and blue, column B) and aliphatic, amide and carboxylic, and o-alkyl carbon (red, green, and blue, column C). Column D shows the pixel-by-pixel correlation of aliphatic C and amide and carboxylic C, in arbitrary units, where pixels with zero value were excluded and Pearson correlation coefficients are shown in the lower corner of each plot.

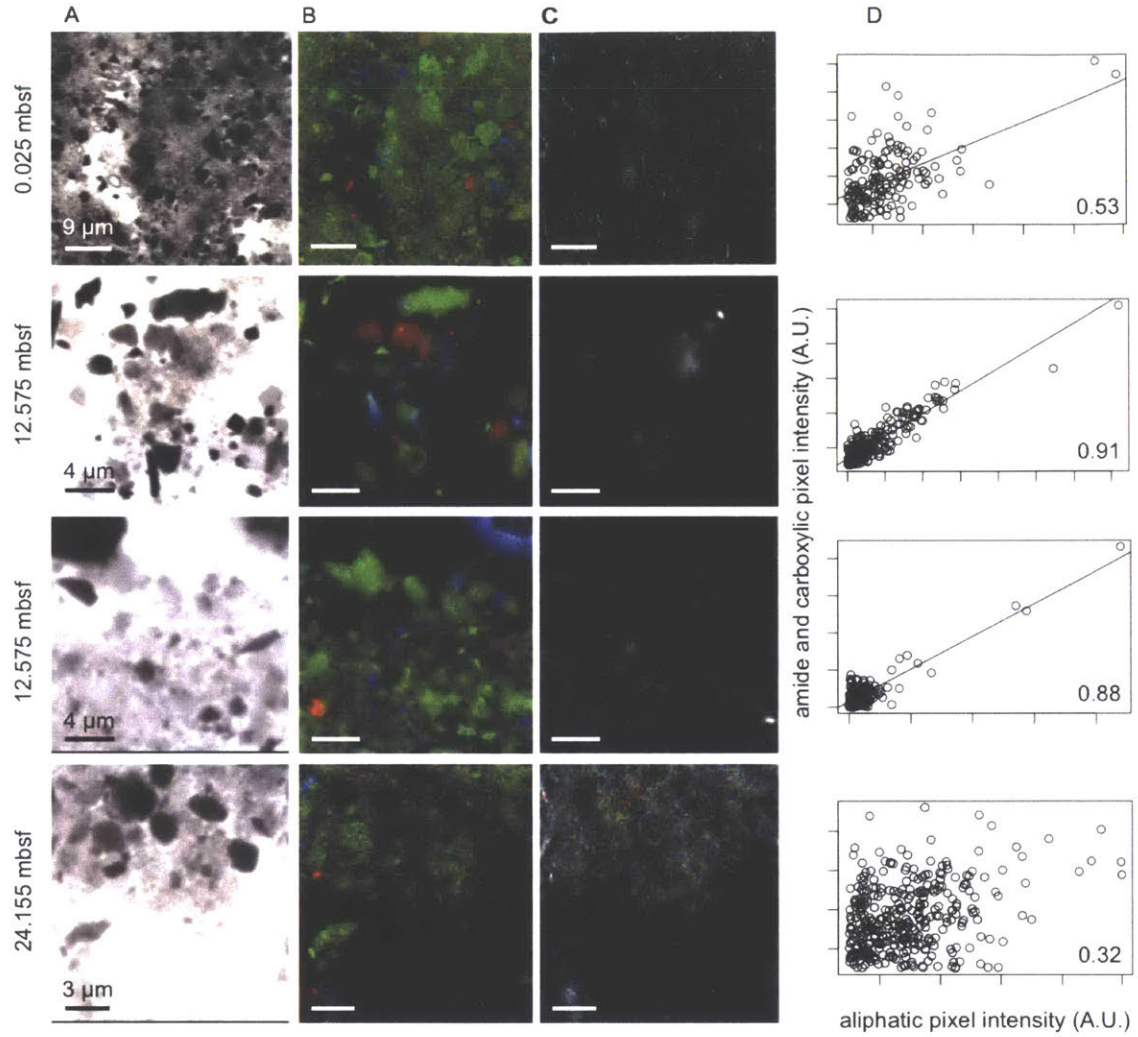

Figure 7. STXM transmission images of samples from three depths along the length of the core from anoxic site NA 15 (column A) and overlaid, false-colored optical density maps showing the distribution of iron, potassium, and carbonate (red, green, and blue, column B) and aliphatic, amide and carboxylic, and o-alkyl carbon (red, green, and blue, column C). Column D shows the pixel-by-pixel correlation of aliphatic C and amide and carboxylic C, in arbitrary units, where pixels with zero value were excluded and Pearson correlation coefficients are shown in the lower corner of each plot. Two sample regions were analyzed from the mid-core sample.

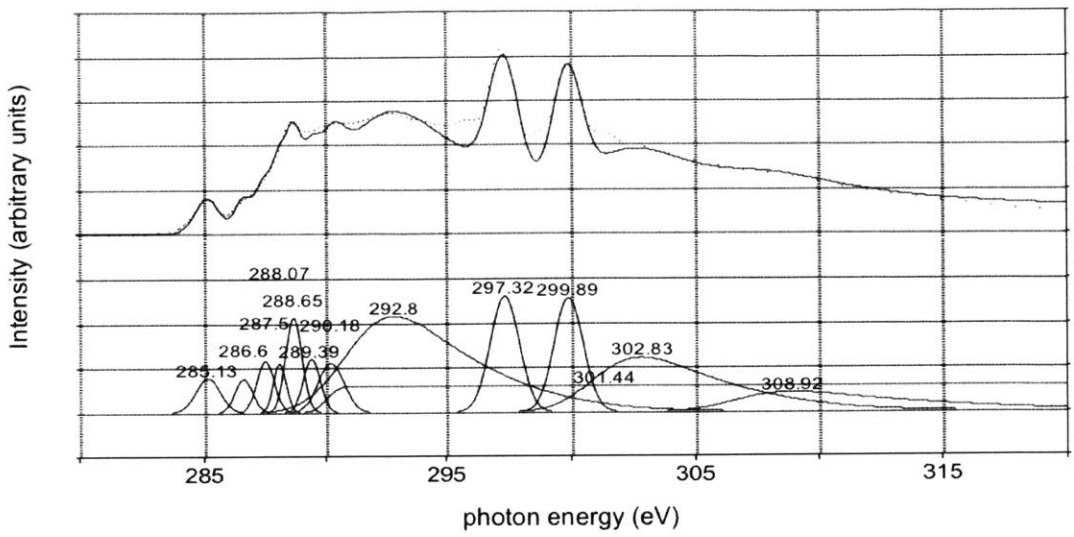

Figure 8. Normalized spectra from NA 15, 12.575 m below seafloor region 1, the "all carbon" mask (top solid line), its deconvoluted peaks (bottom), and the fit line (top, dashed line, R^2 = 0.97). Peaks <295 correspond to carbon transitions, including 285.13 eV (aromatic), 286.6 eV (phenolic and ketonic), 287.5 eV (aliphatic), 288.07 and 288.65 eV (amide and carboxylic), 289.39 eV (O-alkyl), and 290.18 eV (carbonate). Broad σ* transitions are fit with an asymmetric Gaussian at 292.8 eV and the ionization threshold set at 290.0 eV fit with a "transition" function that approximates an arctangent function. Peaks at 297.32 and 299.89 are the L_2 and L_3 edges of potassium. (See methods for details.)

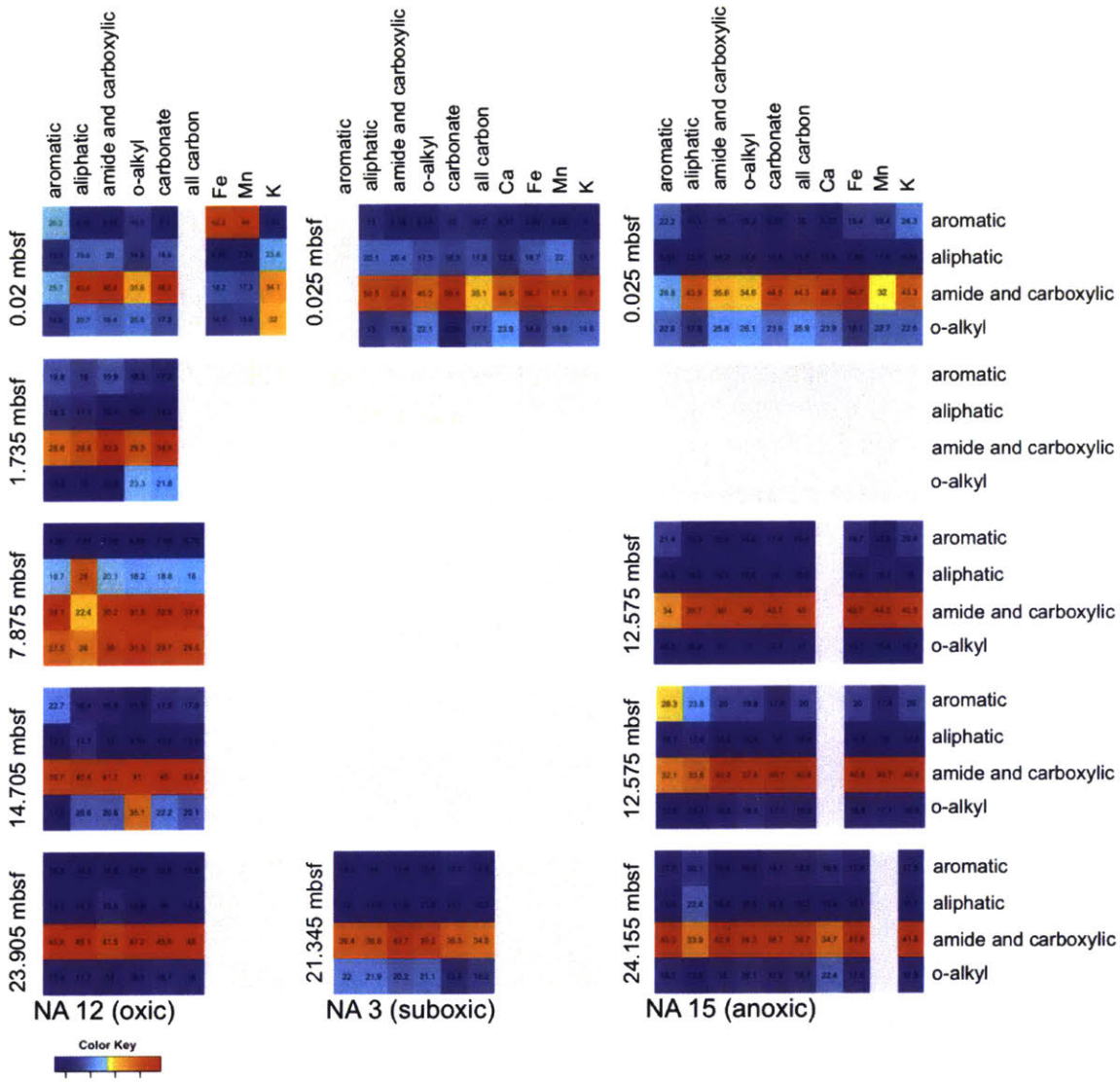

Figure 9. Concentration grid showing composition and variability in composition of STXM samples for NA 12, NA 3, and NA 15 (left, middle, right) along the length of each core (with core top samples at the top of the figure). Individual columns within a grid correspond to region masks, either an organic functional group or mineral-forming element. Rows contain the relative percent abundance of each of the four most abundant functional groups, derived from fitting spectra extracted from mask regions (such that the sum of each column is ~100%). Squares within a grid are color coded by relative percent contribution, with warmer colors higher.

CHAPTER 4 SUPPORTING INFORMATION

SI Table 1. Calculated OC and N degradation rates over a given depth interval, the C/N of degradation, and the average bulk C/N over that depth interval.

Site	depth interval (m)	age interval (approx. Ma)	OC degradation rate ($mol/m^3/kyr$)	N degradation rate ($mol/m^3/kyr$)	C/N degradation	average C/N over depth interval
SPG 1	0.025—1.02	0.08—3.31	0.0488	0.0036	13.7	3.94
SPG 1	2.02—7.42	6.53—23.9	0.0022	0.0009	2.36	2.76
SPG 2	0.02—1.26	0.15—7.38	0.0073	0.0012	5.80	2.93
SPG 2	1.78—8.08	10.4—47.5	0.0010	0.0003	2.89	2.42
SPG 3	0.025—1.07	0.31—13.4	0.0011	0.0005	2.05	3.29
SPG 3	1.52—4.00	19.1—49.9	0.0012	0.0004	2.70	2.83
SPG 4	0.025—1.06	0.09—3.77	0.0238	0.0024	9.74	4.94
SPG 4	2.06—5.18	7.34—18.5	0.0006	0.0002	3.88	4.27
SPG 6	NA	NA	NA	NA	NA	NA
SPG 9	0.075—1.62	0.15—3.19	0.0339	0.0063	5.39	3.73
SPG 9	2.57—5.72	5.05—11.2	0.0055	0.0024	2.26	3.08
SPG 10	0.175—1.06	0.47—2.88	0.0240	0.0066	3.65	2.80
SPG 10	1.78—5.42	4.80—14.7	0.0016	0.0007	2.15	2.64
SPG 12	0.012—0.41	0.01—0.23	0.4192	0.0710	5.90	5.13
SPG 12	1.32—2.72	0.74—1.63	0.0848	0.0095	8.91	4.35
NA 3	0.002—1.52	0.008—0.610	0.2848	NA	NA	NA
NA 3	2.96—27.5	1.18—11.0	0.0017	NA	NA	NA
NA 10	0.05—2.04	0.02—0.816	0.1222	0.0058	21.0	4.52
NA 10	5.10—32.1	2.04—12.8	0.0026	0.0003	8.56	2.32
NA 11	0.1—1.52	0.07—1.07	0.1327	0.0092	14.3	3.46
NA 11	3.01—26.5	2.11—18.5	0.0011	0.0006	1.98	1.92
NA 12	0.02—1.15	0.018—1.06	0.1323	0.0117	11.3	3.37
NA 12	2.51—25.4	2.30—23.4	0.0011	0.0005	2.41	1.83
NA 15	NA	NA	NA	NA	NA	NA
NA 16	5.30—40.1	0.535—4.05	0.0517	0.0044	11.6	6.98
PB-HB	1.75—5.15	0.301—0.886	0.3563	0.0259	13.7	5.40
PB-HB	5.15—57.1	0.886—25.3	0.0088	0.0019	4.72	3.52
PB-HE	NA	NA	NA	NA	NA	NA

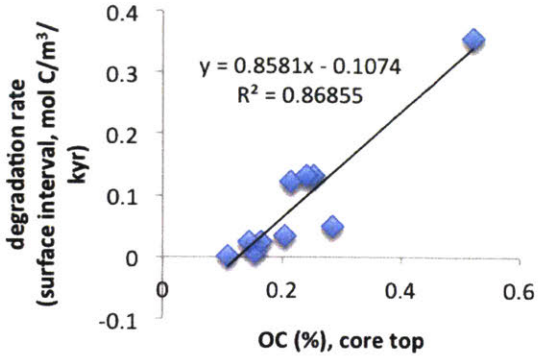
y = 0.8581x - 0.1074
R² = 0.86855
degradation rate (surface interval, mol C/m³/kyr)
OC (%), core top

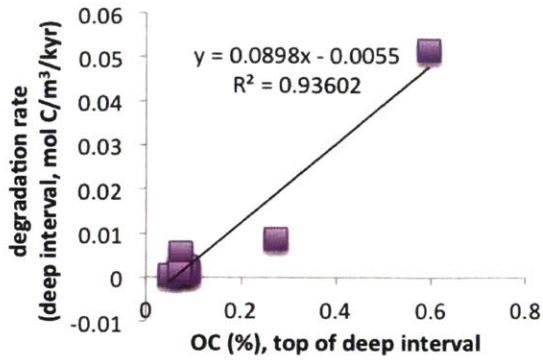
y = 0.0898x - 0.0055
R² = 0.93602
degradation rate (deep interval, mol C/m³/kyr)
OC (%), top of deep interval

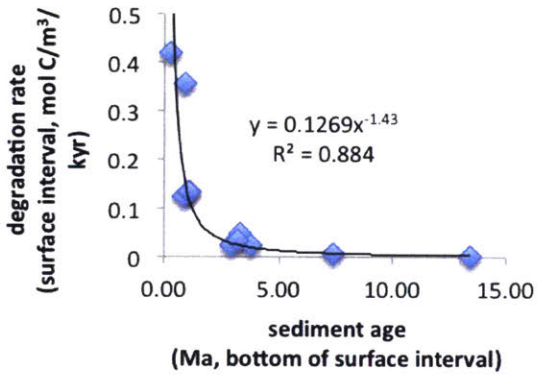
y = 0.1269x^-1.43
R² = 0.884
degradation rate (surface interval, mol C/m³/kyr)
sediment age (Ma, bottom of surface interval)

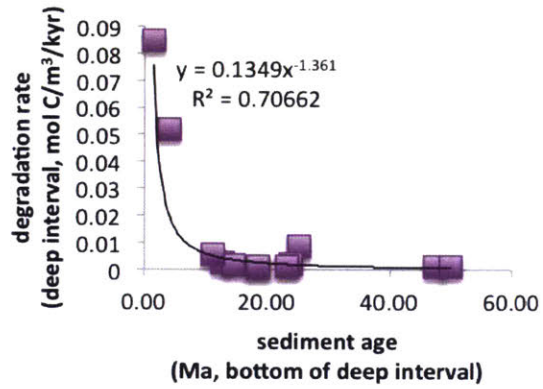
y = 0.1349x^-1.361
R² = 0.70662
degradation rate (deep interval, mol C/m³/kyr)
sediment age (Ma, bottom of deep interval)

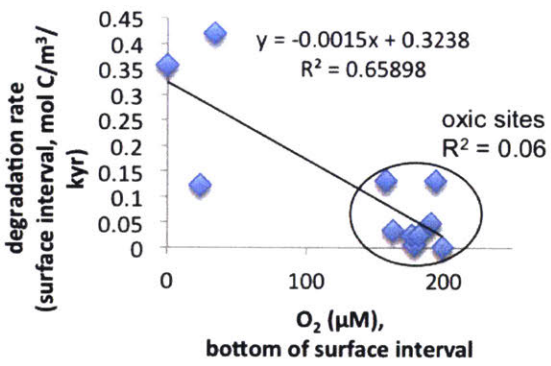
y = -0.0015x + 0.3238
R² = 0.65898
oxic sites
R² = 0.06
degradation rate (surface interval, mol C/m³/kyr)
O2 (µM), bottom of surface interval

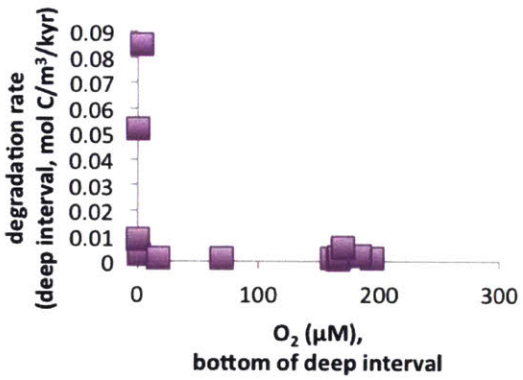
degradation rate (deep interval, mol C/m³/kyr)
O2 (µM), bottom of deep interval

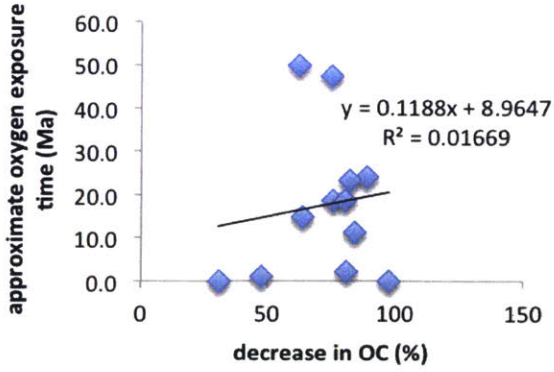
y = 0.1188x + 8.9647
R² = 0.01669
approximate oxygen exposure time (Ma)
decrease in OC (%)

SI Figure 1. Correlations between calculated degradation rates and OC content (A: OC% at core top vs. degradation rate in the surface interval, B: OC(%) at the top of the deep interval vs. deep degradation rate), calculated degradation rate and sediment age (C, D, for the surface and deep intervals respectively), and calculated degradation rate and oxygen content in interstitial waters at the bottom of the given depth interval (E, F, for the surface and deep intervals respectively). Circled area of plot E shows where the oxic sites cluster and gives a R^2 value for oxic sites-only. Plot G shows the lack of correlation between the percent decrease in OC over the entire core (as a proxy for carbon burial efficiency) and sediment age as a proxy for oxygen exposure time (OET, where for suboxic sites OET is set as estimated sediment age where oxygen becomes undetectable).

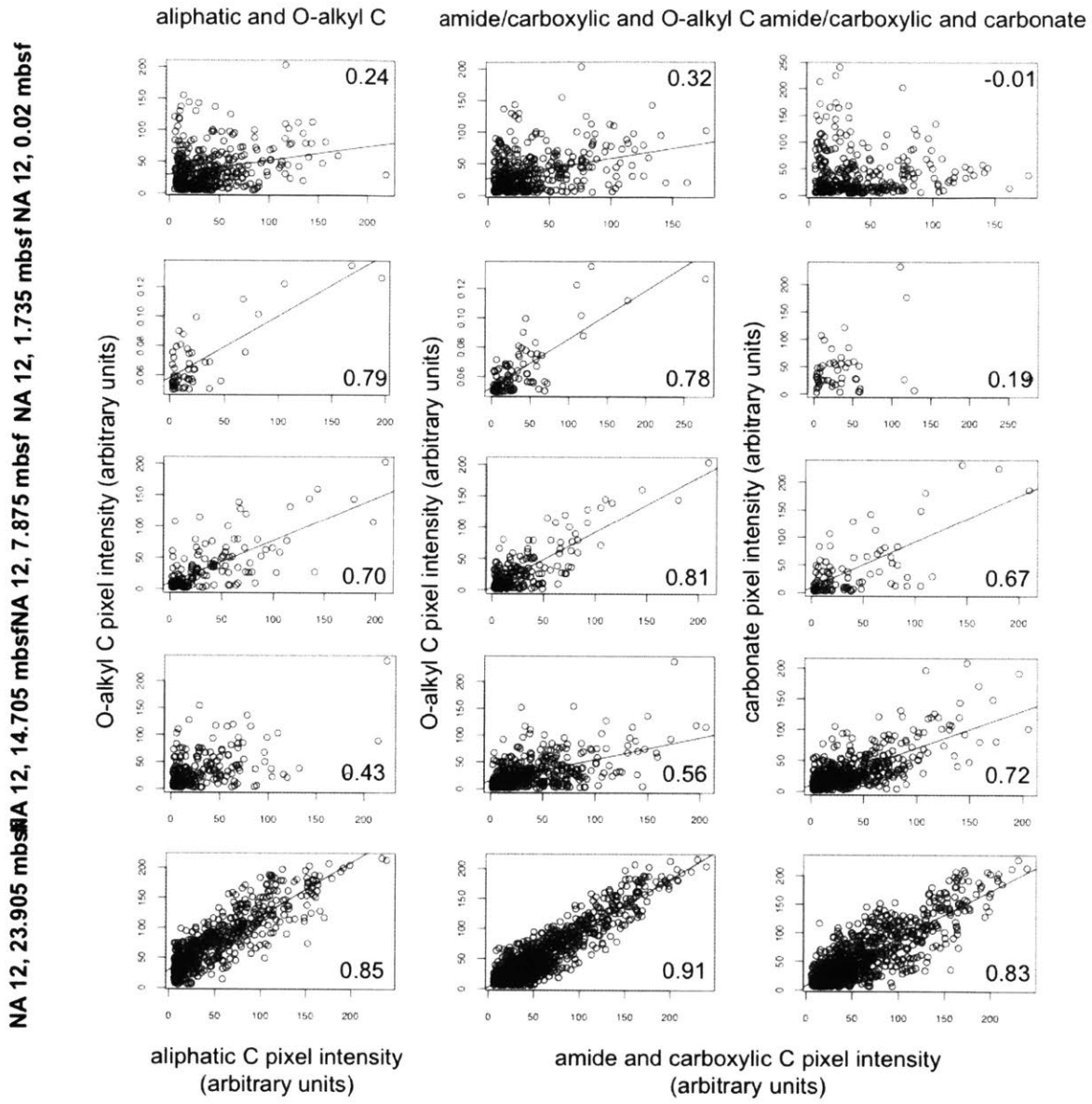

SI Figure 2. Pixel correlation derived from STXM maps of organic functionalities at site NA 12, organized by depth with the sample from NA 12 core top at the top of the Figure. Fit lines are shown for correlations >0.5; Pearson correlation coefficients are shown in the lower corner of each plot.

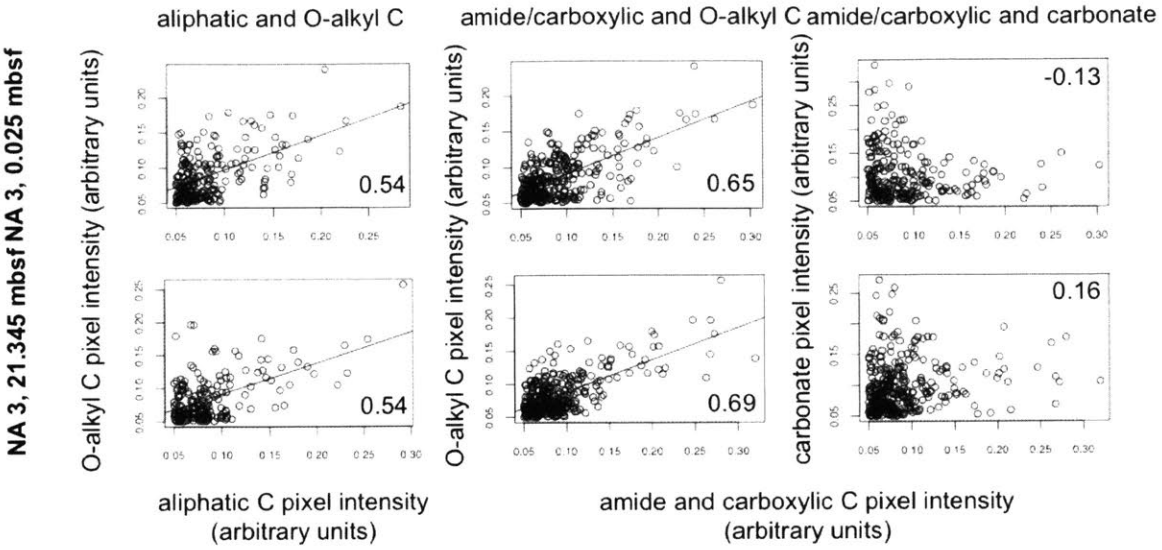

SI Figure 3. Pixel correlation derived from STXM maps of organic functionalities at site NA 3, organized by depth with the sample from NA 3 core top at the top of the Figure. Fit lines are shown for correlations >0.5; Pearson correlation coefficients are shown in the lower corner of each plot. Note the divergent possible fit lines in the amide/carboxylic vs. carbonate plots (right).

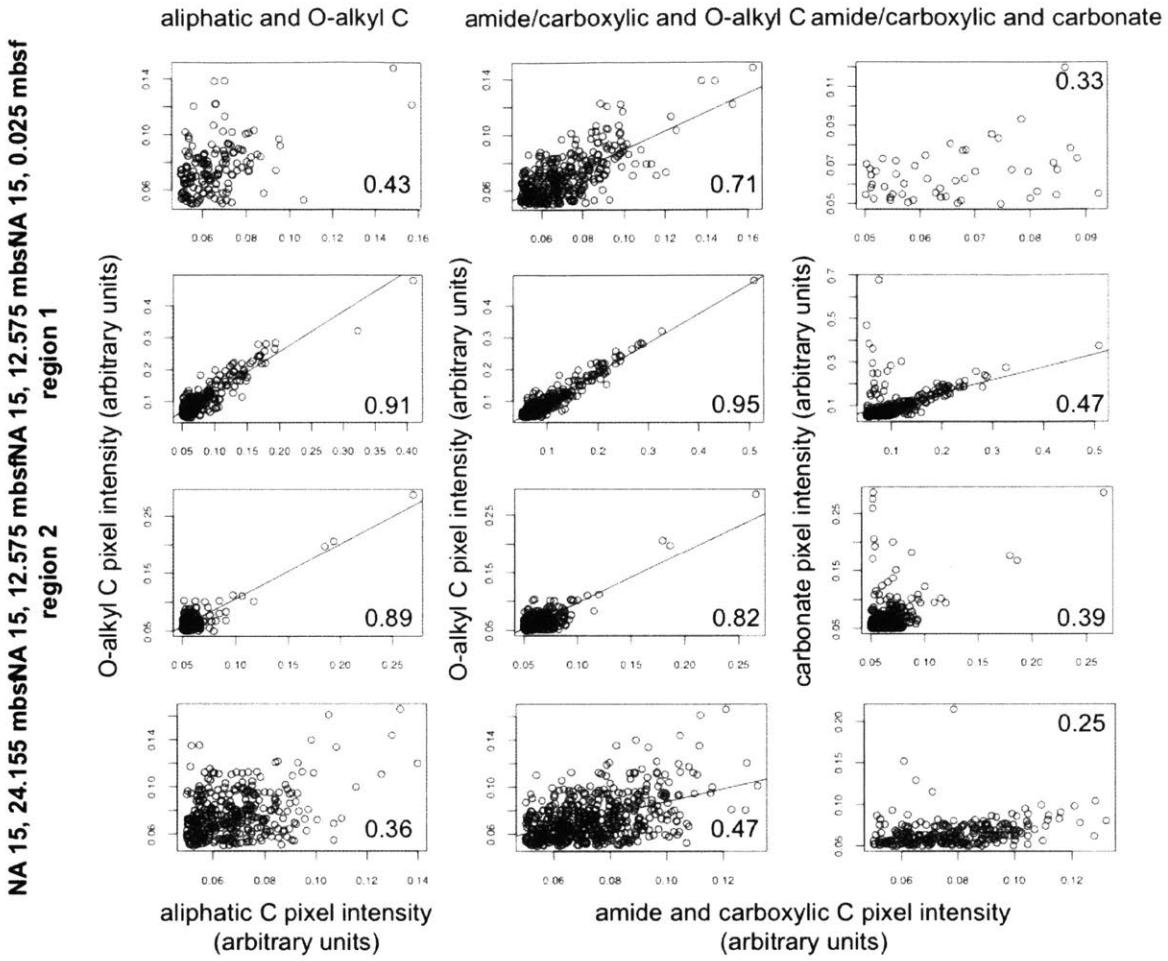

SI Figure 4. Pixel correlation derived from STXM maps of organic functionalities at site NA 15, organized by depth with the sample from NA 15 core top at the top of the Figure. Fit lines are shown for correlations >0.5; Pearson correlation coefficients are shown in the lower corner of each plot. Note the divergent possible fit lines in the amide/carboxylic vs. carbonate plots (right).

SI Table 2. Pearson correlation coefficients for all possible correlations of the most abundant organic functional groups (aromatic, aliphatic, amide and carboxylic, and O-alkyl, abbreviated "arom," "aliph," "ac," and "oalk" respectively) as well as carbonate ("CO3").

	NA 12 0.02 mbsf	NA 12 1.735 mbsf	NA 12 7.875 mbsf	NA 12 14.705 mbsf	NA 12 23.905 mbsf	NA 3 0.025 mbsf	NA 3 21.345 mbsf	NA 15 0.025 mbsf	NA 15L9-1 12.575 mbsf	NA 15L9-2 12.575 mbsf	NA 15 24.155 mbsf
arom/aliph	0.08	0.76	0.34	0.47	0.79	0.35	0.33	0.15	0.73	0.91	0.21
arom/ac	0.01	0.88	0.35	0.33	0.83	0.27	0.32	0.15	0.60	0.90	0.20
arom/oalk	0.19	0.66	0.30	0.06	0.83	0.26	0.34	0.14	0.58	0.93	0.10
arom/CO3	-0.14	-0.04	0.16	0.19	0.76	0.04	0.27	-0.19	0.52	0.87	0.21
aliph/ac	0.64	0.82	0.72	0.50	0.89	0.70	0.52	0.54	0.91	0.88	0.32
aliph/oalk	0.24	0.79	0.70	0.41	0.86	0.54	0.54	0.43	0.91	0.89	0.36
aliph/CO3	0.03	0.04	0.52	0.22	0.72	-0.10	0.24	0.54	0.80	0.76	0.22
ac/oalk	0.32	0.77	0.80	0.51	0.91	0.65	0.69	0.71	0.95	0.82	0.47
ac/CO3	-0.01	0.19	0.68	0.70	0.83	-0.13	0.16	0.33	0.47	0.39	0.25
oalk/CO3	0.53	0.36	0.65	0.43	0.83	-0.19	0.32	0.21	0.45	0.33	0.30

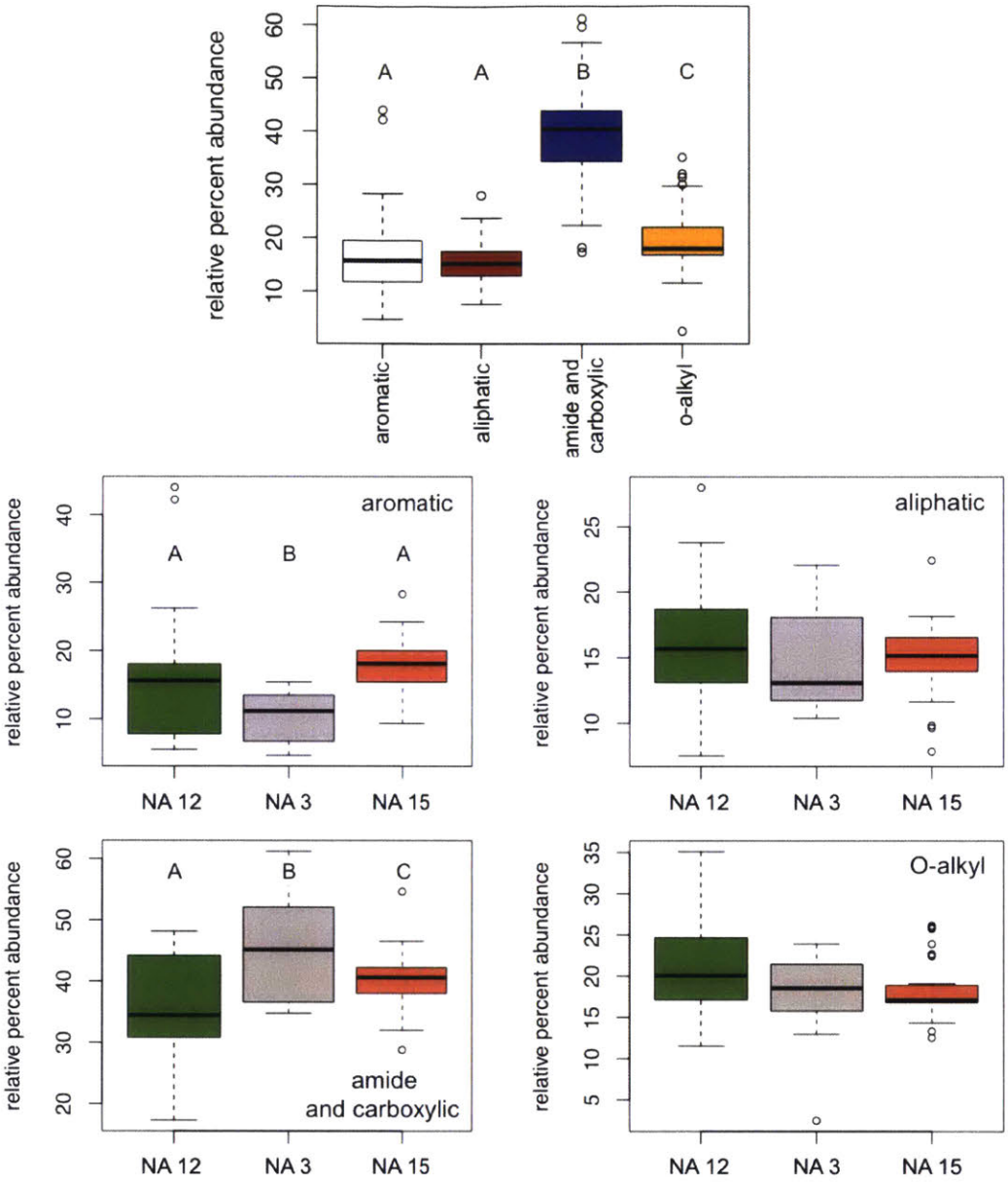

SI Figure 5. Box plots showing the relative abundance of organic functional groups overall (top) or by site (4 lower images, plots separated by functional group and labeled in upper right). Note different y-axis scales. For the overall comparison, aromatic, and amide and carboxylic boxplots, letters above each box designate statistically significant sample groupings ($p = 0.05$, one-way ANOVA).

Chapter 5: Conclusions and future directions

5.1 Concluding remarks

This work examines the concentration and composition of organic carbon (OC) in primarily carbon-poor environments with the goal of identifying the mechanisms that dictate the balance between OC preservation and remineralization over a range of time scales. In Chapter 2, OC associating with biogenic manganese (Mn) oxide minerals was characterized in pure cultures of Mn-oxidizing microorganisms, incubations in brackish estuarine waters, and in ferromanganese precipitates in karstic cave systems in order to examine the selectivity and stability of mineral-organic associations. Chapter 3 tests the effect of long-term exposure to oxygen on the content and composition of OC in oxic pelagic sediments. Chapter 4 then contrasts results from these oxic sediments with suboxic and anoxic pelagic sites. Analyses conducted on both the bulk and micro scale allow examination of the effects of a range of parameters, from sediment age and redox conditions to lithology. All chapters utilize synchrotron-based near edge X-ray absorption fine structure (NEXAFS) spectroscopy to characterize carbon. This work contributes to the development of that technique for application to environmental samples and allows insight into carbon speciation without requiring chemical extractions prior to analysis. Thus, this work is the first to document the composition of the entire, unaltered carbon pool and its micro-scale distribution in pelagic sediments.

In a series of experiments with Mn-oxidizing bacterial and fungal cultures and brackish estuarine waters, Chapter 2 describes how Mn oxide-OC associations form rapidly (on the order of hours) yet are stable over the course of days to weeks as the Mn oxide minerals undergo structural ripening, transforming from hexagonal to triclinic birnessite. Proteinaceous carbon associates particularly strongly with these oxides, suggesting that minerals could act as a protein

shuttle, offering initial protection against remineralization but ultimately transporting the protein to an environment (e.g. the deep subsurface, as in Lloyd *et al.* (2013)) where geochemical conditions or biological adaptations make the compounds more bioavailable. The two bacterial and two fungal cultures tested have consistent, distinct chemical compositions of OC associating with precipitated Mn oxide minerals (bacterial Mn oxides host proteinaceous OC, mycogenic Mn oxides are polysaccharide-rich), suggesting the possibility that biomineral-associated OC could act as a biomarker of the precipitating organism. While these trends do not hold up compared to other studies of biomineralizing organisms (Toner *et al.*, 2005; Chan *et al.*, 2011), proteins extracted and sequenced from the mineral-organic aggregates could provide insight not only into the biomineralizing organism but also the Mn oxidation and precipitation mechanism. Finally, results from incubation experiments with both biogenic and synthetic Mn oxides in estuarine waters combined with results from cave ferromanganese deposits demonstrate the Mn oxides accumulate OC from a range of sources by a range of mechanisms. This observation emphasizes the potential for these minerals to sequester large quantities of OC, but also indicates that biosignatures may be quickly over-written (as also shown in Bennett *et al.* (2014)).

Chapter 3 focuses on the effects of age and continual oxygen exposure on the content and composition of organic carbon in pelagic sediments. We observe a relatively stable reservoir of OC preserved on geological time scales in the deep subsurface despite the availability of oxygen, implying that another mechanism contributes to preservation. More rapid degradation of OC towards the surface of sediments does occur, but in contrast to better-studied coastal and margin systems, this degradation process appears to preferentially remove C relative to N from organic matter, generating the extremely low C/N values observed at depth. Intact proteins are present throughout the sediment column though account for $<<1\%$ of total OC and may exist in a steady-

state equilibrium partitioned between biomass, free, extracellular proteins, and those adsorbed to mineral surfaces. The question remains of how rapidly this small pool turns over and to what extent its recycling sustains life, as the genomic potential for protein metabolisms has been documented in these systems (Lloyd *et al.*, 2013; Tully & Heidelberg, 2016). NEXAFS spectroscopy further reveals preserved OC to be proteinaceous in origin, consisting primarily of amide and carboxylic carbon in a scaffolding of aliphatic and O-alkyl carbon. This composition, found throughout all cores analyzed at all depths, may be the net result of oxidative degradation on extremely long time scales.

To contextualize results from Chapter 3 and to address whether oxygen is the sole variable controlling OC content and composition, Chapter 4 compares pelagic sediments from oxic, suboxic, and anoxic but not sulfidic sites in the South Pacific and North Atlantic. While concentrations of OC, N and the C/N ratio do scale with sediment redox state, concentrations in the deep subsurface are more similar than expected between site types and likewise suggest preferential utilization of C over N in the surface interval. We propose that in these pelagic sediments that are either oxygenated to basement, receive a flux of oxygen diffusing up from the basalt basement ((D'Hondt *et al.*, 2009; Ziebis *et al.*, 2012)), or experience redox gradients extended over tens of meters, organic carbon content and composition is more likely a signature of continual heterotrophy as a dominant metabolism than it is of continual oxygen exposure.

Scanning transmission X-ray microscopy (STXM) coupled to NEXAFS spectroscopy was further employed in Chapter 4 to examine variability in OC content and composition on the micro-scale. Interestingly, we observed minimal differences in composition between site types (oxic, suboxic, and anoxic) or over the 2-5 depth intervals analyzed at each site. Further, OC does not clearly associate with mineral surfaces nor does mineral-associated OC have a

chemically distinct composition from the bulk. While interpretations are limited here due to technical challenges of collecting quality data from mineral particles, these preliminary observations imply that mineral-based protection via chemical adsorption or physical protection may not contribute as substantially to the preservation of OC in these systems. We instead conclude that the remaining OC is recalcitrant and thereby protected from immediate remineralization by microorganisms, resulting in some of the lowest cell counts observed in sediment environments (Kallmeyer *et al.*, 2012) and the extremely slow OC degradation rates calculated here. However, we observe that compositional variability within a single sample on the micro-scale is equal to variability along the entire length of the core in the bulk spectra analyzed in Chapter 3. Thus, a diversity of compounds does persist over the course of millions of years of slow degradation and diagenetic reactions and could continue to fuel the vanishingly small population living at the limits of life.

Combined, these chapters highlight the interplay of a range of geochemical variables in controlling organic carbon content and composition in the environment. On extremely long time scales, recalcitrance of organic carbon may limit life and ensure that a small quantity of OC is preserved and transferred from the surface to the geological carbon cycle. Constancy of OC chemical composition and the relative diversity of percent contributions from different organic functional groups in the deep subsurface suggest non-selective preservation. However, we note that in the first weeks to kilo-years of preservation, we do observe selective preservation both by mineral-OC associations that fractionate composition and by the unique oxygen-driven degradation dynamics that result in preferential utilization of C over N in C-limited pelagic sediments. Thus, while pelagic sediments appear to subvert several paradigms of marine carbon

cycling and preservation (Burdige, 2007), the same combination of mechanisms is at play just in different magnitudes and on differing temporal scales.

5.2 Future steps

5.2.1 Continued development of NEXAFS and STXM-NEXAFS for applications to environmental samples

Relative to other elements, analysis of carbon at synchrotrons is in its infancy. Beamlines designed to access the "soft X-ray" energy range are typically used for materials science applications, but interest has grown in recent years towards adapting these lines for environmental analyses. These techniques hold vast potential for being able to simultaneously speciate carbon, nitrogen, oxygen, sulfur, aluminum, silicon, iron, and manganese (among other elements) and for probing how these elements co-vary and alter each other's speciation on the micro-scale. Chapters 3-4 describe the first application of bulk NEXAFS and STXM-NEXAFS to pelagic sediments, where low OC concentrations generated additional challenges. This work further helps standardize data normalization and spectral fitting methods (e.g. Gaussian peak deconvolution) in order to translate spectra into information that can be assigned geochemical meaning.

In well-constrained systems, these techniques are capable of differentiating and mapping the distributions of individual proteins or peptides (Stewart-Ornstein *et al.*, 2007) and of identifying the specific mineral-organic bonds formed during polypeptide templation of biogenic calcium carbonate (Metzler *et al.*, 2008). For environmental samples, however, the compound mixtures are often too complicated to fully decompose. Increasing the database of standard compounds (Kaznacheyev & Osanna, 2002; Solomon *et al.*, 2009) and developing conversions

for translating peak intensity ratios to molar ratios of individual functional groups will be important next steps. Once biomolecules and degradation products are more readily quantifiable in complicated matrices, it may be possible to couple STXM-NEXAFS and NanoSIMS analyses to examine what compounds cells uptake as well as cellular quotas of biomolecules (e.g., protein content, C/N/O/P/micronutrients, etc.) as a function of sediment geochemistry.

Another vital step in developing NEXAFS spectroscopy will be quantifying spectral differences between mineral-adsorbed and free biomolecules. Theory predicts that direct bonding between hydroxyl groups on mineral surfaces and organic functionalities will alter the functional groups observed, their peak positions, and their relative intensities. Examining this effect will then potentially permit both better characterization and identification of compounds in complicated matrices as well as quantification of the mineral-associated fraction of OC in a given sample.

5.2.2 Linking short-term and geological time scales

Chapters 2—4 address questions regarding biogeochemical controls on carbon content and composition on very different time scales. Chapter 2 documents stable mineral-organic associations, while Chapter 4 finds that extremely old OC is protected from remineralization due to its recalcitrance, but that mineral-based protection and continual exposure to oxygen or other energetically favorable electron acceptors induce preferential preservation and degradation, producing the recalcitrance observed on > 1 million year time scales. A crucial future step will link these time scales, through not only continued analysis of environmental samples but also laboratory incubation experiments.

Turbidite deposits offer an opportunity to study the content and composition of OC protected by anoxia and the rate at which OC degradation occurs following re-exposure to oxygen (Cowie *et al.*, 1995; Meyers & Silliman, 1996). Sediment ponds and other sites where oxygen may diffuse upwards from basement fluids (D'Hondt *et al.*, 2009; Ziebis *et al.*, 2012; Russell *et al.*, 2016) are also good targets. At these sites, oxygen fluxes into sediments both from bottom waters and the basement, often with an anoxic or suboxic zone in the middle of the sediment column. As with turbidites, changes in OC content and composition with depth could be easily correlated with re-exposure to oxygen in such an environment if content and composition are such that they are still susceptible to oxic degradation.

Analyzing sediment cores with a wider range of sediment ages and redox states will also add to the results. This study, in particular, did not fully cover suboxic sites, or anoxic sites where sulfate reduction and methanogenesis predominate. Following the logic applied to results from oxic sediments in this study, old sediments (>1 Ma) will contain a similar content of OC with similar composition to that observed here so long as electron acceptors are not limiting. In locations where sediments become electron-acceptor limited on a shorter time scale, we expect preservation of a greater content of carbon and possibly of a greater chemical compositional diversity. As autotrophic fixation of carbon will contribute to replenishing the carbon pool, and as recently fixed OC will likely be more bioavailable than older OC transported from the surface ocean, a greater contribution from autotrophy to total metabolic activity will support a higher baseline concentration of OC.

Still, extensive field campaigns accessing deep, old sediments are not always possible, particularly at sites with high sedimentation rates, nor do the complicated matrices of environmental samples always allow de-coupling of variables. For these reasons, laboratory

experiments remain critical to linking short-term and long-term preservation dynamics. Having determined in Chapter 2 that mineral-organic associations form rapidly and are stable during mineral structural transformations, a series of experiments subjecting OC associated with varying mineral classes (Mn and Fe oxides, aluminosilicates, carbonates, biogenic silica, etc) to early diagenetic reaction conditions could expand on that work and make it more applicable to understanding sedimentary processes. Picard *et al.* (2016) examined high temperature/pressure effects on preservation of cellular material encrusted in biogenic iron oxides, finding that proteins disappeared in diagenetic treatments but lipids and extracellular polysaccharides were better preserved. However, this study submits samples to more extreme diagenetic conditions without pre-aging the OC and is better designed to address the potential for preservation of biosignatures than assess OC preservation potential more broadly. Experiments following this basic premise, but instead employing lower temperatures and pressures and active microbial communities, may better examine remineralization and re-partitioning of OC during early diagenesis. For instance, mineral-OC associations could be generated as they were in Chapter 2, with mineral precipitates then spiked into sediments maintained at redox potentials and pressures reflective of pelagic seafloor environments. Such a series of incubations would reveal the bioavailability of mineral-associated carbon and, for oxide minerals held at lower redox potentials, the fate of associated carbon during partial or complete mineral reduction. Iron oxides, for instance, may transform from one phase to another depending on redox conditions; whether associated OC would be liberated remains unknown. Experiments such as the one outlined here will test how systems transition from a stage where mineral-OC associations provide preservation to one that has reached a pseudo-steady state preserving only the most inaccessible, recalcitrant carbon.

5.2.3 Evaluating mineral-organic carbon interactions in environmental samples

While this research did not demonstrate a spatial correlation between OC and mineral-forming elements, we do not eliminate the idea of mineral-based protection entirely. Composition data derived from micro-scale STXM-NEXAFS are not high enough quality to assess the possibility of chemically-selective chemisorption processes, while the spatial scales of physical protection are not well-established. Bulk-scale data does implicate some degree of chemisorption and protection in a range of environments (Ransom *et al.*, 1998; Dickens *et al.*, 2006; Arnarson & Keil, 2007; Lalonde *et al.*, 2012; Roy *et al.*, 2013); bulk and micro-scale analyses as well as chemical extractions targeting specific mineral phases or organic compounds should be used in tandem to more intentionally evaluate this mechanism and its role on the geological time scale. Such work should include examination of the rock record and OC stored in lithified, uplifted sediments.

Physical protection was originally conceptualized as involving micropores <10 nm on mineral surfaces, where enzymes could not access OC wedged into those spaces (Mayer, 1994). Sedimentary OC profiles can be fit, however, by a reaction-diffusion model parameterized by cell spacing, sediment porosity, and the distance over which extracellular enzymes can diffuse before becoming inactivated (Rothman & Forney, 2007). Thus, in deeper sediments, a cell may be limited by its distance from bioavailable OC. Metagenomic (Tully & Heidelberg, 2016) and metatranscriptomic (Orsi *et al.*, 2013) evidence exists for motility and chemotaxis in the deep subsurface, but estimated mean metabolic rates suggest that flagellar motility should not be energetically possible (Hoehler & Jørgensen, 2013).

To better evaluate chemical and physical protection mechanisms, then, a multi-pronged approach should be taken. Improved STXM-NEXAFS preparation techniques that ensure even

optical density across the sample window and allow extraction of quality carbon NEXAFS spectra from mineral surfaces will contribute to knowledge regarding if and how mineral surfaces protect OC against remineralization and to what extent such a process is chemically selective. A greater number of STXM-NEXAFS observations, coupled with fluorescence microscopy of cells and transcriptomic analyses, could validate the model of Rothman and Forney (2007) by providing actual observations of cell spacing, OC distributions, and the plausibility of motility.

Higher resolution sampling and sampling techniques (benthic landers, multi-cores) designed to preserve the sediment-water interface will also allow better characterization of the surface interval where C appears to be utilized preferentially over N. This effect could be produced not only by C-limited microorganisms but also, in part, by compositional fractionation due to mineral-based protection. Chemical sorption to mineral surfaces selects for amide and carboxylic functionalities that complex with hydroxyl groups on the mineral surface. Thus, while we did not observe extensive mineral-organic associations in sediments (Chapter 4), that possibility is not fully eliminated.

Another approach to investigate the extent of mineral-organic interactions would be to simultaneously collect interstitial waters and solid phase samples and quantify partitioning between solid and aqueous phases. Amino acids are a promising compound class for this analysis, as their side chains contain a diversity of functionalities that will interact to varying degrees with mineral surfaces. Amino acids may be simultaneously used as a degradation index (Lomstein *et al.*, 2012) and contribute to interpretation of our findings of abundant proteins in these sediments by providing insight into protein source (e.g. detrital or more recent biomass). This information will allow us to distinguish between longer-term protection of proteins

followed by release at depth or a "sediment microbial loop" wherein relatively fresh microbial residues and proteins are temporarily stored on mineral surfaces prior to consumption and further recycling; the difference between these two scenarios has important implications for estimating the extent of life in the deep subsurface.

5.2.3 Identifying active metabolisms

This work advocates the idea that in old (>1 Ma) sediments where life is not limited by electron-acceptors, heterotrophic metabolisms persist and continually degrade OC, ultimately reaching a pseudo-steady state of minimal OC and sparse cells. What organisms in these systems are actually metabolizing and to what extent they are capable of growth and cell division remains uncertain. Microbes likely recycle necromass, but to sustain life this source of OC must be supplemented either by old, recalcitrant carbon delivered from the surface ocean or fixation of new OC by autotrophs. Proteases and oligosaccharide-degrading enzymes have been observed in genomic studies (Lloyd *et al.*, 2013; Tully & Heidelberg, 2016), but linking genomic potential to expression and function has not yet been accomplished. A final remaining question regards the significance of the compositional variability observed and the bioavailability of deep OC. Through NEXAFS and STXM-NEXAFS, we gain an understanding of the relative percent abundance of functional groups and the variability in composition both between sites, along the length of a core, and on the micro-scale. C/N of degradation values that match bulk C/N values suggest that, at depth, microbes non-selectively consume available organic matter and that the compositional diversity may not matter. Without knowing what of that material microbes are accessing and consuming, however, we cannot fully assess what mechanisms determine reactivity.

Efforts to isolate and cultivate organisms from the deep subsurface will aid in determining true metabolic potential (Russell *et al.*, 2016), as will improved genome annotations. For instance, we question whether deep subsurface proteases may be capable of hydrolyzing the amide bonds observed in NEXAFS spectra that are likely hosted by extremely degraded proteinaceous material, and to what extent that reaction continues to be energetically beneficial. Incubation studies using ^{13}C- and ^{15}N labeled compounds combined with NanoSIMS analyses (e.g., Morono *et al.*, 2011) can guide understanding of what compound classes may stimulate the microbial communities; however, in organic matter-limited sediments, addition experiments may not provide an accurate representation of the majority of organisms in that environment, possibly adapted to starvation. An inverse approach could concentrate organic matter from this system and, in controlled laboratory incubations, examine whether and how microbial communities access that material. Newly developed bioreactor systems capable of analyzing the content and isotopic composition of CO_2 generated by OC degradation (Beaupre *et al.*, 2016), for instance, offer an intriguing way to assess bioavailability, particularly if combined with NEXAFS or another spectroscopic approach.

5.3 References

Arnarson TS, Keil RG (2007) Changes in organic matter-mineral interactions for marine sediments with varying oxygen exposure times. *Geochimica et Cosmochimica Acta* **71**, 3545–3556.

Beaupre SR, Mahmoudi N, Pearson A (2016) IsoCaRB: A novel bioreactor system to characterize the lability and natural carbon isotopic (14C, 13C) signatures of microbially respired organic matter. *Limnology and Oceanography: Methods* **14**, 668–681.

Bennett SA, Toner BM, Barco R, Edwards KJ (2014) Carbon adsorption onto Fe oxyhydroxide stalks produced by a lithotrophic iron-oxidizing bacteria. *Geobiology*.

Burdige DJ (2007) Preservation of organic matter in marine sediments: controls, mechanisms, and an imbalance in sediment organic carbon budgets? *Chemical reviews* **107**, 467–85.

Chan CS, Fakra SC, Emerson D, Fleming EJ, Edwards KJ (2011) Lithotrophic iron-oxidizing bacteria produce organic stalks to control mineral growth: implications for biosignature formation. *The ISME journal* **5**, 717–27.

Cowie GL, Hedges JI, Prahl FG, Lange GJ de (1995) Elemental and major biochemical changes across an oxidation front in a relict turbidite: An oxygen effect. *Geochimica et Cosmochimica Acta* **59**, 33–46.

D'Hondt S, Spivack AJ, Pockalny R, Ferdelman TG, Fischer JP, Kallmeyer J, Abrams LJ, Smith DC, Graham D, Hasiuk F, Schrum H, Stancin AM (2009) Subseafloor sedimentary life in the South Pacific Gyre. *Proceedings of the National Academy of Sciences of the United States of America* **106**, 11651–11656.

Dickens AF, Baldock JA, Smernik RJ, Wakeham SG, Arnarson TS, Gélinas Y, Hedges JI (2006) Solid-state 13C NMR analysis of size and density fractions of marine sediments: Insight into organic carbon sources and preservation mechanisms. *Geochimica et Cosmochimica Acta* **70**, 666–686.

Hoehler TM, Jørgensen BB (2013) Microbial life under extreme energy limitation. *Nature Reviews - Microbiology* **11**, 83–94.

Kaznacheyev K, Osanna A (2002) Innershell absorption spectroscopy of amino acids. *The Journal of Physical Chemistry A* 3153–3168.

Lalonde K, Mucci A, Ouellet A, Gélinas Y (2012) Preservation of organic matter in sediments promoted by iron. *Nature* **483**, 198–200.

Lloyd KG, Schreiber L, Petersen DG, Kjeldsen KU, Lever M a, Steen AD, Stepanauskas R, Richter M, Kleindienst S, Lenk S, Schramm A, Jørgensen BB (2013) Predominant archaea in marine sediments degrade detrital proteins. *Nature* **496**, 215–8.

Lomstein BA, Langerhuus AT, D'Hondt S, Jørgensen BB, Spivack AJ (2012) Endospore abundance, microbial growth and necromass turnover in deep sub-seafloor sediment. *Nature* **484**, 101–104.

Mayer LM (1994) Surface area control of organic carbon accumulation in continental shelf sediments. *Geochimica et Cosmochimica Acta* **58**, 1271–1284.

Metzler R a, Kim IW, Delak K, Evans JS, Zhou D, Beniash E, Wilt F, Abrecht M, Chiou J-W, Guo J, Coppersmith SN, Gilbert PUP a (2008) Probing the organic-mineral interface at the molecular level in model biominerals. *Langmuir : the ACS journal of surfaces and colloids* **24**, 2680–7.

Meyers PA, Silliman JE (1996) Organic Matter in Pleistocene to Quaternary turbidites from sites 897, 898, 899 and 900, Iberia Abyssal Plain. *In Proceedings of the Ocean Drilling Program:*

Scientific results **149**, 305–313.
Morono Y, Terada T, Nishizawa M, Ito M, Hillion F, Takahata N, Sano Y, Inagaki F (2011) Carbon and nitrogen assimilation in deep subseafloor microbial cells. *Proceedings of the National Academy of Sciences of the United States of America* **108**, 18295–300.
Orsi WD, Edgcomb VP, Christman GD, Biddle JF (2013) Gene expression in the deep biosphere. *Nature* **499**, 1–6.
Picard A, Obst M, Schmid G, Zeitvogel F, Kappler A (2016) Limited influence of Si on the preservation of Fe mineral-encrusted microbial cells during experimental diagenesis. *Geobiology* **14**, 276–292.
Ransom B, Kim D, Kastner M, Wainwright S (1998) Organic matter preservation on continental slopes: importance of mineralogy and surface area. *Geochimica et Cosmochimica Acta* **62**, 1329–1345.
Rothman DH, Forney DC (2007) Physical model for the decay and preservation of marine organic carbon. *Science (New York, N.Y.)* **316**, 1325–8.
Roy M, McManus J, Goñi M a., Chase Z, Borgeld JC, Wheatcroft R a., Muratli JM, Megowan MR, Mix A (2013) Reactive iron and manganese distributions in seabed sediments near small mountainous rivers off Oregon and California (USA). *Continental Shelf Research* **54**, 67–79.
Russell JA, León-Zayas R, Wrighton K, Biddle JF (2016) Deep subsurface life from North Pond: Enrichment, isolation, characterization and genomes of heterotrophic bacteria. *Frontiers in Microbiology* **7**, 1–13.
Solomon D, Lehmann J, Kinyangi J, Liang B, Heymann K, Dathe L, Hanley K, Wirick S, Jacobsen C (2009) Carbon (1s) NEXAFS Spectroscopy of Biogeochemically Relevant Reference Organic Compounds. *Soil Science Society of America Journal* **73**, 1817.
Stewart-Ornstein J, Hitchcock AP, Cruz DH, Henklein P, Overhage J, Hilpert K, Hale JD, Hancock REW (2007) Using intrinsic X-ray absorption spectral differences to identify and map peptides and proteins. *Journal of Physical Chemistry B* **111**, 7691–7699.
Toner B, Fakra S, Villalobos M, Warwick T, Sposito G (2005) Spatially resolved characterization of biogenic manganese oxide production within a bacterial biofilm. *Applied and environmental microbiology* **71**, 1300–1310.
Tully BJ, Heidelberg JF (2016) Potential mechanisms for microbial energy acquisition in oxic deep- sea sediments. *Applied and Environmental Microbiology* **82**, 4232–4243.
Ziebis W, McManus J, Ferdelman T, Schmidt-Schierhorn F, Bach W, Muratli J, Edwards KJ, Villinger H (2012) Interstitial fluid chemistry of sediments underlying the North Atlantic gyre and the influence of subsurface fluid flow. *Earth and Planetary Science Letters* **323–324**, 79–91.